London's Global University

Surface Modification of Superhydrophobic Materials

Julie Jalila Kalmoni
Primary Supervisor: Prof. Claire Jane Carmalt
Secondary Supervisor: Prof. Christopher Stuart Blackman

Research Degree: Inorganic & Materials Chemistry
Doctor of Philosophy (PhD)

University College London
The Faculty of Mathematics & Physical Sciences
Department of Chemistry

Declaration

I, Julie Jalila Kalmoni, confirm that the work presented in my thesis is my own. Where information has been derived from other sources, I confirm that this has been indicated in the thesis.

Acknowledgements

I must start off by thanking my supervisors (Prof. Claire Carmalt & Prof. Christopher Blackman) who accepted me onto the PhD studentship and have never said “no” to me over the last 4 years. They have always supported me by encouraging me to publish my research, attend conferences, provided me with a spacious lab space and unlimited access to a range of characterisation techniques. Undoubtedly, this has all added value to my overall PhD experience.

I would like to express my gratitude to Dr. Sanjayan Sathasivam, who has a wealth of knowledge and willingly passed this on to me. Initially he trained me on how to carry out AACVD, then manuscript preparation and even after he left UCL, provided me with valuable career advice.

I am grateful to The Carmalt/Parkin research group, both past and present members, including Louise McSeveny. A special thank you goes to Dr. Shuhui Liu and Dr. Kristopher Page, both present and previous lab managers for the research group. They have both helped me to solve my endless “lab problems”.

Many thanks to everyone at UCL Chemistry, especially the technicians for helping me during lab demonstration and Martyn Towner for assisting me with the use of instruments. Thank you to the teaching team in the Chemistry Department and Dr. Sunny Bains in Engineering for both providing me with exceptional teaching experience.

Office 302 (past and present members) – we have had lots of laughs and an unforgettable trip to Italy. So, thank you!

Thank you to my close friends, especially Mathure, Kinza, Mariam, Afsana, Sahla, Hani, Rahaf and Galila who have been an immense form of support not just during my PhD but even during my MSci degree.

Undoubtedly, I would like to thank my mother for encouraging me to pursue a PhD whilst writing up my MSci dissertation during the COVID-19 pandemic. My immediate family in London and extended family in Lebanon (especially my uncle Youssef, my aunt Mariam and my grandmother Amal) have been especially supportive.

I am forever indebted to you all so thank you!

Abstract

This thesis explores the fabrication of fluorine-free superhydrophobic materials and their resultant surface modification with metal oxides via vapour phase deposition techniques, specifically aerosol-assisted chemical vapour deposition (AACVD) and atomic layer deposition (ALD).

Initially, superhydrophobic materials were produced without the use of fluoroalkylsilanes, which are fluorine-based chemicals needed to lower the surface energy of the materials. Low surface energy reagents are a requirement of superhydrophobic coatings. As an alternative, two of the most prevalent fatty acids were used instead. In addition to this, SiO_2 nanoparticles (needed to impart roughness), polydimethylsiloxane and ethyl acetate were used for the one-pot synthesis of this mixture, deposited via AACVD. To optimise the superhydrophobicity of these films, investigations into influential parameters such as temperature, concentration and time were comprehensively trialled.

The next study involved the deposition of TiO_2 via the titanium(IV) isopropoxide (TTIP) precursor by AACVD, as an additional layer on top of the superhydrophobic film. A range of concentrations and loadings were trialled to determine how the surfaces' properties and durability of the superhydrophobic films would change, potentially producing a photocatalytic self-cleaning film. Photocatalytic testing confirmed the improved photocatalytic properties of the films with the superhydrophobic underlayer. Hence the surface properties, morphology and overall durability were studied.

The optimum conditions for the synthesis of fluorine-free superhydrophobic films were selected for the next study involving the deposition of TiO_2 via the ALD of tetrakis(dimethylamido)titanium(IV). Visual inspection and X-ray photoelectron spectroscopy indicated a more uniform deposition of TiO_2 on the superhydrophobic films. Various cycle numbers and temperatures were investigated.

The final study involved depositing CeO_2 by AACVD onto the superhydrophobic films by using a lab-synthesised cerium dibenzoylmethane precursor. Again, the surface was studied and characterised. Unfortunately, the films showed reduced self-cleaning properties, poor thermal stability and relatively low WCAs.

Impact Statement

Work pursued for this PhD was initially centred on the fabrication of superhydrophobic films which did not employ the use of toxic and expensive fluoroalkylsilane reagents, a popular component of current hydrophobic/superhydrophobic materials such as Teflon™. Further steps were taken to reduce the concentration of reagents, overall reducing the cost per deposition, waste and improving the total efficiency. These films were deposited via AACVD, a technique that could be industrially scaled-up.

Once achieved, the superhydrophobic films were surface modified with metal oxides (of various loadings) and deposited via vapour phase deposition techniques such as AACVD and ALD. This was to determine changes at the surface and bulk of the film (including morphology). This relatively unexplored combination was used to introduce greater functionality in the superhydrophobic films such as improved robustness and photocatalytic activity. This novel method could potentially pave a new way to reducing our reliance on fluoroalkylsilanes by using metal oxides to improve the general robustness of the materials.

Increased investigations into this direction of research (in and outside of academia as well as nationally and internationally) could potentially lead to increased incorporation of such materials in sustainable buildings as we seek to move to environmentally friendly housing and developments. For example, possible applications of materials produced by this novel route include easy-to-clean coverings for flooring and public transport to prevent the accumulation of dirt and microorganisms, a catalyst in the spread of the COVID-19 virus. Other applications include self-cleaning floors, windows and solar panels (needed to keep the interface clean, maintaining efficiency).

Hydrophobic/superhydrophobic materials have many small and large applications that are worth millions and even billions of pounds, including anti-fouling coatings on solar panels and anti-corrosion coatings for boats. These monetary amounts are projected to increase further. However, these materials fall short due to their industrial challenges such as the use of toxic fluoroalkylsilanes, poor adhesion of the coating to the substrate and poor robustness.

Although the aforesaid applications have a strong foothold in the global economy, further research must be pursued to solve the technical challenges. This is especially imperative as we transition to less energy intensive processes, in a bid to achieve Net Zero by 2050.

The chapters of this thesis seek to demonstrate our shift from fluorinated superhydrophobic films to alternatives with lower toxicity, while also increasing functionality. Broadening the applications of superhydrophobic materials by tuning their surface with metal oxides is a significant step in the world of sustainable and multi-functional superhydrophobic materials.

UCL Research Paper Declaration Form

referencing the doctoral candidate's own published work(s) - Paper 1

Please use this form to declare if parts of your thesis are already available in another format, e.g. if data, text, or figures:

- *have been uploaded to a preprint server*
- *are in submission to a peer-reviewed publication*
- *have been published in a peer-reviewed publication, e.g. journal, textbook.*

This form should be completed as many times as necessary. For instance, if you have seven thesis chapters, two of which containing material that has already been published, you would complete this form twice.

5. For a research manuscript that has already been published (if not yet published, please skip to section 2)

a) **What is the title of the manuscript?**

A Single-Step Route to Robust and Fluorine-Free Superhydrophobic Coatings via Aerosol-Assisted Chemical Vapor Deposition

b) **Please include a link to or doi for the work**

https://doi.org/10.1021/acs.langmuir.3c00554

c) **Where was the work published?**

Langmuir Journal

d) **Who published the work?** (e.g. OUP)

American Chemical Society (ACS)

e) **When was the work published?**

May 22, 2023

f) **List the manuscript's authors in the order they appear on the publication**

J. J. Kalmoni, F. L. Heale, C. S. Blackman, I. P. Parkin and C. J. Carmalt.

g) **Was the work peer reviewed?**

Yes

h) **Have you retained the copyright?**

Yes

i) **Was an earlier form of the manuscript uploaded to a preprint server?** (e.g. medRxiv). If 'Yes', please give a link or doi)

No

If 'No', please seek permission from the relevant publisher and check the box next to the below statement:

☒

*I acknowledge permission of the publisher named under **1d** to include in this thesis portions of the publication named as included in **1c**.*

5. For a research manuscript prepared for publication but that has not yet been published (if already published, please skip to section 3)

a) **What is the current title of the manuscript?**

Click or tap here to enter text.

b) **Has the manuscript been uploaded to a preprint server?** (e.g. medRxiv; if 'Yes', please give a link or doi)

Click or tap here to enter text.

c) **Where is the work intended to be published?** (e.g. journal names)

Click or tap here to enter text.

d) **List the manuscript's authors in the intended authorship order**

Click or tap here to enter text.

e) **Stage of publication** (e.g. in submission)

Click or tap here to enter text.

5. **For multi-authored work, please give a statement of contribution covering all authors** (if single-author, please skip to section 4)

J.J.K. Wrote the manuscript and fabricated and characterised all the films mentioned in the paper.

F.L.H. initially investigated producing fluoroalkylsilane films using 1*H*,1*H*,2*H*,2*H*-perfluorooctyltriethoxysilane via AACVD.

C.S.B. Supervised the work and contributed to the manuscript.

I.P.P was F.L.H's supervisor therefore supervised her initial experiments and contributed towards the manuscript.

C.J.C Supervised the work and assisted with the writing of the initial draft of the manuscript.

The authors were involved in discussions of the final draft of the manuscript.

5. **In which chapter(s) of your thesis can this material be found?**

   Chapters 2, 3, 4, 5

5. **e-Signatures confirming that the information above is accurate** (this form should be co-signed by the supervisor/ senior author unless this is not appropriate, e.g. if the paper was a single-author work)

Candidate

Julie Jalila Kalmoni

Date:

5.09.2024

Supervisor

Claire Carmalt

Date

05.09.2024

UCL Research Paper Declaration Form

referencing the doctoral candidate's own published work(s) - Paper 2

Please use this form to declare if parts of your thesis are already available in another format, e.g. if data, text, or figures:

- *have been uploaded to a preprint server*
- *are in submission to a peer-reviewed publication*
- *have been published in a peer-reviewed publication, e.g. journal, textbook.*

This form should be completed as many times as necessary. For instance, if you have seven thesis chapters, two of which containing material that has already been published, you would complete this form twice.

1. **For a research manuscript that has already been published** (if not yet published, please skip to section 2)

j) **What is the title of the manuscript?**

Tuneable Wetting of Fluorine-Free Superhydrophobic Films via Titania Modification to Enhance Durability and Photocatalytic Activity.

k) **Please include a link to or doi for the work**

https://doi.org/10.1002/admi.202400519

l) **Where was the work published?**

Advanced Materials Interfaces

m) **Who published the work?** (e.g. OUP)

Wiley-VCH

n) **When was the work published?**

August 13 2024

o) **List the manuscript's authors in the order they appear on the publication**

J. J. Kalmoni, C. S. Blackman, I. P. Parkin and C. J. Carmalt.

p) **Was the work peer reviewed?**

Yes

q) **Have you retained the copyright?**

Yes

r) **Was an earlier form of the manuscript uploaded to a preprint server?** (e.g. medRxiv). If 'Yes', please give a link or doi)

No

If 'No', please seek permission from the relevant publisher and check the box next to the below statement:

☒

*I acknowledge permission of the publisher named under **1d** to include in this thesis portions of the publication named as included in **1c**.*

2. **For a research manuscript prepared for publication but that has not yet been published** (if already published, please skip to section 3)

f) **What is the current title of the manuscript?**

Click or tap here to enter text.

g) **Has the manuscript been uploaded to a preprint server?** (e.g. medRxiv; if 'Yes', please give a link or doi)

Click or tap here to enter text.

h) **Where is the work intended to be published?** (e.g. journal names)

Click or tap here to enter text.

i) **List the manuscript's authors in the intended authorship order**

Click or tap here to enter text.

j) **Stage of publication** (e.g. in submission)

Click or tap here to enter text.

3. **For multi-authored work, please give a statement of contribution covering all authors** (if single-author, please skip to section 4)

J.J.K. Carried out all experiments and characterisation. She wrote the manuscript.

C.S.B. and C.J.C supervised the work and contributed to the manuscript.

4. **In which chapter(s) of your thesis can this material be found?**

   Chapters 3, 4, 5

5. **e-Signatures confirming that the information above is accurate** (this form should be co-signed by the supervisor/ senior author unless this is not appropriate, e.g. if the paper was a single-author work)

   Candidate

   Julie Jalila Kalmoni

   Date:

   5.09.2024

   Supervisor/

   Claire Carmalt

   Date

   05.09.2024

List of Figures

List of Tables

List of Abbreviations

AACVD - Aerosol-assisted chemical vapour deposition

ACA - Advancing contact angle

ALD - Atomic layer deposition

ATR - Attenuated total reflection

CAH - Contact angle hysteresis

$Ce(dbm)_4$ - Cerium dibenzoylmethane

CPS – Counts per second

CVD - Chemical vapour deposition

dbm - Dibenzoylmethanate

DI - Deionised

E_{bg} - Energy band gap

EDS - Energy dispersive spectroscopy

FAS C_8 - 1H,1H,2H,2H-perfluorooctyltriethoxysilane

FTIR - Fourier Transform Infrared Spectroscopy

FTIR-ATR - Fourier Transform Infrared Spectroscopy - Attenuated Total Reflection

N-P - Not plasma treated

NPs - Nanoparticles

PA - Palmitic acid

PDMS - Polydimethylsiloxane

PVD - Physical vapour deposition

RCA - Receding contact angle

RMS - Root-mean-square

SA - Stearic acid

SAs - Sliding angles

SEM - Scanning electron microscopy

SH - Superhydrophobic

SiO_2 - Silicon dioxide

SLIPS - Slippery Liquid-Infused Porous Surfaces

T - Transmittance

TEOS - Tetraethyl orthosilicate

TTIP - Titanium(IV) isopropoxide

WCA - Water contact angle (static)

XPS - X-ray photoelectron spectroscopy

UV - Ultraviolet

UV-vis - Ultraviolet-visible

Table of Contents

Chapter 1 – Introduction

1.1 Superhydrophobicity

Superhydrophobicity, or water repellence, is a growing area of interest within the field of Materials Chemistry. This property was initially observed in lotus leaves by Neinhuis and Barthlott in the late 1990s and is described as the Lotus Effect.[1] It is where water droplets are seen rolling across the surface of the leaf rather than sticking or wetting it. Superhydrophobicity arises due to the hydrophobic waxy cuticle coating in addition to the microscopic bumps and trapped air spaces which are present throughout the leaf.[2]

Water repellence is a vital property for small and large-scale applications where water interactions can cause the material to corrode or worse, hinder performance. Superhydrophobic materials have potential uses in anti-fouling, anti-wetting, self-cleaning and anti-corrosion coatings which are worth millions and even billions of pounds, with these amounts set to increase further. Anti-icing coatings on aeroplanes employ superhydrophobic coating techniques to prevent water adhering to the surfaces of the aircrafts, which could be detrimental to the aerodynamics.[3] The use of superhydrophobic corrosion resistant coatings is becoming prevalent in an effort to reduce the interaction between a corrosive environment and the object via the air pockets in the superhydrophobic film.[4]

Superhydrophobic methods are equally important in small-scale industries, examples include tuning the hydrophilicity of fabrics such as cotton, to create water resistant materials such as rain-proof outerwear.[5] Self-cleaning windows are another application of (super)hydrophobic materials, involving an easy-to-clean coating, incorporated into the manufacturing of domestic glass windows.[6]

1.2 Surface Wettability

Surface wettability determines the interaction between water and a surface and hence its hydrophobicity, which is quantified through a series of measurements including the static water contact angle (WCA).[2] This angle is measured when a water droplet (in the μL range) is dropped and remains stationary on a surface, and it is the angle between the edges or interface of a solid surface and the water droplet. Undoubtedly, this is the most used measurement to determine wettability. Water droplets on superhydrophobic materials have a static WCA greater than or

equal to 150°.[7] Apart from the term superhydrophobic, three other terminologies can be used to describe the wettability of a surface by the size of its static water contact angle, namely hydrophobic (90°≤θ<150°), hydrophilic (10°>θ>90°) and superhydrophilic (θ≤10°), **Figure 1.01**.[8] Average water contact angles and shapes are summarised in . Although the focus of this thesis will be on hydrophobic/superhydrophobic materials, all classes of wettability are important, depending on their application. For example, slippery liquid-infused porous surfaces (SLIPS), possess intricate nano-/micro-scale roughness, impregnated with a lubricating gel causing contaminants to "slip" across the surface.[9] Such materials are being studied for potential applications in anti-icing coatings on aeroplanes due to its low ice adhesion.[9]

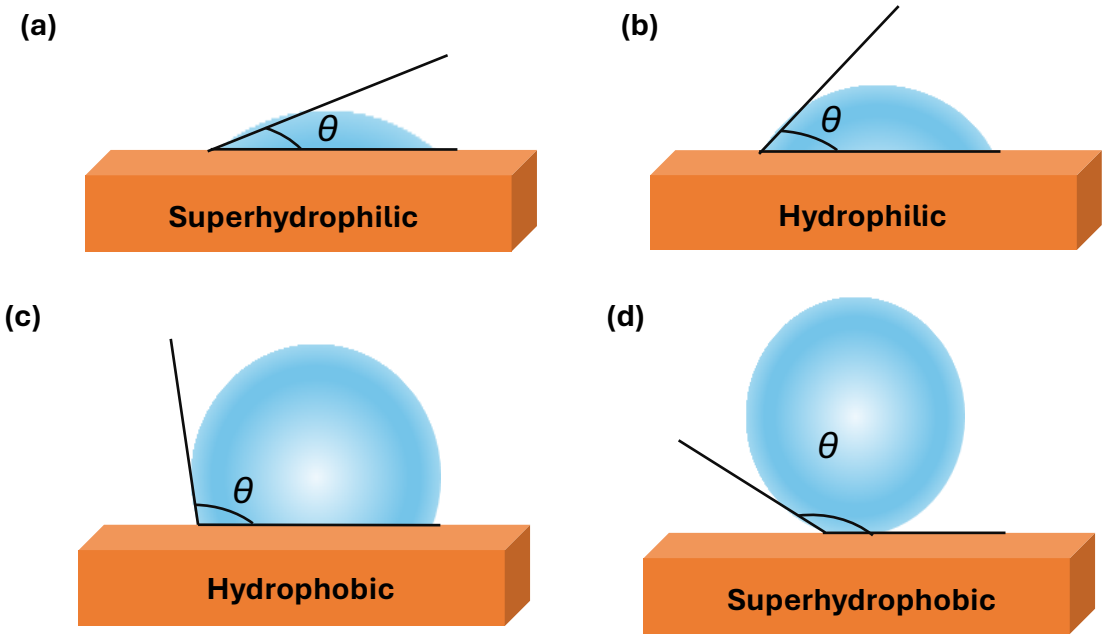

Figure 1.01. *Visual representation of surface wettability - the shapes of the water droplets on a surface and their resultant static water contact angle (WCA). Superhydrophobicity (θ>150°), hydrophobicity (90°≤θ<150°), hydrophilicity (10°>θ>90°) and superhydrophilicity (θ ≤10°).*

The contact angle hysteresis (CAH) is a dynamic water contact angle measurement and is used in conjunction with the static water contact angles to determine the extent of superhydrophobicity of a surface. For superhydrophobic materials, this should be <10°.[4] Unlike the static water contact angle, contact angle hysteresis determines how likely it is for a water droplet to roll off or stick to a surface.[10] The method involves finding the difference between the advancing and receding angles, as shown in **Figure 1.02**.[11] To begin with, a water droplet is placed on a horizontal surface, an additional volume is added to it so that it increases to approximately 10 μL before the advancing angle is measured. Then,

water is removed from the droplet so that it reduces to approximately less than half of that volume and the receding angle is then calculated.[12] The expansion and reduction of the water droplet must take place at the same velocity.[13]

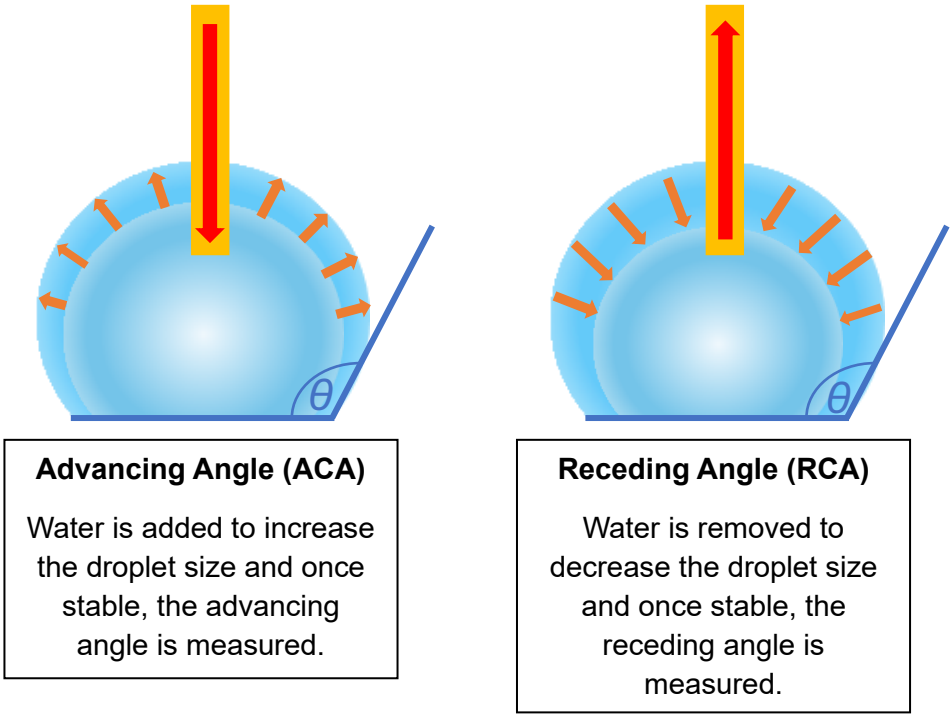

Figure 1.02. *Method used to form the advancing (ACA) and receding angles (RCA) to ultimately calculate the contact angle hysteresis, redrawn from a paper by Huhtamäki et al.[12] ACA is when the volume of the water droplet increases, increasing the distance of contact between the water droplet and the surface. RCA are contrariwise.*

Measuring the tilt angle, also known as the sliding angle, is another important measurement of wettability. Once the substrate is placed onto the tilted platform (a set degree of inclination), water droplets are impinged onto the surface which start to move downwards due to the force of gravity. The sliding angle is the angle between the initial position of the substrate and the position of the substrate as the water droplet begins to move, **Figure 1.03**.[12] The process is repeated at various degrees of inclination until the water droplet can no longer roll off the surface. In summary, a surface is superhydrophobic if it has a static WCA that is greater than or equal to 150°, a contact angle hysteresis that is less than 10° and a sliding angle of less than 10°.[2]

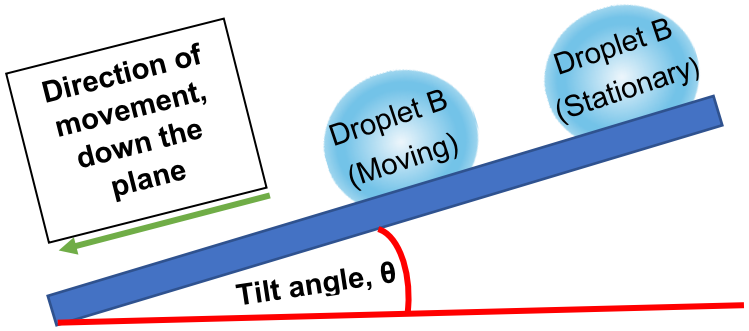

Figure 1.03. *The method used to calculate the sliding angle; measurements are taken as soon as Droplet B begins to move.*

1.3 Models for superhydrophobicity

Superhydrophobicity requires the combination of hierarchical roughness which incorporates nano- and micro-scale particles along with a reagent of low surface energy (e.g. fluoroalkysilanes, long chain hydrocarbons or fatty acids).[14] This can be visualised below in **Figure 1.04**. Fluoroalkylsilanes with terminal -CF_3 groups have water contact angles of only 120°; therefore, hierarchical roughness is required to impart superhydrophobicity.

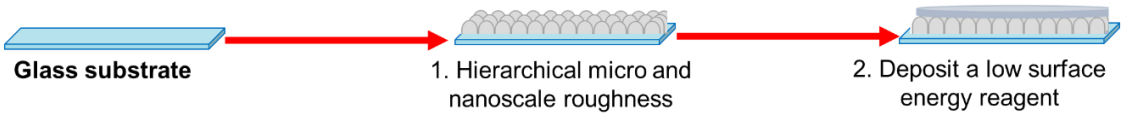

Figure 1.04. *The requirements for producing a superhydrophobic film – hierarchical roughness and a low surface energy reagent.*

A hydrophilic surface would contain an anion or hydrogen acceptor at its surface. Hence, the H_2O molecules arrange themselves on the surface in a specific manner, with the H^+ ions directing towards the electron-rich surface forming strong hydrogen bonds.[15] On the other hand, a hydrophobic surface, which is inert, would not have such a constraint. Hydrophobic surfaces are inert and do not possess an overall charge and therefore disrupt hydrogen bonding of water molecules to the surface. Fluoro- and hydro- carbons are non-polar; the apparent hydrophilicity of polar groups can be defused once attached to a hydrocarbon chain.[16] Hence, strong inter- and intra- molecular bonding such as hydrogen and ionic bonding cannot occur between the surface and H_2O molecules.

As described earlier, water molecules interacting with a hydrophilic surface is directional hence also adding a steric restriction. As a result, the size of the water droplet increases.[16] In addition, such restrictions limits charge transfer mechanisms. On the other hand, such directional bonding is not present in hydrophobic surfaces, where although H_2O molecules are systematically aligned

across the hydrophobic surface, they can orientate without restriction. As a result, charge transfer mechanisms are possible, leading to hydrophobic interactions.[17]

In addition, there is a balance between adhesive and cohesive forces.[18] If the surface energy of the solid surface (i.e. the adhesive force between the substrate and water droplet) is greater than the surface tension of the liquid (i.e. the cohesive forces/hydrogen bonding between the water droplets), this results in complete wetting of the surface.[19] This is a (super)hydrophilic surface. Alternatively, if the adhesive forces are less than the surface tension (i.e. cohesive forces), there is non-wetting of the surface by a water droplet, a (super)hydrophobic surface.

1.3.1 Young's Model

Over the years, several models have been developed and revised to aid our understanding of superhydrophobicity. In 1805, Thomas Young derived **Equation 1** (the Young equation) which determines the shape of a water droplet on a smooth and homogenous surface.[20] It links the solid-liquid interface (surface tension), liquid-vapour (interfacial tension) and vapour-solid interface (surface free energy) as well as the static water contact angle.[20] The wettability is affected by the chemical composition of the surface as this relates to the surface energy.[21] On re-arranging **Equation 1**, it is clear that the surface free energy is inversely proportional to the WCA. The water contact angle can be determined by a drop shape analyser, the surface tension of known liquids can be obtained from literature and the surface free energy can be determined through the Owens-Wendt method.[15,22] All of these parameters can be inserted into The Young Equation to calculate the interfacial tension of the surface, however, this equation can only be applied to entirely smooth homogenous surfaces.

$$\gamma_{sv} = \gamma_{sl} + \gamma_{lv} \cdot \cos\theta \qquad \textbf{(1)}$$

Where γ_{sv} is the surface free energy, γ_{sl} is the surface tension, γ_{lv} is the interfacial tension and θ is the static water contact angle for smooth homogenous surfaces.

1.3.2 Wenzel's Model

Only being able to apply this equation to homogenously flat surfaces posed difficulty for measuring homogenous rough surfaces hence The Young Equation was later modified (**Equation 2**) by Robert Wenzel in 1936.[20] Due to the roughness of the surface, a roughness coefficient has been incorporated to accommodate a rise in surface tension and surface free energy while the

interfacial tension remains the same. The equation demonstrates a linear relationship between all parameters of the equation as the liquid droplet adapts with the surface's morphology. However, this model assumes that the water droplet makes complete contact with the surface, not accounting for the trapped air within the protrusions of the rough surface.[23] Water droplets that exhibit a Wenzel wetting regime tend to "stick" to the surface, moving with more difficulty.

$$\cos\theta_w = r \cdot \cos\theta \qquad (2)$$

Where θ_w is the measured contact angle and θ is the young contact angle. r is the roughness coefficient (the ratio between the actual and projected solid surface area), r > 1. The roughness can be measured using techniques like Atomic Force Microscopy (AFM) and profilometry.

1.3.3 Cassie-Baxter's Model

A further modification was made by Cassie and Baxter to **Equation 2**, applying it to porous heterogenous rough surfaces, where the water droplets do not completely wet the surface. Instead, most of the water droplet is in contact with the peaks of the surface, creating the solid-liquid interface, denoted by f (**Equation 3**). A small proportion of the water droplet will interact with the air spaces of the surface creating the liquid-vapour interface.[24] Here, water droplets are more likely to roll off rather than stick (as seen with Wenzel's model), making this a preferred model for describing superhydrophobic surfaces, **Figure 1.05**.[2]

$$\cos\theta_{CB} = r \cdot f(\cos\theta + 1) - 1 \qquad (3)$$

θ_{CB} is the value of the Cassie-Baxter angle, r is the roughness coefficient, f is the percentage of the surface wetted and θ is the static water contact angle.[25]

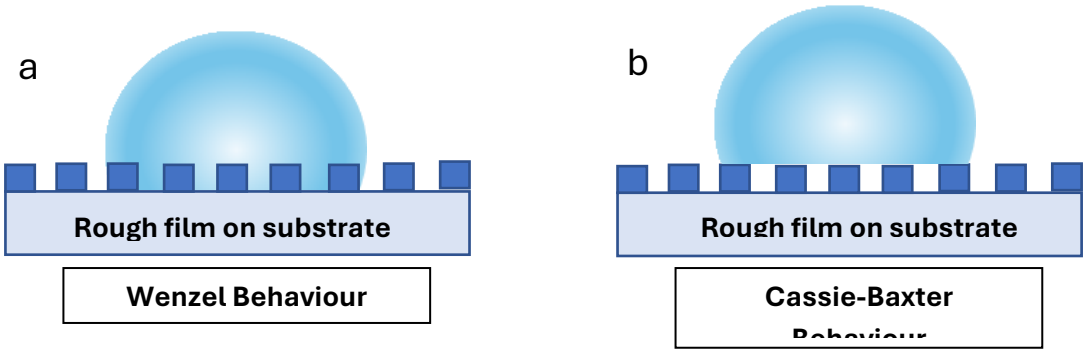

Figure 1.05. *Two models used to display hydrophobicity/superhydrophobicity. a. exhibits Wenzel behaviour where the water droplet 'sticks' to the surface as it can penetrate the protrusions. b. exhibits Cassie-Baxter behaviour where the water droplet interacts with the peaks of the protrusions and air pockets. Here, the water droplet is more likely to slip or roll off.*

1.4 Preparation of Superhydrophobic Surfaces

The production of superhydrophobic films are categorised into top-down, bottom-up and a combination of approaches.[2] Bottom-up methods involve using micro- and nano-scale units to build a structure, whereas top-down approaches are the opposite and involve starting with a bulk material. Examples along with descriptions of each are outlined in **Table 1**.[2] A precursor is a mixture of chemical components in the desired composition to deposit a thin film.

Table 1. *Commonly used top-down and bottom-up techniques for producing superhydrophobic surfaces.*

Top down	**Description**[2,7,26]	**Bottom up**	**Description**[2,7,26]
Lithography[27]	Imprinting a pattern into a substrate to create a structured surface.	Spin coating[28]	A precursor mixture is added to the centre of the substrate, which is then spun using a centrifugal force, spreading the coating to create a uniform film.
Templating[29]	A porous template is made and filled with the coating material. The inverse of this pattern is transferred to the substrate.	Sol–gel[30]	This is where metal alkoxides are repeatedly hydrolysed and condensed to create a network on a substrate.
Plasma Etching[31]	To introduce and improve the micro-scale roughness, parts of the substrate are covered with a protective layer. Reactive gases are sent through with plasma and those with sufficient energy can “etch” or remove the atoms on the substrate’s surface.	Chemical vapour deposition[32]	A chemical precursor is volatilised which reacts with a heated substrate and deposits the precursor mixture as a solid film. There are several versions of this technique including aerosol-assisted chemical vapour deposition which will be discussed in **Section 1.5: Vapour Phase Depositions.**

1.4.1 Top-down Approaches of Fabricating Superhydrophobic Materials

Top-down techniques involve modifying the surface of the substrate, which are highly substrate dependent, for instance, flexible polymer substrates cannot be used in photolithography due to degradation at high temperatures (>120 °C).[33]

Work completed by Zhang *et al*. involved UV nanoimprint lithography comprised of a soft lithography approach, specifically stamp moulding replica and UV-curing methods.[34] Stamp moulding replica is an inexpensive and favourable technique with up-scaling potential due to its low cost. UV-curing methods display features of “E”, relating to its low cost and “green” procedure; examples of the “E” attributes include economical, energy-saving, efficient and ecofriendly.[35] However, this method of UV nanoimprint lithography has drawbacks due to its inability to accurately replicate the complete structure, the nano-tube topology of lotus leaves. Within the research by Zhang *et al*., a negative stamp of the lotus leaf was prepared via polydimethylsiloxane (PDMS), imprinted onto a glass substrate containing polyurethane acrylate and cured under high intensities of UV light, only partially replicating the desired nano-tube structure, however displaying self-cleaning properties and a WCA >160°.[34]

Keerthi *et al.* fabricated a superhydrophobic material for elemental detection of bodily fluids by surface-enhanced laser-induced breakdown spectroscopy however, technical challenges included producing economically feasible and industrially scalable substrates.[36] Within this work, a Teflon™ substrate was laser patterned to generate a nanostructure, filled with PDMS and cured at 75 °C. Although this method proved cheaper and scalable, it employed the use of a Teflon™ substrate, a toxic fluorinated polymer.

Ho *et al.* developed a lotus bioinspired superhydrophobic surface prepared by a multi-step templating method through micromachining domes (200 μm deep) into an aluminium substrate.[37] A polycarbonate membrane was added on top with polypropylene and the polymer imprinting was facilitated by heat and pressure. The dome-like structure was etched into the polymer. Although the film had a superhydrophobic water contact angle (>150°) and contact angle hysteresis <10°, the film involved multiple steps and imprinted into a polymer rather than a conventional substrate (e.g. glass/metal), as required for large scale applications.

Xie *et al.* produced a superhydrophobic coating for a wood substrate through initially O_2 plasma etching the wood surface before depositing a thin film of pentafluoroethane polymer or diamond-like carbon.[31] Both materials displayed superhydrophobicity however, the water molecules stuck/pinned onto the carbon-modified plasma etched wood substrate, even at high tilt angles, limiting its self-cleaning abilities. Although the pentafluoroethane equivalent exhibited high water contact angles of 158°, even at etch times as low as 5 min and deposition thicknesses as low as 100 nm, a fluoroalkylsilane was used and the sliding angle still remained high (>10°). In all mentioned cases, substrate choice was limited, with many resorting to PDMS, the process required multiple steps and occasionally employed fluorinated polymers to give it its superhydrophobic character.

Alternative routes have involved combining several top-down methods to construct a superhydrophobic material. For instance, research by Dong *et al.* combined laser interference lithography with inductively coupled plasma etching to produce a surface with tuneable superhydrophobicity, by adjusting the height of the pillar arrays via the inductively coupled plasma etching step.[38] A photoresist was spin coated onto a Si substrate, which underwent a three-beam laser interference lithography technique, creating a honeycomb structure in the photoresist. A film of Au was deposited onto the hybrid and the honeycomb photoresist was removed for plasma etching onto the Si composite with periodic Au discs, creating a pillar array in the Si substrate.

1.4.2 Bottom-up Approaches of Fabricating Superhydrophobic Materials

Bottom-up approaches involve coating a substrate with a film by chemical or physical techniques rather than modifying the substrate's surface, leading to fewer constraints as the process does not depend on the properties of the substrate.[39] In spite of this, bottom-up approaches form uneven coatings and/or occasionally employ toxic solvents for ease of evaporation.[2] For instance, work by Meena *et al.* involved spin coating a mixture of silica nanoparticles (NPs), hexadecyltrimethoxysilane and polymethylmethacrylate in toluene to produce a superhydrophobic coating with a high static water contact angle of 165° despite using the solvent toluene.[28] Wang *et al.* afforded a superhydrophobic nanocomposite material of poly(methylmethacrylate) and SiO_2 NPs (initially dissolved in chloroform), on glass substrates by a spin coating technique.[40]

Sol-gel methods are low cost, simple and scalable. They are a common bottom-up approach where a reagent (e.g. Tetraethyl orthosilicate (TEOS), a precursor for SiO_2) is initially hydrolysed to form a sol, which then ages via condensation and polymerisation to form a gel. Parameters such as the drying method, pH and precursor selection can affect the properties of the resultant gel. This gel can then coat a variety of substrates from glass through to cotton, silk and wood, via other bottom-up deposition techniques such as spin coating and dip coating. Alternative work by Li *et al.* involved spin coating a sol-gel mixture of SiO_2 NPs onto glass substrates, which were also annealed, followed by the spin coating of hexadecyltrimethoxysilane (HDTMS), forming a highly porous (super)hydrophobic structure with a rough topography.[41] The porosity contributed to the significantly high transmittance of >90% with potential implementation in coatings for solar panels.

1.4.3 Technical Problems for Fabrication of Superhydrophobic Materials

Superhydrophobicity has many real world applications as outlined earlier such as producing biomedical,[42] self-cleaning[43] and corrosion resistant materials.[44] Nevertheless, superhydrophobic coatings have many obstacles that limit complete implementation in industry. As mentioned previously, the fabrication of superhydrophobic materials requires the production of micro-/nano-scale roughness, typically by using NPs and a low surface energy, commonly by a fluorinated or non-fluorinated polymer (e.g. fluoroalkylsilanes or hydrocarbons, respectively).[14]

Non-fluorinated alternatives such as fatty acids have been used to produce superhydrophobic coatings, such as fatty acid coated silica and metal NPs.[45] Fatty acids such as stearic acid and palmitic acid consist of a hydrocarbon chain with a carboxyl group and their properties change depending on the length of the hydrophobic chain, **Figure 1.06**. A specific example includes work produced by Heale *et al*. where the properties of films were investigated with increasing carbon chain length.[46] The work concluded that an increase in length of the hydrophobic carbon chain led to an increase in superhydrophobicity, not only due to its low surface energy but also the ordered, close-packed nature of the alkyl chain leading to water repellence to the impinged water droplet.[45,46,47]

Often fluorine-free superhydrophobic films display good superhydrophobicity but poor transparency relative to their fluorinated equivalent as demonstrated by

work by Huo *et al.* where a composite of HDTMS functionalised SiO_2 NPs and poly(butylmethacrylate), deposited via AACVD exhibited WCAs >160° but transparencies <20% (300 – 800 nm region). Fluoroalkylsilane-based superhydrophobic materials have been reported with transparencies >90%.

However, use of these fluorinated compounds pose a serious risk to the environment and human health, potentially causing kidney disorders, decreased fertility and immunotoxicity.[48,49] There is considerable use of fluorinated silane polymers, **Figure 1.06**, which are used as low surface energy reagents to post-treat films due to their high durability and lower affinity for water relative to hydrocarbons.[50,51] A $-CF_3$ group has a lower surface energy than a $-CH_2$ group due to its strong covalent bonds and low polarizability of the C-F bond.[52] Compounds with terminal $-CF_3$ groups have water contact angles of 120°; therefore hierarchical roughness is required to impart superhydrophobicity.

Also, fluorinated films show higher transparencies than their non-fluorinated equivalents. Zhuang *et al.* reported the AACVD deposition of polytetrafluoroethylene at 450 °C.[53] This produced a film with a static water contact angle of 168°, which also maintained its superhydrophobicity after thorough robustness tests such as acid/base exposure for 24 h and sand grain impingement. In addition, the films exhibited excellent transparencies of up to 92% (in the 340 – 800 nm region), due to the inherent high reflectance of the polytetrafluoroethylene precursor and the resultant distance between the nano-/micro-particles in the film, reducing the scattering and facilitating the penetration of visible light. In addition to using fluorinated polymers to maintain high transparencies, another strategy is to keep film deposition times low (<5 min) and to utilise a layer-by-layer approach as demonstrated by research by Tombesi *et al*.[54] Within this work, layers of SiO_2 (via the tetraethyl orthosilicate precursor) and 3-methacryloxypropyltrimethoxysilane were initially deposited to generate nano-/micro-scale roughness and perfluorooctyltriethoxysilane was deposited as a final coating to reduce the overall surface energy.

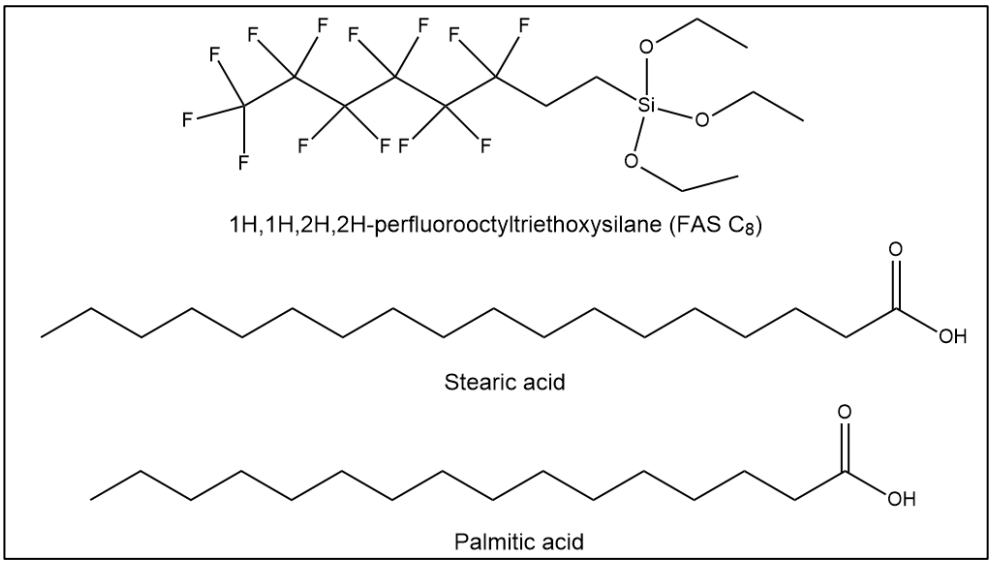

Figure 1.06. *The structure of 1H,1H,2H,2H-perfluorooctyltriethoxysilane (FAS C_8), a toxic fluoroalkylsilane polymer used to produce superhydrophobic surfaces, consisting of an Si atom connected to a C-F backbone and ethoxy leaving groups. Structures of two fatty acids (stearic and palmitic acid) are also included; these non-toxic alternatives consist of an aliphatic carbon backbone (hydrophobic) attached to a carboxyl group.*

Moreover, it is believed that the fragility of the nano-/micro-scale structures that protrude from the surface of a substrate, regardless of whether a fluorinated polymer has been employed, leads to its insufficient mechanical durability for large scale applications. An innovative strategy involves producing “self-healing” films where films “self-heal” by external stimuli such as heat, humidity and UV or even practical conditions such as room temperature.[2] The material can “self-heal” via the transfer of low surface energy molecules from the bulk of the material to its surface through the repair of its morphology after damage, or a combination of both strategies.[55] Although many examples focus on fluorine-based materials (e.g. fluoroalkylsilanes and perfluorooctyl acid), there is interest in fabricating fluorine-free self-healing superhydrophobic films (e.g. octadecylamine).

For example, Wang *et al.* focused on fabricating a PDMS/nonadecane composite onto a glass substrate via templating and chemical vapour deposition (CVD).[56] The concept aimed to mimic the self-replenishment of low surface energy reagents, stored in the hierarchical roughness of a plant’s epicuticle wax, and released under standard or deviations in external conditions or climate (e.g. temperature, humidity). In this case, the PDMS/10wt% of nonadecane composite was exposed to 6 min of O_2 plasma etching and superhydrophobicity was restored whilst the composite was left for 20 min at room temperature. The self-healing ability was co-operative due to the flexibility of the PDMS polymer and

hence rapid movement of nonadecane molecules, as well as the latter's low melting point. Bai *et al.* spray-coated a superhydrophobic mixture of polymethylacrylate, stearic acid and zinc stearate which displayed self-healing properties via the restoration of the rough topology on exposure to water.[57] Water molecules could penetrate the polymethylacrylate structure, leading to an expansion of the flattened structure and on drying, the re-established hierarchical structure remained.

Apart from mechanical damage to the nano-/micro-structure of a superhydrophobic material, these materials are also prone to solvent damage due to the low surface tension of these liquids which can infiltrate into the hierarchical roughness and erode it. Although superhydrophobic materials are water repellent, over time, continuous water exposure (e.g. flowing of tides, water in pipes) infiltrates into the air gaps due to increased pressure. In addition, superhydrophobic materials that do not have water molecules moving across their surface, can potentially accrue and house masses of microorganisms, which can be a challenge to completely remove without damaging the complex microstructure. Although use of metal oxides with antibacterial properties such as zinc oxide and copper oxide with the superhydrophobic precursor can garner some protection.[58]

On the other hand, slippery liquid-infused porous surfaces (SLIPS), are bio-inspired by *Nepenthes* pitcher plants, can act as an alternative material to superhydrophobic films.[59] SLIPS are comprised of hierarchical roughness coated with a lubricating liquid which creates a smooth surface and has potential to contribute to the repair of its own film (i.e. self-healing properties). The contact angle hysteresis of such materials is lower than that of superhydrophobic materials (<5° vs. <10°) allowing water molecules to glide or "slip" across the SLIPS. Similarly, the static water contact angles are lower, 90° vs. >150°. Work by Wang *et al.* fabricated a transparent SLIPS coating comprised of a superhydrophobic hydroxyapatite undercoat in the shape of nanowires with oleic acid infused into the gaps.[60] The resultant SLIPS had a transparency >75% compared to the superhydrophobic hydroxyapatite film (0%). In terms of durability, the film remained stable after high pressure water jet sprays and continuous immersion for a month. Promising performance testing results demonstrated the film's ability to "self-clean" and remove food stains of various

pHs from energy drinks (pH = 4) to tea (pH = 8) at sliding speeds less than 2 mm/s. Nevertheless, SLIPS, like superhydrophobic materials possess many challenges, including the use of low surface energy perfluorinated lubricating oils and slow evaporation of the contaminating solvent which leads to infiltration and hence damage to the complex topology.[59]

A final technical challenge posed by superhydrophobic coatings is their poor adherence to their substrates, namely glass, mainly due to the presence of low surface energy reagents. This is a particular challenge when it is incorporated into a one-pot precursor mixture and hence deposited as a single step, as this lowers the overall surface energy of the film. A low surface energy reagent has difficulty bonding to external entities due to its high stability. Visually, such films are powdery and rub off (even with a gentle force), **Figure 1.07**. Therefore, approaches include pre-/during-/post-treatment of the substrate/coating.

Pre-treatment of a substrate include improving the cleaning of the substrate, by acid/base treatment and plasma treatment as this removes organic contaminants and increases the number of silanol groups for reaction. Another method is the use of adhesion promoters such as epoxy resins, amino silanes and hexamethyldisilazane to encourage surface chemistry reactions, leading to more reactive functional groups to improve the overall reactivity of the new layer of material. During a deposition, a multi-layered deposition approach of adhesion promoters and precursors can provide additional functionality and hence improved adhesion. And finally, films can be post-treated with a polymer binder such as Cerakote.[61]

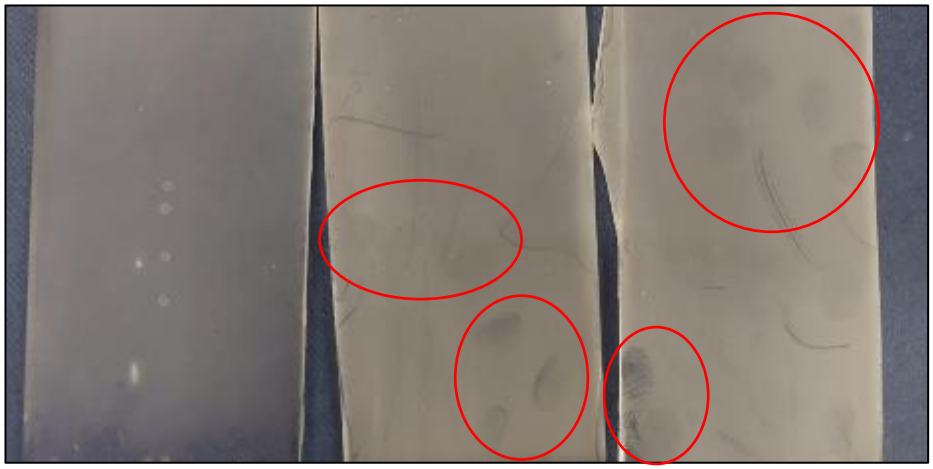

Figure 1.07. *Photographs of a "well-adhered" film (far left) and "powdery" films (middle and far right). Finger marks are circled in red which can be seen in the "powdery" films.*

1.5 Vapour Phase Depositions

Vapour phase deposition techniques are used to deposit thin films (<500 nm) with a range of applications from self-cleaning materials to transparent conducting oxides. The general mechanism involves the vaporisation of precursors, the transport of the precursors to the substrate and finally the nucleation and growth of the film (e.g. layer-by-layer growth or island growth or both). Films can form via chemisorption or physisorption.

1.5.1 Chemical vapour deposition (CVD)

Chemical vapour deposition (CVD) is a process consisting of a number of steps to form a solid film on a substrate which may be through reactions in the gas phase, above the substrate, or on the surface of the substrate.[62] The CVD process can be visualised in **Figure 1.08**. Firstly, the precursor is volatised before it diffuses to the substrate. Here, the gaseous reactant particles either directly adsorb onto the substrate and react (heterogenous reactions) or react in the gas phase (via homogenous reactions) to form intermediates which adsorb and diffuse across the substrate's surface to the lowest energy sites.[63] A heterogeneous reaction between the gaseous particles and hot substrate via repeated nucleation and growth leads to the formation of a solid film.[62] The by-products are desorbed. Resultant films can allow good conformality and purity, even at large coverage.

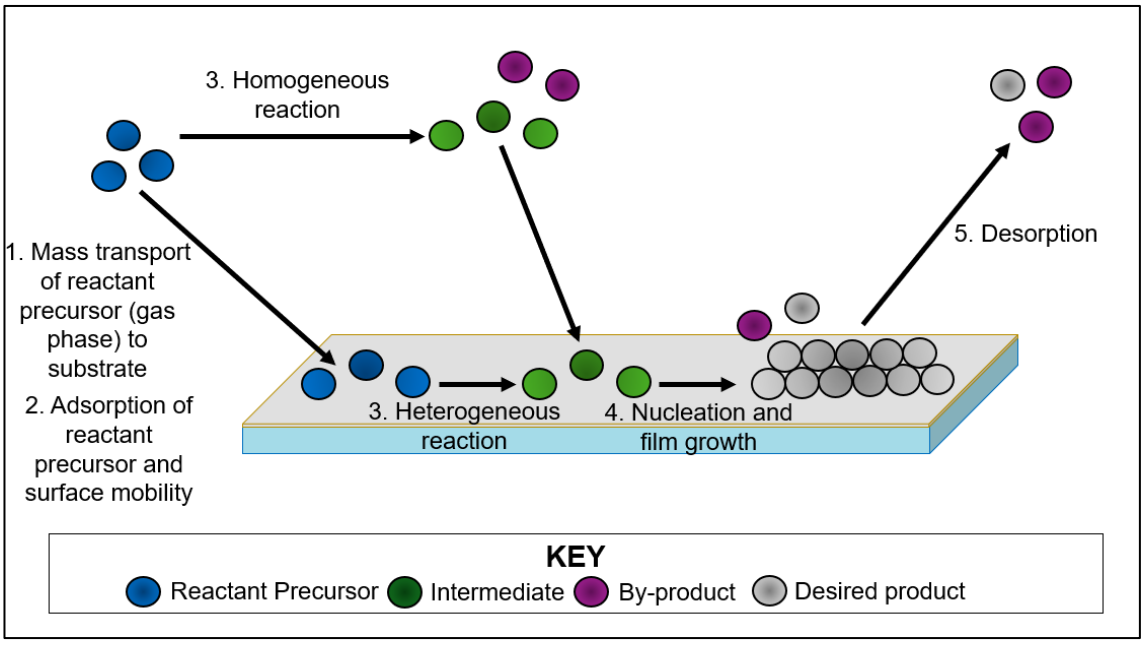

Figure 1.08. *Schematic outlining the chemical vapour deposition (CVD) process.*

1.5.2 Aerosol-assisted chemical vapour deposition (AACVD)

Aerosol-assisted chemical vapour deposition (AACVD) is a variation of chemical vapour deposition. It involves dissolving a precursor into a soluble solvent before aerosolising the liquid precursors via a piezoelectric crystal, contained within an ultrasonic humidifier/nebuliser to create an aerosol of a liquid precursor mixture, **Figure 1.09**. This, along with the carrier gas, travels through to the heated reactor. After the solvent evaporates, the precursor (now in the gas phase) decomposes into intermediates, homogenously or heterogeneously. Homogenous reactions occur prior to adsorption onto the substrate and heterogeneous reactions occur post-adsorption. Finally, the precursor/intermediates undergo a chemical reaction to form a solid film.[32]

Unlike other wet chemical methods such as sol-gel techniques, AACVD minimises the number of steps required by solution-based routes, with the ability to deposit nanoparticles in a single-step. AACVD is advantageous as there is scope for scalability, and it only depends on the volatility of the precursors at the reactor temperature. In addition, AACVD can facilitate the deposition of a wider range of precursors, including polymer-based precursors, provided they are soluble in the aerolising solvent. The AACVD process produces textured rough surfaces which is a requirement for superhydrophobic films.[64] Janowicz *et al.* deposited a superhydrophobic nanocomposite precursor via spin-coating and AACVD and found the latter deposition technique to be beneficial as the resulting film had greater superhydrophobicity and adherence.[65]

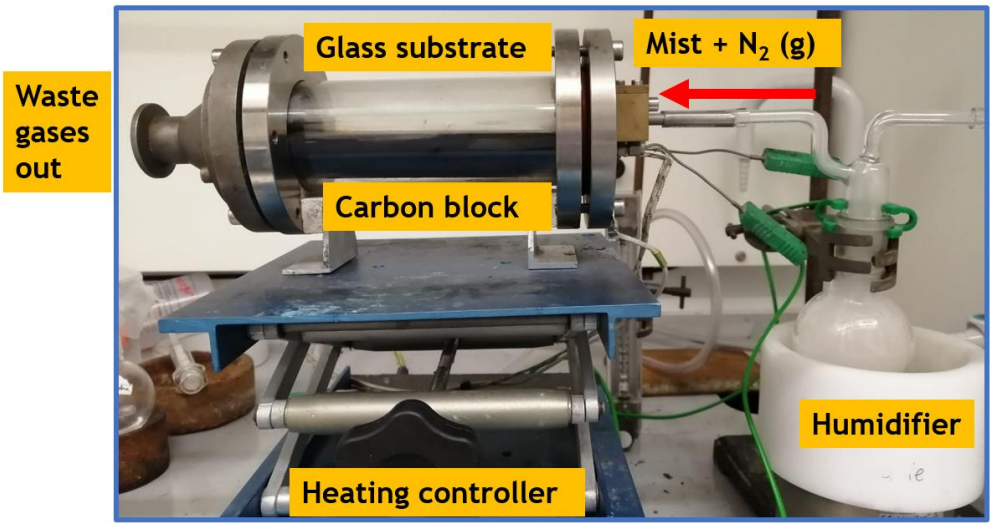

Figure 1.09. *The set up used for aerosol-assisted chemical vapour deposition, the precursor mist is generated in the ultrasonic humidifier on the right and travels through to the reactor on the left via the N_2 carrier gas.*

For AACVD, glass substrates can be placed on the heated carbon block (bottom plate) or a few centimetres above it, cushioned between layers of air (top plate), **Figure 1.09**, making the latter a cooler substrate to deposit on. Depositions involving polymers and silica NPs occur via thermophoresis as the particles move away from the hot carbon block to the cooler glass substrate (top plate) by Brownian motion, **Figure 1.10**.[66] Unlike conventional CVD, which involves a heterogeneous reaction of a vapour with a substrate forming a chemical bond across the interface (i.e. chemisorption), thermophoresis involves homogenous nucleation in the gas phase and hence impacting the solid NPs onto the glass substrate which are physiosorbed.[62,66] Large particles such as polymers lead to particle formation in the gas phase and as a result, thermophoretic effects pull the particle onto the suspended top plate. However, depositions involving metal oxides occur on the bottom plate initially due to the precursor converting from the solid phase to the vapour phase as it heats, melts and vaporises.

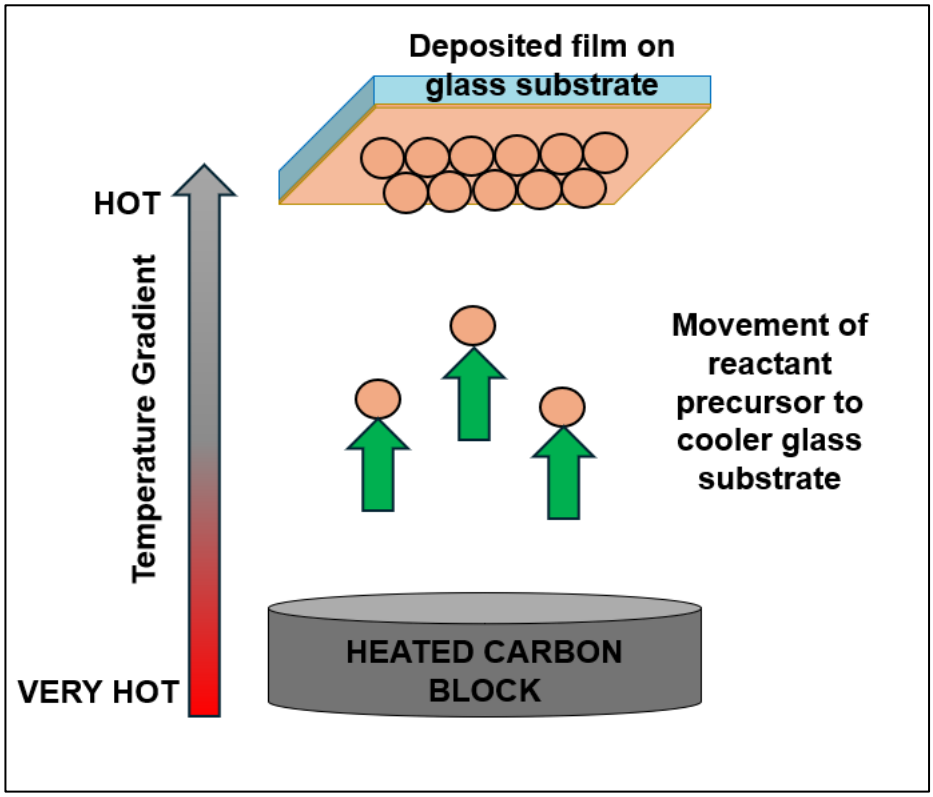

Figure 1.10. *A visualisation of the thermophoretic effect during the deposition of SiO_2 and polymer-based materials via AACVD.*

Li *et al.* deposited mixtures of PDMS and TEOS in different ratios using AACVD at a range of temperatures (290 to 330 °C).[67] The film had a raspberry-like hierarchical morphology due to the PDMS microparticles surrounding the SiO_2 NPs. The optimum deposition conditions included higher temperatures as this led to smaller NPs. A shorter deposition time (of approximately 15 – 30 min) resulted in coatings with a large static water contact angle >162°, although this gave hazier films. Finally, a precursor volume ratio of 3:1 (PDMS:TEOS) was desirable as higher ratios reduced the number of NPs and hence roughness.

Zhuang *et al.* drew on the idea of using AACVD to create a multi-layered film to improve mechanical robustness.[68] Initially Araldite 506 (an epoxy resin) was deposited on a glass substrate, which was then post-treated with SYLGARD 184 (a low-surface energy reagent) before a final layer of the same epoxy resin was deposited. A range of fixed and dynamic temperatures (290 – 350 °C) and deposition times for the first epoxy resin layer were trialled. According to SEM, the individual layers were visible but with different degrees of roughness. An increased temperature led to increased complexity in the roughness of the films, particularly due to the formation of NPs in the 200 – 300 nm range at 350 °C. The larger particles were also able to shield the smaller particles and hence increase the durability of the film. Multi-layering also led to an improvement in mechanical robustness as even after 80 cycles of tape peel tests, water droplet and sand impingements, the films maintained their superhydrophobicity.

1.5.3 Atomic Layer Deposition (ALD)

Atomic layer deposition (ALD) is a branch of CVD comprised of self-limiting reactions, **Figure 1.11**, that is used to produce ultra-thin films (in the nanometre range).[69] Each cycle consists of precursor and purging pulses.[70] Initially the metal-organic precursor is vaporised which adsorbs and reacts with the substrate's surface; these are self-limiting depending on the conditions used. The second part of the cycle involves purging the reactor with a carrier gas to remove excess precursor and by-products.

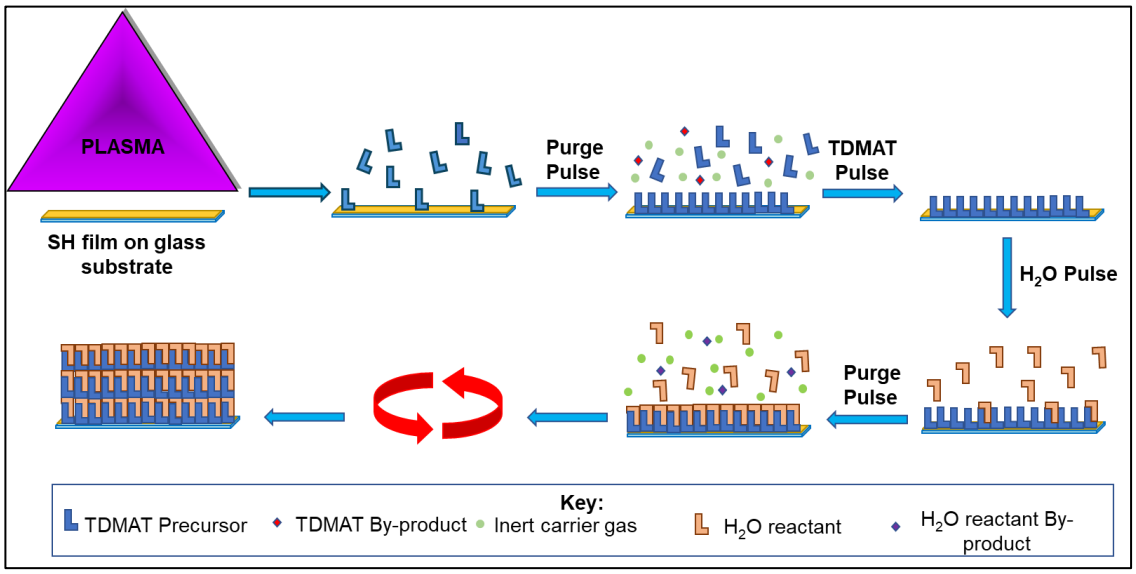

Figure 1.11. *A schematic of the ALD process. The first step is the precursor pulse where the precursor molecules bombard the surface. After a single monolayer coats the surface, a purge pulse of inert carrier gas removes the excess precursor and by-products. A second precursor pulse takes place before another purge pulse. The whole process is repeated. Redrawn from a paper by Johnson et al.*[71]

ALD is a commonly used technique within the semiconductor industry due to its many advantages relative to CVD.[72,73] These include its high conformality of complex objects with high aspect ratios, leading to pinhole free coatings via the growth of a single monolayer across the surface per cycle.[71] Repeated cycles allow for uniformity of the films across a substrate due to more controlled surface reactions relative to conventional CVD.[71] Equally, the film thickness can be regulated through controlling the number of cycles as the growth per cycle can be calculated for certain conditions, depending on the precursor mixtures.[73] The area coverage of both vapour phase deposition techniques is large and low cost to run, hence scalable. In general, it takes longer to grow a film of a specific thickness via ALD rather than CVD. Finally, ALD operates at lower temperatures

relative to conventional CVD, from room temperature to 200 °C and 100 °C to 500 °C, respectively, making it less energy intensive.

1.6 Surface Modification of Thin Films to Control Physisorption, Chemisorption or Wettability

Thin films can be surface modified to tune a film's properties, namely, for additional functionality (hence improve its widespread application) or to potentially control physisorption, chemisorption or wettability. Methods of surface modification include traditional methods such as CVD, PVD, ALD, thermal spray coatings and the deposition techniques mentioned in **Section 1.5**.

CVD surface modification has been implemented industrially due to its adequate growth rates, affordability, large area coverage and ability to fine-tune the microstructure. For example, there has been interest in creating anti-biofouling coatings via CVD for boats through to food wrappers. Bose *et al.* afforded a hydrophilic polyethylene oxide coating on a Si substrate that was pre-treated with an amine to improve reactivity and hence coverage of the hydrophilic polymer on the substrate.[74] The resulting films displayed exceptional anti-fouling properties due to the energetically unfavourable task of proteins displacing water molecules. The group went on to create a thin amphiphilic copolymer coating of monomers (both fluorinated and not) and hydroxyethyl methacrylate, to tune the surface of an industrial membrane for reverse osmosis. This process was also carried out via CVD resulting in good anti-biofouling capabilities as the surface-protein contact was disrupted.

Alternatively, Wang *et al.* deposited sol-gel based SiO_2 NPs onto a wood substrate and later surface modified it with a low surface energy fluorinated polymer via CVD, specifically 1H,2H,2H-perfluorooctyltriethoxysilane for self-cleaning/protection properties.[30] The surface modification of the particles with a fluorinated polymer was to introduce superhydrophobicity. Unfortunately, CVD and other vapour phase deposition techniques can only deposit thin coatings in the nm and μm range. This renders them unsuitable for depositing thick coatings (i.e. millimetre range), a requirement for some large-scale applications, such as coatings for W-based first wall nuclear fusion reactors, required to last at least 15 – 20 years. Hence, alternative techniques are required.

As well as surface modification of a whole substrate, there has been interest in selective surface modification through the use of small molecule inhibitors. Facile selective adsorption of small molecule inhibitors such as methanesulfonic acid on a CuO substate led to controlled growth of Al_2O_3 films. However, the chemisorption potential of the inhibitor varied across the range of substrates studied, namely, RuO_2, SiO_2 and TiO_2 due to the alkalinity of the metal oxide coatings and reduction abilities. CuO displayed the best chemisorption of methanesulfonic acid. The group went on to determine the effect of Al_2O_3 growth on the inhibitor-treated substrates and found that a combination of inhibitors and appropriate reactive precursors such as dimethylaluminium isopropoxide can impact selective growth of Al_2O_3.[75]

In addition, work by Oh *et al.* was carried out to tune the wettability of Si substrates coated with rare earth oxides via thermal ALD and plasma enhanced ALD.[76] All the rare earth oxides deposited (Er_2O_3, Y_2O_3, La_2O_3, Dy_2O_3 and CeO_2) demonstrated variable levels of hydrophobicity relative to the hydrophilic Si substrate, with Y_2O_3 deposited-Si substrates possessing a WCA of 158°. Preliminary theoretical calculations of rare earth oxide thin films indicated they maintained hydrophobicity at temperatures >950 °C, owing to their empty 4f orbitals and filled $5s^2p^6$ shielding orbitals, resulting in minimised interactions with water molecules. In addition, the degree of wear of the rare earth oxide films, a measure of material movement across a distance, was considerably lower than aluminium, indicating high mechanical durability and adhesion. However, oven-treatment of all 5 rare earth oxides indicated a transition from WCAs *ca.* 100 ± 10° to 80° for Er_2O_3, Y_2O_3 and Dy_2O_3; 60° for CeO_2 and 20° for La_2O_3. A reduction in WCA was facilitated by annealing, encouraging the interaction between the rare earth oxides and water molecules. In most cases, the hygroscopicity was inversely correlated to the electronegativity of the metal oxide.

1.7 Photocatalysis

Photocatalysis involves the use of light to catalyse reactions (e.g. water splitting to produce H_2 and degradation of toxic organic pollutants into harmless alternatives) with the aid of a metal oxide such as TiO_2, WO_3 and ZnO. This process has applications in environmental remediation, clean renewable energy generation, and more recently, chemical self-cleaning applications (e.g. Pilkington Activ™).[77]

The mechanism of TiO_2 anatase photocatalysis, **Figure 1.12**, firstly involves the irradiation of light (i.e. photons) with a frequency ≥ the band gap (the difference between the conduction and valence band), also known as solar light harvesting.[78] As a result, this leads to the photoexcitation of electrons in the valence band (low energy) to the conduction band (high energy), generating electron-hole pairs, also known as the separation and transport of charge carriers.[79] Ideally, the electron-hole pairs should form quickly and remain separated and travel to the surface of the material, with the electrons reducing and the holes oxidising the reactant, i.e. photocatalytic redox reaction.

Problems include the recombination of the electron-hole pairs, leading to a reduction in efficiency of the photocatalytic redox reaction, and the dissipation of energy as phonons or photons, depending on if its non-radiative or radiative recombination, respectively. [77,80]

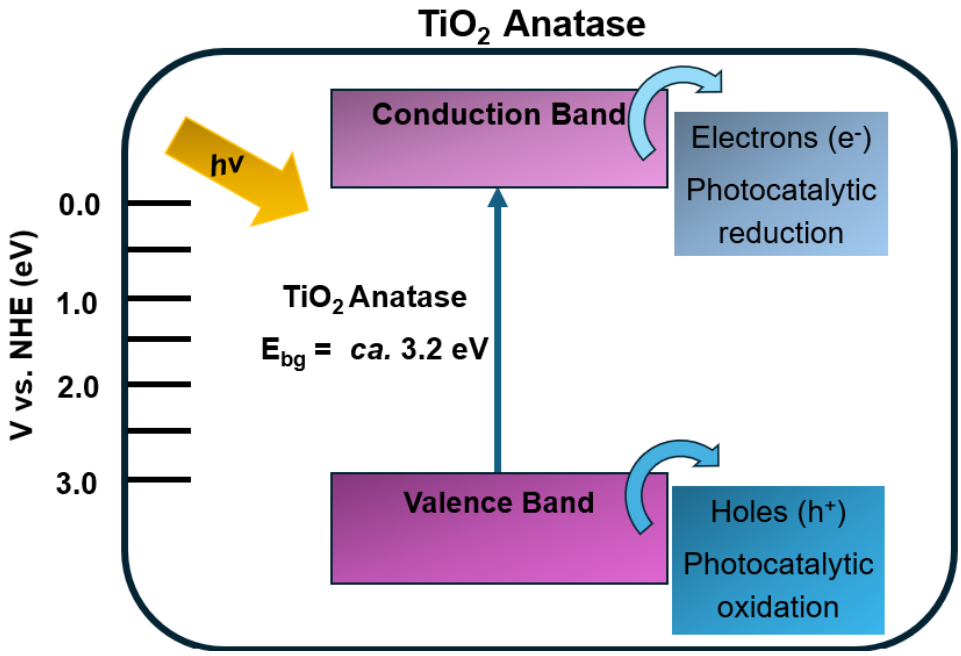

Figure 1.12 *Photocatalytic mechanism for TiO_2 (anatase).*

There has been interest in utilising TiO_2 as a photocatalyst as it is cheap and environmentally non-toxic, whilst displaying enhanced photocatalytic activity and stability relative to films without the incorporation of TiO_2.[80] However, TiO_2 poses technical challenges due to its large band gap which is typically *ca.* 3.2 eV for anatase and *ca.* 3.0 eV for rutile.[81] As a result, high energy UV light is needed which, although is generated from the sun, is shielded by the ozone layer and consequently, only 5% of the UV light is accessible for photoexcitation of the electrons. Hence, reducing the band gap means that visible light, which is available in greater quantities, can be utilised instead of UV light. To reduce the band gap, TiO_2 precursors can be doped with dopants to reduce the band gap or to create structural defects. In addition, it is important that the conduction and valence bands are sufficiently high in energy to produce electrons/holes of sufficient oxidation/reduction potential.[82]

1.8 Applications of Modified Thin Films

As briefly mentioned in **Section 1.1**, surface modified thin films have various applications from anti-biofouling coatings, anti-corrosion coatings to self-cleaning materials. As discussed earlier, not only functional properties but also facile manufacturing (cost and efficiency), reduced toxicity (both to humans and the environment) as well as mechanical robustness are factors for consideration.

1.8.1 Self-cleaning Applications

Self-cleaning materials, inspired by the “cleaning” mechanism of lotus leaves, mentioned in **Section 1.1** can “clean” their surfaces naturally in a muddy environment. These properties can be applied to glass, paints, plastics, metals and ceramics.

Xing *et al.* pursued chemical etching of a brass substrate with a mixture of HCl and HNO_3 post-treated with lauric acid creating a rough topology across the substrate with an exceptional water contact angle >170°.[83] Tilt angles are a particularly important indicator of self-cleaning materials. In this case, the tilt angle remained <10°. Furthermore, high robustness was displayed on exposure to heat, chemical and mechanical testing. Similarly, other studies involved chemical etching polycarbonate substrates with HNO_3, post-treated with methyltrichlorosilane to induce self-cleaning water-repelling abilities. The films

maintained their functionality even after repeated cycles of intensive water jet washes.[84]

There is an interest in transitioning self-cleaning properties into paints to add functionality. For instance, Il'darkhanova *et al.* utilised carbon nanotubes and fibres, surfactants and epoxy silicone resin to fabricate a hydrophobic slurry which was combined with paint and coated a steel substrate.[85] WCAs reached 98° however, they did not display facile self-cleaning abilities due to pinning of the water molecules onto the substrate and poor adhesion and hence stability due to the lack of strong chemical inter-/intra-molecular interactions. In comparison to AACVD films but in contrast to conventional CVD and ALD films, the materials did not adhere well due to the lack of chemisorption between the coating and substrate.

Apart from the increased breadth of applications of self-cleaning materials, a field of self-cleaning materials has arisen, combining conventional physical self-cleaning properties along with the chemical self-cleaning properties to produce a superhydrophobic and photocatalytic self-cleaning material. The photocatalytic chemical self-cleaning ability is due to the photocatalytic nature of TiO_2 and the physical self-cleaning aspect results from its superhydrophobicity.[77] This synergistic combination poses difficulties as photocatalytic activity relies on molecular/microscopic interactions due to the oxidation of impurities while superhydrophobicity relies on macroscopic interactions with the water and material's surface. Nevertheless, this simultaneous relationship facilitates the disintegration of organic impurities into harmless molecules, namely CO_2 and H_2O, as well as the easy movement of liquids across and off a surface, augmenting the self-cleaning properties of a material.[86]

However, 50-70% of the coating's surface must be hydrophobic/ superhydrophobic for this functionality to be realised, evidenced in research by Ansari *et al.* where a chemical and physical self-cleaning material was produced through electrostatic spraying of a slurry of SiO_2 and TiO_2 NPs, along with fluorinated ethylene propylene (FEP).[87,88] As expected, additional layers of the precursor enhanced the hydrophobicity, by imparting roughness. Further studies investigated alterations to the weight percentages; decreasing the TiO_2 loading reduced the photocatalytic activity but increased the hydrophobicity and contrariwise for the SiO_2 loadings. On finding the optimal loadings, the films

withstood low/high pH environments and demonstrated good mechanical robustness during sandpaper tests in addition to photocatalysis.[88]

Improved photocatalysis, promising WCAs >150° and ultra-repellence to emulsions and solvents were observed for films fabricated by Cao *et al.*[79] These materials were a hybrid of pentafluoroethane (PFE) and (3-aminopropyl)trimethoxysilane, (APTMS), with functionalised TiO_2 NPs, all deposited on a stone substrate. PFE and APTMS contributed to the low surface energy and TiO_2 NPs contributed to the rough topography and photocatalytic nature. However, this work utilised fluorinated polymers and deposited both self-cleaning entities as a single precursor, limiting the ability to tune the surface.

A two-step method was employed by Wang *et al.* to fabricate a ZnS superhydrophobic and photocatalytic self-cleaning coating.[77] The first step was a solvothermal technique to deposit ZnS nanostructures and the second step involved a chemical modification of the structures with stearic acid. The ZnS film had improved photocatalysis of the organic contaminants in contrast to the unaltered ZnS film as it decreased the electron-hole recombination.

1.9 Aims

The purpose of this thesis is to document the design and fabrication of polymer based, fluorine-free superhydrophobic, (water-repellent) films and their resultant surface modification with metal oxides via vapour phase deposition techniques such as AACVD and ALD. The surface modification is for added functionality of the film, for example, photocatalysis and enhanced durability.

Superhydrophobic materials can be modified further to tune the properties and add additional functionality. The method of surface modifying hydrophilic/hydrophobic films via AACVD and particularly ALD is a rare find in the literature, with no papers combining this technique with AACVD to determine changes in surface wettability.

Within the literature, there is a lot of work on either the fabrication of superhydrophobic materials or the deposition of only metal oxides via CVD or ALD through a multi-layered approach. Alternatively, work has been published on selective deposition across areas of a substrate, typically for different applications (e.g. electronics and transparent conducting oxides). Therefore, the novelty in the research described herein is due to the combination of superhydrophobic polymers and metal oxides, both deposited via vapour phase deposition techniques to improve durability and provide additional functionality.

The thesis begins with a general introduction to the background theory and literature, followed by the production of a fluorine-free superhydrophobic material (**Chapter 2**). Later, the surface of the superhydrophobic film is tuned with TiO_2 via AACVD (**Chapter 3**) and ALD (**Chapter 4**) and CeO_2 by AACVD (**Chapter 5**). Materials were fully characterised (chemically and functionally), with the effects on the composition, microstructure, wettability and durability studied.

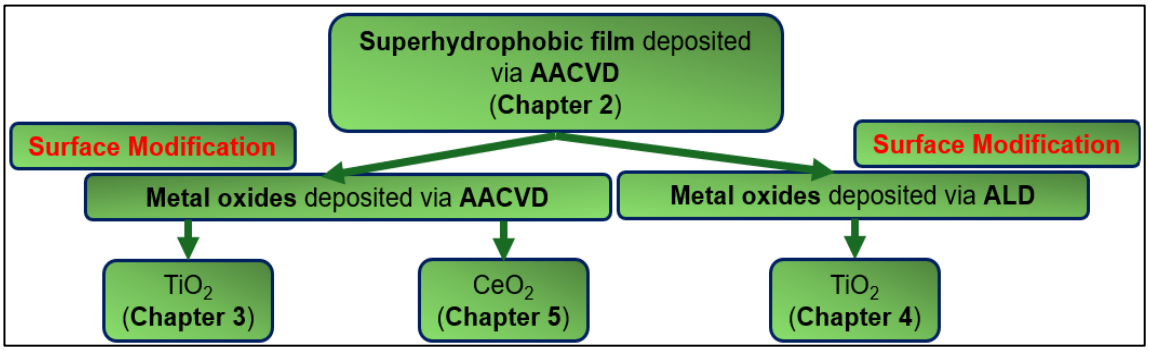

Figure 1.13 *A visual representation of the deposition pathways taken for the chapters contained within this thesis.*

Chapter 2 – Mechanically Durable, Fluorine-Free Superhydrophobic Films Deposited via AACVD for Self-Cleaning Properties

2.1 Background

As mentioned previously superhydrophobic materials require hierarchical roughness and a low surface energy coating.[14] Cassie-Baxter type wetting behaviours are required to display physical self-cleaning properties, where water droplets easily roll off the surface without external support, such as anti-fouling coatings for solar panels. Previous reports on physical self-cleaning materials deposited via AACVD are based on hydrophilic SiO_2/TiO_2 NPs and SYLGARD 184 (and their respective curing agent). Although the former is hydrophilic, it provides the rough microstructure required and a support for non-polar groups to bond to and the latter acts as a glue, also reducing the surface energy.[89] SYLGARD 184 has a low surface energy (19.8 mJ/m^2), however, fluoroalkylsilanes can have even lower surface energies (*ca.* 17 mJ/m^2 and below).[90] Hence numerous publications within the literature utilise a fluoroalkylsilane polymer in addition to SYLGARD 184 to lower the surface energy and thus improve the wettability.[90]

Fluoroalkylsilanes display a decrease in surface energy as the number of fluorine atoms increases, i.e. -CF_3 has a lower surface energy than -CF_2H, as the CF_3 groups can pack in a hexagonal arrangement.[91] Zhuang *et al.* deposited a highly durable polytetrafluoroethylene-based superhydrophobic material with an impressive WCA reaching 170°, displaying good anti-corrosion and self-cleaning abilities.[53] Specifically for AACVD, multi-layered depositions have been reported to achieve superhydrophobicity, in addition to the use of fluoroalkylsilanes. Tombesi *et al.* deposited three layers onto a glass substrate using 3-methacryloxypropyltrimehoxysilane, then SiO_2 (via tetraethyl orthosilicate) and finally 1H,1H,2H,2H-perfluorooctyltriethoxysilane, as a means of improving the transparency and robustness of the film.[54]

Although reports have optimised the deposition conditions such as the deposition duration and temperature, loadings of the reagents and carrier gas flow rate, there is a lack of variation in the precursors used.[54] Most precursors used involve the use of SiO_2 NPs, fluoroalkylsilanes and SYLGARD 184 and hence there is a

pressing need for alternative reagents. Li *et al.* deposited a film of SYLGARD 184 and tetraethyl orthosilicate via AACVD, creating a raspberry-like morphology providing protection for the structure and engendering roughness, corroborated by maintained superhydrophobicity after up to 5 metres of sandpaper abrasion across the surface.[67]

Within the literature, work on the functionalisation of NPs by a single fatty acid rather than multiple fatty acids have been reported. Earlier studies by Crick *et al.* hydrothermally prepared oleic acid-coated TiO_2 NPs, dispersed in a mixture of SYLGARD 184 and chloroform and later deposited via AACVD to afford a superhydrophobic polymer/metal oxide composite.[92] Park *et al.* fabricated a superhydrophobic film with high visible light transmittance (>80%) via AACVD.[93] The films consisted of an epoxy resin, SYLGARD 184 and Al-doped ZnO NPs which were functionalised with stearic acid that enhanced the roughness and hence hydrophobicity. The epoxy resin/SYLGARD 184 film had a Sq value of 109 nm which amplified on the addition of Al-doped ZnO NPs that were functionalised with stearic acid, to 378 nm.

In summary, it is evident that the literature lacks research on the AACVD of novel reagents and the combination of fatty acids to produce superhydrophobic materials. Therefore, within this chapter, the combination of two fatty acids alongside the conventional composition of a superhydrophobic mixture was studied to understand the impact of this hybrid combination.

2.2 Aims

The aim of this work was to fabricate mechanically durable superhydrophobic films with nano-/micro- scale roughness utilising a non-fluorinated low surface energy reagent, namely fatty acids due to their low toxicity to both humans and the environment. The overall aim of the study investigated the effect of replacing a commonly used fluorinated silane (1H,2H,2H-perfluorooctyltriethoxysilane (FAS C_8)) with a non-fluorinated alternative (stearic acid or palmitic acid) or a 50:50 hybrid of stearic acid and palmitic acid. Although SYLGARD 184 and SiO_2 NPs were used as previously reported in the literature, unlike the literature, a 50:50 mixture of the most commonly found fatty acids were used rather than only one. This mixture of fatty acids was used to engender roughness and to lower the surface energy of the film without the use of a fluoroalkylsilane. AACVD was

used as it involves generating aerosols, which contributes to the overall roughness of the film, a requirement for superhydrophobicity. In addition, unlike conventional CVD, AACVD offered a range of relatively inexpensive polymer-based precursors to deposit to achieve superhydrophobicity. Alterations involved various SiO_2 NP sizes, deposition temperatures, reagent concentrations, SiO_2 NP loadings, and deposition durations.

Such superhydrophobic film could have applications in self-cleaning. The overarching goal was to create a superhydrophobic coating, uniform in morphology and water contact angle, to later surface modify with a metal oxide via TiO_2 or CeO_2, via AACVD or ALD, described in **Chapters 3 - 5**.

2.3 Experimental

The fabrication of superhydrophobic films with a hybrid of stearic acid and palmitic acid, deposited by AACVD for self-cleaning applications were realized. Fatty acids were selected due to their low surface energy, SiO_2 was needed to impart roughness and the PDMS, also a low surface energy reagent, was needed to "glue" the particles together due to its viscose nature.

2.3.1 Chemicals and Materials

Vinyl-terminated polydimethylsiloxane (PDMS) also known as SYLGARD™ 184 Silicone Elastomer Base along with its corresponding curing agent were purchased from Dow Corning. Aerosil OX50 SiO_2 nanoparticles (fumed) were procured from Lawrence Industries. 1H,1H,2H,2H-perfluorooctyltriethoxysilane (FAS C_8) 98%, palmitic acid (≥ 99%), stearic acid (reagent grade, 95%) and ethyl acetate (laboratory grade) were all acquired from Merck Chemicals. All chemicals were used as received. NSG provided SiO_2 barrier coated fluorine-doped tin oxide (FTO) glass substrates which were manually cut to 15 cm x 4 cm x 0.3 cm for AACVD. The N_2 carrier gas used in AACVD was supplied by BOC.

2.3.2 Fabrication of a superhydrophobic mixture consisting of fatty acids (individual or 50:50 combination) or FAS C_8 (Study 1)

FAS C_8 (0.6 g, 1.2 mmol), stearic acid (0.6 g, 2.1 mmol) or palmitic acid (0.6 g, 2.3 mmol) or a hybrid 50:50 combination of stearic and palmitic acid (0.6 g, 2.2 mmol), SYLGARD 184 (0.6 g), curing agent (0.06 g) and ethyl acetate (60 cm^3) were stirred vigorously for 5 – 10 min. OX50 SiO_2 NPs (0.25 g, 4.2 mmol) was added to the aforementioned mixture and stirred for a further 15 – 20 min. The resultant mixture was subsequently deposited via AACVD (a cold-walled reactor) onto a barrier coated glass substrate (top plate), **Figure 1.09**. In a cold-wall reactor, the whole reactor is not at a uniform temperature to ensure thermophoretic effects. Prior to deposition, the top plate was initially washed with acetone, then soap and water and finally rinsed with isopropanol. The film was oven-dried at 70 °C for 5 min.

The cold-walled AACVD rig had the following specifications, **Figure 2.01**:

1. A Whatman cartridge heater contained within the graphite heating block, controlled by a Pt-Rh cartridge heater.
2. A quartz tube which confined the reaction from the surrounding environment.

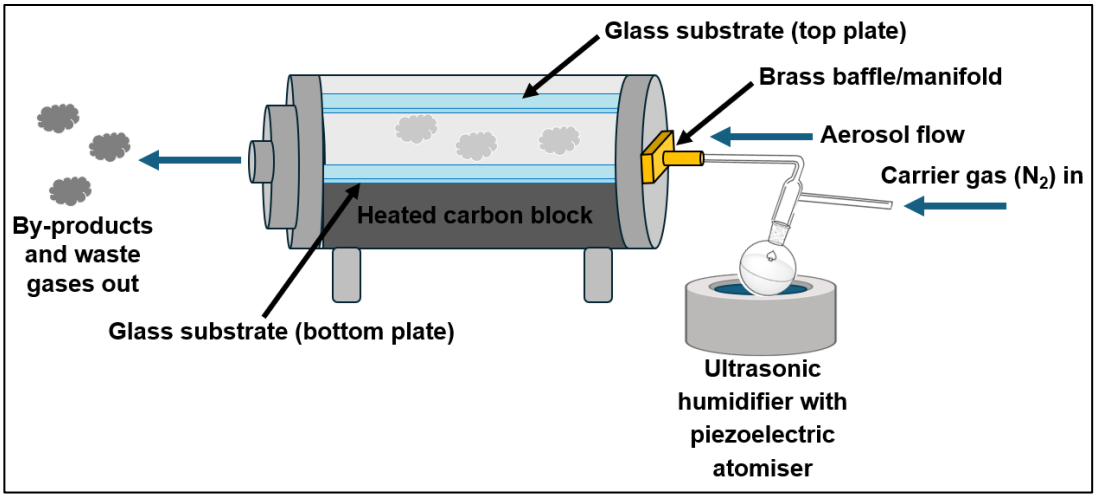

Figure 2.01. *Diagram of the aerosol-assisted chemical vapour deposition set-up.*

At the required temperature, aerosols were generated via a piezoelectric ultrasonic humidifier which were carried to the cold-walled reactor via the N_2 carrier gas (flow rate: 1 L min^{-1}). The precursor mixture was supplemented with further ethyl acetate (30 cm^3) after the initial deposition time of 40 min and deposited for an extra 30 min. A subsequent addition of ethyl acetate (20 cm^3) followed which was deposited for 20 min, totalling a deposition time of 1.5 h.

Once the deposition terminated, the AACVD rig was cooled in a constant stream of N_2 until the films were cool enough to handle (<100 °C). The resulting films were described as: **PDMS/SiO_2/SA, PDMS/SiO_2/PA, PDMS/SiO_2/SA+PA** and **PDMS/SiO_2/FAS**, where SA, PA and FAS denote stearic acid, palmitic acid and 1H,1H,2H,2H-perfluorooctyltriethoxysilane. All the films fabricated in this chapter ranged from translucent to an opaque, white colour.

2.3.3 Additional Information on separate studies

Study 2. Influence of SiO_2 NP size

The experimental method in **Section 2.3.2** was replicated as above but using a hybrid 50:50 combination of stearic and palmitic acid (0.6 g, 2.2 mmol), deposited via AACVD at 300 °C for 1.5 h. Two different sized SiO_2 NPs were used for this study: Aerosil OX50 SiO_2 NPs (45 nm) and SiO_2 NPs (10 – 20 nm). These films either consisted of one or two types of NPs and were labelled as **PDMS/1SiO_2/SA+PA** and **PDMS/2SiO_2/SA+PA**.

Study 3. Influence of deposition temperature

The experimental method in **Section 2.3.2** was replicated as above but using a hybrid 50:50 combination of stearic and palmitic acid (0.6 g, 2.2 mmol), deposited via AACVD at 360 °C or 400 °C for 1.5 h. These films were labelled as **PDMS/SiO_2/SA+PA/360** and **PDMS/SiO_2/SA+PA/400**.

Study 4. Influence of fatty acid concentration

The experimental method in **Section 2.3.2** was replicated as above but using a hybrid 50:50 combination of stearic and palmitic acid at either 0.3 g per fatty acid, 0.5 g per fatty acid or 0.7g per fatty acid, deposited via AACVD at 360 °C for 1.5 h. These films were labelled as **PDMS/SiO_2/0.3g(SA+PA)/360**, **PDMS/SiO_2/0.5g(SA+PA)/360** and **PDMS/SiO_2/0.7g(SA+PA)/360**.

Study 5. Influence of OX50 SiO_2 loading

The experimental method in **Section 2.3.2** was replicated as above but using a hybrid 50:50 combination of stearic and palmitic acid (0.6 g, 2.2 mmol), deposited via AACVD at 360 °C for 1 h 10 min. These films were labelled as **PDMS/0.25g(SiO_2)/SA+PA/360**, **PDMS/0.30g(SiO_2)/SA+PA/360** and **PDMS/0.35g(SiO_2)/SA+PA/360**.

Study 6. Influence of deposition time

The experimental method in **Section 2.3.2** was replicated as above but using a hybrid 50:50 combination of stearic acid and palmitic acid (0.6 g, 2.2 mmol). The deposition temperature remained constant at 360 °C however, the deposition time was changed (45 min, 40 min, 37 min, 35 min, 30 min, 25 min, 10 min). These films were labelled as: **0.5PDMS/SiO_2/0.5(SA+PA)/45min 0.5PDMS/SiO_2/0.5(SA+PA)/40min, 0.5PDMS/SiO_2/0.5(SA+PA)/37min 0.5PDMS/SiO_2/0.5(SA+PA)/35min, 0.5PDMS/SiO_2/0.5(SA+PA)/30min, 0.5PDMS/SiO_2/0.5(SA+PA)/25min** and **0.5PDMS/SiO_2/0.5(SA+PA)/10min**.

Study 7. Influence of variable concentration of precursor mixture (excluding SiO_2 NPs)

The concentration of the precursor mixture (excluding the concentration of SiO_2 NPs) was altered by ¾, ½ and ¼ for the following components and their respective amounts which were taken as 1. The unaltered amounts were as follows: SYLGARD 184 (0.6 g), its corresponding curing agent (0.06 g), and a 50:50 SA:PA combination (0.60 g, 2.2 mmol). The amounts of ethyl acetate (60 cm^3) and OX50 SiO_2 NPs (0.25 g, 4.2 mmol) were unaffected. All films within this investigation were deposited at 360 °C for 40 min and were labelled as: **1.0PDMS/SiO_2/1.0(SA+PA)**, **0.75PDMS/SiO_2/0.75(SA+PA)**, **0.5PDMS/SiO_2/0.5(SA+PA)** and **0.25PDMS/SiO_2/0.25(SA+PA)**.

Study 8. Influence of stearic acid and palmitic acid on adherence

The concentration of the precursor mixture remained constant with OX50 SiO_2 NPs (0.25 g, 4.2 mmol), SYLGARD 184 (0.15 g) and its respective curing agent (0.02 g) and variable amounts of fatty acids were used (from 0.22 g per fatty acid to 0.27 g per fatty acid). The deposition temperature and time remained constant at 360 °C and 40 min, respectively. These films were labelled as: **PDMS/SiO_2/0.18g(SA+PA)**, **PDMS/SiO_2/0.22g(SA+PA), PDMS/SiO_2/0.25g(SA+PA)** and **PDMS/SiO_2/0.27g(SA+PA).**

Study 9. The effect of SYLGARD 184 on adherence

The concentration of the precursor mixture remained constant with OX50 SiO_2 NPs (0.25 g, 4.2 mmol), a hybrid 50:50 combination of stearic and palmitic acid (0.6 g, 2.2 mmol) and variable SYLGARD 184 masses were used (0.10 g, 0.15 g, 0.20 g, 0.25 g, 0.25 g, 0.35 g, 0.45 g). The deposition temperature and time

remained constant at 360 °C and 40 min, respectively. These films were labelled as: **0.10gPDMS/SiO_2/0.22g(SA+PA), 0.15gPDMS/SiO_2/0.22g(SA+PA), 0.20gPDMS/SiO_2/0.22g(SA+PA), 0.25gPDMS/SiO_2/0.22g(SA+PA), 0.35gPDMS/SiO_2/0.22g(SA+PA)** and **0.45gPDMS/SiO_2/0.22g(SA+PA).**

2.3.4 Materials Characterisation

Surface morphologies and cross-sectional SEM of the materials were carried out using the JEOL 6701F and JEOL 7600F Scanning Electron Microscopes (SEMs). Electron acceleration voltages of 5 – 10 keV were used, depending on how much the sample could tolerate the heat of the electron gun. Gold sputtering (physical vapour deposition) of all samples for 10 s occurred to improve the electrical conductivity of the films, for imaging and to prevent charging. The sizes of the particles were measured by the ImageJ 1.52s software. Functional bonds were detected through Fourier-Transform Infrared Spectroscopy (FTIR) using the Brucker alpha platinum-ATR instrument, with a wavenumber range of 400 – 4000 cm^{-1}. Ultra-violet visible spectroscopy (UV-vis) was used to determine the transmittance of electromagnetic radiation through the films using the Shimadzu UV-2700 spectrophotometer with wavelengths of 400 – 800 nm. Finally, a Thermo Scientific X-ray photoelectron spectrometer with a mono-chromated Al-K alpha source (8.3381 Å) was used for compositional analysis. The peaks were analysed using the CasaXPS 2.3.25 software and calibrated with respect to the C 1s peak at *ca.* 285 eV.

2.3.5 Functional, Durability and Performance Testing

Water contact angles (WCAs) were measured using a Kruss DSA 25E drop shape analyser. A mean and the error (one standard deviation) of 10 water droplets of 5 µL was determined which was calculated automatically by ADVANCE 1.14.3. A tilted drop method of water droplets (*ca.* 15 µL) dispensed 4 cm from the surface of the film was used to determine the sliding angle. The stage was tilted at the respective gradient (°) prior to any measurement. The CAH was determined by initially measuring the advancing angle before measuring the receding angle and finally subtracting an average of the two angles. The Ellipse (Tangent) method was used to determine the angles. The size of the angles was calculating by manually adjusting the baseline and utilising the Young-Laplace equation. Qualitative adherence tests were carried out by moving a finger across several sections of the film and holding the coated substrate to a ceiling light;

films were labelled “powdery” if finger marks appeared and well-adhered if they did not. The root-mean-square height (Sq) was measured using the Keyence VHX-S750E optical microscope at x1500 magnification. No S-filter and no L-filter were used, only using a Gaussian filter type.

Self-cleaning performance testing: Gold glitter was used to cover the surface of the films. Then, water droplets were pipetted onto the surface. On a separate sample, methylene blue was directly and continuously pipetted onto the surface. In both cases, samples were tilted at 20° with images taken throughout the testing to qualitatively visualise the superhydrophobicity and self-cleaning properties.

Durability

Elcometer® Testing: An Elcometer® 501 Pencil Hardness Tester (supplier: Elcometer® Ltd.) consisted of pencils of differing hardness (6H – 6B) which were pushed across the surface of a film at a 45° angle. Pencils of increasing hardness were used until a visible line was seen (by eye) in the coating. The standard protocol followed was ASTM D3363.

Tape peel test: Scotch Magic™ Tape was manually attached to and removed from the films up to 400 times. WCAs were initially recorded periodically.

Thermal Stability: Samples were heated at 300 °C for 5 h and the same samples were consequently heated to 400 °C for 5 h. WCAs were taken after each heat rotation and sliding angles were taken after the full 10 h of heat exposure.

UV Stability: WCAs and SAs of samples were measured after 1, 2, 3, 4, 7 and 14 days of exposure to UV in a sealed UV light box. A UV irradiance of 258 mW/cm^2 and emission wavelength of 365 nm were used.

Solvent Stability: Samples were separately submerged in ethanol (highly polar) and toluene (slightly polar) and the performance of these films was determined via WCA measurements, taken every hour for 5 h. After the 5 h cycle SAs were measured.

2.4 Results and Discussion

2.4.1 Study 1: The effect of replacing 1H,1H,2H,2H-perfluorooctyltriethoxysilane (FAS C_8) with stearic acid, palmitic acid, or a combination of both fatty acids

1H,2H,2H-perfluorooctyltriethoxysilane (FAS C_8)), a non-fluorinated alternative (stearic acid or palmitic acid) or a 50:50 hybrid of stearic acid and palmitic acid as well as SYLGARD 184 and SiO_2 NPs were incorporated into the precursor mixture, **Table 2**. The FAS film was made as a comparison to the fatty acid films. To avoid the influence of additional parameters, the deposition temperature for all films remained constant at 300 °C. The purpose of the SiO_2 was to contribute to the rough topology, the fatty acids not only lowered the surface energy but also imparted roughness – on visual inspection of the crystallised pure materials, stearic acid has a diamond-like morphology and palmitic acid is bead-like. SYLGARD 184 is also a low surface energy reagent, producing a superhydrophobic film moreover, owing to its viscous nature, binds the particles together.[19] As mentioned previously, FAS is a low surface energy reagent and contributes to the overall durability of the film due to its strong C-F bonds.

Experiments by Heale *et al.* corroborated that altering the length of the hydrocarbon chain affects the hydrophobicity of the films.[46] **PDMS/SiO_2/SA**, made with stearic acid, ($C_{18}H_{36}O_2$), had a water contact angle (WCA) of 145° but **PDMS/SiO_2/PA**, the film with palmitic acid ($C_{16}H_{32}O_2$) had a WCA of 129°. Intriguingly a 50:50 hybrid of both fatty acids led to a superhydrophobic WCA (162 ± 3°), like that of the fluoroalkylsilane equivalent (163 ± 2°) and other fluorinated films deposited via AACVD and reported in literature.[54]

Table 2. *A study of fumed SiO_2 NPs with SYLGARD 184 and its respective curing agent coated in FAS C_8, palmitic acid or stearic acid or a 50:50 mix of stearic and palmitic acid. Films were deposited via AACVD using the following conditions:* ***flow rate:*** *1 L/min,* ***deposition temperature:*** *300°C,* ***total deposition time:*** *1.5 hr.*

Film code	**Fatty acid/FAS C_8: mass used (g) and total solution concentration (mol dm^{-3})**	**WCA ± 1 Standard Deviation (°)**	**Sq (µm)**	**Transmittance (%) Plain glass: *ca.* 91%**
PDMS/SiO_2/PA	Palmitic acid (0.6 g, 0.092 mol dm^{-3})	129 ± 3	0.27	12
PDMS/SiO_2/SA	Stearic acid (0.6 g, 0.090 mol dm^{-3})	145 ± 11	0.69	5
PDMS/SiO_2/SA + PA	Stearic acid (0.3 g) and Palmitic acid (0.3 g), 0.11 mol dm^{-3}	162 ± 3	1.32	5
PDMS/SiO_2/FAS	FAS C_8 (0.6 g), 0.092 mol dm^{-3}	163 ± 2	1.35	4

XPS (**Figure 2.02**) and FTIR (**Figure 2.05**) on film **PDMS/SiO_2/SA+PA** were carried out and included to understand the surface composition of this novel material due to its high WCA and fluorine-free composition. **Figure 2.02(a)** (O 1s) indicated SiO_2 (O-Si) and organic C-O due to the peaks at 532.6 eV and 533.6 eV, respectively. **Figure 2.02(b)** (Si 2p) confirmed organic silicon (102.6 eV) and SiO_2 (Si-O) at *ca.* 104.0 eV, verified by the 532.6 eV peak in the O 1s spectrum. The peak at 285.0 eV, **Figure 2.02(c)** (C 1s) revealed a C-O bridge that connects the SiO_2 NP to the carboxyl group of the fatty acid. Finally, **Figure 2.02(d),** the survey spectrum of **PDMS/SiO_2/SA+PA**, indicated that the film did not contain contaminants but only O, Si and C. However, **PDMS/SiO_2/FAS** contained fluorine due to the use of FAS C_8 (a fluorinated polymer) confirmed by F 1s XPS scan, **Figure 2.03**.[94] In all cases, there were minor shifts from the expected values (automatically picked by the CasaXPS software) due to issues with the instrument's flood gun. The proposed structure of the surface modified SiO_2 NPs product is displayed in **Figure 2.04**.

.

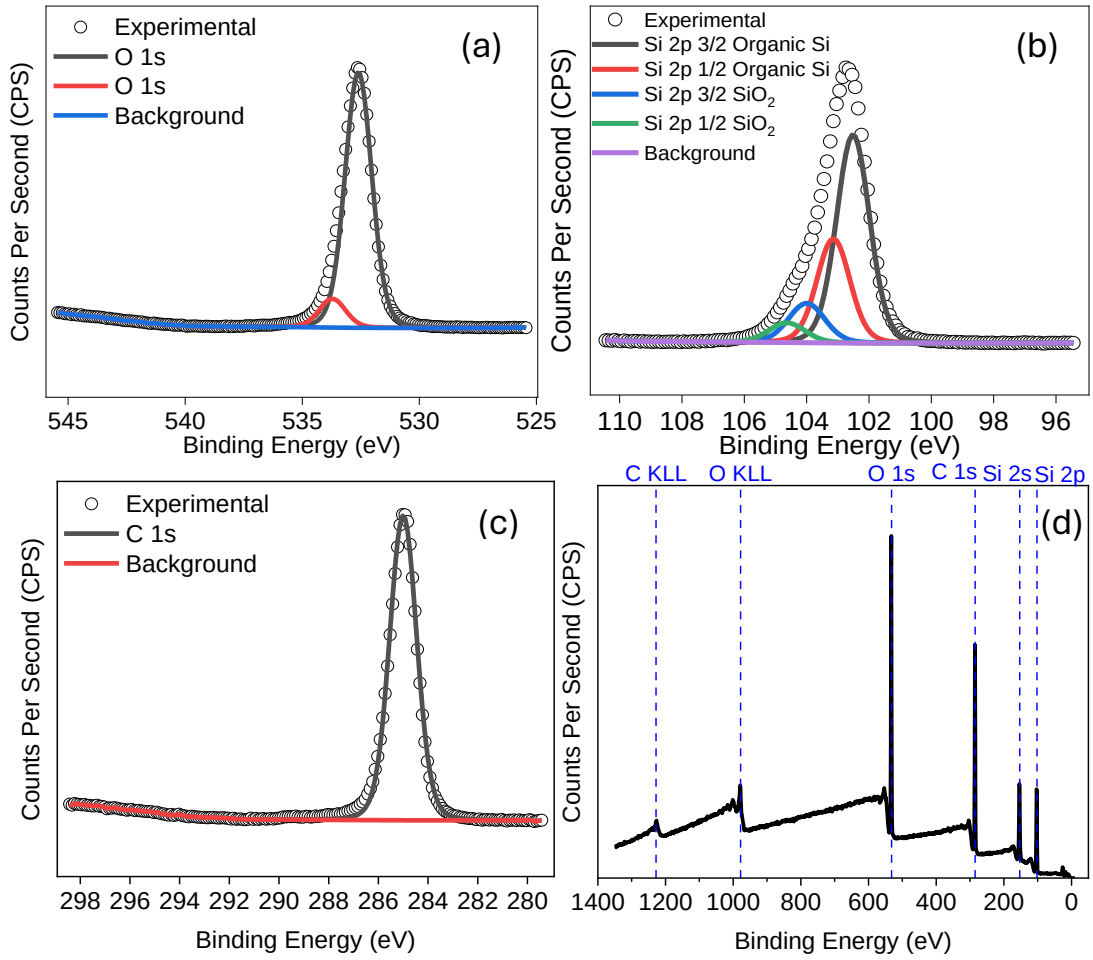

Figure 2.02. *XPS scans for* ***PDMS/SiO₂/SA+PA*** *(a) O 1s (b) Si 2p (c) C 1s and (d) survey spectrum. Scans (a) – (c) indicated the presence of O, Si, C and (d) a survey spectrum. The peaks were slightly shifted due to problems with the XPS instrument's flood gun. Figure reproduced with permission from ACS Langmuir.*[95]

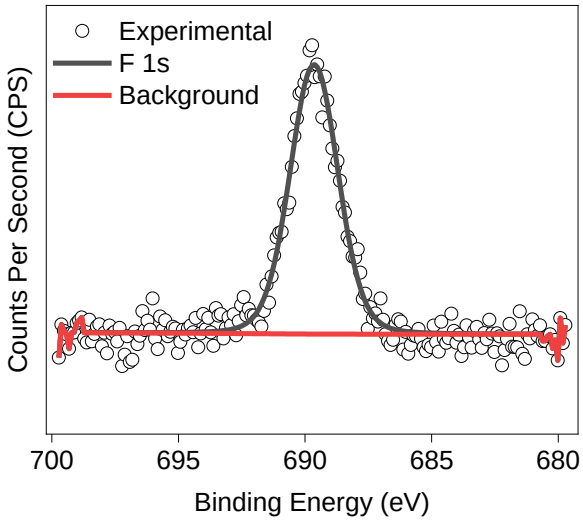

Figure 2.03. *XPS F 1s scan for* ***PDMS/SiO₂/FAS****. O 1s, Si 2p, C 1s scans were similar to* ***PDMS/SiO₂/SA+PA*** *and hence not included. Figure reproduced with permission from ACS Langmuir.*[95]

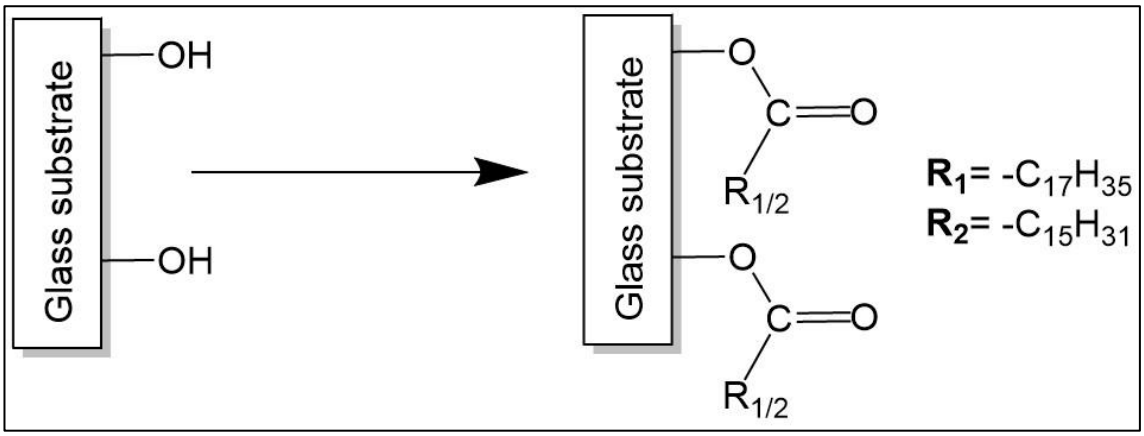

Figure 2.04. *A proposed structure of the fatty acids attached to the SiO_2 NPs. The fatty acids attach to the NP via the carboxyl group. The PDMS polymer (product of the SYLGARD 184 and its curing agent) has been omitted for simplicity.*

An FTIR spectrum, **Figure 2.05**, was recorded for film **PDMS/SiO_2/SA+PA**, indicating successful incorporation of SYLGARD 184, stearic acid and palmitic acid on the glass substrate. Their structures are drawn in **Figure 2.06**. The FTIR spectra of the films made with a single fatty acid were similar to those with a 50:50 hybrid mixture of both fatty acids, despite the mixture. Individual peaks pertained to several reagents as the materials had the same elemental composition of C, H, O, Si (apart from film **PDMS/SiO_2/FAS**), confirmed by XPS, **Figure 2.02**. A strong stretch was visible at *ca.* 1015 cm^{-1} with its assignment to Si-O-Si asymmetric stretching vibrations. The Si-CH_3 group, namely sp^3 C-H asymmetric stretch, was confirmed by the small sharp peak at *ca.* 2962 cm^{-1}. This group could be attributed to the -CH_3 groups of SYLGARD 184. The sp^3 C-H deformation was confirmed by a strong peak at *ca.* 1260 cm^{-1}.[96] Strong and small stretches at 798 cm^{-1} and 866 cm^{-1}, respectively were the stretching vibrations of CH_3. Si-O-Si symmetric and asymmetric stretches, belonging to the SYLGARD 184 and fumed SiO_2 NPs were visualised as sharp and broad peaks at *ca.* 790 cm^{-1} and *ca.* 1076 cm^{-1}, respectively.[97,98] O-H stretches pertaining to the carboxyl groups of the fatty acids were not present, indicating the bonding of the fatty acids to the SiO_2 NPs, confirmed by XPS. All peaks were confirmed by the literature of similar materials. The spectra for all resulting films were similar regardless of modifications to the loadings of components or AACVD conditions as the components of the precursor mixture remained the same, with no changes to the structure of the resulting film.

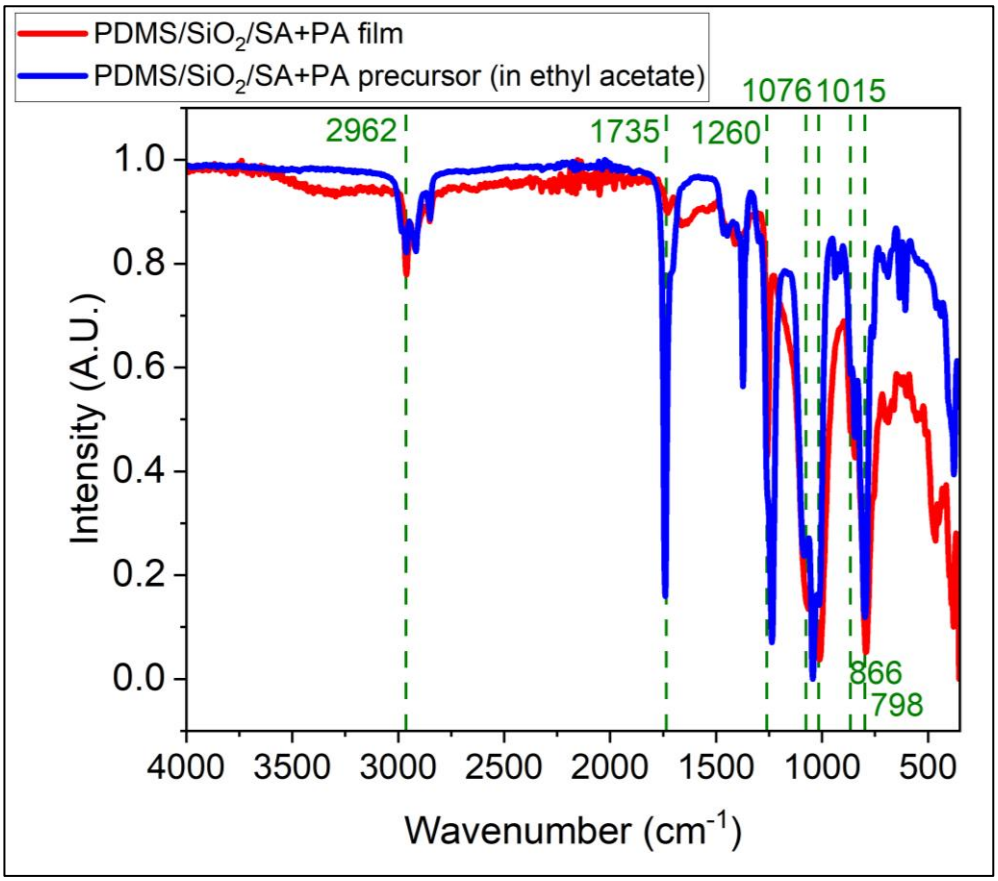

Figure 2.05. *Fourier Transform Infrared (FTIR) of film* ***PDMS/SiO₂/SA+PA*** *and its precursor prior to deposition. Figure reproduced with permission from ACS Langmuir.*[95]

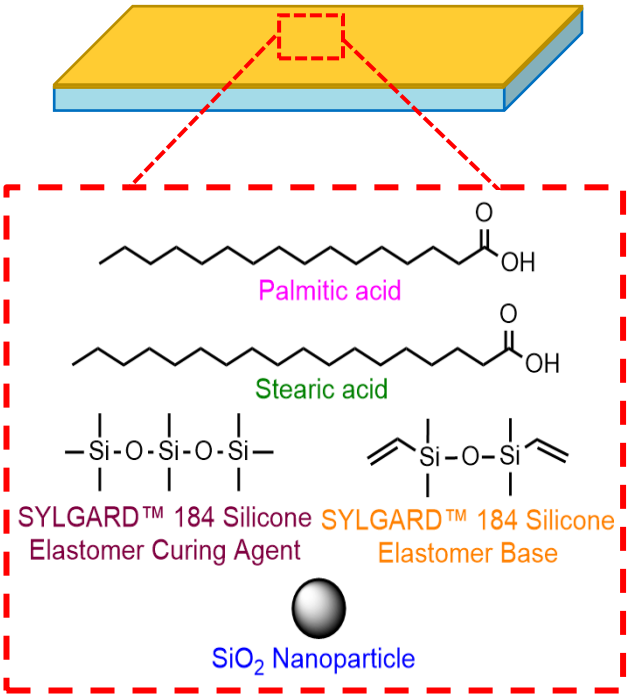

Figure 2.06 *A visual representation of the components of the superhydrophobic film, deposited via AACVD. The chemical structures of the components of the precursor mixture: fatty acids (stearic acid and palmitic acid), SiO_2 NPs, SYLGARD 184 elastomer and its respective curing agent. The terminal vinyl group of the elastomer reacts with the* ***H*** *atom of the Si-C****H****₃ group of the curing agent via an addition reaction. A Pt catalyst aids this oligomerisation to form the PDMS polymer.*

SEM images taken at high magnifications, **Figure 2.07**, visualised the interconnected network of agglomerates that were inconsistently sized and of varying shapes, which were more profound in films **PDMS/SiO_2/SA** and **PDMS/SiO_2/SA+PA**. For the former, the distance in length across the interconnected network was small and spanned 1.1 – 1.6 μm. For film **PDMS/SiO_2/PA**, the agglomerates spanned 1.3 – 6.2 μm and finally, for the 50:50 mix of stearic acid and palmitic acid, film **PDMS/SiO_2/SA+PA**, the sizes ranged from 1.2 μm (individual particles) to 9.1 μm (the separation between ends of the interlinked arrangement). This rough morphology was due to the AACVD method, specifically the piezoelectric humidifier which generates aerosols that are transported into the heated reactor, reacting homogenously or heterogeneously before impacting the substrate.[99]

The standard deviation of the WCAs for **PDMS/SiO_2/SA** was significant (11°), highlighting the differences in hydrophobicity across the whole film. It was not confirmed that the images of **PDMS/SiO_2/SA** were of the superhydrophobic areas however, the idea of networks leading to high superhydrophobicity was attested by the properties of **PDMS/SiO_2/SA+PA**. The WCAs highlighted that **PDMS/SiO_2/FAS** had the highest superhydrophobicity.

Coating the SiO_2 NPs with a single fatty acid (i.e. films **PDMS/SiO_2/SA** and **PDMS/SiO_2/PA**) led to variable hydrophobicity but a blend of stearic acid and palmitic acid (film **PDMS/SiO_2/SA+PA**) engendered superhydrophobicity throughout the film, without the use of a fluorinated polymer. The positive correlation between roughness (Sq) and WCA was corroborated quantitatively by the increase in WCA. The Sq value increased due to the presence of air spaces between the peaks which penetrated between the peaks, cushioning the water droplet and elevating it.[18] **PDMS/SiO_2/PA, PDMS/SiO_2/SA, PDMS/SiO_2/SA+PA, PDMS/SiO_2/FAS** had Sq values/WCAs of 0.27 μm/129°, 0.69 μm/145°, 1.32 μm/162° and 1.35 μm/163°, respectively. This relationship was observed qualitatively when compared to the SEM images, **Figure 2.07**.

The transparency and WCAs of films are negatively correlated.[100] The greater the roughness of the film, the more complex the morphology and the lower the transparency, this trend was apparent in all films, **Table 2, Figure 2.07**. The low transmittance for films **PDMS/SiO_2/SA** and **PDMS/SiO_2/SA+PA** (relative to that of plain glass *ca.* 91%) is reasoned by the lower magnification images where

there were more particles per unit area, relative to film **PDMS/SiO$_2$/PA**, making the penetration of visible light difficult. Similarly, large particles (>100 nm) led to increased scattering of visible light, contributing to lower transmittance values. Low magnification SEM images of film **PDMS/SiO$_2$/PA** appeared like those of film **PDMS/SiO$_2$/SA** however, the NPs coated in just stearic acid were more consistent in size and shape hence the lower WCA. Fluorinated superhydrophobic films reported in the literature have transmittance values >90% however, even the fluoroalkysilane equivalent reported herein, film **PDMS/SiO$_2$/FAS**, had a transmittance of 5% which could have been due to the AACVD process and hence complex rough morphology generated as a result.[53,54]

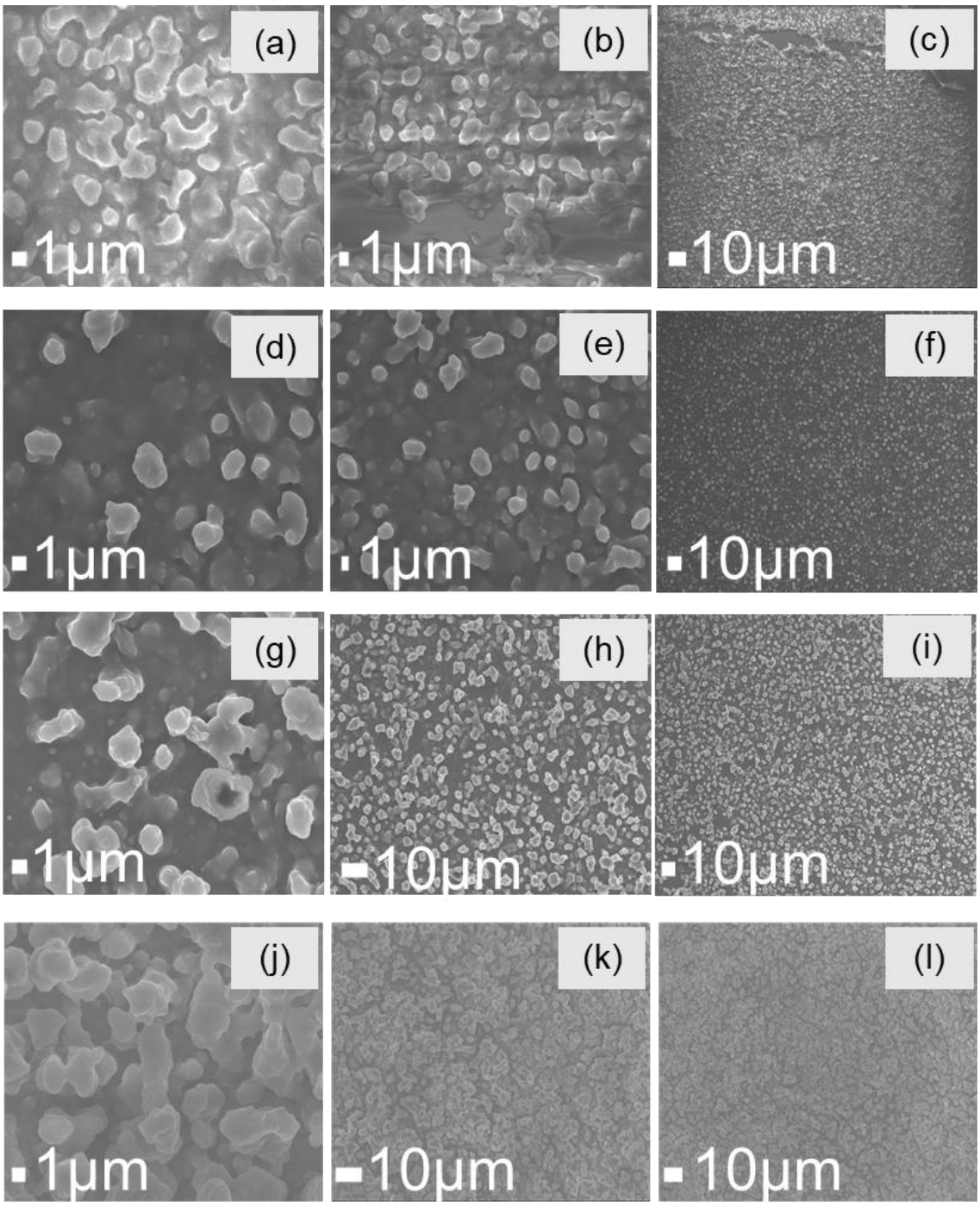

Figure 2.07. *SEM images of films produced in* ***Study 1****. Images a – c depict the morphology of film* ***PDMS/SiO₂/SA*** *(stearic acid only). Images d – f represents film* ***PDMS/SiO₂/PA*** *(palmitic acid only). Images g – i depict film* ***PDMS/SiO₂/SA+PA*** *(a 50:50 hybrid mixture of stearic and palmitic acid). Images j – l are of film* ***PDMS/SiO₂/FAS****. Images reproduced with permission from ACS Langmuir.*[95]

2.4.2 Study 2: The influence of different sized SiO_2 NPs on superhydrophobicity

Film **PDMS/SiO_2/SA+PA** had the highest WCA so this procedure was used and modified to further increase the WCA. Previous research had shown that using NPs of two different sizes influenced the roughness and hence superhydrophobicity.[101] Hence, two different sized SiO_2 NPs were used for this study: Aerosil OX50 SiO_2 NPs (45 nm) and SiO_2 NPs (10 – 20 nm). These films either consisted of one or two types of NPs and were labelled as **PDMS/1SiO_2 /SA+PA** and **PDMS/2SiO_2/SA+PA**, indicating NPs of one or two types of sizes, **Table 3**.

Table 3. *A study of fumed SiO_2 NPs of different sizes with SYLGARD 184, its respective curing agent, stearic acid and palmitic acid. Films were deposited via AACVD using the following conditions:* ***flow rate:*** *1 L/min,* ***deposition temperature:*** *300 °C,* ***total deposition time:*** *1.5 hr.*

Film code	**Type, mass of SiO_2 NPs (g) and total solution concentration (mol dm^{-3})**	**WCA ± 1 Standard Deviation (°)**	**Transmittance (%) Plain glass: *ca.* 91%**
PDMS/1SiO_2 /SA+PA	Aerosil OX50 SiO_2 NPs (0.26 g), 0.11 mol dm^{-3}	162 ± 3	5
PDMS/2SiO_2/SA+PA	Aerosil OX50 SiO_2 NPs (0.13 g) and SiO_2 NPs (0.13 g), 0.11 mol dm^{-3}	152 ± 1	22

Overall, the SEM images for film **PDMS/2SiO_2/SA+PA**, **Figure 2.08**, indicated more structure and porosity on the surface than for film **PDMS/1SiO_2/SA+PA**. This allowed the water droplets to seep into the microstructure, increasing its area of contact with the interface and reducing its WCA. Transmittance values for film **PDMS/2SiO_2/SA+PA** were higher than for that of film **PDMS/1SiO_2/SA+PA** although film **PDMS/2SiO_2/SA+PA** was visibly denser with SiO_2 NPs. This could be because film **PDMS/1SiO_2/SA+PA** (**Figure 2.08**, **images a – c**) included smaller particles <100 nm embedded into the film, leading to less scattering of visible light and hence higher transmittance values.

The surface topography of film **PDMS/2SiO_2/SA+PA** was highly textured with many particles protruding from the surface which may have contributed to the

"powdery" layer seen in film **PDMS/2SiO$_2$/SA+PA**, **Figure 2.08**. These agglomerates which also created the roughness, were less strongly bound to one another as they were physically impacted onto the well-adhered hydrophobic film formed initially and hence were easily abraded.

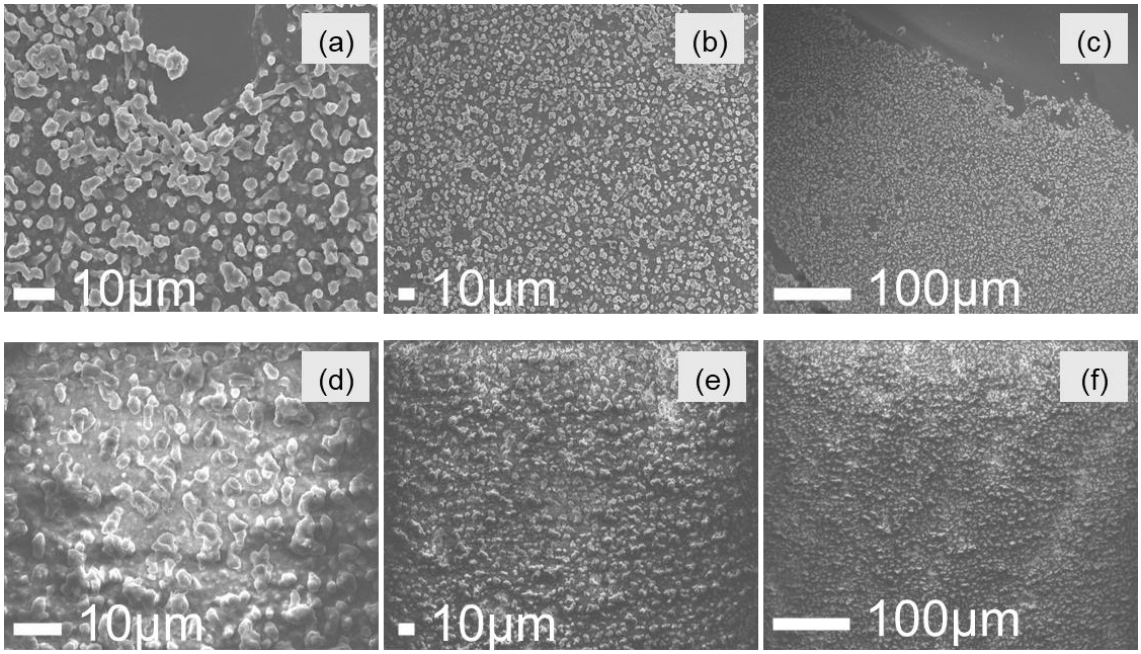

Figure 2.08. *SEM images of films produced in* ***Study 2****. Images a - c depict the morphology of film* ***PDMS/1SiO$_2$/SA+PA*** *(SiO_2 NPs of a single size, each NP is said to be ca. 45 nm), coated with a 50:50 mixture of stearic and palmitic acid. Images d - f show the morphology of film* ***PDMS/2SiO$_2$/SA+PA*** *(SiO_2 NPs of two different sizes* ca. *45 nm and 10 – 20 nm), coated with a 50:50 mixture of stearic and palmitic acid).*

2.4.3 Study 3: The effect of deposition temperature on the film's properties

The procedure for film **PDMS/1SiO$_2$/SA+PA** was carried through as it had the best adherence and water contact angle. To be specific, a 50:50 hybrid mixture of SA:PA, SYLGARD 184, its respective curing agent and SiO_2 NPs were dissolved in ethyl acetate and deposited via AACVD. Different deposition temperatures were studied, namely 300 °C, 360 °C and 400 °C to alter the microstructure of the films to ultimately improve its superhydrophobicity, **Table 4**.

Table 4. *A study of fumed SiO_2 NPs with SYLGARD 184, its respective curing agent, stearic acid and palmitic acid deposited via AACVD at different temperatures using the following conditions:* ***flow rate:*** *1 L/min,* ***deposition temperature:*** *300 - 400 °C,* ***total deposition time:*** *1.5 hr.*

Film code	Temperature (°C)	WCA ± 1 Standard Deviation (°)	Sq (µm)	Transmittance (%) Plain glass: *ca.* 91%
PDMS/SiO$_2$ /SA+PA/300	300	162 ± 3	1.32	5
PDMS/SiO$_2$ /SA+PA/360	360	162 ± 2	1.24	9
PDMS/SiO$_2$ /SA+PA/400	400	129 ± 7	0.34	8

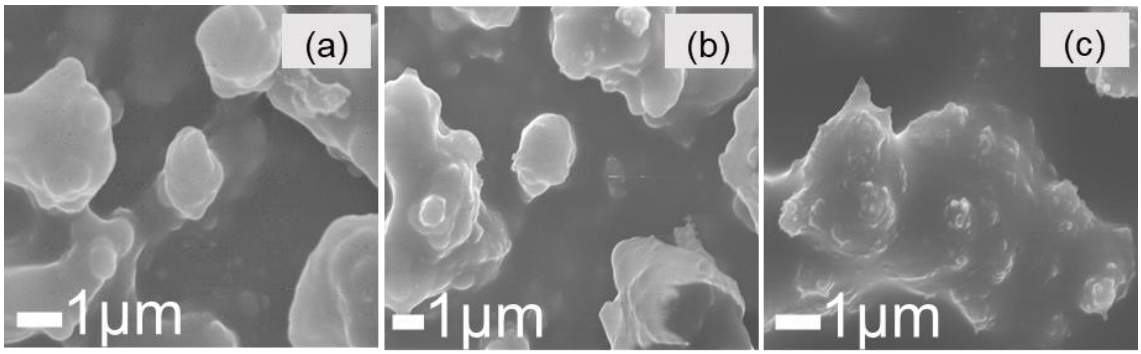

Figure 2.09. *SEM images of the morphology of all films produced in* ***Study 3*** *which all consisted of SiO_2 NPs coated with a 50:50 mixture of stearic acid and palmitic acid but deposited at different temperatures. Image a depicts the morphology of film* ***PDMS/SiO$_2$/SA+PA/300*** *(deposition temperature: 300 °C), film* ***PDMS/SiO$_2$/SA+PA/360*** *(deposition temperature: 360 °C) and film* ***PDMS/SiO$_2$/SA+PA/400*** *(deposition temperature: 400 °C). Images reproduced with permission from ACS Langmuir.*[95]

Depositing above the decomposition temperature of the intermediates formed in the gas phase has been shown to create powdery deposits. Therefore, the procedure was repeated at *ca.* 300 °C, below the decomposition temperature of the fatty acids and SYLGARD 184. SYLGARD 184 has the lowest decomposition temperature of *ca.* 300 - 310 °C.[102] Stearic acid has a decomposition temperature of *ca.* 360 °C.[103] Even though the procedure was repeated at a temperature below the decomposition temperature of the reagents, i.e. 300 °C, the deposited films were still powdery. The lower deposition temperature also had a lower WCA and did not improve the transmittance.

Increasing the deposition temperature from *ca.* 300 °C to 365 °C did not increase the WCA. However, increasing the temperature further led to hydrophobicity. The electron microscope images, **Figure 2.09**, showed the Volmer Webber island growth of the films where the interactions between the particles are stronger than to the surface. There are also sphere-shaped nano- and micro- particles on the interlinked arrangement of microparticles. Films **PDMS/SiO_2/SA+PA/300** and **PDMS/SiO_2/SA+PA/360** had microparticles of 0.50 – 1.1 µm and 0.68 – 1.0 µm, respectively. Smaller particles were more prominent on extended networks of particles of the films deposited at 360 °C and 400 °C, which were more noticeable in film **PDMS/SiO_2/SA+PA/400.** For film **PDMS/SiO_2/SA+PA/360**, these microparticles range from 0.14 – 0.33 µm and for film **PDMS/SiO_2/SA+PA/400**, these range from 0.08 – 2.3 µm. The prevalence of these small NPs, particularly evident in film **PDMS/SiO_2/SA+PA/400**, could have been due to the high deposition temperature and as a result, rapid curing of PDMS and rapid evaporation of ethyl acetate.[14] This study indicated that having particles of three different size ranges (rather than just two), can enhance the superhydrophobicity. Interestingly, a deposition temperature of 400 °C afforded hydrophobic films (WCA: 129 ± 7°) because of a reduction in Sq value to 0.34 µm. Deposition temperatures of 300 °C and 360 °C did not affect the WCA, verified by the comparable root-mean square height values of Sq= 1.32 µm and Sq = 1.24 µm, respectively. Transmittance remained low relative to plain glass (>91%) due to adding several layers of the precursor mixture, creating a white opaque film.

2.4.4 Study 4: The influence of increasing the concentration of the fatty acids

The deposition temperature for film **PDMS/SiO_2/SA+PA/360** was used as it created a more superhydrophobic film. In this study, the concentration of fatty acids was increased to increase the superhydrophobicity of the film, **Table 5**.

Table 5. *A study of fumed SiO_2 NPs with SYLGARD 184, its respective curing agent, varying concentrations of stearic acid and palmitic acid deposited via AACVD using the following conditions:* ***flow rate:*** *1 L/min,* ***deposition temperature:*** *360 °C,* ***total deposition time:*** *1.5 hr.*

Film code	**Mass of Stearic acid, Palmitic acid (g) and total solution concentration (mol dm^{-3})**	**WCA ± 1 Standard Deviation (°)**	**Transmittance (%) Plain glass: *ca.* 91%**
PDMS/SiO_2/0.3g(SA+PA)/360	Palmitic acid (0.3 g), Stearic acid (0.3 g), 0.11 mol dm^{-3}	162 ± 2	9
PDMS/SiO_2/0.5g(SA+PA)/360	Palmitic acid (0.5 g), Stearic acid (0.5 g), 0.13 mol dm^{-3}	162 ± 1	3
PDMS/SiO_2/0.7g(SA+PA)/360	Palmitic acid (0.7 g), Stearic acid (0.7 g), 0.16 mol dm^{-3}	167 ± 3	3

Increasing the mass of stearic acid and palmitic acid led to an increased WCA from 162 ± 2° to 167 ± 3° due to the formation of more interconnected particles per unit area enhancing the coverage, which also explains the reduction in transmittance. The higher magnification images, **Figure 2.10(a) & (d),** illustrated that the interconnected networks were smooth with spherical microparticles (*ca.* 0.66 – 0.83 μm) mounted onto the network as well as very small NPs (<0.23 μm), all contributing to the textured hierarchical morphology. Undoubtedly this altered the water molecules' interaction with the surface by trapping air underneath the water droplet as seen in the Cassie-Baxter model (**Section 1.3.3**). All films in this study were well-adhered.

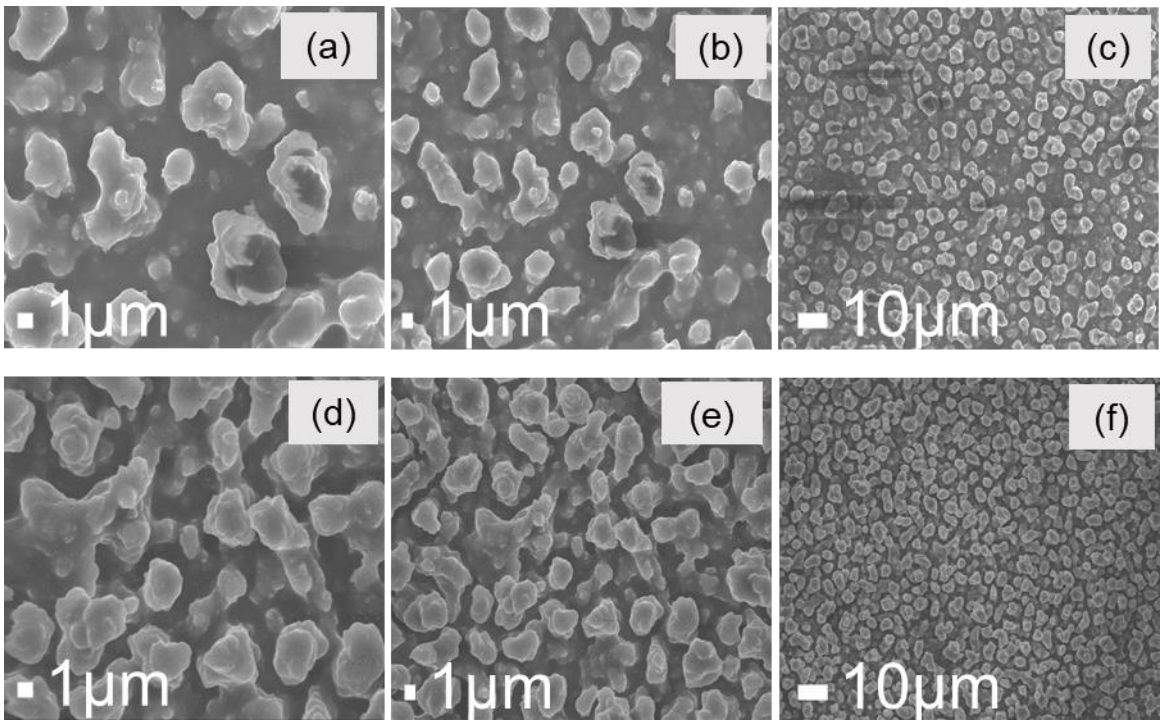

Figure 2.10 *SEM images illustrating the morphologies of films* ***PDMS/SiO_2 /0.3g(SA+PA)/360*** *and* ***PDMS/SiO_2/0.7g(SA+PA)/360*** *from* ***Study 4*** *which all consist of SiO_2 NPs coated with a 50:50 mixture of stearic and palmitic acid of different concentrations. Images a – c relate to film* ***PDMS/SiO_2/0.3g(SA+PA)/360*** *(0.3 g of both palmitic and stearic acid) and images d – f relate to film* ***PDMS/SiO_2/0.7g(SA+PA)/360*** *(0.7 g of both palmitic and stearic acid).*

2.4.5 Study 5: The effect of varying the loading of OX50 SiO_2 NPs

The ratio of OX50 SiO_2 NPs to fatty acids was altered to determine its effect on the film's water contact angle, **Table 6**.

Table 6. *A study of three concentrations of fumed SiO_2 NPs with SYLGARD 184, its respective curing agent, stearic acid and palmitic acid deposited via AACVD using the following conditions:* ***flow rate:*** *1 L/min,* ***deposition temperature:*** *360 °C,* ***total deposition time:*** *1 hr 10 min.*

Film number	**Mass of OX50 SiO_2 NPs (g) and total solution concentration (mol dm^{-3})**	**WCA ± 1 Standard Deviation (°)**	**Transmittance (%)** **Plain glass: *ca.* 91%**
PDMS/0.25g(SiO_2)/SA+PA/360	0.25, 0.11 mol dm^{-3}	163 ± 2	12
PDMS/0.30g(SiO_2)/SA+PA/360	0.30, 0.12 mol dm^{-3}	163 ± 1	27
PDMS/0.35g(SiO_2)/SA+PA/360	0.35, 0.13 mol dm^{-3}	165 ± 2	17

High magnification SEMs for these films, **Figure 2.11**, demonstrated the network structure discussed in earlier studies however here, WCAs were >160°, possibly due to more consistently shaped NPs creating a rough microstructure. Even though the particle density and hence coverage was high for film **PDMS/0.25g(SiO_2)/SA+PA/360**, the transmittance was still higher than for previous studies. This could have been because here, the deposition time was shorter, leading to thinner films as well as the integration of NPs <100 nm. The film thickness was not measured however, could be quantified via cross-sectional SEM, which was measured to be < 3 μm.

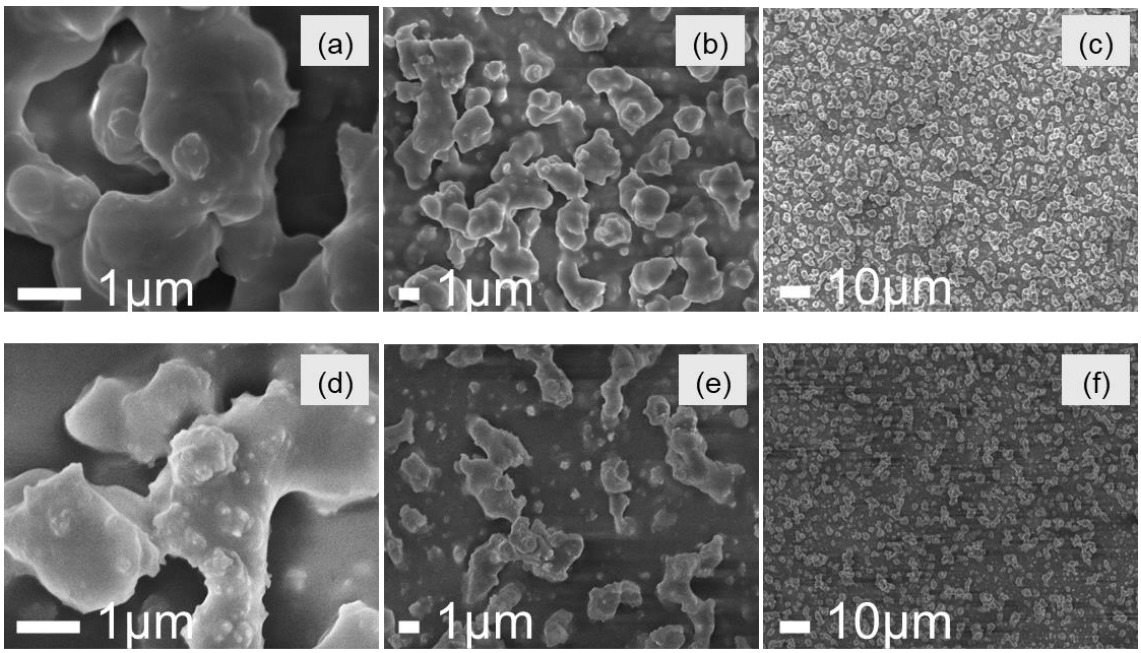

Figure 2.11. *SEM images illustrating the morphologies of some of the films from* ***Study 5*** *which consist of two different concentrations of SiO_2 NPs coated with a 50:50 mixture of stearic and palmitic acid. Images a – c relate to film* ***PDMS/0.25g(SiO_2)/SA+PA/360*** *(ca. 0.25 g of SiO_2 NPs) and images d – f relate to film* ***PDMS/0.35g(SiO_2)/SA+PA/360*** *(*ca. *0.35 g of SiO_2 NPs).*

2.4.6 Study 6: The effect of deposition time

A large concentration of reagents and excessive volumes of solvent were used in **Studies 1 – 5** which was inefficient therefore changes were made to improve the efficiency of the overall procedure. Optimisation into minimising waste was pursued provided it did not negatively influence the functional properties of the films.

Even though film **PDMS/0.25g(SiO_2)/SA+PA/360** had the lowest transmittance, the WCA did not vary too much with the additional 0.05 g/0.1 g of SiO_2 therefore this original procedure was carried through. The deposition time was varied (ranging from 45 min to 10 min) to investigate its influence on the materials' thickness and hence transparency, **Table 7**. The significantly shorter deposition time of 45 min relative to the initial deposition time of 1 h 30 min was studied as there was not a significant difference in WCA.

Table 7. *A study of fumed SiO_2 NPs with SYLGARD 184, its respective curing agent, stearic acid and palmitic acid deposited via AACVD at varying deposition times using the following conditions:* ***flow rate:*** *1 L/min,* ***deposition temperature:*** *360 °C,* ***total deposition time:*** *10 min – 45 min.*

Film number	AACVD total length of deposition (min)	WCA ± 1 Standard Deviation (°)	Transmittance (%) Plain glass: *ca.* 91%
PDMS/SiO_2/SA+PA/45min	45	160 ± 2	15
PDMS/SiO_2/SA+PA/40min	40	161 ± 2	32
PDMS/SiO_2/SA+PA/37min	37	163 ± 2	18
PDMS/SiO_2/SA+PA/35min	35	161 ± 2	18
PDMS/SiO_2/SA+PA/30min	30	146 ± 14	30
PDMS/SiO_2/SA+PA/25min	25	132 ± 8	46
PDMS/SiO_2/SA+PA/10min	10	112 ± 5	53

There is a clear link between reducing the deposition time and the level of hydrophobicity, as demonstrated in **Table 7**. The longer the deposition time, the more hydrophobic the film. A longer deposition time resulted in thicker films with less porosity and vice versa. For this study, the deposition time was reduced from 1.5 hr (WCA: 162°) to 10 – 45 min (WCA range: 112° to 160°) as it was hypothesised that allowing the mixture to deposit for longer may have been the

cause of powdery films. The idea was that longer deposition times may have led to more time for the precursor mixture to nucleate, accumulating as large particles on the surface, leading to a powdery deposition. Alternatively, it was thought that the solid deposits produced via homogenous reactions in the gas phase would disturb the nucleation process hence the adhesion of the deposited film to the substrate.

No clear link between the deposition length and the level of adherence was observed as the superhydrophobic films were still powdery, including the repeats. However, all the hydrophobic films (films deposited at 10, 25, 30 min) were well-adhered which may have been due to chemisorption where nucleation and growth (originating from the substrate) led to the formation of a strong chemical bond between the substrate and particle. Longer deposition times may have led to an impaction of additional SiO_2 NPs onto other SiO_2 NPs, which did not “stick” well.

The transmittance of film **PDMS/SiO_2/SA+PA/40min** appeared to be an outlier, potentially due to the lack in uniformity of film coverage across the film. The transmittance varied regardless of deposition time due to the thickness of the film which was not as controlled as changing the concentration of the components of the precursor mixture. AACVD occasionally results in a film of different thicknesses across the substrate, especially when attempting to control the deposition time as this is not a reliable indicator of how much precursor mixture has been transferred. This is because the rate of deposition changes over time (it is slower at the start when the flask is full and faster at the end when the flask is emptier). Therefore, the volume of precursor mixture per unit time is not continuous through the experiment hence a 25 min deposition rather than a 50 min deposition is not equivalent to half of the precursor mixture deposited on the substrate. Apart from the density of particles across the area, the film’s thickness and sizes of the particles contributed to the transmittance values recorded. In this study, a short deposition time potentially formed the thinnest film with the highest recorded transmittance value for this study, %T = 53% and hence lowest WCA (112 ± 5°), **Table 7**.

2.4.7 Study 7: The effect of halving and quartering the concentration of the components of the precursor mixture (excluding [SiO_2])

A large concentration of reagents and excessive volumes of solvent were used in **Studies 1 – 6** which was inefficient therefore changes were made to improve the efficiency of the overall procedure. Optimisation into minimising waste was pursued provided it did not negatively influence the functional properties of the films; the following films were deposited for 40 min, **Table 8**.

Table 8. *A study of the effect of varying the concentration of SYLGARD 184, its respective curing agent, stearic acid and palmitic acid deposited via AACVD using the following conditions:* ***flow rate:*** *1 L/min,* ***deposition temperature:*** *360 °C,* ***total deposition time:*** *40 min.*

Film number	Fraction of all reagents used with respect to above procedure and total solution concentration, (mol dm^{-3})	WCA ± 1 Standard Deviation (°)	Transmittance (%) Plain glass: *ca.* 91%
1.0PDMS/SiO_2/1.0(SA+PA)/40min	1, 0.11 mol dm^{-3}	161 ± 2	32
0.75PDMS/SiO_2/0.75(SA+PA)/40min	¾, 0.080 mol dm^{-3}	162 ± 2	14
0.5PDMS/SiO_2/0.5(SA+PA)/40min	½, 0.053 mol dm^{-3}	161 ± 2	34
0.25PDMS/SiO_2/0.25(SA+PA)/40min	¼, 0.027 mol dm^{-3}	151 ± 7	30

The aim was to reduce the amount of precursor mixture proportionately but to keep the volume of solvent the same. In other words, the concentration of the mixture was fractionally varied (relative to the precursor mixture: **1.0PDMS/SiO_2/1.0(SA+PA)/40min**), **Table 8**. Unlike for **Study 6** where the deposition time was changed, the concentration of precursor mixture was changed, the solvent volume was kept the same but left to deposit via AACVD for the same length of time. It is very difficult to make reproducible depositions with short deposition times via AACVD. However, reducing the concentration but keeping the deposition time the same can reduce variability which was confirmed by the similar water contact angles and transmittance values relative to **Study 6**. For instance, films **PDMS/SiO_2/SA+PA/45min** and **PDMS/SiO_2/SA+PA/25min**

(approximately ½ and ¼ of the original deposition time) had a difference in WCA of *ca.* 28° and a difference of *ca.* 31% in transmittance. Films **0.5PDMS/SiO_2/0.5g(SA+PA)/40min** and **0.25PDMS/SiO_2/0.25g(SA+PA)/40min** (½ and ¼ of the original concentration) had a difference in WCA of *ca.* 10° and a difference of *ca.* 4% in transmittance. Although these pairs of films are not directly comparable, they confirmed that varying the concentration of the precursor mixture is an easier parameter to control than the deposition length. Even though all films produced in **Study 6** were powdery, they were consistent among themselves. Film **0.75PDMS/SiO_2/0.75(SA+PA)/40min** had the lowest transmittance due to the thickness of the film. As film **0.5PDMS/SiO_2/0.5(SA+PA)/40min** utilised a minimum amount of precursor while displaying superhydrophobicity, cross-sectional SEM was carried out on the film to determine its thickness, **Figure 2.12**, which was approximately 0.25 µm – 3 µm. A series of investigations were carried out to understand the effect of the individual components/reagents and their loadings on the adhesion of the films.

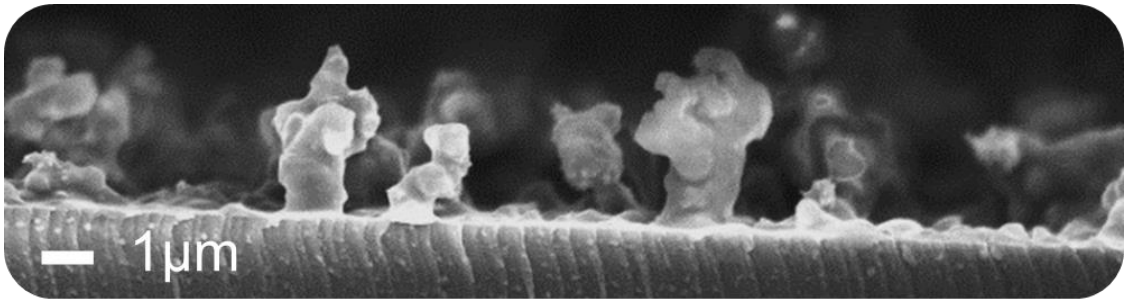

Figure 2.12. *Cross-sectional SEM of film* ***0.5PDMS/SiO_2/0.5(SA+PA)/40min*** *with a measured thickness of ca. 0.25 µm – 3 µm.*

2.4.8 Study 8: The influence of stearic and palmitic acid on adherence

Film **0.5PDMS/SiO_2/0.5(SA+PA)/40min** had the best properties in terms of transmittance and water contact angle (>160°) whilst using only half the concentration of reagents. Therefore, all parameters were kept the same and the concentration of fatty acids in the precursor mixture was varied for this procedure to determine if it influenced the film's adherence, **Table 9**. All films were deposited at 40 min. Films **PDMS/SiO_2/0.22g(SA+PA)** and **PDMS/SiO_2/0.22g(SA+PA)_2** are repeats of each other, **Table 9**.

Table 9. *A study of the effect of varying the concentration of stearic acid and palmitic acid deposited via AACVD using the following conditions:* ***flow rate:*** *1 L/min,* ***deposition temperature:*** *360 °C,* ***total deposition time:*** *40 min. Films* ***PDMS/SiO$_2$/0.22g(SA+PA)*** *and* ***PDMS/SiO$_2$/0.22g(SA+PA)_2*** *are repeats of each other.*

Film number	Mass of stearic and palmitic acid each (i.e. value of x) (g) and total concentration of the solution, mol dm^{-3}	WCA ± 1 Standard Deviation (°)	Transmittance (%) Plain glass: *ca.* 91%
PDMS/SiO$_2$/0.18g(SA+PA)	0.18, 0.080 mol dm^{-3}	161 ± 2	34
PDMS/SiO$_2$/0.22g(SA+PA)	0.22, 0.083 mol dm^{-3}	158 ± 2	34
PDMS/SiO$_2$/0.22g(SA+PA)_2	0.22, 0.083 mol dm^{-3}	156 ± 2	38
PDMS/SiO$_2$/0.25g(SA+PA)	0.25, 0.085 mol dm^{-3}	150 ± 4	27
PDMS/SiO$_2$/0.27g(SA+PA)	0.27, 0.086 mol dm^{-3}	138 ± 14	28

Although stearic acid and palmitic acid are inherently hydrophobic due to their hydrophobic carbon chain, increasing the masses of fatty acids decreased the water contact angle and transmittance. The fatty acids are both white solids and may have contributed to the “whiteness” of the films hence the low transmittance. Films **PDMS/SiO$_2$/0.22g(SA+PA)** and **PDMS/SiO$_2$/0.22g(SA+PA)_2** are repeats of each other.

There was no difference between the FTIR spectra of films **PDMS/SiO$_2$/0.22g(SA+PA)** and **PDMS/SiO$_2$/0.22g(SA+PA)_2**. This confirmed that differences in adherence were due to the morphology of the films, **Figure 2.13**. Although their conditions were the same, film **PDMS/SiO$_2$/0.22g(SA+PA)** had a rough morphology along with clustering of the particles nevertheless, these were smaller than the particles in film **PDMS/SiO$_2$/0.22g(SA+PA)_2** which were larger aggregates of material. There were some areas of the films where the water droplets could seep into the morphology a bit more in this study relative to

previous studies (e.g. **2.4.4 Study** 4: The influence of increasing the concentration of the fatty **acids**). Overall, varying the concentration of fatty acids in the precursor mixture had no effect on the adherence of the film.

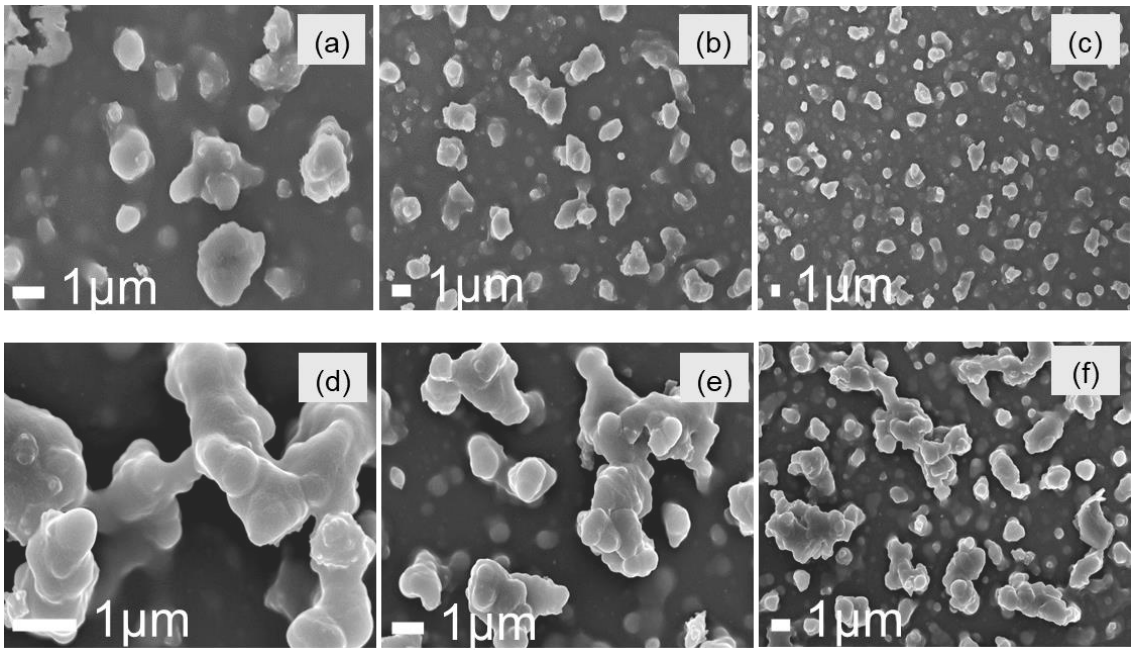

Figure 2.13. *SEM images illustrating the morphologies of films* ***PDMS/SiO$_2$/0.22g(SA+PA)*** *and* ***PDMS/SiO$_2$/0.22g(SA+PA)_2*** *from* ***Study 8*** *which are repeats of each other, but with different levels of adherence. Images a – c relate to film* ***PDMS/SiO$_2$/0.22g(SA+PA)*** *(well-adhered) and images d – f relate to film* ***PDMS/SiO$_2$/0.22g(SA+PA)_2*** *(powdery).*

2.4.9 Study 9: The influence of SYLGARD 184 on adherence

Film **PDMS/SiO_2/0.22g(SA+PA)** had the best properties in terms adherence so the concentration of SYLGARD 184 was varied for this procedure to determine whether its viscose nature would improve the adhesion of the films to the glass substrate, **Table 10**. Changes in concentration of the solution as a function of increasing SYLGARD 184 concentrations could not be calculated due to undisclosed information by the manufacturer.

Table 10. *A study of the effect of varying the concentration of SYLGARD 184. The films were deposited via AACVD using the following conditions:* ***flow rate:*** *1 L/min,* ***deposition temperature:*** *360 - 365 °C,* ***total deposition time:*** *40 min.*

Film number	Mass of SYLGARD 184 (g)	WCA ± 1 Standard Deviation (°)	Transmittance (%) Plain glass: *ca.* 91%
0.10gPDMS/SiO_2/0.22g(SA+PA)	0.10	158 ± 2	35
0.15gPDMS/SiO_2/0.22g(SA+PA)	0.15	158 ± 2	34
0.20gPDMS/SiO_2/0.22g(SA+PA)	0.20	157 ± 1	17
0.25gPDMS/SiO_2/0.22g(SA+PA)	0.25	157 ± 1	12
0.35gPDMS/SiO_2/0.22g(SA+PA)	0.35	155 ± 1	14
0.45gPDMS/SiO_2/0.22g(SA+PA)	0.45	156 ± 2	7

As the concentration of SYLGARD 184 increased, the water contact angles decreased and so did the transmittance. SYLGARD 184 is a viscous liquid which smoothed the surface of the SiO_2 clusters which can be seen in **Figure 2.14**. Similarly, the particles in film **0.45gPDMS/SiO_2/0.22g(SA+PA)** agglomerated in larger clusters relative to film **0.15gPDMS/SiO_2/0.22g(SA+PA)**. A combination of a smoother surface and larger particles led to a reduction in WCA. The clusters increased in size as the concentration of SYLGARD 184 increased (from an average of 1.6 μm to an average of 6.5 μm). This indicated that it improved the adhesion of the particles to each other, creating even larger protruding structures on the surface, compromising the hydrophobicity and overall robustness of the

film. All lengths were measured across the longest side of the particle.

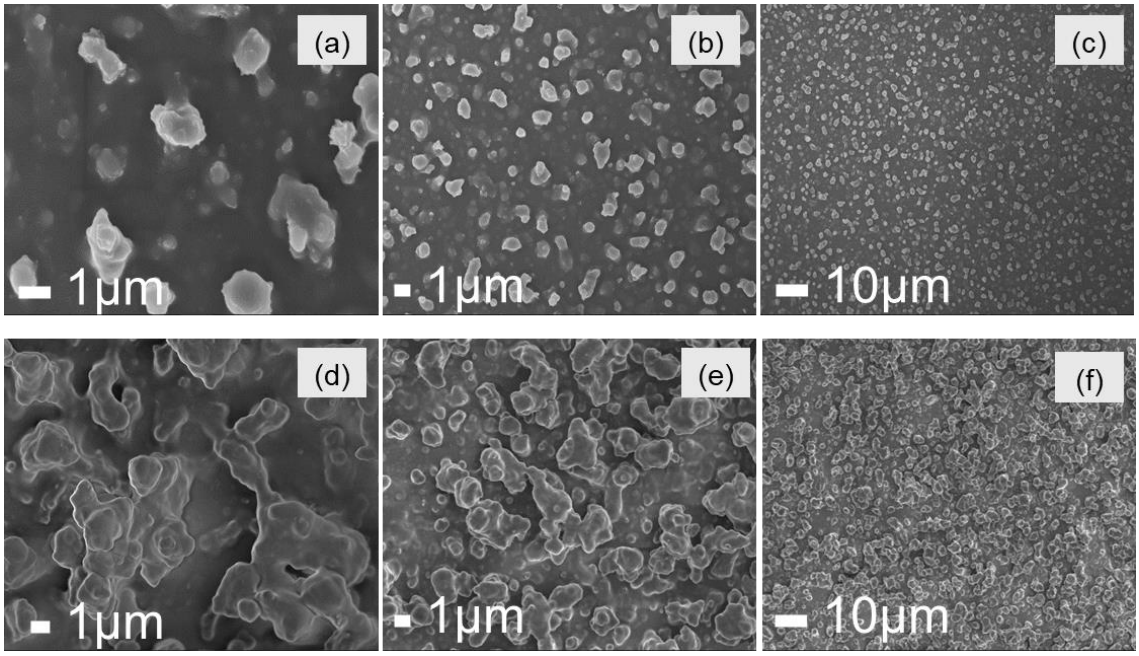

Figure 2.14. *SEM images illustrating the morphologies of films* ***0.15gPDMS/SiO$_2$/0.22g(SA+PA)*** *and* ***0.45gPDMS/SiO$_2$/0.22g(SA+PA)*** *from* ***Study 9*** *which all consisted of two different concentrations of SYLGARD 184. Images a – c relate to film* ***PDMS/SiO$_2$/0.22g(SA+PA)*** *(ca. 0.15 g of SYLGARD 184) and images d – f relate to* ***film 0.45gPDMS/SiO$_2$/0.22g(SA+PA)*** *(ca. 0.45 g of SYLGARD 184).*

2.5 Functional, Durability and Performance Testing

Ultimately, film **0.5PDMS/SiO_2/0.5(SA+PA)/40min** was best in terms of WCA, coverage and adherence. As a result, this film was deposited at 360 °C for 40 min and performance and durability tests were carried out on it. A fluoroalkysilane equivalent **0.5PDMS/SiO_2/0.5FAS/40min**, was deposited with the same reagents and under the same conditions but with FAS C_8 rather than a 50:50 SA:PA mixture. As well as measuring the WCA, the contact angle hysteresis (CAH) and sliding angles (SAs) were also measured, **Table 11**.

Table 11. *Functional testing summary for films **0.5PDMS/SiO_2/0.5(SA+PA)/40min** and **0.5PDMS/SiO_2/0.5FAS/40min** (presence and absence of FAS C_8, respectively). As well as WCAs, SAs, CAH and Sq values of the films are also tabulated. Table reproduced with permission from ACS Langmuir.*[95]

Film	FAS C_8 / Fatty acid used and total concentration of solution (mol dm^{-3})	Deposition time (min)	WCA (°)	SAs (°)	CAH (°)	Sq (μm)
0.5PDMS/SiO_2/0.5(SA+PA)/40min	50:50 ratio of stearic acid & palmitic acid, 0.053 mol dm^{-3}	40 min	163 ± 1	4 ± 1	14 ± 4	0.60
0.5PDMS/SiO_2/0.5FAS/40min	FAS C_8, 0.044 mol dm^{-3}	40 min	161 ± 2	4 ± 1	20 ± 9	0.66

Both films **0.5PDMS/SiO_2/0.5(SA+PA)/40min** and **0.5PDMS/SiO_2/0.5FAS/40min**, had sliding angles of 4°. In this test, a 15 uL water droplet was suspended 4 cm from the surface of the film and rolled off at an inclination of 4°. As this was less than 5°, it demonstrated water repellence. On the other hand, CAH measurements demonstrated a Wenzel wetting regime as the water droplet stuck to the coating, infiltrating the troughs of the rough complex microstructure as seen in all SEM images of the film with a 50:50 hybrid mixture of SA:PA, reducing the ability for the water droplet to roll along the horizontal surface.[10,11,104] To understand the films' durability, various performance tests were pursued such as adhesive tape peel cycles, immersion in solvents of opposing polarities and UV exposure.

Films **0.5PDMS/SiO_2/0.5(SA+PA)/40min** and **0.5PDMS/SiO_2/0.5FAS/40min** demonstrated sustained superhydrophobicity, post-300 tape peel cycles with WCAs remaining >150° and sliding angles <10°, **Figure 2.15**, signifying well-

adhered coatings to glass substrates. On the other hand, film **PDMS/SiO₂** demonstrated a shift in WCA from superhydrophobic to hydrophobic (159 ± 2° to 147 ± 2°) after 20 tape peel cycles.

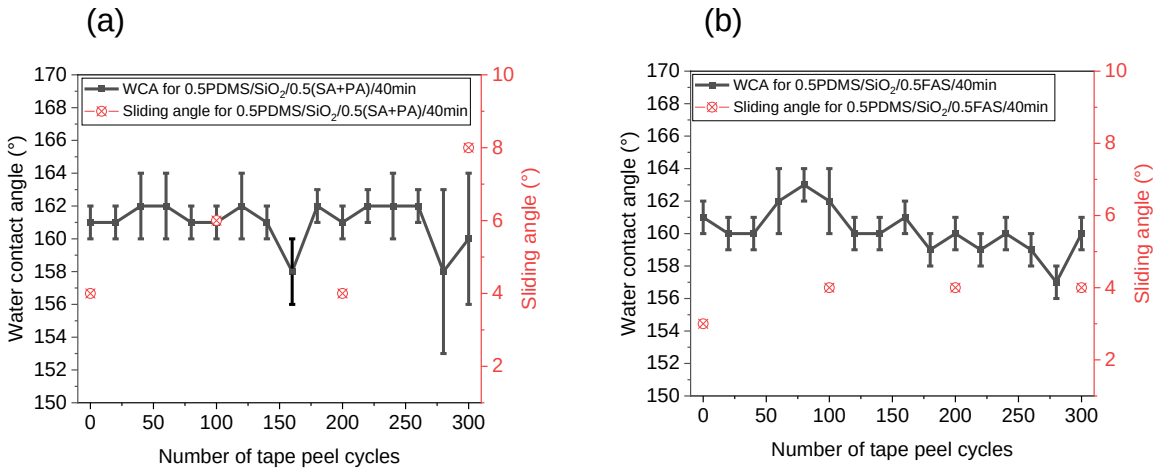

Figure 2.15 *300 tape peel cycles with WCA and sliding angle measurements taken regularly for films (a)* ***0.5PDMS/SiO₂/0.5(SA+PA)/40min*** *and (b)* ***0.5PDMS/SiO₂/0.5FAS/40min.*** *Figure reproduced with permission from ACS Langmuir.*[95]

Both films were in contact with UV irradiation (λ = 365 nm) for up to 2 weeks, measuring water contact angles and sliding angles regularly, demonstrating maintained superhydrophobicity (WCAs >155°, SAs <10°), **Figure 2.16**. UV irradiation oxidises organic components inducing hydrophilicity however this did not pose a challenge as the SiO_2 NPs are not photoactive thus UV-resistant.

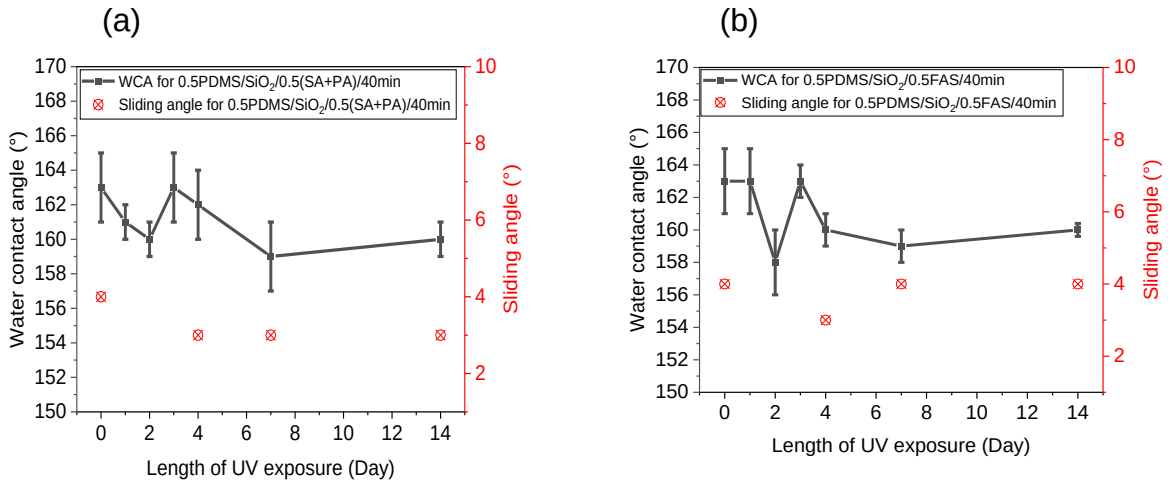

Figure 2.16. *UV irradiation for 2 weeks and the resulting WCA and sliding angle measurements for films (a) 0.5PDMS/SiO₂/0.5(SA+PA)/40min and (b) 0.5PDMS/SiO₂/0.5FAS/40min. Figure reproduced with permission from ACS Langmuir.*[95]

Thermal stability testing confirmed retained superhydrophobicity for both films after being in contact with 300 °C heat for 5 h. These films were also exposed to 5 h of 400 °C heat demonstrating a minimal reduction in WCA for film

0.5PDMS/SiO$_2$/0.5FAS/40min to 159°. This reduction may have been due to the degradation of the SYLGARD 184 polymer where its first stage of degradation takes place at 339 °C.[105] Interestingly, film **0.5PDMS/SiO$_2$/0.5(SA+PA)/40min** exhibited an increase in WCA to 170° either as a result of carbon contamination, diffusion of the carbon backbone from the bulk of the superhydrophobic film to the surface or owing to evaporation of additional ethyl acetate within the grooves of the film.[106]

Table 12. *WCA values, photographs of the water droplets on the surface and SAs for films* ***0.5PDMS/SiO$_2$/0.5(SA+PA)/40min*** *and* ***0.5PDMS/SiO$_2$/0.5FAS/40min*** *after 5 h heating at 300 ^{o}C and subsequently 5 h heating at 400 ^{o}C. Table reproduced with permission from ACS Langmuir.*[95]

	0.5PDMS/SiO$_2$/0.5(SA+PA)/40min 50:50 ratio of SA + PA		**0.5PDMS/SiO$_2$/0.5FAS/40min** FAS C_8	
	After 5 h of 300 ^{o}C exposure	After 5 h of 400 ^{o}C exposure	After 5 h of 300 ^{o}C exposure	After 5 h of 400 ^{o}C exposure
	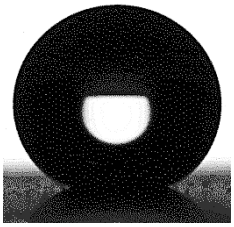		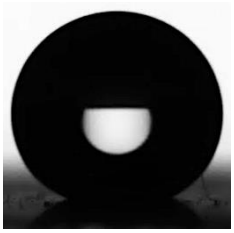	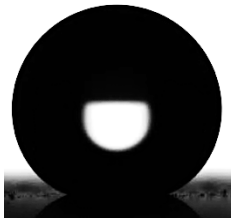
WCA (^{o})	159 ± 2	170 ± 2	161 ± 2	159 ± 6
SA(^{o})	N/A	1	N/A	7

Films **0.5PDMS/SiO$_2$/0.5(SA+PA)/40min** and **0.5PDMS/SiO$_2$/0.5FAS/40min** were immersed in toluene and ethanol for 5 h, these solvents have opposing polarities. Both films had a negligible change in sliding angle, with a maximum decrease of 1° for film **0.5PDMS/SiO$_2$/0.5FAS/40min**. In both cases, the WCAs reduced by <10°, potentially owing to robust physical interactions between the glass substrate and the coating, **Figure 2.17**. Zhuang *et al.* fabricated a multi-layered film via AACVD consisting of epoxy resin and SYLGARD 184 layers. The resulting film was superhydrophobic and 80-84 μm thick, with a regular arrangement of the nano-/micro-structures, which remained even after immersion in pH 1 and pH 14 for 72 h.[68]

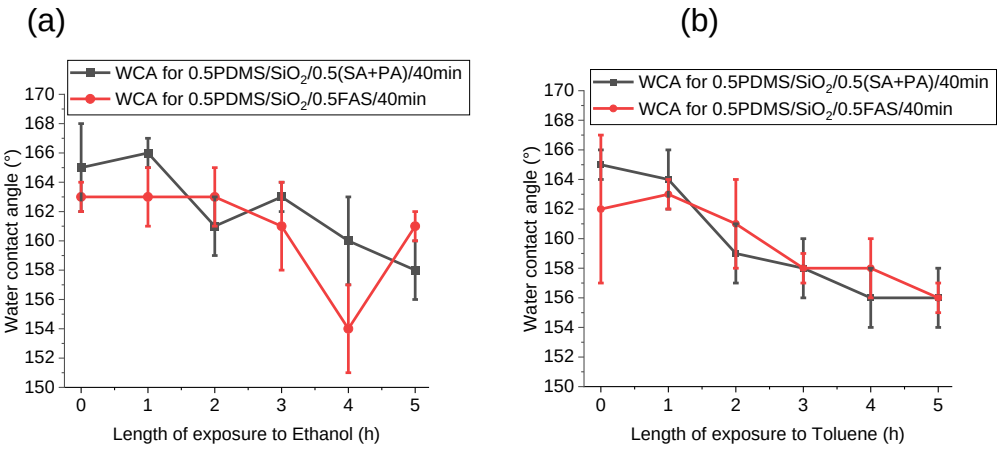

Figure 2.17. *Solvent immersion test in (a) ethanol (b) toluene with WCAs recorded every one hour for 5 h. Figure reproduced with permission from ACS Langmuir.*[95]

To determine the films' tolerable "hardness", a pencil hardness test was completed. Here, an elcometer with pencils of different hardness was pushed across the film at a 45° angle. Interestingly, film **0.5PDMS/SiO$_2$/0.5(SA+PA)/40min** exhibited greater hardness than film **0.5PDMS/SiO$_2$/0.5(FAS)/40min** due to the film's protective microstructure, **Figure 2.18**. Nonetheless, as these films were deposited via AACVD, the coating was physisorbed onto the substrate rather than chemisorbed, confirming the films' low mechanical durability relative to films deposited via other techniques such as conventional CVD. [62,66]

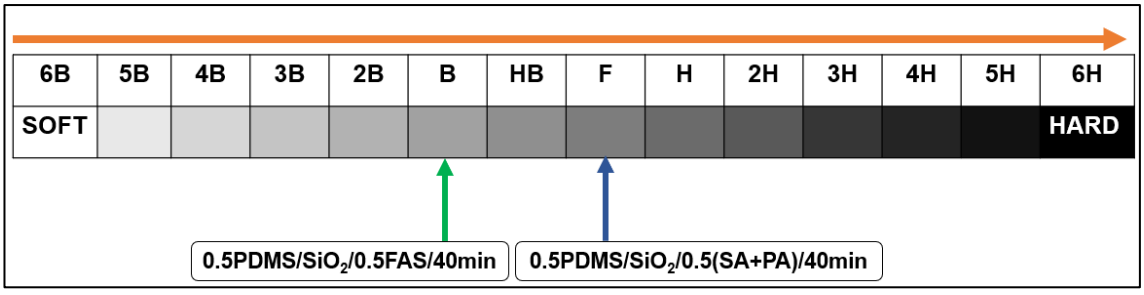

Figure 2.18. *Elcometer testing (pencil hardness durability) of films* ***0.5PDMS/SiO$_2$/0.5(SA+PA)/40min*** *and* ***0.5PDMS/SiO$_2$/0.5FAS/40min****. Figure reproduced with permission from ACS Langmuir.*[95]

To determine the self-cleaning behaviour of film **0.5PDMS/SiO$_2$/0.5(SA+PA)/40min**, self-cleaning tests were executed by using gold glitter to cover the film and manually impinge water droplets. It was clear from **Figure 2.19** that with the help of the water droplets, the material could easily "self-clean" the glitter from its surface. To determine the water repellence of the film, methylene blue dye was manually impinged onto the film. Subsequently, the films were observed and remained clean and dry owing to the film's low surface energy and water's high surface tension.[107]

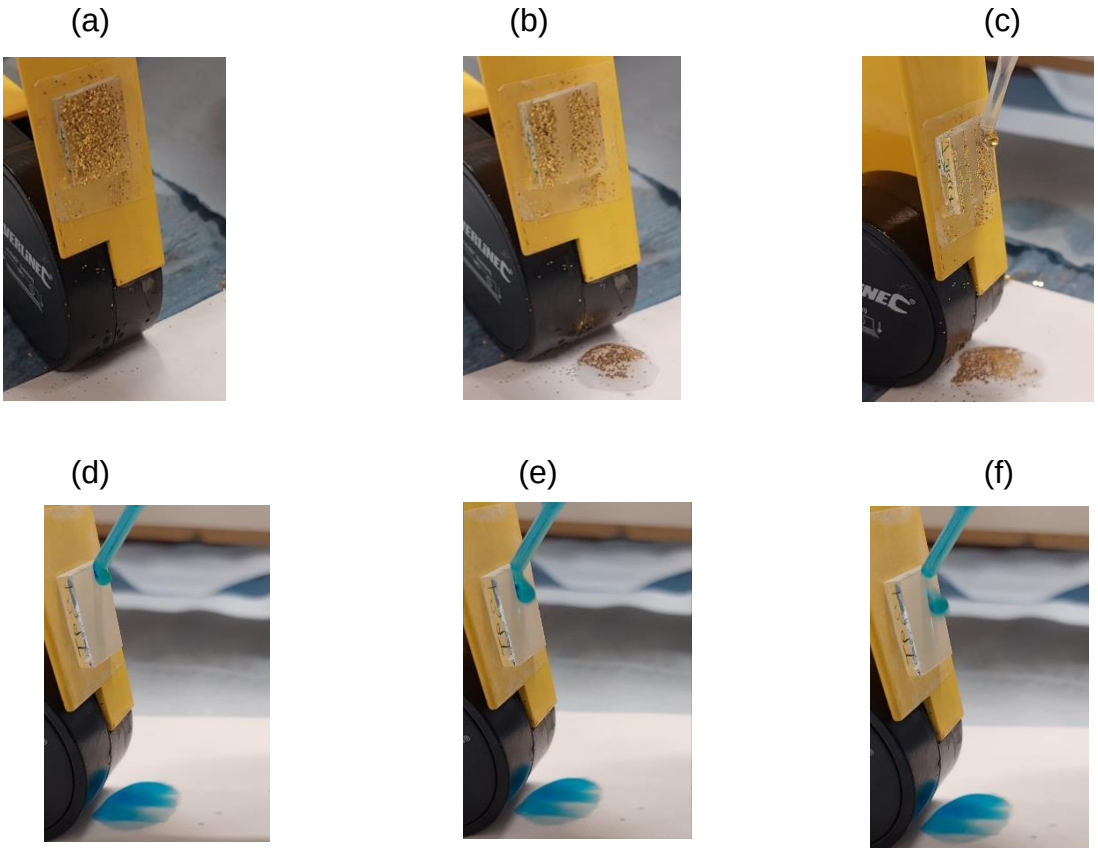

Figure 2.19. *Testing the self-cleaning properties of film* ***0.5PDMS/SiO2/0.5(SA+PA)/40min*** *with gold glitter, photographs (a) – (c) and qualitatively determining the water repellence with methylene blue dye, photographs (d) – (f). In both cases, the stage was tilted at an inclination of 80°. Images reproduced with permission from ACS Langmuir.*[95]

2.6 Summary

Reproducible fluorine-free superhydrophobic films displaying Cassie-Baxter wetting behaviour were successfully fabricated from SYLGARD 184, a 50:50 combination of stearic acid and palmitic acid and SiO_2 NPs using AACVD. Surface characterisation, specifically FTIR and XPS indicated the successful incorporation of the precursor mixture. SEM imaging revealed the complex rough topology consisting of a network of interconnected particles, consistent with all films regardless of variations in concentration/loadings of reagents and deposition temperature, although different size ranges were observed.

The outlined work details that a combination of two fatty acids rather than a single fatty acid can be used to impart superhydrophobicity, with WCAs of the latter (162 ± 3°) similar to those of fluoroalkylsilane equivalents (>160°). Transparencies remained low (<20% in most cases) due to the intricate morphologies, as well as the dense network and agglomeration of the precursor particles, facilitated by the AACVD process. Interestingly, greater SiO_2 loadings led to increased transmittance values. (i.e. for a 0.25 g SiO_2 loading, T = 12% vs. a 0.35 g SiO_2 loading T = 17%). From additional studies, it was evident that increased loadings of fatty acids contributed to the low transmittance, potentially due to the "whiteness" of fatty acids as well as increased agglomeration of the particles. Similarly, increased SYLGARD 184 loadings reduced transmittance values, potentially due to increased agglomeration of the particles.

Deposition temperatures below the decomposition temperature of the precursor components (i.e. 300 °C) did not generate a superhydrophobic film, neither did significantly higher temperatures (i.e. 400 °C), however, an in-between temperature of 360 °C did, even when the deposition was repeated, corroborated by the Sq root-mean square height values. Reduced deposition times led to reduced WCAs from 160° at 45 min to 112° at 10 min and increased transmittance values from 15% to 53%, respectively. The efficiency of the precursor mixture was improved by halving the deposition time and concentration of mixture. This work demonstrated the ease of tuning various conditions of not only the film precursor mixture but also the AACVD process, to improve the overall efficiency of the process relative to other deposition techniques such as dip-coating.

The optimum film was film **0.5PDMS/SiO_2/0.5(SA+PA)/40min**, consisting of half of the concentration of all precursor components (excluding [SiO_2]), deposited for 40 min at 360 °C via AACVD. The film presented good robustness on exposure to 5 h of solvents, temperatures at (300 °C) and even above the decomposition temperature of the films' components (400 °C), retained superhydrophobicity following 300 tape peel cycles and after 2 weeks of UV exposure. Self-cleaning properties and water repellence were visualised. Reports from the literature state that the incorporation of fluorinated polymers or multi-layered films are required to yield superhydrophobicity.[50,54,108] Nevertheless, within this chapter, the formation of a mixture of naturally occurring stearic acid and palmitic acid introduced superhydrophobicity and mechanical durability, similar to the fluoroalkylsilane equivalent, film **0.5PDMS/SiO_2/0.5FAS/40min**. Nonetheless, the robustness could be improved further to increase its applications, such as self-cleaning flooring. Although, as mentioned previously, the low transmittance values of the films in visible light must be enhanced to increase its implementation for self-cleaning domestic windows.

The work in the forthcoming chapters describe the surface modification of the described films, namely, film **0.5PDMS/SiO_2/0.5(SA+PA)/40min** via the deposition of metal oxides via AACVD and ALD. The rationale of this work was to determine changes to the properties of the film and to introduce additional functionality.

Chapter 3 – Surface Modification of Fluorine-Free Superhydrophobic Coatings via AACVD

3.1 Background

Titanium dioxide, TiO_2, is an intrinsically hydrophilic material (WCA <90°). For example, Diesen *et al.* reported the AACVD of TTIP to afford TiO_2 films with a water contact angle of 82°.[109] TiO_2 is utilised within the fields of photocatalysis, water splitting and chemical self-cleaning materials. TiO_2 films are deposited via chemical or physical vapour deposition techniques (CVD/PVD).[110] For chemical self-cleaning properties, the light energy absorbed should be ≥ the band gap (anatase E_{bg} = *ca.* 3.2 eV). As a result, charge carriers are generated by the photoexcitation of electrons from the valence band to the conduction band, creating holes in the former.[79,81] TiO_2 and other photocatalysts can be incorporated into superhydrophobic film precursors to generate films exhibiting physical and chemical self-cleaning properties, respectively and simultaneously. Such films are also known as superhydrophobic and photocatalytic self-cleaning materials.

Cao *et al.* manufactured a durable nanocomposite coating for stone-based buildings comprised of TiO_2 NPs coating with the low surface energy reagents, PFE (pentafluoroethane) and APTMS ((3-aminopropyl)trimethoxysilane).[79] The TiO_2 NPs engendered roughness and introduced photocatalytic properties. Even though SiO_2 NPs were not used, the WCAs were superhydrophobic, with impressive photocatalysis and excellent repellence to emulsions and solvents. Nevertheless, a fluorinated low surface energy reagent was used, with the physical and chemical self-cleaning aspects included into a single nanocomposite precursor. Wang *et al.* utilised solvothermal techniques to prepare ZnS which was subsequently modified with stearic acid to afford a physical and chemical self-cleaning material.[77] Interestingly, the stearic acid modified ZnS film demonstrated improved photocatalytic activity due to its ability to limit charge carrier recombination. Yu *et al.* coated a chitosan film with ZnO to engender roughness and to impart photocatalytic properties, before soaking the film in stearic acid to make the film superhydrophobic.[111] The overall film demonstrated stability with potential applications in self-cleaning coatings.

Within the manufacture of superhydrophobic and photocatalytic self-cleaning materials, PDMS is regularly used as a low surface energy reagent as it does not impede the photocatalytic activity of the photocatalytic metal oxide. Wang *et al.* fabricated a PDMS/TiO_2 hybrid by spray coating a mixture of PDMS and TiO_2 NPs to yield a physical self-cleaning material with good photocatalytic abilities.[112] Most research integrates TiO_2 (liquid precursor or NPs) into the superhydrophobic-based mixture and deposits this as a single precursor, commonly via spin coating or sol-gel methods. Wahyuningsih *et al.* utilised TTIP to form TiO_2 NPs which were then deposited onto glass substrates by sol-gel deposition.[113] Janowicz *et al.* spin coated and used AACVD to separately deposit a suspension of APTES modified mesoporous SiO_2, PDMS and TTIP, affording superhydrophobic films through both deposition routes.[65] Photocatalytic testing was not carried out however, the formation of strong Ti-O-Si bonds resulted in improved adhesion and resistance to abrasion, especially for the film deposited via AACVD.

However, reports on employing a dual-layered approach with the deposition of separate films (superhydrophobic and TiO_2) is uncommon. Miao *et al.* deposited a SiO_2-TiO_2 bilayer onto glass substrates via a sol-gel method affording WCAs of *ca.* 90°.[114] In their work, the purpose of the SiO_2 layer (*ca.* 23 nm) was to provide antireflection and the TiO_2 layer (*ca.* 49 nm) acted as protection for the underlying film. The overall hydrophobic film had some applications in self-cleaning coatings. In other works, Lee *et al.* pursued an aqueous layer-by-layer technique to deposit TiO_2/SiO_2 films on glass substrates.[115] The first film had a TiO_2 film of 7 nm and an SiO_2 film of 22 nm and the other film had equal thicknesses of each film. Interestingly, the resulting films were superhydrophilic although displayed poor mechanical durability due to the lack of heat and hence limited reaction between the particles and the substrate. Therefore, separate studies on the calcination of the films were suggested.

A multi-layered approach is advantageous compared to dissolving all the constituents of a superhydrophobic and photocatalytic self-cleaning film as it is easier to tune the surface chemistry and wettability of the material.[116] While multi-layered films are a facile way to tune the hydrophobicity of a material, the ordering of the TiO_2 and superhydrophobic films can also be studied.[117] Liu *et al.* adjusted the hydrophobicity of TiO_2 by depositing a PDMS film of *ca.* 2.2 nm on top.[118] In

addition, this multi-layered approach can potentially enhance the mechanical robustness of superhydrophobic films as a separate “protective” film of metal oxides is deposited on top. As well as this, depositing a TiO_2 topcoat can amplify the overall photocatalytic properties of the film as it has greater exposure to light in comparison to depositing a single hybrid superhydrophobic and photocatalytic film precursor onto a glass substrate.

In alternative work, Powell *et al.* fabricated a multilayered and multifunctional film on glass substrates consisting of VO_2, SiO_2 and a TiO_2 (topcoat).[119] The initial VO_2 film induced thermochromic properties, the intermediate SiO_2 film inhibited the Ti^{4+} from reaching the VO_2 layer and finally, the TiO_2 film imparted photocatalytic behaviour.

3.2 Aims

The aim of this work was to surface modify the mechanically durable fluorine-free superhydrophobic films, outlined in **Chapter 2**, with TiO_2 (precursor: titanium(IV) isopropoxide, TTIP dissolved in anhydrous toluene) via AACVD. Titanium dioxide is a photocatalytic and inherently hydrophilic film. However, the water contact angle can change depending on the deposition method used. Therefore, TiO_2 was deposited onto the superhydrophobic films by AACVD to determine changes in the WCA and to fabricate multi-functional materials exhibiting both chemical and physical self-cleaning properties. Additional aims looked at improving the robustness and overall durability of the superhydrophobic films. Alterations only involved the TTIP concentrations. The assumption was that variable TTIP concentrations varied the thickness of the TiO_2 films and consequently, alterations to the morphology, functional properties (photocatalytic activity, wettability and self-cleaning) as well as robustness were studied. Comparisons to the uncoated superhydrophobic film and the film deposited on a plain FTO glass substrate were made. All films were deposited via AACVD due to the benefits outlined in **Section 1.5.2**.

3.3 Experimental

The fabrication of superhydrophobic films with a hybrid of stearic acid and palmitic acid, deposited by AACVD for self-cleaning applications were surface modified via titanium(IV) isopropoxide (TTIP). TTIP was used due to its low cost and ease of deposition via AACVD.

3.3.1 Chemicals and Materials

Vinyl-terminated polydimethylsiloxane (PDMS) also known as SYLGARD™ 184 Silicone Elastomer Base along with its corresponding curing agent were purchased from Dow Corning. Aerosil OX50 SiO_2 nanoparticles (fumed) procured from Lawrence Industries. Palmitic acid (≥ 99%), stearic acid (reagent grade, 95%), titanium(IV) isopropoxide (97%), anhydrous toluene (99.8%) and ethyl acetate (laboratory grade) were all acquired from Merck Chemicals. All chemicals were used as received. NSG provided SiO_2 barrier coated fluorine-doped tin oxide (FTO) glass substrates which were manually cut to 15 cm x 4 cm x 0.3 cm for AACVD. The N_2 carrier gas used in AACVD was supplied by BOC.

Plasma treatment of the superhydrophobic films was carried out with a HPT-100 Henniker plasma cleaner. All films were plasma cleaned for 4 min with 100% power and a N_2 carrier gas flow rate of 2 sccm.

3.3.2 Synthesis of the fluorine-free superhydrophobic film

A hybrid 50:50 combination of stearic acid and palmitic acid (0.6 g, 2.2 mmol), SYLGARD 184 (0.6 g), curing agent (0.06 g) and ethyl acetate (60 cm^3) were stirred vigorously for 5 – 10 min. OX50 SiO_2 NPs (0.25 g, 4.2 mmol) was added to the mixture and stirred for a further 15 – 20 min. The resultant mixture was subsequently deposited via AACVD (a cold-walled reactor) onto a barrier coated glass substrate (top plate). A diagram of the AACVD rig can be seen in **Chapter 2, Figure 2.01**. Prior to the deposition, the top plate was initially washed with acetone, then soap and water and finally rinsed with isopropanol. The film was oven-dried at 70 °C for 5 min. The specifications of the cold-walled AACVD rig can be found in **Chapter 2, Section 2.3.2**.

At the required temperature of 360 °C, aerosols were generated via a piezoelectric ultrasonic humidifier which were carried to the cold-walled reactor via the N_2 carrier gas (flow rate: 1 L min^{-1}). The precursor mixture was

supplemented with further ethyl acetate (10 cm^3) after the initial deposition time of 40 min and deposited for an extra 10 min, totalling a deposition time of 50 min.

Once the deposition terminated, the AACVD rig was left to cool under a constant stream of N_2 until the films were cool enough to handle (<100 °C). The obtained films were described as **SH** (i.e. superhydrophobic).

3.3.3 Surface Modification of the SH film with TiO_2 via AACVD

The **SH** films described in **Section 3.3.2** were plasma treated (duration: 4 min; carrier gas flow rate: 2 sccm) to improve the adhesion between the superhydrophobic coating and TiO_2 film. The superhydrophobic film became superhydrophilic after plasma treatment due to the generation of hydroxyl groups on the surface of the "superhydrophobic" film. Each film was re-inserted into the AACVD rig with the **SH** film on the carbon block (bottom plate) and an FTO substrate used as a top plate for by-product deposits.

Titanium(IV) isopropoxide of a range of volumes were added to anhydrous toluene (40 cm^3) and swirled vigorously for 5 min to generate variable concentrations of TTIP. The volumes and concentrations of TTIP are listed in **Table 13**. The resulting precursor was deposited at 350 °C until the precursor was used up. Once the deposition terminated, the AACVD rig was left to cool under a constant stream of N_2 until the films were cool enough to handle (<100 °C). The obtained films were described as **SH/TiO_2/x** where x = volume of TTIP (cm^3) used for the deposition. The colours of the **SH/TiO_2/x** films were diverse from translucent to grey and films with higher concentrations of TTIP occasionally had a rainbow pattern across the surface. The top plates had thick white and brown powder deposits, occasionally with a rainbow pattern across sections of the films. A schematic outlining the deposition of the superhydrophobic film and TiO_2 surface tuning via AACVD is shown in **Figure 3.01**.

Table 13. *The volumes and concentration of titanium(IV) isopropoxide, TTIP, deposited on the* ***SH*** *films via AACVD at 350 °C for the respective films and their corresponding water contact angles, transmittance, contact angle hysteresis and root-mean-square (RMS) height.*

Film name	**Volume in 40 cm^3 anhydrous toluene (cm^3) and concentration (mol dm^{-3}) of TTIP**	**WCA (º)**	**T at 400 – 800 nm (%)**	**CAH (º)**	**RMS height, Sq (µm)**
Barrier coated FTO glass substrate	0 cm^3	61 ± 4	91	20 ± 9	Immeasurable
TiO_2/0.4	0.4 cm^3, 1.47 mol dm^{-3}	65 ± 0	74	22 ± 14	Immeasurable
TiO_2/1.4	1.4 cm^3, 5.13 mol dm^{-3}	77 ± 4	65	24 ± 12	0.20 ± 0.04
Superhydrophobic (SH)	0 cm^3	165 ± 2	34	13 ± 6	0.28 ± 0.03
SH/TiO_2/0.4	0.4 cm^3, 1.47 mol dm^{-3}	142 ± 26	28	23 ± 8	0.27 ± 0.03
SH/TiO_2/0.5	0.5 cm^3, 1.83 mol dm^{-3}	143 ± 14	24	22 ± 7	0.24 ± 0.07
SH/TiO_2/0.6	0.6 cm^3, 2.20 mol dm^{-3}	94 ± 11	21	23 ± 8	0.24 ± 0.02
SH/TiO_2/0.8	0.8 cm^3, 2.93 mol dm^{-3}	83 ± 8	7	21 ± 7	0.24 ± 0.04
SH/TiO_2/1	1 cm^3, 3.67 mol dm^{-3}	73 ± 6	19	21 ± 7	0.26 ± 0.01
SH/TiO_2/1.2	1.2 cm^3, 4.40 mol dm^{-3}	82 ± 2	16	22 ± 8	0.20 ± 0.07
SH/TiO_2/1.4	1.4 cm^3, 5.13 mol dm^{-3}	70 ± 3	9	14 ± 6	0.18 ± 0.03

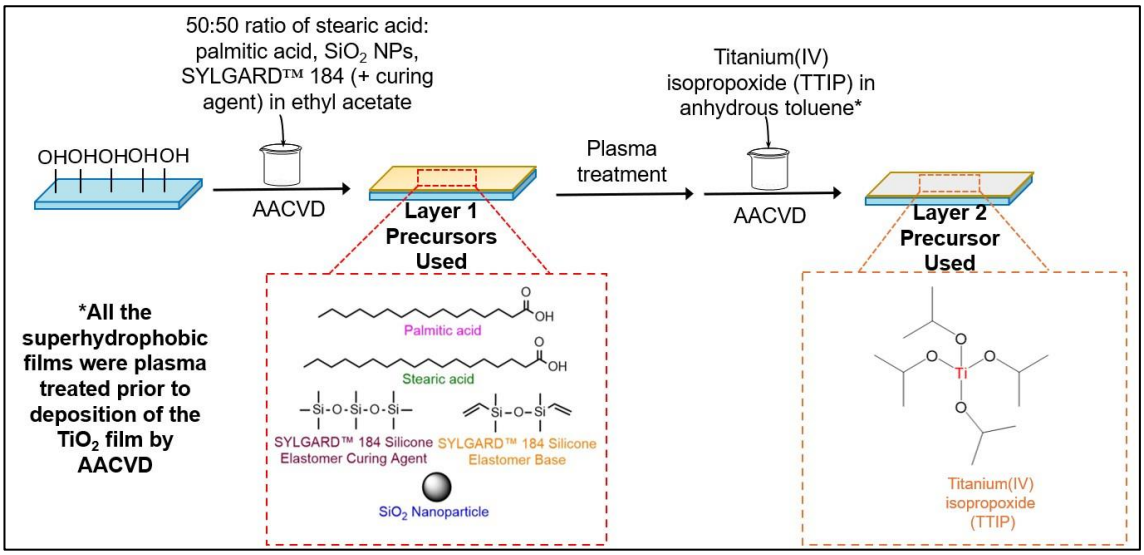

Figure 3.01. *The step-by-step method to produce dual-layered physical and self-cleaning films. The first step involved the deposition of a fluorine-free mixture via AACVD to form a superhydrophobic film. Subsequently, the film was surface engineered via TiO_2 to introduce additional functionality. Figure reproduced with permission from Wiley.*[120]

3.3.4 Materials Characterisation

Surface morphologies of the materials were carried out using the JEOL 6701F and JEOL 7600F Scanning Electron Microscopes (SEMs). Electron acceleration voltages of 5 – 20 keV were used, depending on how much heat from the electron gun the sample could tolerate. Carbon sputtering (physical vapour deposition) of all samples for 10 s occurred to improve the electrical conductivity of the films, for imaging and to prevent charging. The sizes of the particles were measured by the ImageJ 1.52s software. Energy Dispersive X-ray Spectroscopy (EDS) scans were taken with an Oxford Instruments EDS set up with variable scan durations of 10 min to 20 min. Functional bonds were detected through Fourier-Transform Infrared Spectroscopy (FTIR) using the Brucker alpha platinum-ATR instrument, with a wavenumber range of 400 – 4000 cm^{-1}. Ultra-violet visible spectroscopy (UV-vis) was used to determine the transmittance of electromagnetic radiation through the films using the Shimadzu UV-2700 spectrophotometer with wavelengths of 400 – 800 nm. Finally, a Thermo Scientific X-ray photoelectron spectrometer with a mono-chromated Al-K alpha source (8.3381 Å) was used for compositional analysis. The peaks were analysed using the CasaXPS 2.3.25 software and calibrated with respect to the C 1s peak at *ca.* 285 eV. Four spots were scanned per film via XPS. The phase composition of the films was determined through powder X-ray diffraction (PXRD), utilising a Malvern

PANalytical Empyrean Grazing Incidence-PXRD comprised of a Xe point detector and monochromated Cu Kα source at a voltage of 40 kV and current of 40 mA. Additional parameters included a step size: 0.05°, 2θ = 20° - 80°, ω (incident beam) = 1°. A Bruker Senterra II Raman Spectrometer (λ = 532 nm, power = 25mW) was used to generate Raman spectra. The thickness of the TiO_2-only films (without the superhydrophobic undercoat) was calculated with a Filmetrics F20 thin-film analyser.

3.3.5 Functional Durability and Performance Testing

Water contact angles were measured using a Kruss DSA 25E drop shape analyser. A mean and the error (one standard deviation) of 10 water droplets of 5 µL was determined which was calculated automatically by ADVANCE 1.14.3. A tilted drop method of water droplets (*ca.* 15 µL) dispensed 4 cm from the surface of the film was used to determine the sliding angle. The stage was tilted at the respective inclination (°) prior to any measurement. The size of the angles was calculating by manually adjusting the baseline and utilising the Young-Laplace equation. The CAH was determined by initially measuring the advancing angle before measuring the receding angle and finally subtracting an average of the two angles. The Ellipse (Tangent) method was used to determine the angles. The root-mean-square height (Sq) was measured using the Keyence VHX-S750E optical microscope at x1500 magnification. No S-filter and no L-filter were used, only using a Gaussian filter type.

Photocatalytic activity testing

Stearic acid degradation test: The films were immersed overnight in a beaker of a 0.05M stearic acid standard solution (solvent: chloroform). The next day the films were irradiated with UV light for up to 30 h. FTIR scans were recorded frequently via a PerkinElmer Fourier Transform Lambda RX I spectrometer (range: 2800 – 3000 cm^{-1}). For consistency, the corrected area was calculated by the instrument for each of the tested films and hence the stearic acid percentage coverage and errors (one standard deviation) were calculated.

Resazurin staining assay: Resazurin dye was spin coated onto the films which were subsequently irradiated with UV light, transforming the Resazurin compound (blue) to Resorufin (pink). This test was discontinued due to problems

of adhesion between the Resazurin dye and the films. The dye was prepared by a protocol from the literature.[121]

Self-cleaning performance testing: Gold glitter was used to cover the surface of the films. Then, water droplets were pipetted onto the surface. On a separate sample, methylene blue was directly and continuously pipetted onto the surface. In both cases, samples were tilted at 20° with images taken throughout the testing to qualitatively visualise the superhydrophobicity and self-cleaning properties.

Durability

Elcometer® Testing: An Elcometer® 501 Pencil Hardness Tester (supplier: Elcometer® Ltd.) consisted of pencils of differing hardness (6H – 6B) which were pushed across the surface of a film at a 45° angle. Pencils of increasing hardness were used until a visible line was seen (by eye) in the coating. The standard protocol followed was ASTM D3363.

Thermal Stability: Samples were heated at 300 °C for 5 h and the WCAs were taken prior and post heating.

UV Stability: WCAs and SAs of samples were measured after 1, 2, 3, 4, 7 and 15 days of exposure to UV in a sealed UV light box. A UV irradiance of 260 mW/cm^2 and emission wavelength of 365 nm were used.

Tape peel test: Scotch Magic™ Tape was manually stuck to and removed from the films up to 400 times. WCAs were initially recorded periodically. EDS scans were taken at the end of the tape peel cycle.

Solvent Stability: Samples were separately submerged in ethanol (highly polar) and toluene (slightly polar) and the performance of these films was determined via WCA measurements, taken every 1 h for 5 h.

3.4 Results and Discussion

To understand the effect of depositing an intrinsically hydrophilic metal oxide on top of a **SH** film, a range of concentrations of titanium(IV) isopropoxide (TTIP) were subsequently deposited by AACVD at 350 °C, **Table 13**. The superhydrophobic undercoat was based on the composition described previously in **Chapter 2**, comprised of SYLGARD 184, a 50:50 hybrid mixture of stearic acid and palmitic acid which are all low surface energy reagents, along with silica NPs, needed to provide the roughness, also a pre-requisite.

AACVD of the **SH** film occurred by thermophoretic effects leading to the physisorption of the gas phase polymer-fatty acid-coated SiO_2 NPs onto the glass substrate top plate (furthest away from the carbon block).[66] After characterisation of the **SH** film, the substrate was removed and placed onto the carbon block of the AACVD rig for the TTIP deposition and hence the formation of the TiO_2 film over-layer. Generally, metal oxide depositions occur on the bottom plate (substrate placed on the carbon block) as it is a CVD-like process unlike using superhydrophobic polymers. As soon as the aerosol enters the heated rig, the solvent evaporates, transforming the precursor into a gas. As a result, the gaseous precursor reacts heterogeneously with the hot substrate affording the metal oxide film.

Initially, the **SH** films were not treated with a plasma surface cleaner, leading to patchy depositions, observed from the large standard deviation errors for the water contact angles reaching 50°. However, on plasma treatment, the errors of the WCAs reduced significantly, potentially due to improved TiO_2 coverage, **Table 13**. Plasma treatment resulted in the **SH** film becoming superhydrophilic because of the generation of hydroxyl groups on the superhydrophobic surface for the TTIP to deposit onto and nucleate. It was not possible to measure the WCA of the **SH** film post-plasma cleaning due to its very low WCA (<10°). On depositing a range of TTIP volumes, the wettability of the resulting **SH** films was tuned, as displayed in **Table 13**. For instance, film **SH** had a WCA of 165 ± 2°, on depositing 0.4 cm^3 of TTIP by AACVD (film **SH/TiO_2/0.4**), variable hydrophobicity was evident as the WCA reduced to 142 ± 26°. Similarly, depositing 1.4 cm^3 of TTIP by AACVD (film **SH/TiO_2/1.4**) reduced the WCA significantly to 70 ± 3°, making the resultant film hydrophilic. In addition, increased

volumes of TTIP also reduced the patchiness of the depositions, confirmed by the reduction in standard deviation for film **SH/TiO$_2$/1.4** relative to film **SH/TiO$_2$/0.4**. For comparison, TiO$_2$ films were deposited on glass substrates without the superhydrophobic undercoat by AACVD at 350 °C. These were films **TiO$_2$/0.4** and **TiO$_2$/1.4** with WCAs of 65 ± 0° and 77 ± 4°, respectively and film thicknesses of 80 nm and 510 nm, respectively. The errors of the WCA for the **TiO$_2$/x** films were close to zero indicating uniform depositions. Although attempted, it was not possible to precisely measure the film thickness of the **SH/TiO$_2$** films because of the rough topology of the **SH** films due to the SiO$_2$ NPs and the AACVD process (i.e. aerosol generation and deposition).

The TiO$_2$-surface modified **SH** films were characterised by analytical, chemical and performance testing. Namely, FTIR, PXRD, UV-vis, Raman, XPS, SEM/EDS, performance, functional (wettability and self-cleaning) and photocatalytic activity.

To determine whether TiO$_2$ was successfully deposited onto the **SH** film, XPS, a surface sensitive characterisation method, was pursued. Successful depositions were initially confirmed by the survey spectrum, demonstrating the presence of Ti, O, Si and C, **Figure 3.02**.

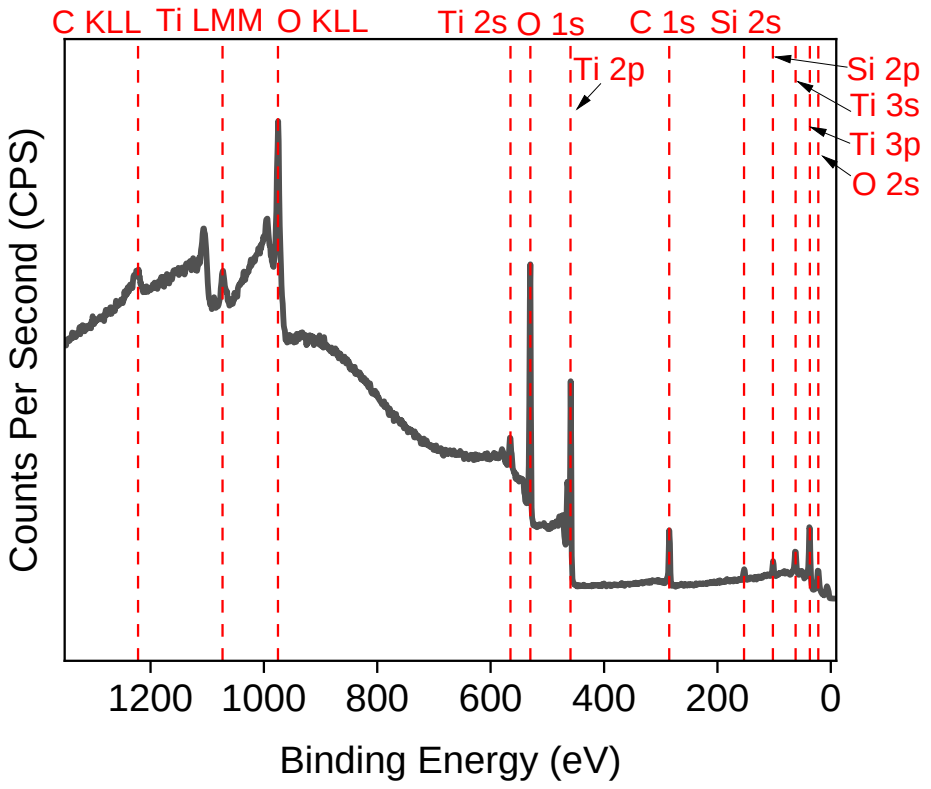

Figure 3.02. *XPS survey spectrum indicating the successful incorporation of Ti, C, O, Si. The hump in the spectrum is due to problems with the XPS instrument. Figure reproduced with permission from Wiley.*[120]

On closer examination, the appearance of peaks in the Ti and O scans demonstrated the deposition of TiO_2, **Figure 3.03**. Potential deviances in the fitting of the O 1s were due to the C 1s and Si 2p of the superhydrophobic underlayer and were overlooked in the O1s fitting; oxygen bound to carbon or to silicon would contribute to the O 1s spectrum, but these contributions have not been fitted. All spectral scans are shown in **Figure 3.03**. For Ti 2p, the $2p_{3/2}$ peak was present at *ca.* 459.2 eV confirming Ti^{4+}.[122,123] The O 1s scan had a peak at 530.5 eV indicating O-Ti and a peak at 532.2 eV indicating the presence of adsorbed water (i.e. O-TiO_2), common for TiO_2 films.[124,125] Due to the penetration depth of the XPS instrument and patchiness of the depositions, in scans of some of the films, the C and Si of the superhydrophobic underlayer were occasionally observed. The overall counts per second (CPS) for the Si was low relative to the other elemental scans indicating minimal breakthrough to the Si underlayer in the case of **SH/TiO_2/1.4**. Likewise, the CPS for C were also low and the peak at 285.0 eV was observed, indicative of organic carbon contamination.

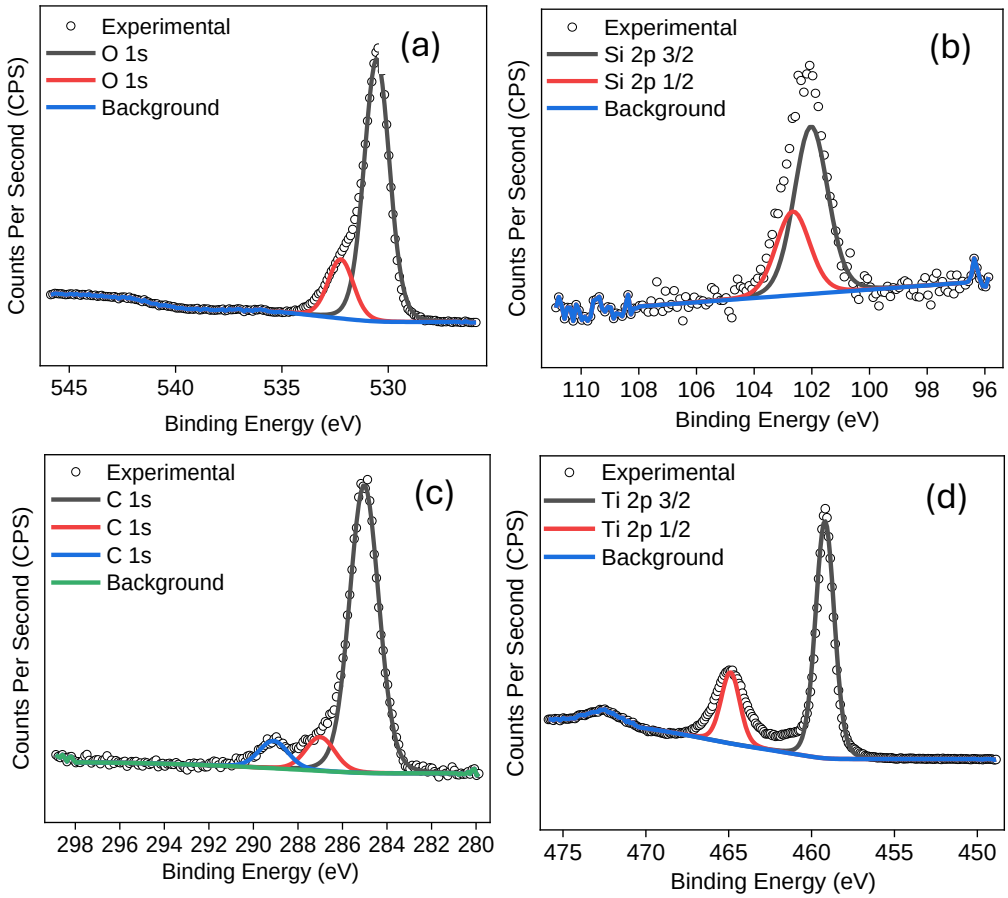

Figure 3.03. *XPS scans for* ***SH/TiO_2*** *films (a) O 1s (b) Si 2p (c) C 1s and (d) Ti 2p. Figure reproduced with permission from Wiley.*[120]

Generally, increasing the [TTIP] increased the thickness of the TiO_2 films confirmed by a graphical representation of the raw peak areas of films (generated via XPS) vs. the volumes of TTIP used, **Figure 3.04**. In line with this trend, increasing the [TTIP] not only increased the TiO_2 film thickness but also reduced the WCA. Where there are slight deviations in the thickness as the [TTIP] increased, this was also observed in the WCA, such as for film **SH/TiO₂/1.4** (i.e. 1.4 cm^3 of TTIP deposited).

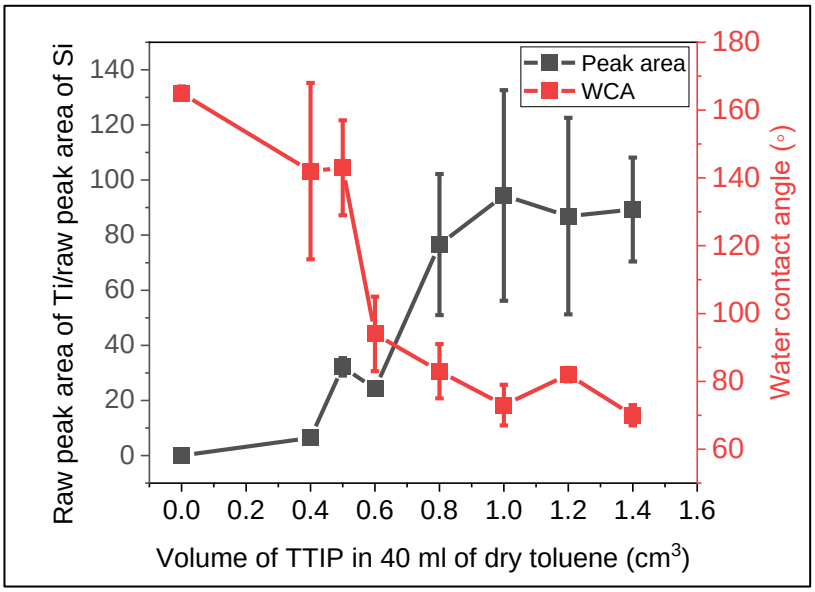

Figure 3.04. *A graph showing the relationship between the water contact angle and the raw peak area of Ti and Si generated from XPS vs. volume of TTIP used.*

FTIR scans were taken prior and post surface modification of the **SH** films via TiO_2, **Figure 3.05**. The scans revealed the appearance of Ti-O due to TiO_2 (anatase) at *ca.* 542 cm^{-1}.[126] For film **SH/TiO₂/1.4**, the peaks pertaining to the superhydrophobic underlayer discussed in **Chapter 2** were not present due to the thickness of the TiO_2 coating however, for the films with thinner TiO_2 coatings, these characteristic superhydrophobic peaks were detected.[95] The Raman spectrum, **Figure 3.06**, also verified TiO_2 (anatase) due to the appearance of peaks at 147 cm^{-1}, 198 cm^{-1}, 395 cm^{-1}, 515 cm^{-1} and 637 cm^{-1}.[78] Similarly, TiO_2 (anatase), **Figure 3.07**, was corroborated by PXRD due to the presence of the following peaks in the pattern: 25.3°, 37.1°, 37.9°, 38.6°, 48.1°, 53.9°, 55.2°, 62.8°, 68.9° and 70.4°.[127] An incident beam angle (ω) of 1° was used for all measurements. Lower ω values magnified misalignments in the sample. Similarly, scanning at higher ω values (i.e. 10°) led to broad amorphous peaks pertaining to the glass substrate.

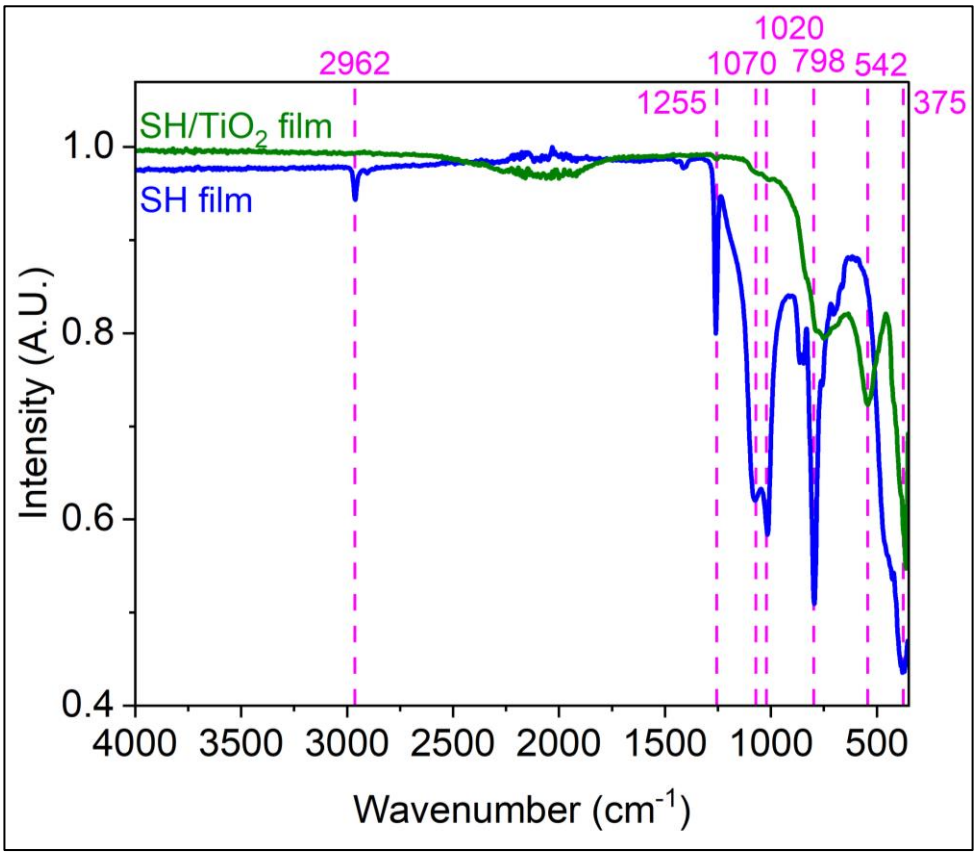

Figure 3.05. *Combined FTIR spectrum of films* ***SH*** *and* ***SH/TiO₂/1.4*** *after surface modification with TiO_2 via AACVD. Figure reproduced with permission from Wiley.* [120]

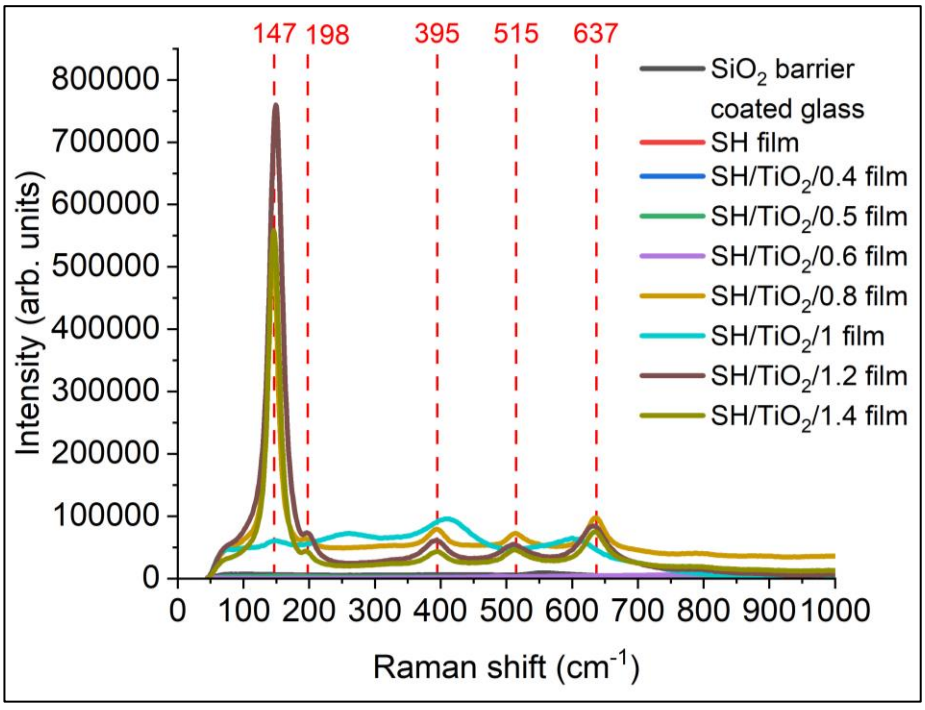

Figure 3.06. *Combined Raman spectrum for plain glass, the uncoated* ***SH*** *film and all films* ***SH/TiO₂.***

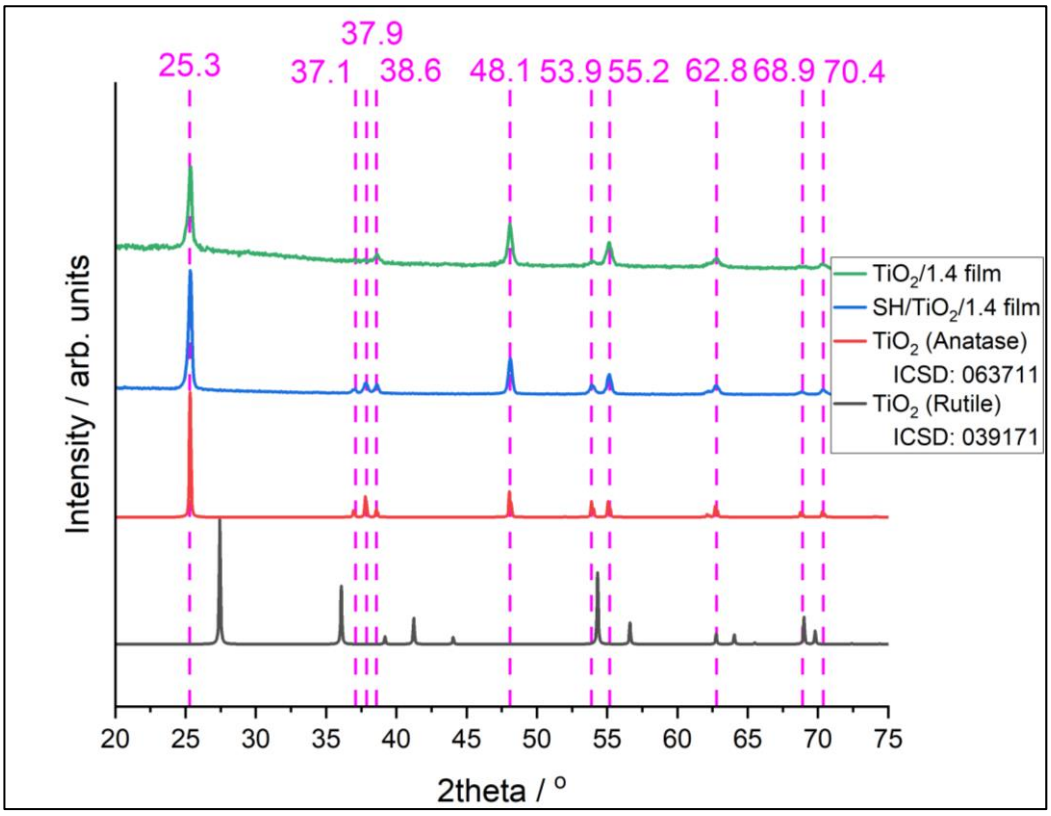

Figure 3.07. *Standard PXRD patterns of TiO_2 (anatase & rutile) as well as films measured patterns for* ***SH/TiO₂/1.4*** *and* ***TiO₂/1.4*** *confirming presence of TiO_2 (anatase). Figure reproduced with permission from Wiley.*[120]

On increasing the volume of TTIP deposited, greater quantities of TiO_2 agglomerates covering the superhydrophobic fatty acid-SYLGARD 184 coated-SiO_2 NPs were observed. These were not present in the SEM images of the **SH** films. Prior to surface modification, the **SH** films had nano- and micro-particles (1 µm – 9 µm) which were non-uniform and asymmetrical, engendering a rough morphology. More detail on the morphology of the uncoated **SH** films can be found in **Chapter 2**. Interestingly, the TiO_2 clusters also agglomerated in the matrix of the films (particularly for film **SH/TiO₂/1.2**), contributing to a decrease in root-mean-square roughness, **Table 13**.

Figure 3.08 clearly depicts changes in morphology and topology as the [TTIP] increases, as well as "flatter" morphologies, also confirmed by the Sq values, **Table 13**. The TiO_2 appeared to nucleate on the islands of the polymer-based superhydrophobic material particles. Interestingly, only low electron beam voltages of 2 keV could be used to image film **SH/TiO₂/0.4** as the film was getting damaged by higher voltages. However, as the TiO_2 film became thicker, it was possible to image the resulting materials at higher electron beam voltages of up to 20 keV.

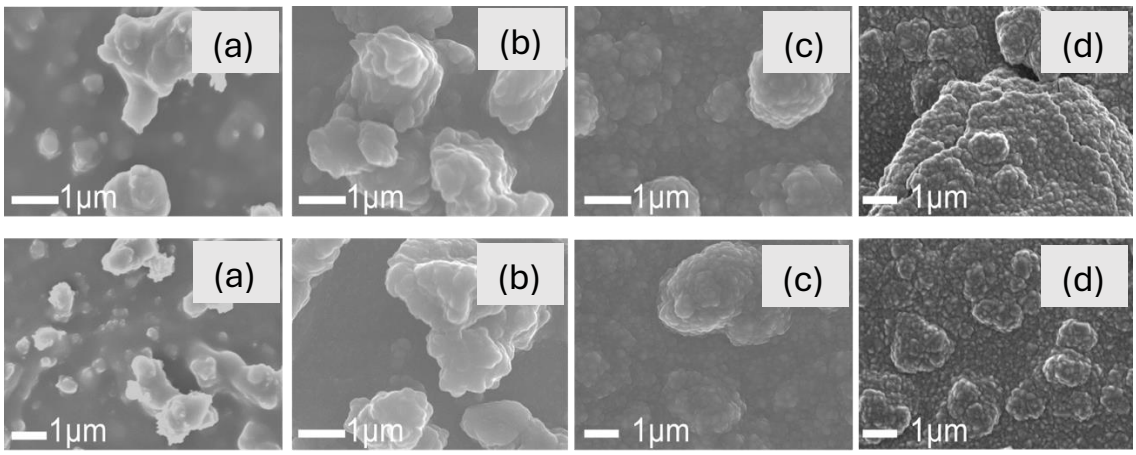

Figure 3.08. *SEM images depicting changes in morphology of the films as [TTIP] rises. (a)* ***SH*** *(b)* ***SH/TiO₂/0.4*** *(c)* ***SH/TiO₂/0.8*** *(d)* ***SH/TiO₂/1.2***. Figure reproduced with permission from Wiley.[120]

The thickness of the TiO_2 coatings on the **SH/TiO₂** films was inferred by the reported percentage transmittance, **Table 13**. The thickness also influenced the root-mean-square roughness and changes in WCA. Overall, a reduction in percentage transmittance was due to a greater depth of the TiO_2 coating; deviations from this trend was due to the rapid rate of the AACVD process, making it difficult to carefully regulate the rate and hence thickness of the TiO_2 film.

The greater the volume of TTIP used, the lower the WCA due to increased thickness of the intrinsically hydrophilic TiO_2. To generate a superhydrophobic film, hierarchical roughness, and a low surface energy reagent are required. TiO_2 has a relatively high surface energy of 1.28 J/m^2 when compared to SYLGARD 184 (surface energy 0.019 – 0.021 J/m^2), potentially decreasing the WCA, even at the lowest [TTIP].[19,128] Interestingly, film **SH/TiO₂/1.4** and film **TiO₂/1.4** have similar WCAs, demonstrating that the superhydrophobic undercoat is masked by the TiO_2 film. The standard deviation of the **SH** film was minimal (2°) relative to the **SH/TiO₂** films, especially the lower [TTIP] (e.g. **SH/TiO₂/0.4**) where the error was 26° but this decreased significantly to 2° for film **SH/TiO₂/1.4**, indicating a more uniform TiO_2 film deposition. This implied that it was challenging to coat the rough topology, hence higher [TTIP] were needed to cover the peaks and troughs of the film, which can also be visualised in the SEM images, **Figure 3.08**.

The homogeneity and flatness/evenness of the film was determined via contact angle hysteresis (CAH) quantification. Films with high WCAs have high CAHs due to their coarse morphology. On the other hand, reduced CAH was observed

for flatter surfaces because of decreased lateral energy barriers, decreasing friction between the film and water droplet.[129] Within this work, the CAH increased when the depth of the TiO_2 film decreased. Interestingly, a significant reduction of 8° in CAH was observed for the highest [TTIP] deposited, namely films **SH/TiO_2/1.2** and **SH/TiO_2/1.4**, possibly due to partially flattening the rough superhydrophobic topology, **Table 13**. As the [TTIP] increased, the root-mean-square roughness decreased, with limited variability in RMS roughness when 0.5 cm^3, 0.6 cm^3, 0.8 cm^3 and 1 cm^3 of TTIP were deposited, indicating conformality of the TiO_2 film. Another cause for the limited variability in the Sq values may have been due to the large beam spot size (diameter = 10 μm) therefore integrating the roughness over a large area even with small patches of TiO_2 island growth did not influence the roughness as much. The inhomogeneity smoothed out as the spot size averaged the area of the film. However, it appeared that as more TiO_2 was deposited, it infilled the matrix, causing the thickness to drop.

For film **SH/TiO_2/1.4,** the rough morphology becomes significantly smoother (RMS height reduced from 0.28 μm to 0.18 μm), with TiO_2 also coating the matrix, **Figure 3.08**. Another rationale for the CAH difference could have been due to the patchiness in the TiO_2 deposition, leaving several sections uncoated hence superhydrophobic, this is also confirmed by the error associated with the WCAs, **Table 13**.

3.5 Functional, Durability and Performance Testing

To determine the mechanical durability and functional properties of the films, performance testing was pursued. Results of the **SH/TiO_2** films were compared to the **SH** film to understand the influence of a dual-layered approach of a **SH** film and metal oxide overcoat.

Initially, to investigate the photocatalytic potential of the films, it was attempted to carry out a Resazurin staining assay where blue Resazurin dye was spin coated onto the (super)hydrophobic **SH/TiO_2** films, **Figure 3.09**. If photocatalytic activity took place, the blue Resazurin dye would become a pink Resorufin compound. However, due to the hydrophobic nature of the film, the dye coating was not uniform or evenly spread across the substrate. This also led to reduced contact between the Resazurin dye and the TiO_2 film and as a result, the dye took 7 days

to change colour. The expected colour change is usually 35 min for a 300 – 500 nm thick TiO_2 film.[109]

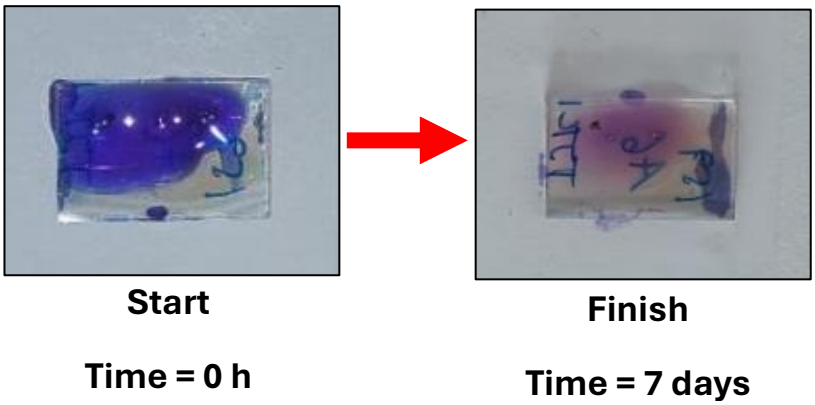

Figure 3.09. *(a)* ***SH/TiO₂*** *film spin coated with blue Resazurin dye. (b)* ***SH/TiO₂*** *film after it was left on a lab bench for 7 days, the blue dye became pink indicating the formation of Resorufin.*

Consequently, to quantitatively determine the photocatalytic properties of the dual-layered **SH/TiO₂** films without the influence of the hydrophobic nature of the film, stearic acid degradation testing was carried out with the equation displayed below.

$$CH_3(CH_2)_{16}COOH + 26O_2 \rightarrow 18CO_2 + 18H_2O \quad \textbf{(4)}$$

where the energy of the wave must be ≥ *the bandgap of metal oxide being studied.*

Comparisons were made to the **SH** and TiO_2 films (without the superhydrophobic undercoat). Within this study, all films were immersed in a known concentration of a stearic acid standard solution, irradiated with UV (for up to 30 h) and FTIR spectra were recorded frequently. The resulting peak areas were converted into stearic acid coverage percentages. A general overview of the photocatalysis of stearic acid includes charge carrier (electrons and holes) photogeneration within TiO_2, provided the energy is at least 3.2 eV (anatase).[81] As a result, the photogenerated entities travel within the stearic acid film where CO_2 and H_2O are generated (using O_2) due to photocatalytic redox. Research within photocatalysis is on the prevention of charge carrier recombination as it reduces the efficiency of the redox reaction.[130]

For films **SH**, **SH/TiO₂/0.4** and **SH/TiO₂/1.4**, a 42%, 52% and 65% decrease in stearic acid coverage was observed by 30 h. These **SH/TiO₂** films were assumed to have the thinnest and thickest TiO_2 films and were the focus of the study. Films **SH/TiO₂/0.4** and **SH/TiO₂/1.4** demonstrated high photocatalytic activity relative to the **TiO₂** films. Films **TiO₂/0.4** and **TiO₂/1.4** only displayed a reduction of 32%

and 27%, respectively. Films **SH** and **TiO_2/0.4** had similar drops in stearic acid coverage of 42% and 52% by 30 h, respectively, confirming that the latter film had a thin coating, and that oxygen was facilitating the photocatalytic degradation. Interestingly, all films exhibited a decrease in stearic acid coverage from the start time to 4 h and each plot had a similar shape. Surprisingly, the **SH** film had a reduction in stearic acid coverage that was similar to film **TiO_2/0.4** which could have been due to the superhydrophobic nature of the **SH** film. As the standard solution used was stearic acid in chloroform, the water repelling effect of the film may have not led to an even coverage of stearic acid. Hence the 42% reduction for the **SH** film may not have been accurate. Alternatively, the roughness of the **SH** film was highest for all films, **Table 13**. Therefore, the standard solution may have penetrated the grooves rather than coated the matrix in between the particles. As a result, an even coating may have enhanced photocatalytic degradation of stearic acid relative to the TiO_2 films.

This testing demonstrated the successful fabrication of physical and self-cleaning films (i.e. photocatalytic behaviour and superhydrophobicity). As expected, a thicker TiO_2 coating on the **SH** film, led to enhanced photocatalytic activity, nevertheless the rate of degradation for films **TiO_2/0.4, SH/TiO_2/0.4, SH/TiO_2/1.4** were similar. The test demonstrated enhanced stearic acid degradation while maintaining (super)hydrophobicity. There are reports of good photocatalytic activity of SiO_2/TiO_2 films however, the method of determination was different as well as the absence of superhydrophobic wettability in addition to photocatalytic properties. For example, Lin *et al.* prepared SiO_2/TiO_2 films via a sol-gel method which exhibited increased photocatalytic degradation of Rhodamine B ranging from 21% through to 88% as the TiO_2 loading increased.[131] Although water contact angles were not measured, these films potentially lacked hydrophobicity. Similarly, Tao *et al.* dip coated SiO_2/TiO_2 films onto glass substrates which demonstrated a photocatalytic degradation efficiency of >80% but hydrophilicity.[132]

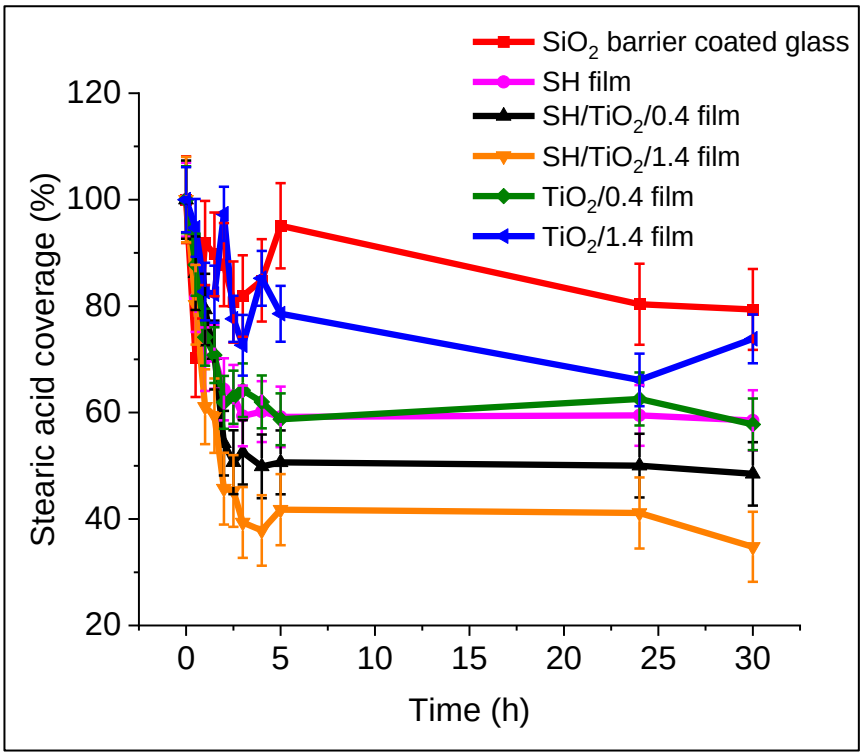

Figure 3.10. *The changes in stearic acid coverage determined by the stearic acid degradation test (a measure of photocatalytic activity) for films* ***SH****,* ***SH/TiO₂*** *and* ***TiO₂****. Figure reproduced with permission from Wiley.*[120]

Surprisingly, film **TiO₂/0.4** had higher stearic acid degradation than film **TiO₂/1.4** which could relate to the thickness and recombination rate of the holes and electrons. Dundar *et al.* fabricated various TiO_2 films by ALD with thicknesses ranging from 2.6 nm to 260 nm; the TiO_2 film of 130 nm exhibited maximum photocatalytic behaviour.[133] Within our work, films **TiO₂/0.4** (80 nm) and **TiO₂/1.4** (510 nm) had a lower decline in stearic acid coverage in comparison to films **SH/TiO₂**, potentially due to the lower surface area, corroborated by the flat topography of the pure **TiO₂** films, **Figure 3.11**, and small RMS roughness values, **Table 13**. The hierarchical roughness of the **SH** film enhanced the superhydrophobicity and hence surface area for the TiO_2 overcoat, confirmed by **Figure 3.08** where the roughness remained in film **SH/TiO₂/0.4** and TiO_2 did not smooth the underlying **SH** film completely, proved by the Sq value (0.18 µm). On the other hand, film **TiO₂/1.4**, **Figure 3.11**, demonstrated a smooth, even and uniform morphology and the absence of sizeable particles. Vahl *et al.* showed that nano-cracks within materials enhanced the photocatalytic activity of the films, potentially due to increased surface area – these nano-cracks were only observed in film **SH/TiO₂/1.4**, **Figure 3.12**.[134]

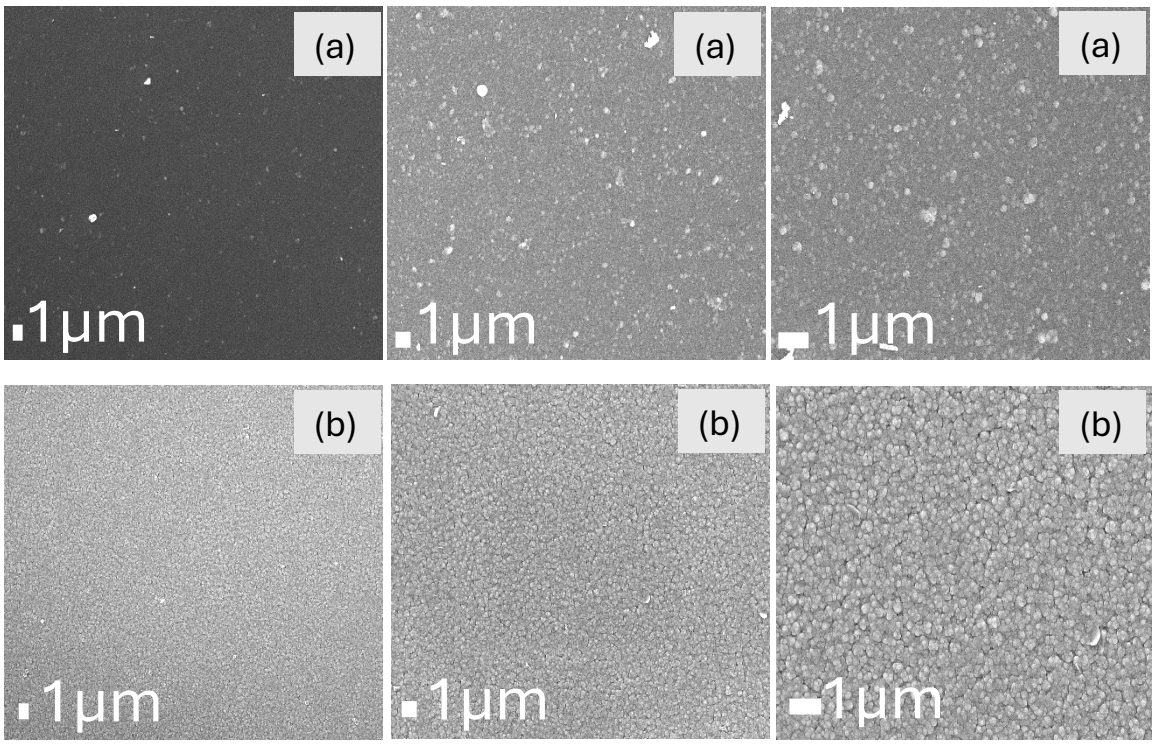

Figure 3.11. *Low magnification SEM images of (a)* ***TiO_2/0.4*** *(b)* ***TiO_2/1.4*** *depicting differences in the number of clusters. Figure reproduced with permission from Wiley.* [120]

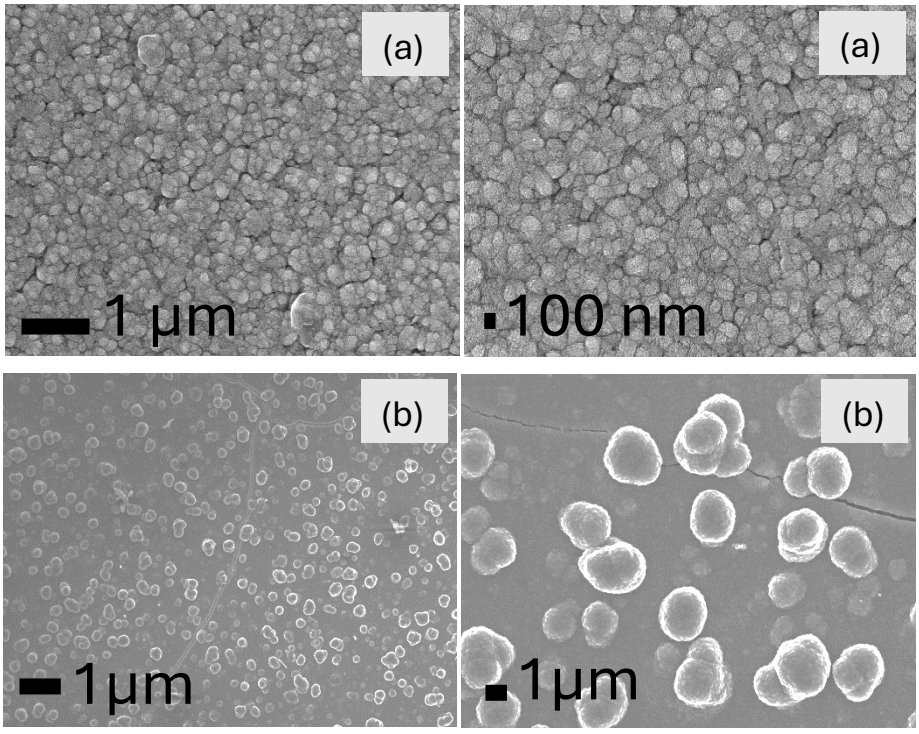

Figure 3.12. *The morphologies of films showing (a) the absence of nano-cracks seen in film* ***TiO_2/1.4*** *and (b) the presence of nano-cracks seen in film* ***SH/TiO_2/1.4.*** *Figure reproduced with permission from Wiley.* [120]

Figure 3.13 exhibits the WCAs of the films immersed in toluene and ethanol for up to 5 h. Toluene and ethanol were used as they have polarities close to 0 and 1, respectively. Prior to immersion in solvents, film **SH/TiO₂/1.4** had a hydrophobic WCA (*ca.* 110-115°) which decreased by 11° in toluene and 28° in ethanol. Film **SH/TiO₂/0.4** started with a WCA of 153° but this reduced to 148° in toluene and to 146° in ethanol. For films **SH/TiO₂/0.4** and **SH/TiO₂/1.4** there was a larger reduction in WCA for ethanol than toluene because the former solvent adsorbs dissociatively on titania. H^+ bond to surface O^{2-} to form surface -OH whereas the $CH_3CH_2O^-$ bond to surface Ti^{4+}. The increase in -OH groups decreased the overall WCA. The thicker the TiO_2 film, the larger the decrease in WCA on exposure to ethanol; by the end of the 5 h immersion period, the **SH** film showed the smallest reduction in WCA of 7°, then film **SH/TiO₂/0.4** (7°) and finally film **SH/TiO₂/1.4** (26°). Films **SH** and **SH/TiO₂/0.4** showed similar reductions in WCA due to the very thin TiO_2 film causing minimal changes in the wettability of the film.

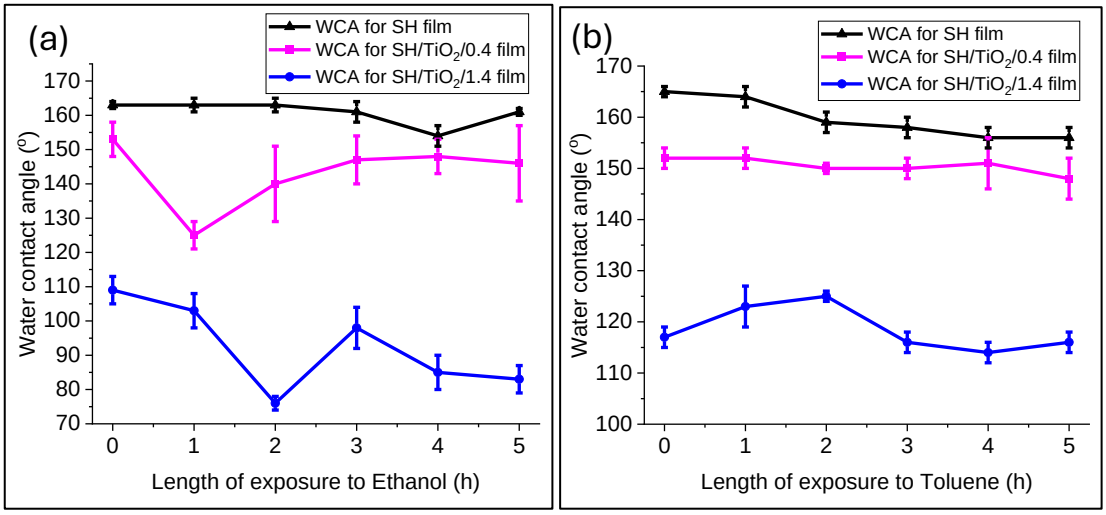

Figure 3.13. *Exposure of films **SH**, **SH/TiO₂/0.4** and **SH/TiO₂/1.4** to (a) ethanol and (b) toluene, both over a 5 h period and their resultant water contact angles. Figure reproduced with permission from Wiley.*[120]

In all cases, films **SH**, **SH/TiO₂/0.4** and **SH/TiO₂/1.4** had even a slight reduction in WCA on exposure to UV light by the end of the two-week period, **Figure 3.14**. For films **SH/TiO₂/0.4** and **SH/TiO₂/1.4**, a decrease in WCA was observed due to bidentate bonding of the Ti^{4+} to the O^{2-} vacancies of the fatty acid and other organic components (both either from the film or the atmosphere) and subsequently, photocatalytic decomposition of these components, reducing the WCA to 120° (film **SH/TiO₂/0.4**) or less (film **SH/TiO₂/1.4**).

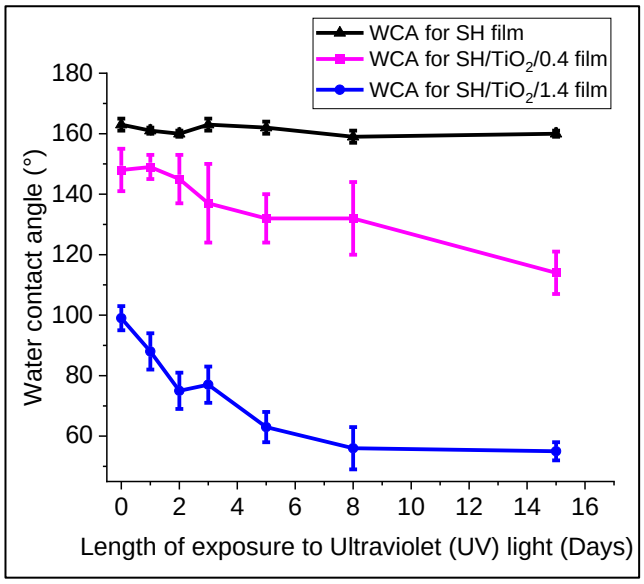

Figure 3.14. *Exposure of films* ***SH****,* ***SH/TiO₂/0.4*** *and* ***SH/TiO₂/1.4*** *to UV light over a 15-day period and their resultant water contact angles*. Figure reproduced with permission from Wiley.[120]

To determine the films' ability to withstand high temperatures, films **SH**, **SH/TiO₂/0.4** and **SH/TiO₂/1.4** were heat-treated at 300 °C for 5 h. The greatest fall in WCA was for film **SH/TiO₂/1.4** (27°) relative to films **SH/TiO₂/0.4** (10°) and **SH** (6°). A potential cause for the drop in WCA was owing to the removal of organic carbon-based particles on annealing; organic contaminants impart hydrophobicity by reducing the surface energy and engender roughness.[110] Such particles may have formed prior to annealing due to precursor degradation or impurities from the air. This concept is confirmed by Gorthy *et al.* where annealing TiO_2 films (*ca.* 600 °C) did not cause a phase transformation or affect the morphology of the films but rather reduced the carbon contamination.[135]

To assess the adhesion of the coating and overall mechanical durability of the films, a tape peel test was carried out. Here, adhesive tape was continually attached and detached from the film with WCAs measured regularly, **Table 14**. Films **SH/TiO₂/0.4** and **SH/TiO₂/1.4** both had a drop in WCA of 15° and 20°, respectively. According to **Table 14**, the WCA fluctuated throughout the test, potentially as a result of taking off the TiO_2 layer and therefore uncovering the superhydrophobic undercoat as well as not measuring the WCA at precisely the same part of the film during each measurement. Interestingly, the removal of the films caused grooves in the film, seen in **Figure 3.15** and **Figure 3.16** which are EDS-generated image of the middle of film **SH/TiO₂/1.4** before and after the tape peel test, respectively. EDS is a bulk analysis technique with a large penetration

depth of 10 μm therefore, any X-rays emitted from the film are from the bulk rather than the surface. Dark-coloured agglomerates are only covered with purple and green specks in the Si Kα and O Kα scans, respectively. Therefore, these dark-coloured particles pertained to the superhydrophobic layer as they remain speck-free in the Ti Kα scan. Prior to the tape peel test, **Figure 3.15**, O, C and Si mainly covered the matrix whereas the Ti was evenly distributed across the film. After the tape peel test, the number of coloured specks on the Si and O Kα scans increased. The darker coloured particles had a larger number of pink and green coloured specks in the Si and O scans respectively.

To determine how the adhesion and durability varied across the dual-layer film, a shorter tape peel test was repeated at the edge of film **SH/TiO_2/1.4** and then scanned via EDS, **Figure 3.16**. The coverage of C remained like the middle of the film and the O and Si coverage concentrated on the exposed superhydrophobic region (right hand side of image). Ti was prominent in the TiO_2 section which had not been detached by the adhesive tape. Visually, there was a clear separation between the **SH** film (right hand side) and TiO_2 film (left hand side), also corroborated by the coloured specks for the O, Si and Ti Kα scans. This was confirmed in **Figure 3.16** by the coloured specks on right-hand side of the Si Kα scan and minimal spots on the left-hand side of the same scan and vice versa for the Ti Kα scan. Hence it was easier to remove the film from the edge relative to the centre. The C Kα scan confirmed successful carbon coating via carbon sputtering which remained uniformly spread out across the film. There were green-coloured specks across the film in the O Kα scan due to the O present in the TiO_2 film (left hand side) and in the superhydrophobic underlayer (right hand side).

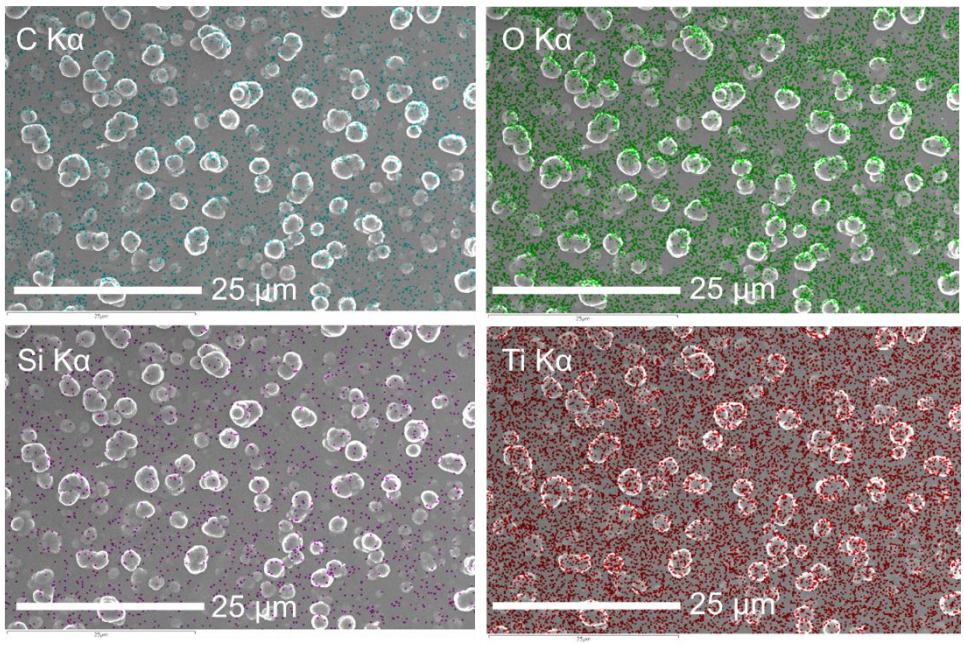

Figure 3.15. *EDS-generated images of film* ***SH/TiO$_2$/1.4*** *(middle) prior to the tape peel test.*

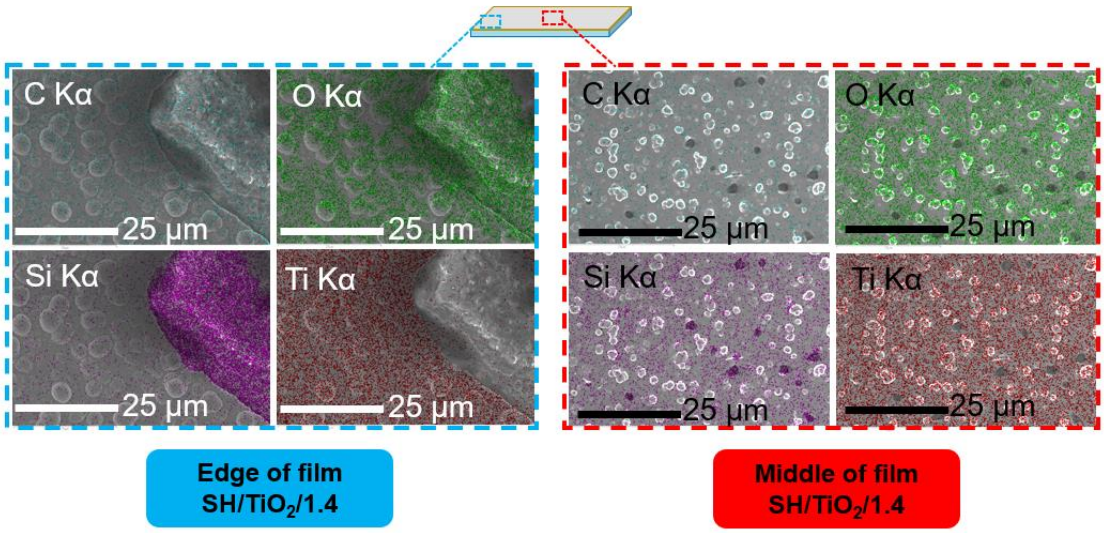

Figure 3.16. *EDS-generated images of film* ***SH/TiO$_2$/1.4*** *(middle & edge) after the tape peel test. Figure reproduced with permission from Wiley.*[120]

Shadowing effects can be seen in **Figure 3.17**. This was further investigated to determine whether it was due to the positioning of the set-up, low electron beam voltage or reabsorption of the generated X-rays by the TiO_2 film. Various tests such as varying the electron beam voltage and EDS scan duration for film **SH/TiO$_2$/1.4** were pursued. Initially, a shadowing effect was observed for the O Kα scan (middle of film) both before and after the tape peel test, **Figure 3.15** and **Figure 3.16**. The thicker the TiO_2 film, the greater the reabsorption of the X-rays and hence the greater the shadowing effect. Other potential reasons for the

shadowing effect may have been due to the instrumental set up with the detector being offset from the film. Also, oxygen is a light element so this may have contributed although this shadowing effect was not observed in the C Kα scans, an atomically lighter element.

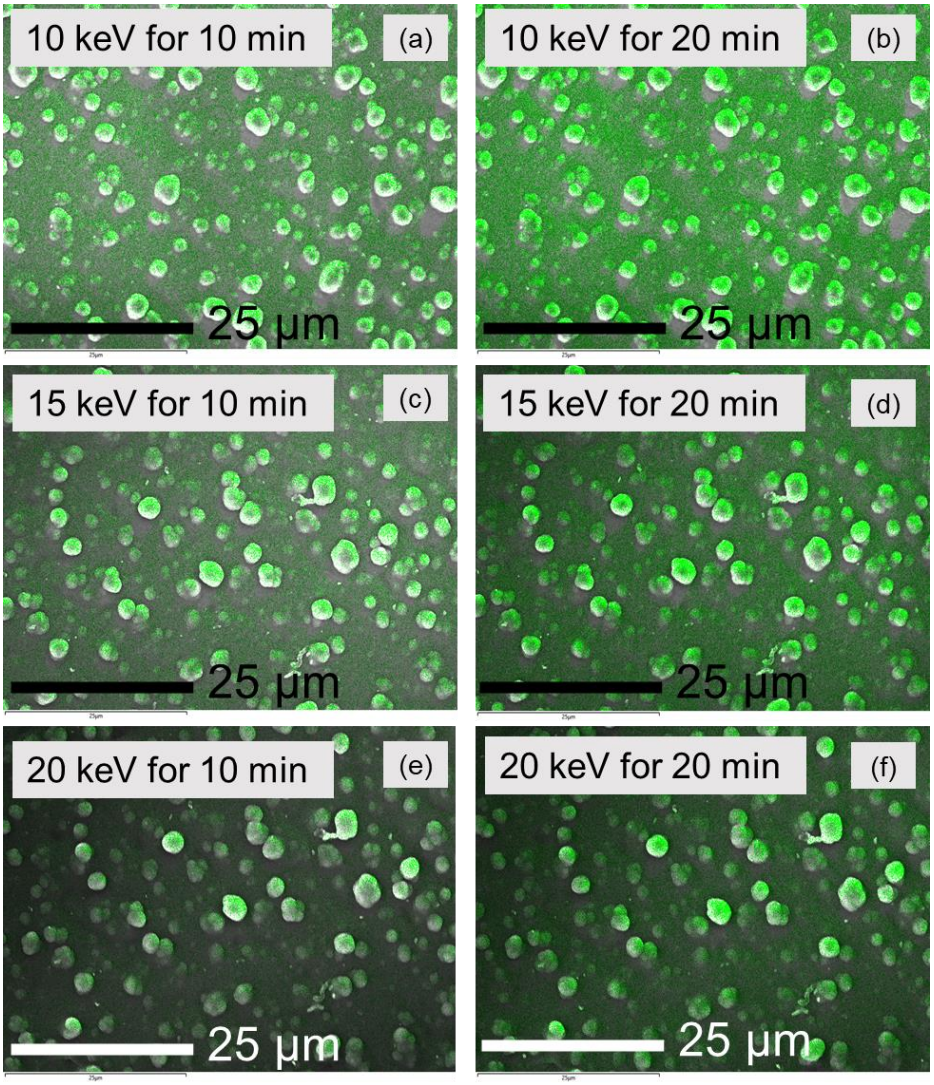

Figure 3.17. *O 1s scans of* ***SH/TiO₂/1.4*** *taken before the tape peel test at different electron beam voltages and scan durations. The films demonstrate the misalignment of the green overlay with the SEM image due to a shadowing effect.*

Potential solutions to this problem included increasing the scan duration and electron beam voltage. On attempting these changes, shadowing effects were still present, even at high electron beam voltages. Therefore, the main cause of the shadowing effect was thought to be due to the geometry of the instrument. The detector is positioned on the top right and hence not directly on top of the stage, relative to the image. In addition, the morphology of the films included large agglomerates directly on the surface, causing the TiO_2 film to re-absorb some of

the X-rays, leading to shadowing. This shadowing effect was not observed for film **SH/TiO$_2$/0.4**.

Comparing film **SH/TiO$_2$/1.4** before and after the tape peel test (middle), a decrease in Ti wt% coverage of *ca.* 9%, generated by EDS and an increase in O wt% and Si wt% coverages to *ca.* 3% and *ca.* 5% confirmed the removal of the TiO$_2$ layer and exposure of the superhydrophobic film underneath. The same was true for the edge of film **SH/TiO$_2$/1.4**, although a greater reduction in Ti was observed here to 35%, confirming that it was easier to peel off the TiO$_2$ film from the edge of the film.

Pencil hardness testing, **Figure 3.18**, was carried out on films **SH/TiO$_2$/0.4** and **SH/TiO$_2$/1.4** which had differences in tolerable hardness due to differences in TiO$_2$ thickness. A visible mark was made in film **SH/TiO$_2$/0.4** with a pencil with a hardness level of "H". As expected, film **SH/TiO$_2$/1.4** endured pencils of all hardness, up to and including 6H; even at this level of hardness, the abrasion made was filled with debris hence confirming the coating's capability to withstand higher levels of hardness. Of all three films tested, the **SH** film without the TiO$_2$ overcoat withstood the lowest pencil hardness of "F", film **SH/TiO$_2$/0.4** withstood a hardness that was 1 degree higher and film **SH/TiO$_2$/1.4** tolerated a hardness of 6 degrees higher. This test demonstrated that even a thin TiO$_2$ film can provide some robustness. A reason for the increased durability of the TiO$_2$ overcoat also deposited via AACVD was that the AACVD of TiO$_2$ is analogous to standard chemical vapour deposition methods where gas-phase precursor particles chemisorb onto the substrate rather than physisorb via thermophoresis.[62,66]

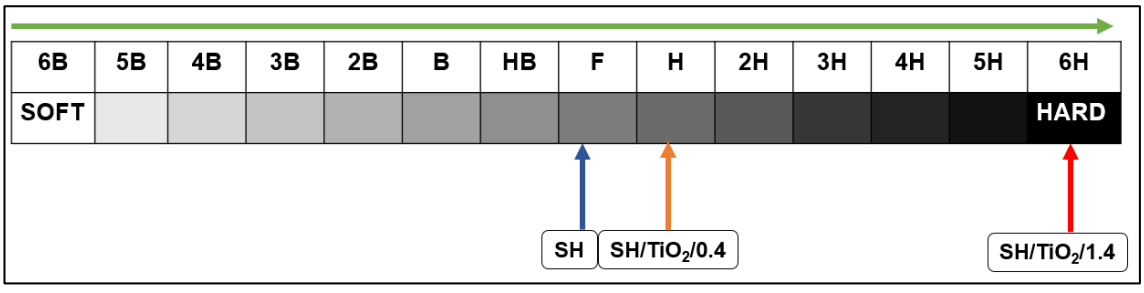

Figure 3.18. *Pencil Hardness Testing of the uncoated* ***SH*** *film and TiO$_2$ coated,* ***SH/TiO$_2$/0.4*** *and* ***SH/TiO$_2$/1.4*** *films. Figure reproduced with permission from Wiley.* [120]

To determine the water repellence and self-cleaning capability of the films, a series of qualitative tests were carried out, **Figure 3.19**. Firstly, methylene blue was pipetted onto the surface of films **SH/TiO$_2$/0.4** and **SH/TiO$_2$/1.4,** with the

former film having a sliding angle of *ca.* 6° and the latter, *ca.* 18°, **Figure 3.19(a) – (f)**. In a separate test, film **SH/TiO$_2$/0.4** was coated with gold glitter although it was not possible to coat film **SH/TiO$_2$/1.4** as the gold glitter would not adhere to the surface. Although film **SH/TiO$_2$/1.4** demonstrated good chemical self-cleaning properties (determined via photocatalytic testing), it had limited physical self-cleaning properties (determined via methylene blue/attempted gold glitter removal). Nevertheless, both **SH/TiO$_2$** films had some chemical self-cleaning properties regardless of the decreased physical self-cleaning abilities.

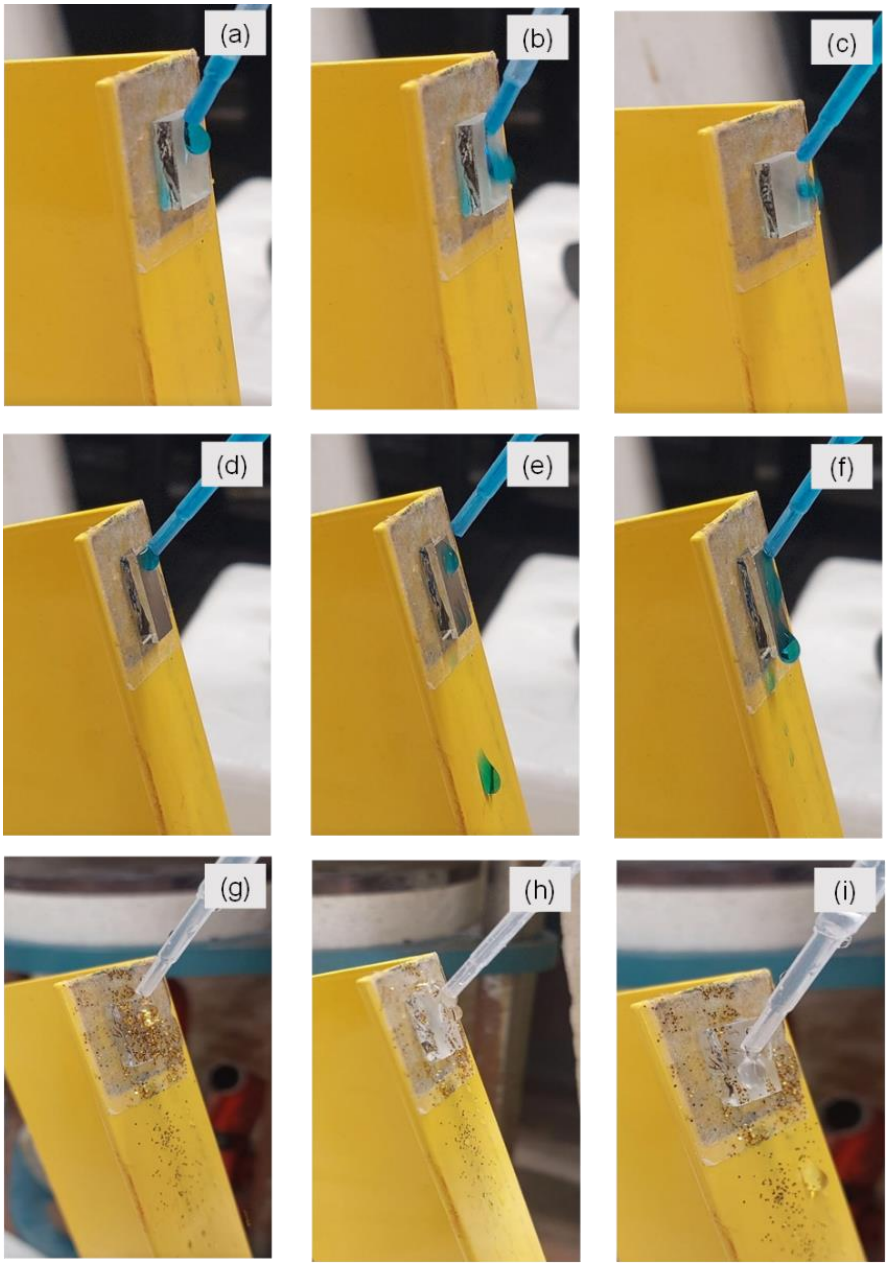

Figure 3.19. *Water repellence testing of* ***SH/TiO$_2$*** *films with methylene blue (images a – f); images (a) - (c) are of film* ***SH/TiO$_2$/0.4****; images (d) - (f) are of film* ***SH/TiO$_2$/1.4****. Images (g) - (i) demonstrated the self-cleaning behaviour of film* ***SH/TiO$_2$/0.4****. Film* ***SH/TiO$_2$/1.4*** *could not be coated with gold glitter. Figure reproduced with permission from Wiley.*[120]

Table 14. *Changes in WCA for films* ***SH/TiO$_2$/0.4*** *and* ***SH/TiO$_2$/1.4*** *during the tape peel test.*

Cycle number	Water contact angle of Film **SH/TiO$_2$/0.4 (°)**	**Cycle number**	Water contact angle of Film **SH/TiO$_2$/1.4 (°)**
Before test	94 ± 25	**Before test**	70 ± 3
After 1 cycle	104 ± 21		-
After 2 cycles	89 ± 16		-
After 3 cycles	83 ± 22		-
After 4 cycles	67 ± 15		-
After 5 cycles	73 ± 16	**After 5 cycles**	70 ± 2
After 6 cycles	78 ± 17		-
After 7 cycles	76 ± 17		-
After 8 cycles	78 ± 6		-
After 9 cycles	76 ± 9		-
After 10 cycles	80 ± 10	**After 10 cycles**	63 ± 3
After 15 cycles	75 ± 13	**After 15 cycles**	68 ± 1
After 20 cycles	76 ± 10	**After 20 cycles**	75 ± 3
After 25 cycles	75 ± 12	**After 25 cycles**	72 ± 3
After 30 cycles	78± 5	**After 30 cycles**	69 ± 2
After 40 cycles	75 ± 11	**After 40 cycles**	70 ± 2
After 50 cycles	81 ± 12	**After 50 cycles**	70 ± 6
After 60 cycles	72 ± 11		-
After 70 cycles	83 ± 13		-
After 75 cycles	-	**After 75 cycles**	60 ± 4
After 80 cycles	79 ± 11		
After 90 cycles	81 ± 6		-
After 100 cycles	77 ± 9	**After 100 cycles**	62 ± 7
After 125 cycles	80 ± 10	**After 125 cycles**	61 ± 7
After 150 cycles	83 ± 10	**After 150 cycles**	60 ± 5
After 175 cycles	83 ± 10	**After 175 cycles**	51 ± 1
After 200 cycles	78 ± 7	**After 200 cycles**	49 ± 2
After 225 cycles	79 ± 8	**After 225 cycles**	52 ± 4
After 250 cycles	78 ± 7	**After 250 cycles**	55 ± 7
After 275 cycles	82 ± 6	**After 275 cycles**	50 ± 3
After 300 cycles	85 ± 5	**After 300 cycles**	55 ± 5
After 325 cycles	76 ± 9	**After 325 cycles**	49 ± 2

After 350 cycles	79 ± 7	**After 350 cycles**	48 ± 3
After 375 cycles	82 ± 4	**After 375 cycles**	51 ± 1
After 400 cycles	79 ± 4	**After 400 cycles**	50 ± 1

3.6 Summary

Dual-layered superhydrophobic and photocatalytic self-cleaning materials were successfully fabricated by varying the [TTIP] to tune the surface properties of the underlying fluorine-free superhydrophobic film, all deposited by AACVD at 350 °C. Surface characterisation, namely XPS, demonstrated the successful deposition of TiO_2 at all concentrations of TTIP. Raman and PXRD confirmed that the anatase phase had been deposited. SEM imaging revealed the smoothing out of complex rough topology of the underlying superhydrophobic film and the subsequent clustering of TiO_2 agglomerates and filling of the matrix as [TTIP] increased, corroborated by the reduction in root-mean-square roughness values. Low electron beam voltages (<10 keV) were used to image the films with low [TTIP] but this increased up to and including 20 keV as the TiO_2 films became thicker. As expected, the percentage transmittance reduced from *ca.* 34% (uncoated **SH** film) to *ca.* 9% for the highest [TTIP], i.e. film **SH/TiO_2/1.4**. These transmission values were significantly lower than the TiO_2 films due to the absence of the superhydrophobic undercoat in the latter. WCAs and their changes (as well as errors) confirmed the wettability and the one standard deviation, taken to be the error, confirmed the patchiness of the depositions. Standard deviations were initially large, approximately 26° for the lowest concentration of [TTIP] deposited on a superhydrophobic undercoat however, this reduced significantly to 3° on depositing 1.4 cm^3 of TTIP.

Enhanced photocatalytic behaviour (>50% reduction in stearic acid coverage) was observed in all TiO_2 functionalised superhydrophobic films, demonstrating chemical self-cleaning properties through a stearic acid degradation test. The increase in surface area due to the rough superhydrophobic underlayer and presence of nano-cracks improved the photocatalytic activity more so than the TiO_2 films without the undercoat. In addition to quantitative water contact angle measurements, qualitative self-cleaning and water repellence tests demonstrated some physical self-cleaning behaviour. Unfortunately, this synergistic self-cleaning behaviour did not display both forms of dual functionality equally, as the photocatalytic activity improved, there was a reduction in superhydrophobicity and vice versa.

Decreases in water contact angle were observed for the films immersed in ethanol (up to 30° reduction) and irradiated with UV light (up to 40° reduction)

due to the generation of hydroxyl groups. All films demonstrated retained hydrophobicity once immersed in toluene or tested against adhesive tapes or pencils of the “H” bracket level of hardness when compared to the unmodified **SH** film. In all cases, depositing a thin film of TiO_2 contributed to better mechanical robustness, even for film **SH/TiO_2/0.4**.

Within the literature, TiO_2 NPs incorporated into a superhydrophobic mixture is a route to fabricating physical and chemical self-cleaning materials. The work outlined within this chapter demonstrated that depositing TiO_2 onto a **SH** film by AACVD (via the TTIP precursor) can create a physical and chemical self-cleaning material. Such multi-layered films have the same functionality as a film one-pot mixture (with TiO_2 NPs incorporated). However, for the dual-layered route, it is easier to tune the hydrophobicity of **SH** films with TiO_2 by a layer-by-layer AACVD approach, attaining a range of TiO_2 hydrophobicities. Invariably, the **SH/TiO_2** films demonstrated better wettability and photocatalytic activity than the TiO_2 films without the undercoat and improved durability than the unmodified **SH** film.

Chapter 4 – TiO_2 Surface Modification of Fluorine-Free Superhydrophobic Coatings via ALD

4.1 Background

ALD can be used to deposit very thin, nanometre-thick metal oxides/sulfides/nitrides films, providing better control of the deposition process relative to CVD.[136,137,138] Although deposited films are ultrathin, they have important applications such as adhesion promotion, tuning of wettability and protection of the underlying materials against UV radiation.[139] Hence ALD films can introduce additional functionality without negatively impacting critical attributes. ALD deposited films are conformal, following the shape of the underlying film/substrate. Therefore, there is a growing interest in depositing such films onto high aspect ratio materials, such as superhydrophobic films. Zhang *et al.* fabricated a superhydrophobic material by depositing TiO_2 via ALD onto a microporous substrate which provided some roughness.[140] Then, the TiO_2 top coat was surface modified with a nano silane emulsion which lowered the overall surface energy. The superhydrophobic composite formed maintained water repellence and anti-fouling properties.

The method of surface modifying inorganic films via ALD has gained interest in the last 10 years to generate hydrophilic surfaces. Wang *et al.* reported surface modification of a polyvinyl chloride surface via thermal ALD and plasma enhanced ALD by using trimethylaluminum and H_2O to ultimately deposit Al_2O_3.[141] Al_2O_3 is inherently hydrophilic however, surface modifying via thermal ALD made the film hydrophobic due to increased carbon residues on the surface. Water (used in T-ALD) is not as reactive as oxygen radicals (used in PE-ALD), making the surface less hydrophilic. This was confirmed by XPS and SEM images which demonstrated similarity in the structure's surface through the growth of the island aggregates. Al_2O_3 films have potential in minimising water vapour transmission rates in electronic gadgets, ultimately, improving their service life.[74] Zhukovsky *et al.* tuned the surface of a Si substrate by depositing multiple layers (200 nm) of Al_2O_3 and TiO_2 via ALD for prospective applications in sensing.[142] Nikkola *et al.* presented a report on the ALD surface modification of a thin film composite with Al_2O_3 (precursor: trimethylaluminium ($AlMe_3$)) to introduce anti-fouling properties.[143] ALD cycles were either 10, 50 or 100 and the deposition

temperatures were either 70 °C or 100 °C. It was found that low temperatures and low cycle numbers were directly proportional to the film thickness. As a result, the films had better anti-fouling properties to hydrophobic organic contaminants due to improved hydrophilicity, because of the -OH groups and lower surface roughness.

Lee *et al.* deposited HfO_2 films by ALD to understand the inherent hydrophilicity of the subsequent films deposited on Si substrates.[144] It was found that increased hydrophilicity correlated to the presence of surface oxygen molecules. Interestingly, heat treatment changed the microcrystal particle sizes and crystal orientation which affected the surface free energy and hence WCA of the films. On the other hand, the WCA of the HfO_2 films increased up to *ca.* 100° 1-month post-deposition due to the absorption of hydrocarbons. Nevertheless, there are some reports on the ALD surface modification of powders. Hirschberg *et al.* deposited <10 nm-thick TiO_2 films onto amorphous and crystalline powders resulting in enhanced flowability without hindering other essential properties such as water-solid interactions, vital for pharmaceutical applications.[145]

TiO_2 is one of the most studied metal oxides deposited by ALD due to its enticing attributes such as biocompatibility and photocatalytic properties. Common ALD precursors to afford TiO_2 films include titanium(IV) tetrachloride, titanium(IV) ethoxide, titanium(IV) isopropoxide (TTIP) and tetrakis(dimethylamino)titanium(IV) (TDMAT).[146] Halogen containing Ti precursors include titanium(IV) tetrachloride and titanium(IV) tetraiodide ($TiCl_4$ and TiI_4) with O_2 pulses have been employed due to reduced impurities (e.g. hydrogen contamination) in the resulting TiO_2 films. Aarik *et al.* combined $TiCl_4$ with O_3 which was then deposited onto Si wafers.[147] By changing the purge pulse from water to ozone for the $TiCl_4$ ALD process, it was possible to tune the properties of the film such as the root-mean-square roughness due to producing thicker TiO_2 films. There was also an observable change in the growth rates. Similarly, the replacement of a water pulse with an ozone pulse reduced hydrogen contamination and led to improved properties of the films such as dielectric constants for potential applications in capacitors. When $TiCl_4$ precursor pulses were utilised with water purge pulses, this generated corrosive by-products, such as HCl and $TiCl_4$, and required high evaporation temperatures.[148]

Alternatively, Ti alkoxides, such as titanium(IV) ethoxide and TTIP, have been precursors of interest due to the absence of halogens and corrosive by-products. Jang *et al.* utilised the TTIP precursor to deposit ultrathin TiO_2 films of 6 nm, 11 nm and 16 nm onto Si wafers and subsequently tuned the surface's wettability by irradiating it with UV for up to 10 min.[149] However, the required ALD deposition temperatures for these precursors is variable and usually outside of the standard ALD film growth window hence are used for CVD processes such as AACVD.[120]

On the other hand, TDMAT has been explored as an alternative Ti precursor due to its improved reactivity with water pulses relative to the Ti alkoxides and halides. However, the TDMAT precursor pulses alongside water pulses can lead to the formation of impure TiO_2 films and if deposited at <150 °C, require long purge times.[148] Jin *et al.* fabricated TiO_2 films via TDMAT on Si wafers due to its large ALD film growth window of *ca.* 150 °C; in this case, Ti was equivalent to Ti^{3+}.[148] The authors used ozone pulses rather than water pulses due to the described challenges. Kaariainen *et al.* surface modified a polymethylacrylate (PMMA) substrate with TDMAT, deposited by plasma assisted-ALD (PA-ALD).[139] The results demonstrated that it was possible to successfully deposit TiO_2 onto alternative substrates such as PMMA by PA-ALD. However, the carrier gases and plasma power must have been carefully selected to control film growth and prevent film delamination.

4.2 Aims

The aim of the experiments within this chapter was to deposit very thin (nanometre-thick) TiO_2 films by ALD by varying the number of cycles or temperature. Depositing thin layers is easier to control via ALD relative to AACVD. ALD is known to deposit conformal coatings on Si wafers therefore investigations were carried out to determine if this conformality would occur on a superhydrophobic film with a rough and complex morphology.

4.3 Experimental

Tetrakis(dimethylamino)titanium(IV) (TDMAT) was used as it is a more reactive precursor than TTIP to improve the film's coverage as ALD involves surface-controlled reactions. Some of the **SH** films were plasma treated prior to ALD deposition and others were not to determine the influence of plasma treatment on the TiO_2 deposition. In conjunction with the **SH** films, Si wafers were placed

into the reactor to estimate the thickness, and plain FTO glass substrates were also inserted to compare the deposition pattern.

4.3.1 Chemicals & Materials

Vinyl-terminated polydimethylsiloxane (PDMS) also known as SYLGARD™ 184 Silicone Elastomer Base along with its corresponding curing agent were purchased from Dow Corning. Aerosil OX50 SiO_2 nanoparticles (fumed) procured from Lawrence Industries. Palmitic acid (≥ 99%), stearic acid (reagent grade, 95%), ethyl acetate (laboratory grade) and tetrakis(dimethylamido)titanium(IV) (99.99%) were all acquired from Merck Chemicals. All chemicals were used as received. NSG provided SiO_2 barrier coated fluorine-doped tin oxide (FTO) glass substrates which were manually cut to 15 cm x 4 cm x 0.3 cm for AACVD.

4.3.2 Synthesis of fluorine-free superhydrophobic film

The **SH** film was deposited as per **Chapter 3, Section 3.3.2**.

4.3.3 Surface Modification of the SH film with TiO_2 via ALD

Plasma treatment of the **SH** films was carried out with a HPT-100 Henniker plasma cleaner. All films were plasma cleaned for 4 min with 100% power and a N_2 carrier gas flow rate of 2 sccm. All **SH** films were plasma treated prior to TiO_2 ALD except for film **SH/TiO_2/1000C/N-P** where N-P signifies “Not plasma treated”.

Ultrathin films of TiO_2 were deposited using a PicoSun R-200 ALD rig at 225°C on p-type FTO glass substrates, Si (100) wafers and **SH** films by thermal ALD using TDMAT and ozone as precursors. The deposition took place under a constant flow of N_2 (99.9999%, BOC; 400 sccm intermediate space, 50 sccm all other lines). A vapour draw technique was used to pulse the precursors from the TDMAT precursor bubbler (no prefill) and ozone was generated locally (50% power).

For **Study A**, the TDMAT bubbler temperature was set to provide an observable pressure ‘pulse’ on opening the bubbler to demonstrate dosing. However, due to the decreasing amount of precursor in the bubbler this was increased from 130 °C for the first 200 cycles, to 150 °C for the next 400 cycles and finally 170 °C for the final 300 cycles. Each ALD cycle had a 1.6 s pulse of TDMAT (120 sccm carrier N_2 flow), a 16 s TDMAT purge, a 0.3 s ozone pulse (500 sccm O_2 flow, 100 sccm

carrier N_2 flow) and a 6.0 s ozone purge. The resulting films and substrates went through various ALD cycle numbers leading to a range of thicknesses presented in **Table 15**.

The pulse and purge times used in **Study A** led to total process times that made completing large numbers of cycles in a given workday problematic. For **Study B,** the TDMAT and ozone pulse and purge times, and TDMAT bubbler temperature (after refilling), were optimised in order to give saturative growth (growth rate ~ 0.3-0.4 Å/cycle) on a planar silicon wafer (still at a reactor temperature of 225 °C); TDMAT, 90 °C, 1.0 s pulse, 4.0 s purge; ozone 0.3 s pulse, 6.0 s purge. However, when introducing multiple **SH** substrates the measured growth rate (on a piece of Si) dropped below 0.1 Å/cycle, possibly due to the larger surface area to be coated, and so the TDMAT bubbler temperature was increased to 100 °C to provide measurable growth. However, this is too high for true saturative (ALD) growth (1 Å/cycle), and hence this process can only be considered CVD-like. The resulting films and substrates are presented in **Table 15.**

All TiO_2-surface modified **SH** films were denoted as **SH/TiO_2/xC** where **x** = number of ALD precursor cycles. All **SH** films were plasma treated prior to TiO_2 ALD except for film **SH/TiO_2/1000C/N-P** where N-P signifies “Not plasma treated”. All TiO_2 films deposited on FTO glass substrates were denoted as **TiO_2/xC** where x = number of ALD precursor cycles. All TiO_2 films deposited on Si (100) wafers were denoted as **Si/TiO_2/xC** where **x** = number of ALD precursor cycles.

The overall aims of **Studies A** & **B** were identical however, an additional aim was incorporated within **Study B** to understand the influence of plasma-treatment on the TiO_2-surface modification. A schematic outlining the deposition of the superhydrophobic film and TiO_2 surface tuning via ALD is shown in **Figure 4.01**.

Table 15. *The number of cycles, estimated thickness, WCA, sliding angles, CAH and RMS height of all films from Studies A & B.*

Study	Film name	No. of TiO_2 cycles	Estimated thickness (nm)	WCA (°)	Sliding angle (°)	CAH (°)	RMS height, Sq (μm)
-	SH	-	-	165 ± 2	4 ± 1	13 ± 6	0.28 ± 0.03
-	Barrier coated FTO glass substrate	-	-	62 ± 3	42 ± 2	20 ± 9	Immeasurable
-	Si wafer	-	-	128 ± 5	53 ± 3	-	Immeasurable
Study A	SH/TiO_2/100C	100	3.7	104 ± 7	34 ± 1	17 ± 7	0.25 ± 0.00
	TiO_2/100C	100	3.7	45 ± 7	46 ± 1	13 ± 4	
	Si/TiO_2/100C	100	3.7	80 ± 1	-	-	-
	SH/TiO_2/200C	200	11.6	115 ± 14	24 ± 1	18 ± 6	0.26 ± 0.01
	TiO_2/200C	200	11.6	63 ± 10	33 ± 3	13 ± 9	
	Si/TiO_2/200C	200	11.6	72 ± 2	-	-	-
	SH/TiO_2/600C	600	41.2	89 ± 3	35 ± 1	17 ± 7	0.25 ± 0.01
	TiO_2/600C	600	41.2	70 ± 4	33 ± 3	19 ± 3	
	Si/TiO_2/900C	900	41.2	51 ± 1	-	-	-
	SH/TiO_2/900C	900	41.2	70 ± 7	33 ± 3	17 ± 8	0.25 ± 0.00
	TiO_2/900C	900	41.2	52 ± 2	40 ± 1	15 ± 4	
	Si/TiO_2/900C	900	41.2	54 ± 2	-	-	-
Study B	SH/TiO_2/1000C	1000	100	64 ± 4	33 ± 2	22 ± 6	0.25 ± 0.07
	SH/TiO_2/1000C/ N-P	1000	100	71 ± 6	36 ± 3	20 ± 7	0.25 ± 0.00
	TiO_2/1000C	1000	100	74 ± 1	36 ± 1	25 ± 7	
	Si/TiO_2/1000C	1000	100	66 ± 3	-	-	-

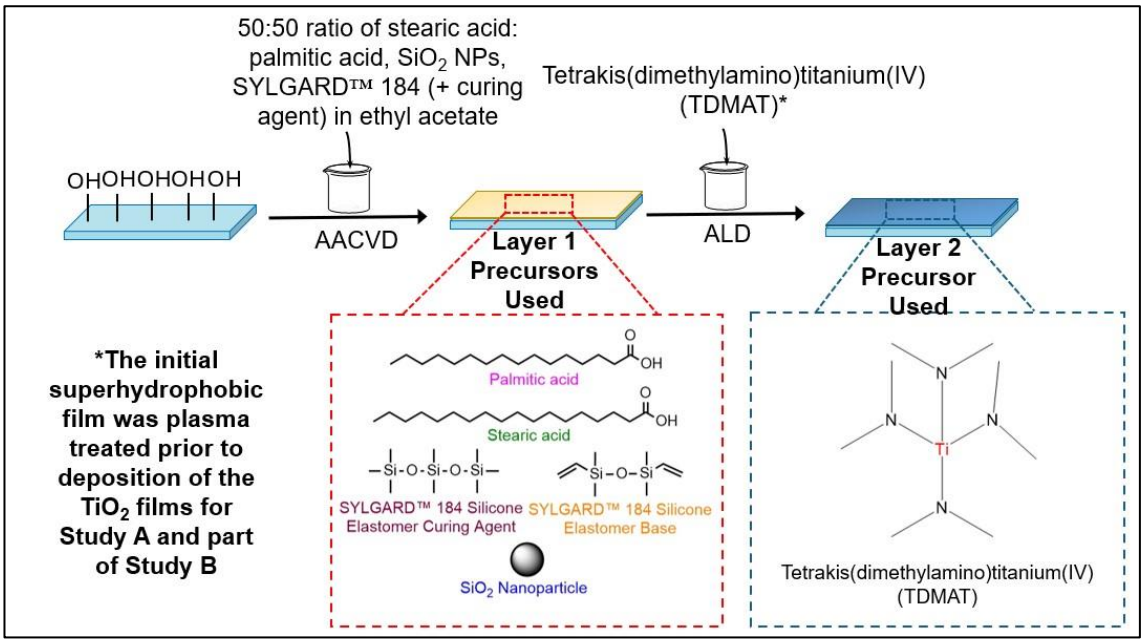

Figure 4.01. *The method to fabricate dual-layered* ***SH/TiO₂lxC*** *films. The first step involved the deposition of a fluorine-free mixture via AACVD to fabricate a superhydrophobic film. Subsequently, the film was surface engineered with TiO_2 by ALD to introduce additional functionality.*

4.3.4 Materials Characterisation

Visualisation of the surface morphologies and cross-sectional SEM of the materials were carried out using the JEOL 6701F and JEOL 7600F Scanning Electron Microscopes (SEMs). Electron acceleration voltages of 5 – 20 keV were used, depending on how much heat from the electron gun the sample could tolerate. Carbon sputtering (physical vapour deposition) of all samples for 10 s occurred to improve the electrical conductivity of the films for imaging and to prevent charging. The sizes of the particles were measured by the ImageJ 1.52s software. Energy Dispersive X-ray Spectroscopy (EDS) scans were taken with an Oxford Instruments EDS set up with variable scan durations of 10 min to 20 min. Functional bonds were detected through Fourier-Transform Infrared Spectroscopy (FTIR) using the Brucker alpha platinum-ATR instrument, with a wavenumber range of 400 – 4000 cm^{-1}. Finally, a Thermo Scientific X-ray photoelectron spectrometer with a mono-chromated Al-K alpha source (8.3381 Å) was used for compositional analysis. The peaks were analysed using the CasaXPS 2.3.25 software and calibrated with respect to the C 1s peak at *ca.* 285 eV. Four spots were scanned per film via XPS. The phase composition of the films was determined through powder X-ray diffraction (PXRD), utilising a Malvern PANalytical Empyrean Grazing Incidence-PXRD comprised of a Xe point

detector and monochromated Cu Kα source at a voltage of 40 kV and current of 40 mA. Additional parameters include step size: 0.05°, 2θ = 20° - 80°, ω (incident beam) = 1°. A Bruker Senterra II Raman Spectrometer (λ = 532 nm, power = 25mW) was used to generate Raman spectra. The thickness of the TiO_2-only films deposited on Si wafer (without the superhydrophobic undercoat) was calculated an M-2000® Ellipsometer. The root-mean-square height (Sq) was measured using the Keyence VHX-S750E optical microscope at x1500 magnification. No S-filter and no L-filter were used, only using a Gaussian filter type.

4.3.5 Functional Durability and Performance Testing

Water contact angles were measured using a Kruss DSA 25E drop shape analyser. A mean and the error (one standard deviation) of 10 water droplets of 5 µL was determined which was calculated automatically by ADVANCE 1.14.3. A tilted drop method of water droplets (*ca.* 15 µL) dispensed 4 cm from the surface of the film was used to determine the sliding angle. The stage was tilted at the respective inclination (°) prior to any measurement. The size of the angles was calculating by manually adjusting the baseline and utilising the Young-Laplace equation. The CAH was determined by initially measuring the advancing angle before measuring the receding angle and finally subtracting an average of the two angles. The Ellipse (Tangent) method was used to determine the angles. The root-mean-square height (Sq) was measured using the Keyence VHX-S750E optical microscope at x1500 magnification. No S-filter and no L-filter were used, only using a Gaussian filter type.

Photocatalytic activity testing

Stearic acid degradation test: The films were immersed overnight in a beaker of a 0.05M stearic acid standard solution (solvent: chloroform). The next day the films were irradiated with UV light for up to 30 h. FTIR scans were recorded frequently via a PerkinElmer Fourier Transform Lambda RX I spectrometer (range: 2800 – 3000 cm^{-1}). For consistency, the corrected area was calculated by the instrument for each of the tested films and hence the stearic acid percentage coverage and errors (one standard deviation) were calculated.

Self-cleaning performance testing: Methylene blue was directly and continuously pipetted onto the surface. The samples were tilted at 20° with

images taken throughout the testing to qualitatively visualise the superhydrophobicity and self-cleaning properties.

Durability

Elcometer® Testing: An Elcometer® 501 Pencil Hardness Tester (supplier: Elcometer® Ltd.) consisted of pencils of differing hardness (6H – 6B) which were pushed across the surface of a film at a 45° angle. Pencils of increasing hardness were used until a visible line was seen (by eye) in the coating. The standard protocol followed was ASTM D3363.

Thermal Stability: Samples were heated at 300 °C for 5 h and the WCAs and CAH measurements were taken prior and post heating.

UV Stability: WCAs and SAs of samples were measured after 1, 2, 3, 4, 5, 6 and 7 days of exposure to UV in a sealed UV light box. The CAH was measured after 7 days of UV exposure. A UV irradiance of 260 mW/cm^2 and emission wavelength of 365 nm were used.

Tape peel test: Scotch Magic™ Tape was manually stuck to and removed from the films up to 400 times. WCAs were initially recorded periodically, and the CAH was recorded at the end.

4.4 Results and Discussion

ALD was utilised to compare the effect of depositing thinner layers of TiO_2 relative to AACVD (described in **Chapter 3**). Unlike for TiO_2 deposited via AACVD, the films described within this chapter were deposited at significantly lower temperatures (*ca.* <225 °C) due to the use of ozone.[150] These dual-layered films were formed from a **SH** film deposited directly onto the FTO glass substrate followed by TiO_2 deposited by ALD. ALD operates by depositing one atomic layer of film per cycle making it a surface-controlled reaction.[69] On the contrary, this atomic-layer control is not possible for AACVD.

The depositions were split into two separate studies, **Study A** and **Study B** with the overall aim of achieving ALD-growth on the **SH** films of each study. For **Study A**, between 100 ALD cycles and 900 ALD cycles (inclusive) were attempted to deposit films of thicknesses from *ca.* 4 nm to *ca.* 41 nm. For **Study B**, 100 ALD cycles were trialled on plasma and non-plasma cleaned **SH** films depositing *ca.* 100 nm-thick films. In both studies, TiO_2 was successfully deposited on all films

which was corroborated by the reduction in WCA from *ca.* 160° - 165° to a minimum of 115 ±14°. The large standard deviations, particularly for films **SH/TiO$_2$/100C** and **SH/TiO$_2$/200C** was indicative of patchy depositions, leaving coated and uncoated parts of the underlying superhydrophobic film. The thickness of films **SH/TiO$_2$/600C** and **SH/TiO$_2$/900C** were identical *ca.* 41 nm. The thickness was measured by ellipsometry on their counterparts deposited on Si wafers (films **Si/TiO$_2$/600C** and **Si/TiO$_2$/900C**). The reason for equal thicknesses was due to running out of precursor during the final 300 cycles for film **SH/TiO$_2$/900C**.

Interestingly, there were changes in WCA, even with 3 or 4 nm of TiO$_2$ (**Study A**) suggesting better TiO$_2$ coverage via ALD (WCA: 104 ± 7°) than AACVD. The AACVD deposited TiO$_2$ films (**Chapter 3**) did not lead to similar reductions in WCA as the ALD deposited TiO$_2$ films; film **SH/TiO$_2$/0.4**, presumed to have an 80 nm thick TiO$_2$ film had a WCA of 142 ± 26°. The growth per cycle for the films of **Study B** was high (1 Å/cycle) indicating CVD-like growth rather than ALD growth. This may have been due to increasing the bubbler temperature to *ca.* 100 °C leading to overdosage of the TDMAT precursor.

From **Study B** it appeared that plasma-treating the film and the subsequent deposition of TiO$_2$ via ALD led to a WCA of 64°. However, the deposition of TiO$_2$ via ALD on the non-plasma treated film lowered the WCA to 71°. With respect to thickness, film **TiO$_2$/1000C** had a thickness of 100 nm and WCA of 74°. Relative to the films from **Chapter 3**, film **TiO$_2$/0.4** had an estimated thickness of 80 nm and a WCA of 65° and film **TiO$_2$/1.4** had an estimated thickness of 510 nm and WCA of 77°. The results for films **TiO$_2$/1.4** and **TiO$_2$/1000C/N-P** were in line with each other and confirmed that thicker TiO$_2$ films should have a WCA of *ca.* 70-80°. Therefore, from this evaluation, film **SH/TiO$_2$/1000C** (WCA: 64°) may have had a slightly thinner TiO$_2$ coating than film **SH/TiO$_2$/1000C/N-P** (WCA: 71°).

According to reports by Wilson *et al.*, the growth rate per cycle for TiO$_2$ (precursor: TTIP) deposited by ALD at 200 °C was *ca.* 0.4 Å/cycle.[151] For the films reported herein for **Study B**, growth rates per cycle were 1 Å/cycle at significantly lower temperatures indicating CVD-like growth rates. During this study, a pre-trial was carried out where only Si wafers were inserted into the ALD rig and the bubbler temperature was set to *ca.* 90 °C (lower relative to **Study A**) leading to a uniform deposition across the wafer. However, on insertion of the **SH** films, the deposition

rate fell significantly, restricting the TiO_2 deposition only to the planar Si wafers. A rationale for this was that the superhydrophobic thin films have significantly higher surface areas than Si wafers.[152] As a result, the bubbler temperature was increased to *ca.* 100 °C and the ozone purge time was also reduced to speed up the deposition process. Hence CVD-like growth occurred due to not completely purging the ozone by reducing the purge time too far.

All the **SH** films surface tuned by TiO_2 via ALD (**SH/TiO₂/xC**) were characterised by analytical and chemical techniques using XPS, PXRD, FTIR, Raman and SEM/EDS. Functional and performance testing (e.g. self-cleaning and photocatalytic testing) were primarily carried out on films **SH/TiO₂/1000C** and **SH/TiO₂/1000C/N-P**. Photographs of the films of **Study A** were taken to visualise the change in film colour as a function of cycle numbers/film thickness, **Figure 4.02**. Films **TiO₂/600C** and **TiO₂/900C** were very dark in colour potentially indicating high growth rates. Interestingly, the colours of the **SH/TiO₂/xC** films remained relatively unchanged, except for a gold tinge on films **SH/TiO₂/600C** and **SH/TiO₂/900C**.

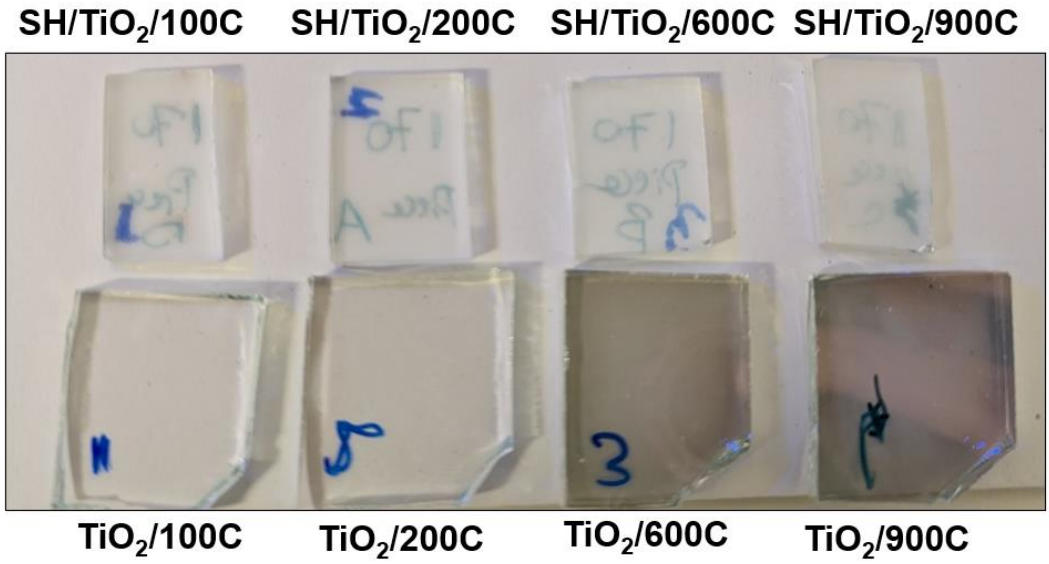

Figure 4.02. *Photographs of the films of* ***Study A****. From left to right, films* ***SH/TiO₂/100C****,* ***SH/TiO₂/200C****,* ***SH/TiO₂/600C*** *and* ***SH/TiO₂/900C*** *along with their respective counterparts deposited on a plain FTO glass substrate.*

Due to difficulty in determining the successful deposition of TiO_2 by visual inspection, XPS was carried out on all films. An example scan of film **SH/TiO₂/1000C** can be seen in **Figure 4.03**. Potential deviances in the fitting of the O 1s were due to the C 1s and Si 2p of the superhydrophobic underlayer and

were overlooked in the O1s fitting; oxygen bound to carbon or to silicon would contribute to the O 1s spectrum, but these contributions have not been fitted. For **Figure 4.03(a)**, the O 1s spectrum had two environments at 529.9 eV and 531.0 eV, which were indicative of O-Ti and adsorbed water, respectively. Apart from the Ti 2p scan, the best indication of film thickness was to study the Si 2p intensity. In this case, the Si 2p, **Figure 4.03(b)**, was very low and almost immeasurable relative to that of the uncoated **SH** film (**Chapter 2, Figure 2.02**). In these cases, it was assumed that the Si signal pertained to the superhydrophobic coating. The films (except film **SH/TiO_2/100C**) were sufficiently thick (> 5 nm as XPS has an analysis depth of approximately 5 nm for the aluminium source used here), indicating that there was no Si breakthrough to the underlying superhydrophobic film. For **Figure 4.03(c)**, the C 1s spectrum, the peak at 285 eV was indicative of organic carbon and was used to calibrate all other spectra. **Figure 4.03(d)**, the Ti 2p scan, confirmed that Ti was equivalent to Ti^{4+} by the positioning of the $2p_{3/2}$ peak at 458.4 eV.[122,123] The XPS spectra were in line with the literature and TiO_2 films deposited via AACVD (**Chapter 3, Figure 3.03**) indicating successful TiO_2 surface modification.

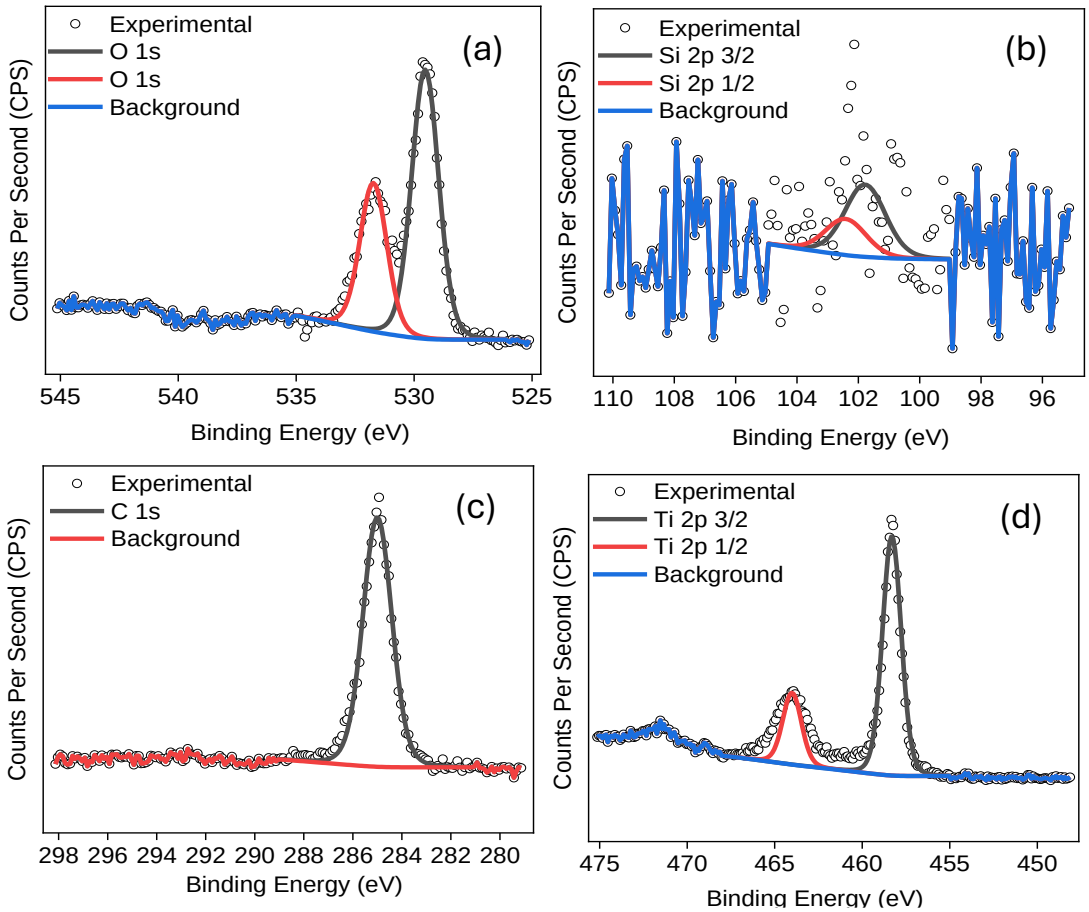

Figure 4.03. *XPS scans for film* ***SH/TiO₂/1000C*** *(a) O 1s (b) Si 2p (c) C 1s and (d) Ti 2p.*

The WCAs were contextualised by graphically plotting these with the raw peak area ratios of Ti/Si against the ALD cycles, **Figure 4.04**. In general, as the cycle number increased the Ti/Si raw peak area ratio also increased. This trend line is smoother than for the **SH/TiO₂** films deposited via AACVD **(Chapter 3)** which corroborated the improved deposition control with the ALD process. The range of the Ti/Si raw peak area ratios *(ca.* 0 – 30) were lower than for the **SH/TiO₂** films deposited via AACVD (*ca.* 0 – 90) confirming that thinner TiO_2 films were deposited via ALD relative to AACVD. In addition, the WCAs decreased as a function of increased cycle numbers which was also the case for the **SH/TiO₂** films from **Chapter 3**. However, the points at 100 cycles and 200 cycles (i.e. films **SH/TiO₂/100C** and **SH/TiO₂/200C**) were inconsistent with the trend confirming some patchiness however, this inconsistency was accommodated for in the standard deviation of the WCA. For the **SH/TiO₂** films deposited via ALD, the Ti/Si ratio of 30 achieved a WCA of 70°. However, for the **SH/TiO₂** films deposited via AACVD (**Chapter 3**), a Ti/Si ratio of 30 resulted in a WCA of 140°.

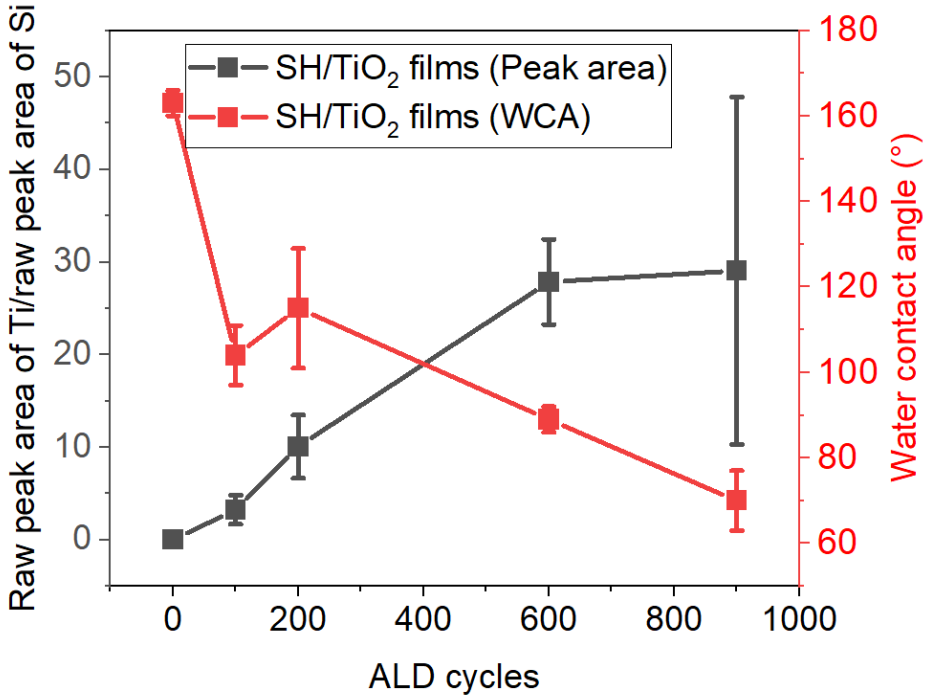

Figure 4.04. *A graph showing the relationship between the water contact angle and raw peak area of Ti and Si generated from XPS vs. ALD cycles.*

FTIR scans of the superhydrophobic undercoat and TiO_2 surface modified **SH** film (**SH/TiO₂/1000C)** was taken and are presented in **Figure 4.05**. Peaks within the 800 – 400 cm^{-1} section of the spectrum were indicative of stretching vibrations for the Ti-O-Ti bridge and Ti-O stretching mode.[120] For film **SH/TiO₂/1000C**, the majority of the peaks pertaining to the superhydrophobic underlayer discussed in **Chapter 2** were not present (except for the peak at 2950 cm^{-1} representing sp^3 C-H) due to the thickness of the TiO_2 coating.[95]

Raman spectroscopy for **Study B**, **Figure 4.06** confirmed the successful deposition of TiO_2 (anatase) by the emergence of peaks at 142 cm^{-1}, 197cm^{-1}, 395 cm^{-1}, 515 cm^{-1} and 636 cm^{-1} Both sets of peaks were present in the plasma and non-plasma treated films **SH/TiO₂/1000C** and **SH/TiO₂/1000C/N-P**, respectively. However, clear signals were not present in the Raman spectrum of the **TiO₂/1000C** film even though peaks were present in the PXRD pattern, **Figure 4.07**. This could have potentially been due to scanning a different part of the film. Ekoi *et al.* demonstrated that increased surface roughness increased the Raman intensity of a TiO_2 film.[153] Although films **SH/TiO₂/1000C** and **SH/TiO₂/1000C/N-P** both had Sq values of 0.25 µm, the former had a larger standard deviation, indicating that some areas of the film had Sq values >0.25 µm. As well as a potentially higher roughness value, film **SH/TiO₂/1000C** also

exhibited a higher Raman intensity, **Figure 4.06**, corroborating the findings of Ekoi *et al*.[153]

In addition, a PXRD pattern of film **SH/TiO₂/1000C** of **Study B** was generated and compared to a reference TiO_2 pattern for anatase (**ICSD: 063711**) to also verify the successful deposition of TiO_2 via ALD, **Figure 4.07**. The main peaks pertaining to TiO_2 (anatase) were present although at lower intensities relative to the **SH/TiO₂** films deposited via AACVD (**Chapter 3, Figure 3.07**). These peaks were at 25.2°, 37.2°, 37.9°, 38.7°, 48.1°, 53.9°, 55.1°, 62.8°, 68.9° and 70.4°.[127] For the **SH/TiO₂/xC** films, the signal intensity was relatively lower than for the **SH/TiO₂** films; for the former, the baseline was noisier than for the latter, reducing the overall signal intensity. The rationale for this difference related to film thickness.

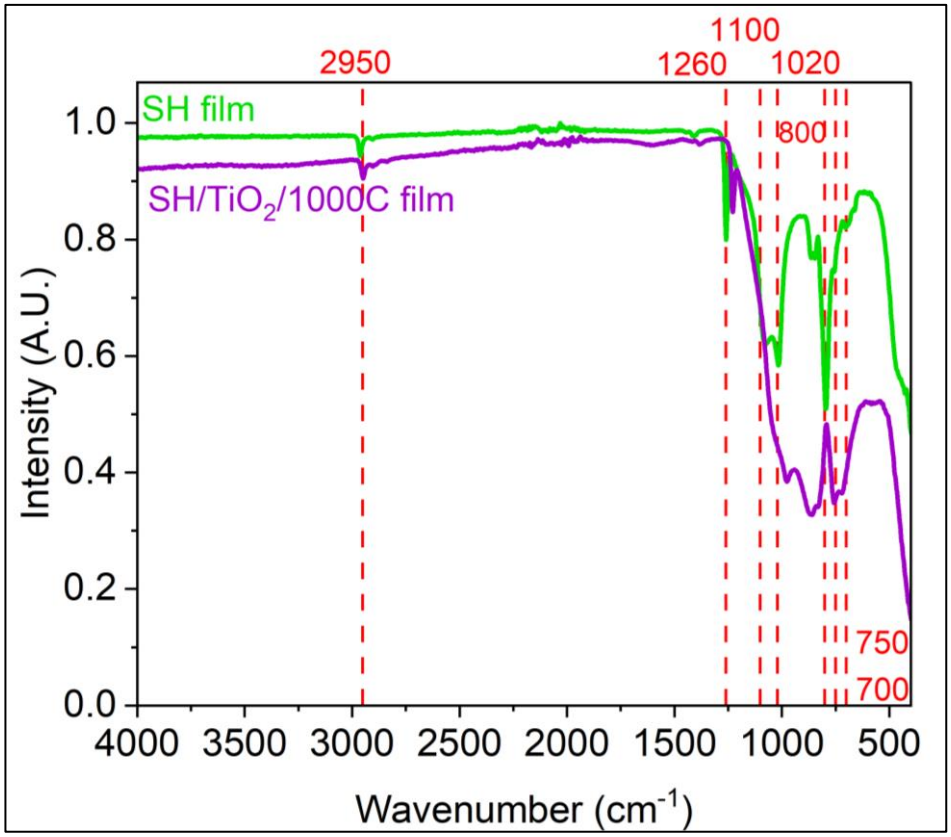

Figure 4.05. *Combined FTIR spectrum of films* ***SH*** *and* ***SH/TiO₂/1000C*** *after surface modification with TiO_2 via ALD.*

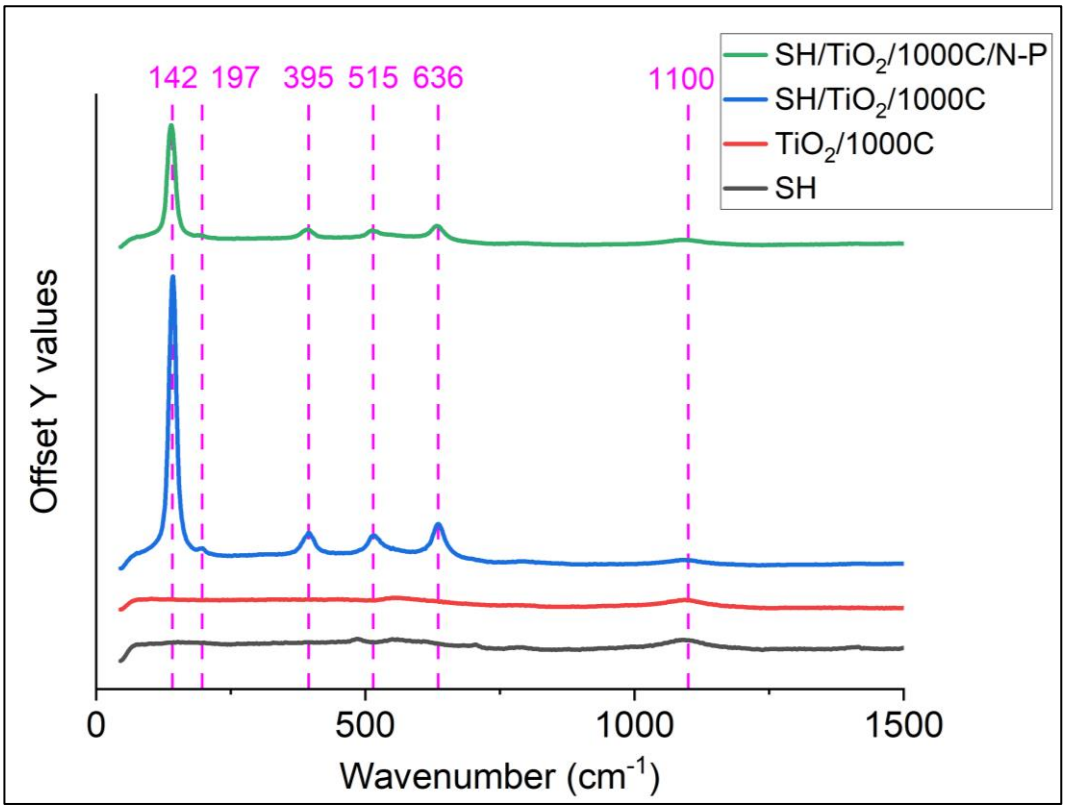

Figure 4.06. *Combined Raman spectrum for* ***Study A****, films* ***SH/TiO₂/1000C/N-P****,* ***SH/TiO₂/1000C****,* ***TiO₂/1000C*** *and the uncoated* ***SH*** *film.*

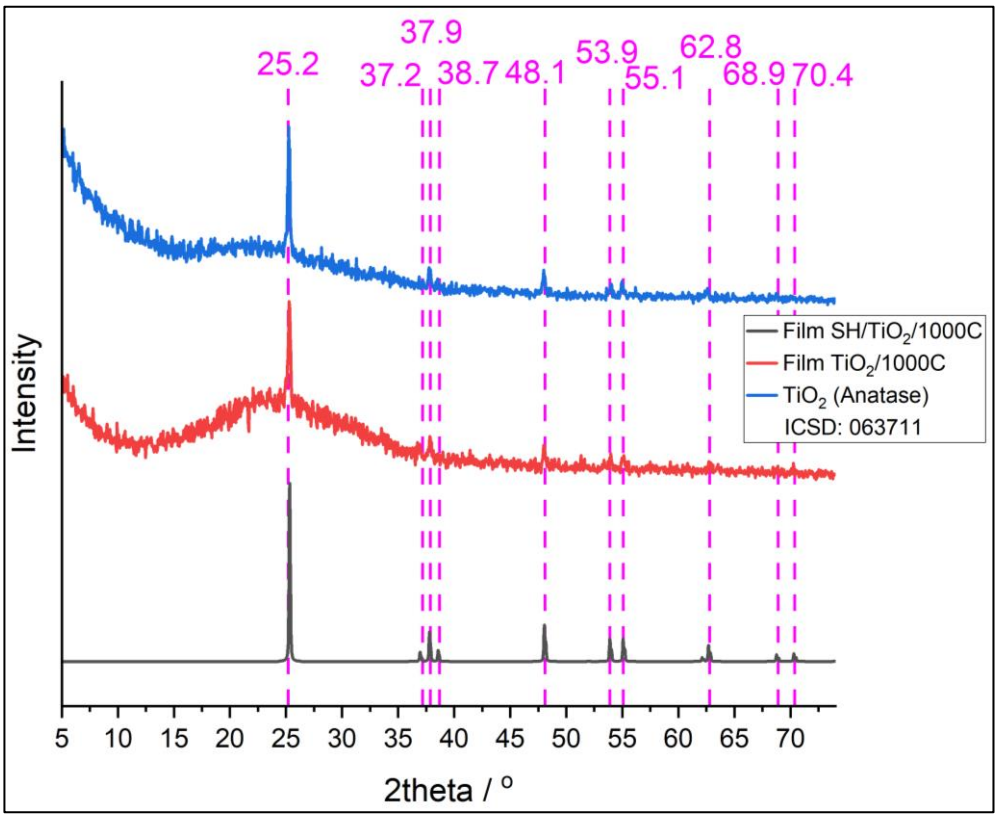

Figure 4.07. *PXRD patterns of the thickest TiO_2 film, film* ***SH/TiO₂/1000C*** *(blue) and film* ***TiO₂/1000C*** *(red), both compared to TiO_2 Anatase reference pattern (****ICSD: 063711****).*

SEM images only of the films of **Study B** were taken as they had the thickest TiO_2 films (films **TiO_2/1000C**, **SH/TiO_2/1000C** and **SH/TiO_2/1000C/N-P**), **Figure 4.08**. The deposited TiO_2 films of **Study A** were ultrathin and hence could not be seen even at high magnification owing to their conformality, featureless nature and thinness. Therefore, it was difficult to conclusively identify TiO_2 deposition for these films.

The large particle on the right of **Figure 4.08(a)** was due to carbon coating as this was on top of the suspected TiO_2 layer, which was carried out to increase the electrical conductivity. An FTO glass substrate was carbon coated and imaged for comparison to affirm these conclusions. Nevertheless, the cracking on the right of the same figure suggested a TiO_2 layer. Abendroth *et al.* deposited TiO_2 also using TDMAT via ALD at various temperatures and the subsequent SEM image taken for the film deposited at 250 °C contained cracks which can also be seen on the top right of **Figure 4.08(a)**.[150]

Szindler *et al.* also deposited TiO_2 onto glass substrates at 300 °C which had a grainy morphology which was also visible for film **TiO_2/1000C**, **Figure 4.08(b)**.[146] The **SH/TiO_2** films deposited via AACVD (**Chapter 3, Figure 3.08**) contained TiO_2 clusters which increased with increasing TTIP concentration however, the **SH** films modified with TiO_2 via ALD were featureless. The aerosol droplets of the TTIP precursor through the AACVD process could have generated the TiO_2 clusters, leading to a rough morphology, whereas the conformality of ALD created a film that thinly coated over the **SH** film.[64] Although film **SH/TiO_2/0.4** was estimated to have a thickness of *ca.* 80 nm, it presented a similar morphology to the films in **Figure 4.08.**

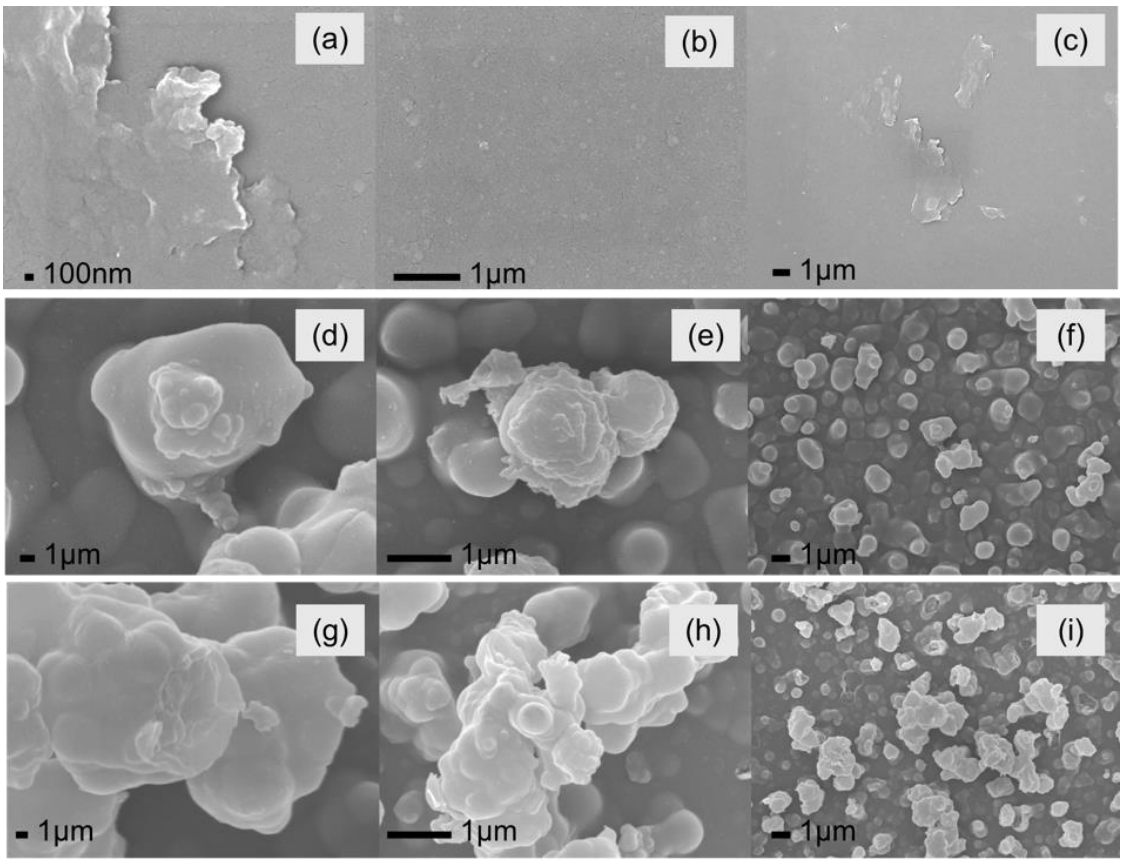

Figure 4.08. *SEM images (a) – (c) are of film* ***TiO₂/1000C****, (d) – (f) are of film* ***SH/TiO₂/1000C*** *and (g) – (i) are of film* ***SH/TiO₂/1000C/N-P****.*

The Sq roughness values for the **SH/TiO₂/0.4** and **SH/TiO₂/1.4** films from AACVD (**Chapter 3, Table 13**) ranged from 0.27 µm to 0.18 µm, respectively. On the other hand, the **SH/TiO₂/100C** and **SH/TiO₂/1000C** films had consistent roughness values of 0.25 µm, initially reduced from 0.28 µm for the **SH** film, **Table 15**. This also confirmed that the ALD TiO_2 coatings were conformal and that the nanoscale changes were not precisely detected due to being out of the detection limit of the microscope. Szindler *et al.* also saw minimal changes in roughness on depositing TiO_2 via ALD (precursor: $TiCl_4$).[146] A film of 630 cycles had a Sq value of 0.00252 µm which fell to 0.00118 µm by 1030 cycles, suggesting a reduction in roughness with increasing TiO_2 film thickness. As TiO_2 ALD films were generally featureless, it was difficult to visualize changes in the morphologies post-deposition. As a result, EDS scans were taken and overlayed onto SEM images of the morphologies, to put the electron images into context.

It is important to note that EDS penetrates a material much more deeply than XPS. As a result, the substrate in addition to the underlying film may be scanned. Hence the resulting scans would display no clear structure once overlayed onto the SEM morphology scans or it may be seen in the EDS map sum

spectrum.[120,146] This can be visualised in the Si Kα EDS scans of all films and the and O Kα EDS scan of film **TiO$_2$/1000C** in **Figure 4.09**.

All films in **Figures 4.09, 4.10** and **4.11** proved successful carbon coating, which was necessary to prevent charging or damage of the film by the electron beam during the scans. Interestingly, the Ti wt% for film **SH/TiO$_2$/1000C/N-P** was higher (23%) than for film **SH/TiO$_2$/1000C** (21%). Although this Ti wt% difference was small it is interesting as it was initially hypothesized that plasma treatment would improve the TiO_2 coverage as this was the case for the **SH/TiO$_2$** films from (**Chapter 3**). However, it may have been that the reactivity of the TDMAT precursor was such that plasma treatment was not necessary. TDMAT is generally known to be more reactive than TTIP due to its amine groups. TDMAT could adequately react with the C-**H**/**O**/**Si** active groups of the **SH** film; the precursor may have reacted better with the active groups over the hydroxyl groups which are usually generated during plasma treatment, making the resulting film superhydrophilic.

The O Kα scans of film **SH/TiO$_2$/1000C**, **Figure 4.10**, illustrated that the oxygen (either from the **SH** or TiO_2 film) was concentrated on the agglomerated particles. For film **SH/TiO$_2$/1000C/N-P**, **Figure 4.11**, O was also concentrated on the particles however, shadowing effects were more pronounced for this film. Shadowing effects for the O Kα scans were also visualised in the **SH/TiO$_2$** films deposited via AACVD (**Chapter 3, Figure 3.17**). The reason the shadowing effect may have been seen in film **SH/TiO$_2$/1000C** rather than film **SH/TiO$_2$/1000C/N-P** is because there was a greater Ti wt% in the latter. More TiO_2 could have led to greater reabsorption of some of the emitted X-rays.[120]

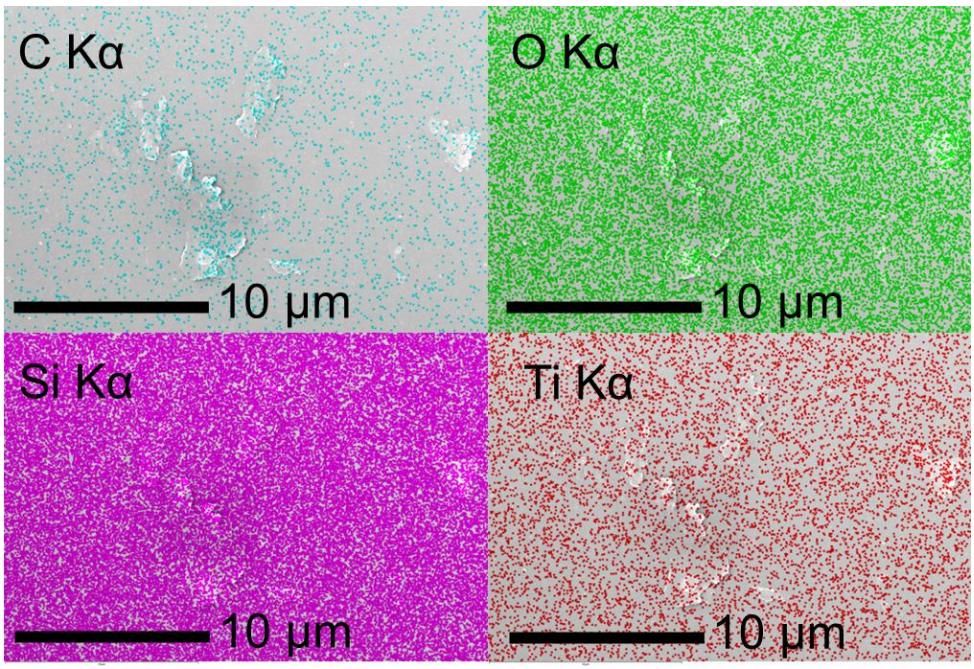

Figure 4.09. *C Kα, O Kα, Si Kα and Ti Kα EDS scans of film* ***TiO_2/1000C****.*

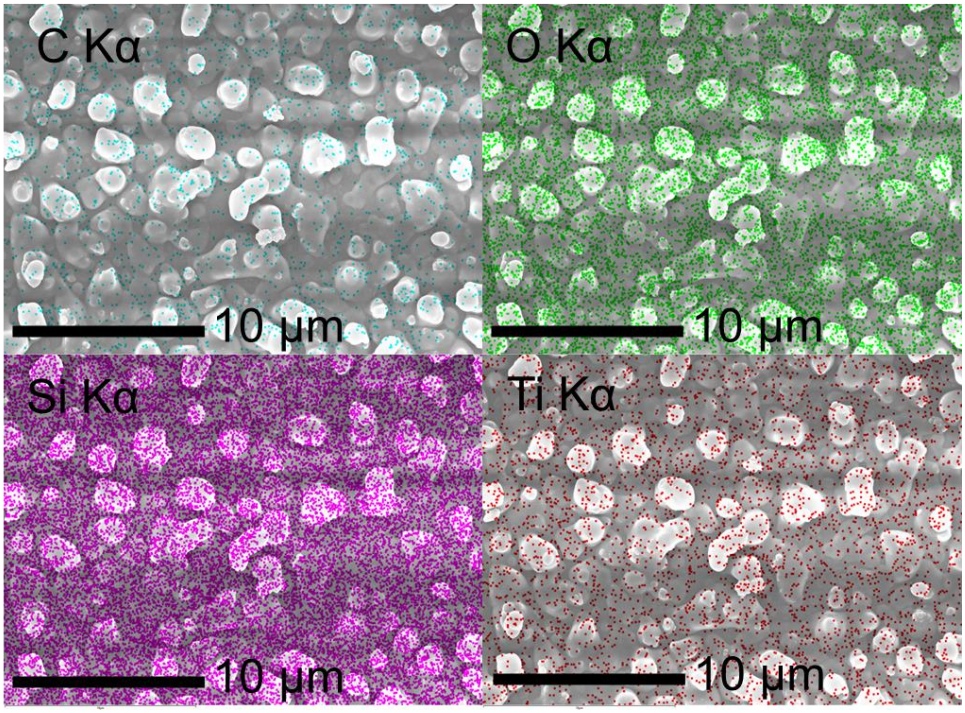

Figure 4.10. *C Kα, O Kα, Si Kα and Ti Kα EDS scans of film* ***SH/TiO_2/1000C****.*

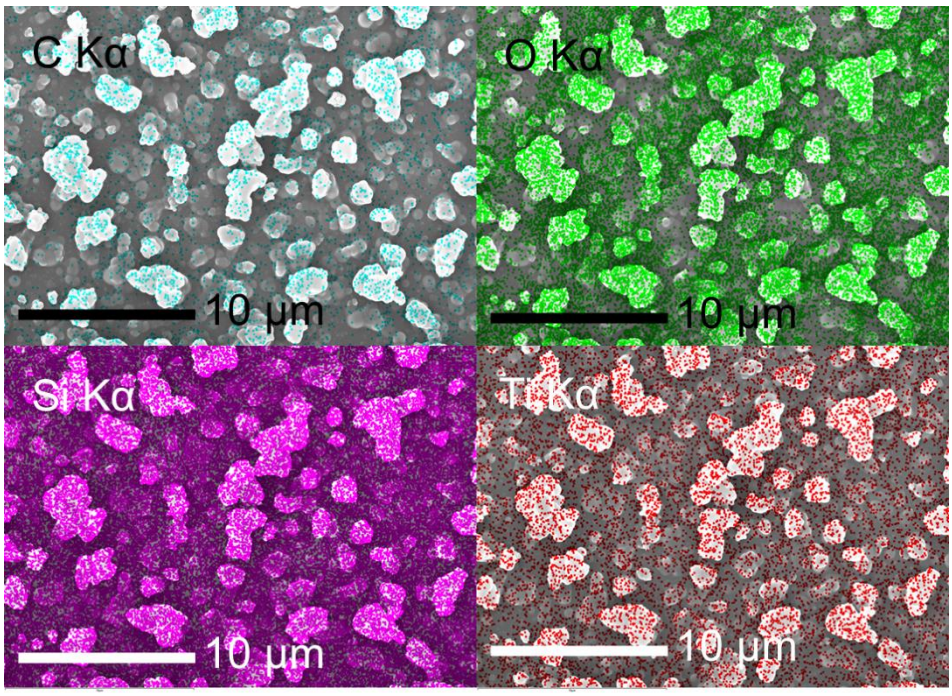

Figure 4.11. *C Kα, O Kα, Si Kα and Ti Kα EDS scans of film* ***SH/TiO₂/1000C/N-P****.*

4.5 Functional, Durability and Performance Testing

Films **SH**, **SH/TiO₂/1000C/N-P**, **SH/TiO₂/1000C** and **TiO₂/1000C** were tested for their photocatalytic activity by measuring the reduction in stearic acid coverage, **Figure 4.12**. Interestingly, the **SH** film had the greatest reduction in stearic acid coverage due to the stearic acid already being incorporated in the **SH** film. The stearic acid was most probably deposited on the nano-/micro-particles, increasing its exposed surface area. Of the two **SH** films modified with TiO_2 via ALD, film **SH/TiO₂/1000C/N-P** had the highest reduction in stearic acid coverage (*ca.* 92% reduction by 30 h). This could be due to having more TiO_2 on the surface to facilitate electron-hole transportation through the film especially because TiO_2 is highly absorbing of UV light.[154] By 30 h, film **SH/TiO₂/1000C** only had a reduction in stearic acid coverage of *ca.* 16%.

Interestingly, both films **SH/TiO₂/1000C** and **SH/TiO₂/1000C/N-P** had higher stearic acid coverage reductions than film **TiO₂/1000C**. This confirmed that the superhydrophobic underlayer aided the photocatalytic activity by increasing the film's surface area although the exact mechanism is unclear.[120] In some cases, the stearic acid coverage exceeded 100% due to noise from the instrument. Nonetheless, the **SH/TiO₂** films fabricated via AACVD (**Chapter 3**) demonstrated higher photocatalytic activity than film **SH/TiO₂/1000C** due to the TiO_2 film being

thicker. A 42% and 52% reduction in stearic acid coverage by 30 h was observed for films **SH/TiO_2/0.4** and **SH/TiO_2/1.4**, respectively. All three films (**SH/TiO_2/1000C, SH/TiO_2/0.4** and **SH/TiO_2/1.4**) not only had the superhydrophobic underlayer but were also plasma treated prior to the TiO_2 deposition. Therefore, reductions in stearic acid coverage may have been due to the morphology of the as-deposited TiO_2 films. The TiO_2 agglomerates for the AACVD films may have increased the overall surface area more, relative to the conformal TiO_2 film deposited via ALD, despite film **SH/TiO_2/0.4** having a thinner coating (*ca.* 80 nm) than film **SH/TiO_2/1000C** (*ca.* 100 nm). This rationale is verified by the featureless TiO_2 film deposited via ALD, **Figure 4.08**. Thickness of the TiO_2 coatings may have played a small part in the photocatalytic activity of the films. Dundar *et al.* deposited TiO_2 via ALD and found that films that were 170 – 230 nm displayed the highest photocatalytic activity.[133] Therefore, film **SH/TiO_2/1.4**, estimated to have a TiO_2 film that is 510 nm thick, had the highest reduction in stearic acid coverage after 5 h. However, relative to the **SH/TiO_2/1.4** film, film **SH/TiO_2/1000C/N-P** demonstrated a lower reduction in stearic acid coverage (by 5 h), potentially due to the deposition of a thicker TiO_2 film, assumed to be 510 nm. This can be explained by the differences in TiO_2 film thickness which were corroborated by the Ti/Si ratios which were used as an indirect measure of TiO_2 film thickness. Film **SH/TiO_2/1.4** had a Ti/Si ratio of 90 and film **SH/TiO_2/1000C/N-P** had a Ti/Si ratio of 51.

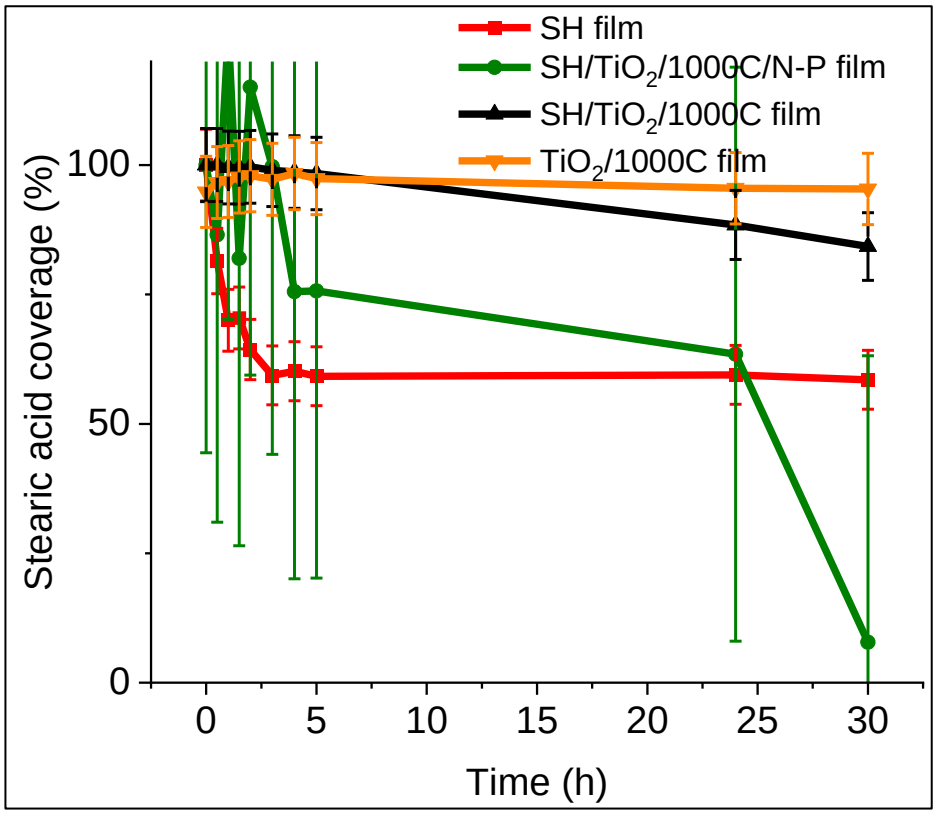

Figure 4.12. *The changes in stearic acid coverage determined by the stearic acid degradation test (a measure of photocatalytic activity) for films* ***SH***, ***SH/TiO₂/1000C/N-P***, ***SH/TiO₂/1000C*** *and* ***TiO₂/1000C****.*

The CAH, a determination of a film's homogeneity, mobility and roughness was measured for films **SH/TiO₂/xC** and **TiO₂/xC**, **Table 15.** Interestingly, as the thickness of the TiO_2 films increased so did the CAH, contrary to the **SH/TiO₂** films deposited via AACVD. These differences may have been due to the morphological changes and formation of 'pointy' TiO_2 clusters generated by AACVD which may have decreased the roughness but increased the mobility of the TiO_2 NPs. On the other hand, the ALD TiO_2 films may have had featureless, conformal TiO_2 films, a slight decrease in roughness but a decrease in mobility due to conformally covering the low surface energy components and hierarchical roughness. TiO_2 has a high surface energy of 1.28 J/m^2 in comparison to SYLGARD 184 (surface energy 0.019 – 0.021 J/m^2).[19,128] This reduction in mobility across the film was confirmed by the increase in sliding angles for both films **SH/TiO₂/1000C** and **SH/TiO₂/1000C/N-P** and can be visualised in **Figure 4.13**. Both films displayed similar water repellence patterns and hence only photographs for film **SH/TiO₂/1000C** have been included in the figure.

Methylene blue water droplets were manually pipetted onto the films at a tilted angle. These water droplets pinned to the surface of the film, forming an irregularly shaped sphere. In both cases, although the water droplet eventually slid down the material's surface, subsequent methylene blue drops on the same area were completely immersed in the droplet's water trail. As a result, they did not slide off in the form of an irregularly shaped droplet, as previously described. The methylene blue droplet only regained its pinned-spherical shape on reaching a dry part of the film. This wetting behaviour was in between that of films **SH/TiO$_2$/0.4** and **SH/TiO$_2$/1.4**, deposited via AACVD (**Chapter 3, Figure 3.19**). The water repellence was poorer than that of film **SH/TiO$_2$/0.4**, with more pinning to the surface**.** Although the water repellence was better than that of film **SH/TiO$_2$/1.4**, with faster movement of the water-based methylene blue droplet. Nevertheless, in both cases, the **SH** films modified with TiO_2 via ALD demonstrated poorer physical self-cleaning properties than the unmodified **SH** film.

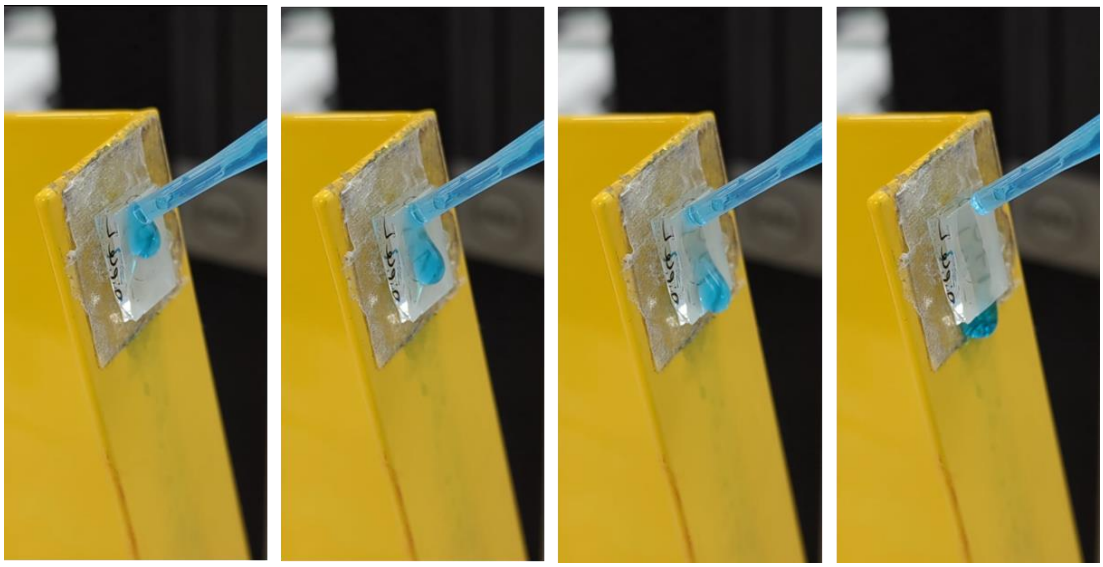

Figure 4.13. *The visual representation of the water repellence of films* ***SH/TiO$_2$/1000C*** *using methylene blue.*

Initially, the heat durability of the films was investigated by exposing films **SH/TiO$_2$/1000C** and **SH/TiO$_2$/1000C/N-P** to 300 °C of heat for 5 h. After heat-treatment, film **SH/TiO$_2$/1000C/N-P** became superhydrophilic. However, film **SH/TiO$_2$/1000C** became hydrophobic with a WCA of 122 ± 0°. It was challenging to record the CAH of film **SH/TiO$_2$/1000C/N-P** due to its superhydrophilicity. However, after heat treatment for film **SH/TiO$_2$/1000C**, the CAH increased from 22 ± 6° to 28 ± 8° indicating increased roughness, potentially due to the

absorption of hydrocarbons during the cooling process, considering that it had a lower wt% of Ti than the non-plasma treated film. Hydrocarbons induce hydrophobicity as they have a low surface energy and contribute to the roughness.[120,110] The sliding angle of the same film reduced to 24 ± 1°. Han *et al.* utilised a sputtering technique on glass substrates to afford TiO_2 thin films which were heat-treated at 400 °C for 30 min.[155] The treated films also became hydrophilic with the WCA dropping from 66° to 21° due to the removal of organic compounds.

The plasma and non-plasma treated TiO_2 films from **Study B** were also irradiated with UV light with WCAs measured every day for a 7-day period, **Figure 4.14**. Intriguingly, the WCA of film **SH/TiO_2/1000C** reduced significantly from 96° to 38° by Day 5 of UV exposure. Due to the ultrathin TiO_2 film (100 nm on Si wafers), there may have been bidentate bonding of the Ti^{4+} and O^{2-} vacancies to the fatty acid and other organic components (both either from the film or the atmosphere) and subsequently, photocatalytic decomposition of these components. Nevertheless, this decrease in WCA was considerably less than that of film **SH/TiO_2/1000C/N-P** which exhibited a slower decrease in WCA from 91° to 74° by Day 4 of exposure but a relatively large standard deviation (error) of *ca.* 21°. This large error compensated areas of the film that had become hydrophilic due to the Ti^{4+} and O^{2-} bidentate bonding, areas that were not affected by UV irradiation and areas with exposed parts of the superhydrophobic underlayer. In comparison to the **SH/TiO_2** films deposited via AACVD of **Chapter 3**, film **SH/TiO_2/1000C/N-P** displayed a greater decrease in WCA (94°), a contrast to films **SH/TiO_2/0.4** (16° reduction) and **SH/TiO_2/1.4** (36° reduction). Jang *et al.* deposited 16 nm TiO_2 films by ALD which became superhydrophilic after <10 min of UV irradiation (3 mW/cm^2).[149] Although the TiO_2 films fabricated in this chapter were estimated to be *ca.* 5x thicker (when comparing the measured TiO_2 thickness deposited on a Si wafer) and irradiated under extremer conditions (260 mW/cm^2 of UV light for 7 days), the dual-layered **SH/TiO_2** films may have provided some protection to the TiO_2 coating. By the end of the 7 days of UV irradiation, the CAH of film **SH/TiO_2/1000C** was immeasurable and for **SH/TiO_2/1000C/N-P**, it reduced slightly to 31 ± 7°.

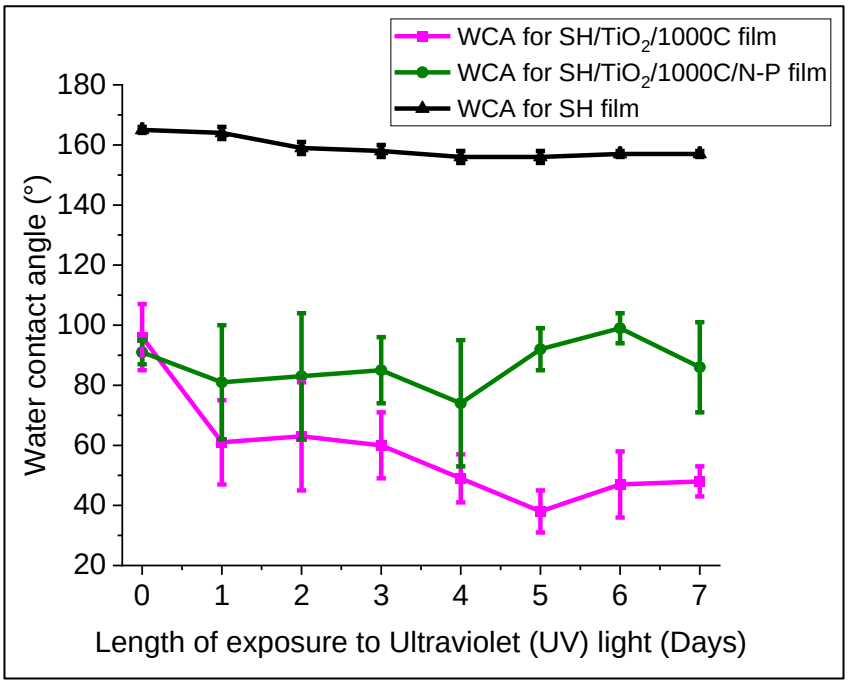

Figure 4.14. *Changes in WCA on irradiation with UV for 7 days.*

To determine the mechanical durability of the films, pencil hardness testing was carried out. The tolerable hardness for films **SH/TiO$_2$/1000C** and **SH/TiO$_2$/1000C/N-P** were the same as that of the uncoated **SH** film, potentially due the TiO$_2$ film being ultrathin (*ca.* 100 nm thick).[95] In contrast, the **SH/TiO$_2$/1.4** films tolerated a greater degree of hardness (>6H) potentially due to the TiO$_2$ film being thicker, providing several layers of thickness.

The WCAs were periodically measured prior to, during and after the tape peel test, **Table 16**. For comparison, the WCAs recorded prior to, and post-tape peel cycles were subtracted from each other. Film **SH/TiO$_2$/1000C** had a difference of 17° and film **SH/TiO$_2$/1000C/N-P** had a difference of 46°. The non-plasma treated **SH/TiO$_2$** ALD film exhibited a drastic reduction in WCA, potentially due to the films being slightly thicker, giving the higher recorded Ti wt % than the plasma-treated equivalent (**SH/TiO$_2$/1000C**). In both cases, this reduction in WCA was greater than for the uncoated **SH** film which retained superhydrophobicity after 300 tape peel cycles.[95] This may have been because the TiO$_2$ was strongly chemically attached (chemisorbed) to the superhydrophobic underlayer which was confirmed by the WCA never becoming >150° at any point during the tape peel cycle, confirming that the **SH** film was well adhered to the TiO$_2$ film.

As a result, the adhesive tape pulled off the whole film rather than sections of TiO$_2$. Zhang *et al.* experimentally demonstrated via tape peel testing the strong

adhesion for a composite consisting of an ALD deposited TiO_2 film that was sandwiched between a microporous substrate and silica film.[140] For both films **SH/TiO_2/1000C** and **SH/TiO_2/1000C/N-P**, the CAH decreased, revealing of reduced roughness and increased homogeneity. The decline in WCA was not continuous with occasional increases in WCA, potentially due to exposure of areas of the hierarchical roughness.

Relative to the **SH/TiO_2** films deposited by AACVD after 400 tape peel cycles (**Chapter 3, Table 14**), the **SH/TiO_2/1000C** film exhibited a 1° lower WCA than for film **SH/TiO_2/0.4** but a 4° higher WCA after the 400 tape peel cycles for film **SH/TiO_2/1.4**. Film **SH/TiO_2/1000C/N-P** had a 28° reduction in the final WCA after 400 tape peel cycles relative to film **SH/TiO_2/0.4** which had a 18° drop in the final WCA. Potential differences in reductions in WCA may have been due to the reactivity of the precursors leading to different levels of attachment as well as the deposition processes (ALD vs. AACVD) leading to different morphologies of the deposited TiO_2 film.

Table 16. *Changes in WCA for films* ***SH/TiO$_2$/1000C*** *and* ***SH/TiO$_2$/1000C/N-P*** *during the tape peel test.*

Cycle number	**Water contact angle (°)**	
	Film **SH/TiO$_2$/1000C**	Film **SH/TiO$_2$/1000C/N-P**
Before test	63 ± 1	84 ± 2
After 5 cycles	58 ± 1	90 ± 7
After 10 cycles	63 ± 0	70 ± 4
After 15 cycles	61 ± 5	56 ± 18
After 20 cycles	62 ± 3	55 ± 8
After 25 cycles	61 ± 4	36 ± 3
After 30 cycles	61 ± 5	48 ± 8
After 40 cycles	56 ± 2	49 ± 13
After 50 cycles	56 ± 1	45 ± 13
After 75 cycles	53 ± 5	38 ± 1
After 100 cycles	44 ± 2	48 ± 13
After 125 cycles	43 ± 0	37 ± 5
After 150 cycles	42 ± 1	47 ± 11
After 175 cycles	39 ± 3	35 ± 3
After 200 cycles	39 ± 1	45 ± 6
After 250 cycles	43 ± 0	38 ± 0
After 300 cycles	40 ± 0	43 ± 7
After 350 cycles	44 ± 3	33 ± 0
After 400 cycles	46 ± 1	38 ± 4
CAH	20 ± 15	20 ± 12

4.6 Summary

TiO_2 via a TDMAT precursor were deposited onto **SH** films via ALD by two routes. The first study (**Study A**) looked at changes in properties, namely wettability as the cycle number increased. The cycle numbers ranged from 100 to 1000 cycles and thicknesses ranged from *ca.* 4 nm to *ca.* 41 nm. For **Study A**, the WCAs of the TiO_2 modified **SH** films ranged from 104° (100 cycles) to 70° (900 cycles).

The second study (**Study B**) investigated the deposition of a set number of cycles (1000 cycles) onto plasma and non-plasma treated **SH** films. For each deposition, there were variations in deposition/bubbler temperatures and precursor and ozone purge pulses. Here, the films were expected to have *ca.* 100 nm deposited on the **SH** film, with WCAs ranging from 64° for film **SH/TiO_2/1000C** to 71° for film **SH/TiO_2/1000C/N-P**. Although there were no clear morphological, chemical or analytical changes, there were differences in the functional, physical and chemical self-cleaning properties of the film on plasma treatment of the films. Unlike the **SH/TiO_2** films from **Chapter 3**, where TTIP was used, the ALD process was such that a non-plasma treated **SH** film was more preferable for surface modification by TiO_2 ALD than a plasma treated **SH** films.

In **Study B**, the as-deposited TiO_2 films indicated CVD-like growth rather than ALD-like growth due to the increased surface area of the **SH** films relative to the FTO glass substrates or Si wafers. This was confirmed by the calculated growth rate per cycle at the deposition temperature utilised. Nevertheless, the as-deposited TiO_2 films demonstrated conformal TiO_2 coatings, verified by the small standard deviations for the WCAs measured which were lower relative to the uncoated **SH/TiO_2** films of **Chapter 3**. XPS also demonstrated the significant reduction in measurable Si, pertaining to the **SH** film. In addition to XPS, Raman, FTIR and PXRD patterns confirmed the successful deposition of TiO_2 via ALD.

Interestingly, the plasma and non-plasma treated films of **Study B** demonstrated improved photocatalytic activity relative to film **TiO_2/1000C**. However, this enhancement was higher for film **SH/TiO_2/1000C/N-P** than for film **SH/TiO_2/1000C**, potentially due to the former having more Ti per unit area as demonstrated by EDS. Film **SH/TiO_2/1000C** demonstrated lower photocatalytic activity compared to the **SH/TiO_2** films. However, film **SH/TiO_2/1000C/N-P** exhibited higher photocatalytic activity by 30 h of UV irradiation relative to the

SH/TiO_2 films of **Chapter 3**. Despite the greater photocatalytic activity relative to the uncoated **SH** film, the self-cleaning and water repellence properties of the TiO_2 coated **SH** films worsened, with the methylene blue water droplets pinning to the surface. The sliding angles were high, reaching 36° for the films of **Study B**. The CAH also increased with increasing TiO_2 thickness due to reduced mobility across the films surface.

Functional testing was restricted to films **SH/TiO_2/1000C and SH/TiO_2/1000C/N-P** as it was hypothesised that the greatest changes to the functional properties would be observed in these films. Heat treatment affected the wettability of the plasma treated **SH** film with WCAs becoming immeasurable. Nevertheless, the non-plasma treated films saw an increase in WCA potentially due to the absorption of hydrocarbons, adding to the overall roughness. Again, UV irradiation reduced the WCAs of the plasma treated films however, the non-plasma treated films had gradual reductions and occasional increases in WCA. With respect to the tape peel cycles, both films had drastic reductions in WCA possibly demonstrating the strong adhesion between the superhydrophobic coating and TiO_2 film, causing the whole film to pull away from the FTO glass substrate. This may be true because TDMAT is a more reactive precursor than TTIP and the ALD process generated a TiO_2 film with a different morphology to the AACVD process.

Chapter 5 – CeO_2 Surface Modification of Fluorine-Free Superhydrophobic Coatings via AACVD

5.1 Background

Initially, superhydrophobic materials were primarily based on organic materials, displaying poor mechanical durability due to the low C-H bond enthalpy which can be broken at *ca.* 200 - 300 °C. This led to possible fractures in the coating thus water infiltration and damage to the underlying object. Consequently, inorganic, metal oxide (MO) reagents have been incorporated into superhydrophobic precursors (e.g. TiO_2/FAS) or deposited to produce pure separate films. There are limited reports on the incorporation of ceria in superhydrophobic films. In fact, it is difficult to generate hierarchical roughness with rare earth oxides, needed for these superhydrophobic surfaces therefore, current research has combined rare earth oxides with polymer based reagents.[156] An *et al.* spray-coated a mixture of PDMS and CeO_2 NPs surface modified with trimethoxy(1H,1H,2H,2H-heptadecafluorodecyl)silane onto carbon steel substrates.[157] The films demonstrated stability against sandpaper testing, UV exposure and retained superhydrophobicity at all tested pHs (pH = 1 – 14). The authors claimed that the CeO_2 NPs not only imparted roughness but also provided protection against corrosion due to cerium's inherent ability to inhibit corrosion. Interestingly, Oh *et al.* also spray-coated a mixture of a CeO_2 and PDMS hybrid and investigated potential self-healing properties.[156] Although slow, the CeO_2 films could return to their original hydrophobic state as they absorb volatile organic components from their surroundings. Hence, PDMS was incorporated not only as an adhesion promoter but also as a source of hydrocarbons for self-recovery of the films' superhydrophobicity.

Although most MO films possess greater physical durability, they are intrinsically hydrophilic hence, rare earth oxides have been studied as an alternative due to their inherent hydrophobicity.[158] CeO_2 is hydrophobic although the absolute cause of its hydrophobicity remains ambiguous. A proposed rationale is the electron-filled $5s^2p^6$ shielding the unfilled 4f orbital leading to limited polarity and no interaction between the water molecules and the full $5s^2p^6$ orbital or shielded and unfilled 4f orbital.[159] Therefore, the electrons from cerium are less likely to exchange with the water molecules to create hydrogen bonds which would create

a hydrated and hydrophilic CeO_2 structure. Alternatively, justifications relating to the geometry of the CeO_2 structures have been computationally derived. Carchini *et al.* reported the disparity between the lattice parameter of CeO_2 and ice molecules, with the former having a smaller value.[160] Therefore, water molecules cannot interact and surround CeO_2, limiting potential acid-base interactions which would induce hydrophilicity.

Ce-based precursors, used to deposit CeO_2 via vapour phase deposition techniques, have been studied briefly. Precursors such as cerium alkoxides and amides have low volatility.[161] Therefore, to improve the deposition for vapour phase depositions, fluorinated β-diketonates have been studied due to their improved volatility, heat and moisture stability. However, such precursors involves the use of fluorine and the inclusion of fluorine contamination in the final CeO_2 film.[162] Liang *et al.* fabricated CeO_2 films via Metal-Organic CVD using $[Ce(tmhd)_4]$ (where tmhd is tetrakis(2,2,6,6-tetramethylheptane-3,5-dionato), however, the precursor decomposed as temperatures exceeded 350 °C.[163] The $[Ce(fod)_4]$ (where fod is 1,1,1,2,2,3,3-heptafluoro-7,7-dimethyloctane-4,6-dione) precursor also demonstrated thermal instability and fluorine contamination in the final CeO_2 film, as well as pre-decomposition and repeatability issues.[162] Despite the improved volatility, the CeO_2 film-growth rates with the $[Ce(fod)_4]$ precursor remained low.

To surmount the low volatility and avoid the use of fluorinated precursors, research into the AACVD of $[Ce(thd)_4]$ (where thd is tetrakis(2,2,6,6-tetramethylheptane-3,5-dionato) was investigated, but the fims displayed limited durability. In addition, there were reports of incompatibility between precursors when co-deposition of $[Ce(thd)_4]$ with gold precursors was attempted, with Evans *et al.* co-depositing cerium dibenzoylmethane $[Ce(dbm)_4]$ and NH_4AuCl_4 to afford crystalline CeO_2 films with scattered Au NPs, displaying some catalytic activity.

Yasmeen *et al.* fabricated CeO_2 films via spin coating and spray coating of CeO_2 NPs.[164] These deposition methods were chosen as a simple and economical method to potentially replace toxic Teflon™ polymers. However, this route of deposition led to poor adhesion between the CeO_2 NPs and Si wafer because of the weak van der Waal forces. Hence, a binder was added to improve the adherence. It was evident from the tape peel test that the binder had improved

the overall durability of the film relative to its counterpart. Nevertheless, the binder had no impact on the WCA prior to testing.

In other works, there have been reports on combining TiO_2 and CeO_2 multi-layered films, primarily due to the photocatalytic properties of both metal oxides. Kumar *et al.* confirmed that the photocatalytic activity of CeO_2 was not on par with TiO_2, with the latter performing significantly better. Intriguingly, a combination of both metal oxides (a TiO_2 film on top of a CeO_2 film) did not enhance the photocatalytic activity primarily due to active site blockage for nucleation and film growth and some recrystallisation of the phases present within the thin film.[165] Ehsan *et al.* deposited a single CeO_2-TiO_2 precursor to enhance the overall photocatalytic activity of the resulting films.[166] AACVD was used to overcome the incompatibility of the precursors by using a mutually compatible solvent and improving the uniformity of the resulting film.

Common disadvantages of CeO_2 films included the lack of reproducibility of the films due to its complex structure, forming inhomogeneous films.[162]

5.2 Aims

Recent studies within the literature have shown that rare earth oxides possess some hydrophobicity, especially once deposited as a thin film. Apart from cerium dioxide's hydrophobicity, it has demonstrated chemical stability, all while being low cost. Therefore, the purpose of this research was to surface tune the fluorine-free superhydrophobic films fabricated in **Chapter 2**, with CeO_2 deposited by AACVD from cerium(IV) dibenzoylmethane [$Ce(dbm)_4$], dissolved in anhydrous toluene. Such dual-layered films displayed improved mechanical durability however reduced self-cleaning properties compared to the original superhydrophobic film. [$Ce(dbm)_4$] has a narrow vaporization window (as confirmed by previously published TGA and DSC characterisation) therefore, it decomposes quickly in the hot baffle blocking and stopping the overall deposition process.[167] Hence modifications were initially restricted to minimal changes of the [$Ce(dbm)_4$] precursor deposited by AACVD for a set deposition time (to prevent complete blockage).

Due to limited flexibility with varying the [$Ce(dbm)_4$] precursor, the number of layers of a known concentration of [$Ce(dbm)_4$] were instead deposited until the precursor was completely used up. It was assumed that increasing the number

of layers or the concentration would increase the thickness of the CeO_2 film. Effects on the morphology and functional properties (wettability and self-cleaning) as well as robustness were investigated and compared to their counterparts deposited on FTO glass (without the superhydrophobic undercoat) as well as the original **SH** film.

5.3 Experimental

Superhydrophobic films comprised of a hybrid of stearic acid and palmitic acid were deposited by AACVD and subsequently surface tuned by CeO_2. $[Ce(dbm)_4]$ was used due to its good solubility in toluene and reasonable deposition temperature of 450 °C.

5.3.1 Chemicals & Materials

Vinyl-terminated polydimethylsiloxane (PDMS) also known as SYLGARD™ 184 Silicone Elastomer Base along with its corresponding curing agent were purchased from Dow Corning. Aerosil OX50 SiO_2 nanoparticles (fumed) procured from Lawrence Industries. Palmitic acid (≥ 99%), stearic acid (reagent grade, 95%), 1,3-Diphenyl-1,3-propanedione (dibenzoylmethane) (98%), ammonium cerium(IV) nitrate (≥98.5%), sodium hydroxide pellets, anhydrous toluene (99.8%), ethanol (laboratory grade) and ethyl acetate (laboratory grade) were all acquired from Merck Chemicals. All chemicals were used as received. NSG provided SiO_2 barrier coated fluorine-doped tin oxide (FTO) glass substrates which were manually cut to 15 cm x 4 cm x 0.3 cm for AACVD.

Plasma treatment of the **SH** films was carried out with a HPT-100 Henniker plasma cleaner. All films were plasma cleaned for 4 min with 100% power and a N_2 carrier gas flow rate of 2 sccm.

5.3.2 Synthesis of the fluorine-free superhydrophobic film

The **SH** film was deposited as per **Chapter 3, Section 3.3.2**.

5.3.3 Synthesis of the $Ce(dbm)_4$ precursor

Sodium hydroxide pellets (0.76 g, 19 mmol) were added to distilled water (75 cm^3) and stirred vigorously for approximately 10 min. Dibenzoylmethane (4.04 g,

18 mmol) and ethanol (100 cm^3) were then added to the solution and stirred for 45 min at room temperature and pressure until it became a green solution. This was labelled as solution 1.

In a separate beaker, ammonium cerium(IV) nitrate (2.58 g, 4.7 mmol) was added to ethanol (50 cm^3) and dissolved for 5 min, forming a dark red solution. This was labelled as solution 2.

Solution 2 was added dropwise over a course of 10 min to solution 1, resulting in a deep red-brown suspension. The resulting mixture was initially stirred for 20 min at 50 °C and then stirred at room temperature for 20 min, affording a mixture of the $[Ce(dbm)_4]$ precursor. The mixture was washed with ethanol via centrifugation (4500 RPM) twice. The $[Ce(dbm)_4]$ solid was then placed on pieces of filter paper to dry by air for *ca.* 2 nights.

The solids on the filter paper were put in a round bottom flask and vacuum dried for *ca.* 4.5 h. A water bath at 45 – 50 °C. was used to speed up the drying process. A ^1H NMR spectrum was taken with chloroform-d as the solvent. ^1H NMR and FTIR values were in line with the literature.[167]

^1H NMR δ/ppm ($CDCl_3$, 400 MHz): 6.9 (s, 1H), 7.4 (m, 6H), 8.1 (m, 4H). FTIR values of $[Ce(dbm)_4]$ precursor: 1588, 1517, 1476, 1453, 1439, 1378, 1353, 1308, 1286, 1223, 1180, 1157, 1123, 1098, 1064, 1023, 1000, 966, 939, 925, 835, 812, 786, 749, 712, 682, 602, 510.

5.3.4 Surface Modification of the SH film with CeO_2 via AACVD

Study 1: Deposition of variable $[Ce(dbm)_4]$

$[Ce(dbm)_4]$ (A g) was dissolved in dry toluene (B cm^3) and left to sonicate for approximately 35 min. The concentrations used are listed in **Table 17**.

The **SH** films described in **Section 5.3.2** were plasma treated (duration: 4 min; carrier gas flow rate: 2 sccm). The film became superhydrophilic by the end of the plasma treatment and each film was re-inserted into the AACVD rig with the **SH** film on the carbon block (bottom plate) and an FTO substrate used as a top plate for by-product deposits.

Then the precursor mixture was deposited via AACVD, forming a dark orange solution as it misted. **AACVD conditions:** 1L/min, 50 min, 450 °C. Once the

deposition terminated, the AACVD rig was left to cool under a constant stream of N_2 until the films were cool enough to handle (<100 °C).

The resulting films were labelled as **SH/CeO_2/x** and **CeO_2/x** (for their counterparts) where **x** = mass of [$Ce(dbm)_4$] used for AACVD. The colours of the **SH/CeO_2/x** films were diverse, some were translucent with a silver/brown tint and films with higher [$Ce(dbm)_4$] were yellow with brown streaks across the surface. The top plates had thick white/yellow or brown powder deposits, occasionally with rainbows across sections of the films. In all cases, the precursor decomposed in the AACVD baffle but did not block it completely.

5.3.5 Surface Modification of the SH film with CeO_2 via AACVD

Study 2: Variable layers of a [$Ce(dbm)_4$]

The lowest concentration of [$Ce(dbm)_4$] was used to avoid any blockages and to ensure that the precursor was completely dissolved in the solvent. This process was repeated several times to attempt to add multiple layers of CeO_2.

[$Ce(dbm)_4$] (0.2 g, 0.19 mmol) was dissolved in dry toluene (30 cm^3) and left to sonicate for approximately 35 min.

The **SH** films described in **Section 5.3.2** were plasma treated (duration: 4 min; carrier gas flow rate: 2 sccm). The film became superhydrophilic by the end of the plasma treatment and each film was re-inserted into the AACVD rig with the **SH** film on the carbon block (bottom plate) and an FTO substrate used as a top plate for by-product deposits.

Then the precursor mixture was deposited via AACVD, forming a dark orange solution as it misted. **AACVD conditions:** 1L/min at 450 °C until the precursor stopped misting.

The baffle was cleaned physically with a spatula prior to the deposition of the next layer. The films were not cooled in between each [$Ce(dbm)_4$] deposition and were only cooled once all desired layers were deposited onto the film. At that point, the AACVD rig was left to cool under a constant stream of N_2 until the films were cool enough to handle (<100 °C).

The resulting films were labelled as **SH/CeO_2/yL** and **CeO_2/yL** (for their counterparts) where **y** = number of layers of [$Ce(dbm)_4$]. The colours of the

SH/CeO_2/y films were a silver/grey tint, occasionally with streaks of brown. The top plate had a dark brown powdery film.

A schematic outlining the deposition of the superhydrophobic film and CeO_2 surface tuning via AACVD (**Studies 1** and **2**) is shown in **Figure 5.01**.

Table 17. *The water contact angles, transmittance and root-mean-square (RMS) height for the films from* ***Study 1*** *as well as the volumes and concentrations of cerium(IV) dibenzoylmethane, [Ce(dbm)$_4$], deposited on the* ***SH*** *films via AACVD at 450 °C.*

Film name	**Concentration of [Ce(dbm)$_4$], mol dm^{-3}**	**Mass of [Ce(dbm)$_4$], A (g)**	**Volume of anhydrous toluene, B (cm^3)**	**WCA (º)**	**T at 400 – 800 nm (%)**	**RMS height, Sq (µm)**
Barrier coated FTO glass substrate	0	0	0	61 ± 4	91	Immeasurable
CeO_2/0.2	0.0064	0.2	30	51 ± 6	63	0.27 ± 0.05
CeO_2/0.7	0.0084	0.7	80	50 ± 4	73	1.49 ± 0.04
Superhydrophobic (SH)	0	0	0	165 ± 2	34	0.28 ± 0.03
SH/CeO_2/0.2	0.0064	0.2	30	94 ± 6	45	0.24 ± 0.03
SH/CeO_2/0.3	0.0072	0.3	40	77 ± 4	48	0.26 ± 0.01
SH/CeO_2/0.4	0.0077	0.4	50	130 ± 11	36	0.25 ± 0.01
SH/CeO_2/0.5	0.0080	0.5	60	112 ± 6	39	0.25 ± 0.00
SH/CeO_2/0.6	0.0083	0.6	70	93 ± 2	33	0.25 ± 0.00
SH/CeO_2/0.7	0.0084	0.7	80	110 ± 6	27	0.23 ± 0.04

Table 18. *The water contact angles, transmittance, contact angle hysteresis and root-mean-square (RMS) height for the films from* ***Study 2*** *as well as the number of layers of CeO_2 deposited via the [$Ce(dbm)_4$] precursor onto the* ***SH*** *films via AACVD at 450 °C.*

Film name	Number of layers of CeO_2	WCA (°)	T at 400 – 800 nm (%)	Sliding angle (°)	CAH (°)	RMS height, Sq (µm)
Barrier coated FTO glass substrate	0	61 ± 4	91	42 ± 2	20 ± 9	Immeasurable
CeO_2/1L	1	51 ± 6	63	29 ± 2	23 ± 17	0.27 ± 0.05
CeO_2/5L	5	53 ± 13	63	24 ± 1	21 ± 7	0.36 ± 0.10
Superhydrophobic (SH)	0	165 ± 2	34	4 ± 1	20 ± 6	0.28 ± 0.03
SH/CeO_2/1L	1	94 ± 6	45	21 ± 1	9 ± 3	0.24 ± 0.03
SH/CeO_2/2L	2	106 ± 12	26	16 ± 1	5 ± 3	0.26 ± 0.01
SH/CeO_2/3L	3	85 ± 2	26	25 ± 0	13 ± 7	0.25 ± 0.00
SH/CeO_2/4L	4	83 ± 14	23	24 ± 1	12 ± 5	0.25 ± 0.01
SH/CeO_2/5L	5	57 ± 12	22	29 ± 2	14 ± 4	0.25 ± 0.01

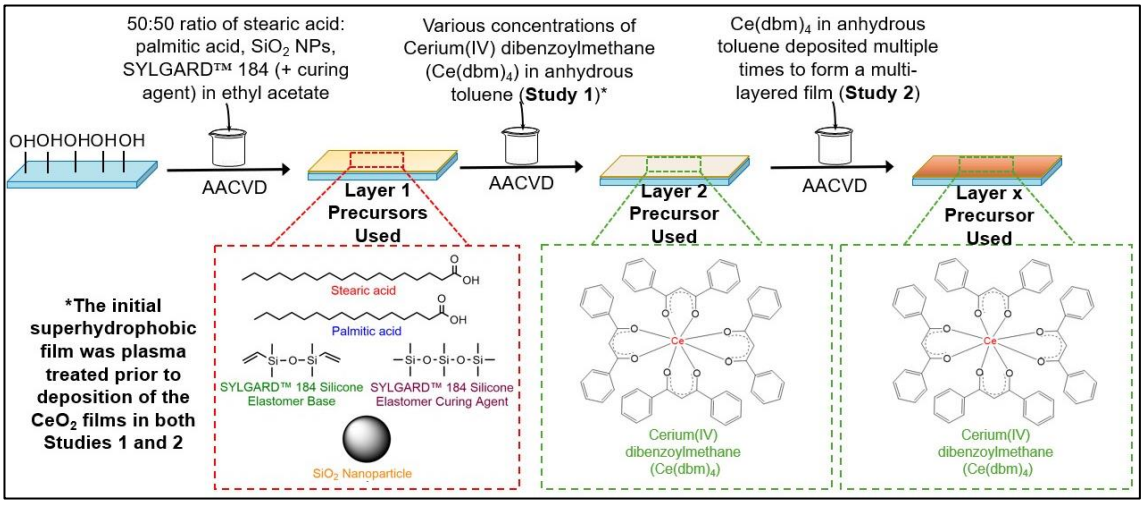

Figure 5.01. *The method to fabricate multi-layered* ***SH/CeO_2*** *films. The first step involved the deposition of a fluorine-free mixture via AACVD to fabricate a superhydrophobic film. Subsequently, the film was surface engineered with CeO_2 also by AACVD to introduce additional functionality.*

5.3.6 Materials Characterisation

Surface morphologies of the materials were carried out using the JEOL 6701F and JEOL 7600F Scanning Electron Microscopes (SEMs). Electron acceleration voltages of 5 – 20 keV were used, depending on how much the sample could tolerate the heat of the electron gun. Carbon sputtering (physical vapour deposition) of all samples for 10 s occurred to improve the electrical conductivity of the films, for imaging and to prevent charging. The sizes of the particles were measured by the ImageJ 1.52s software. Energy Dispersive X-ray Spectroscopy (EDS) scans were taken with an Oxford Instruments EDS set up with variable scan durations of 10 min to 20 min. Functional bonds were detected through Fourier-Transform Infrared Spectroscopy (FTIR) using the Brucker alpha platinum-ATR instrument, with a wavenumber range of 400 – 4000 cm^{-1}. Ultra-violet visible spectroscopy (UV-vis) was used to determine the transmittance of electromagnetic radiation through the films using the Shimadzu UV-2700 spectrophotometer with wavelengths of 400 – 800 nm. Finally, a Thermo Scientific X-ray photoelectron spectrometer with a mono-chromated Al-K alpha source (8.3381 Å) was used for compositional analysis. The peaks were analysed using the CasaXPS 2.3.25 software and calibrated with respect to the C 1s peak at *ca.* 285 eV. Four spots were scanned per film via XPS. The phase composition of the films was determined through powder X-ray diffraction (PXRD), utilising a Malvern PANalytical Empyrean Grazing Incidence-PXRD comprised of a Xe point detector and monochromated Cu Kα source at a voltage of 40 kV and current of 40 mA. Additional parameters included a step size: 0.05°, 2θ = 20° - 80°, ω (incident beam) = 1°. A Bruker Senterra II Raman Spectrometer (λ = 532 nm, power = 25mW) was used to generate Raman spectra. The thickness of the CeO_2-only films (without the superhydrophobic undercoat) was calculated with a Filmetrics F20 thin-film analyser.

5.3.7 Functional, Durability and Performance Testing

Water contact angles (WCAs) were measured using a Kruss DSA 25E drop shape analyser. A mean and the error (one standard deviation) of 10 water droplets of 5 µL was determined by an automatic calculation by ADVANCE 1.14.3. A tilted drop method of water droplets (*ca.* 15 µL) dispensed 4 cm from the surface of the film was used to determine the sliding angle. The stage was tilted at the respective inclination (°) prior to any measurement. The size of the

angles was calculating by manually adjusting the baseline and utilising the Young-Laplace equation. The CAH was determined by initially measuring the advancing angle before measuring the receding angle and finally subtracting an average of the two angles. The Ellipse (Tangent) method was used to determine the angles. The root-mean-square height (Sq) was measured using the Keyence VHX-S750E optical microscope at x1500 magnification. No S-filter and no L-filter were used, only using a Gaussian filter type.

Self-cleaning performance testing: Methylene blue was directly and continuously pipetted onto the surface. The samples were tilted at 20° with images taken throughout the testing to qualitatively visualise the superhydrophobicity and self-cleaning properties.

Durability

Elcometer® Testing: An Elcometer® 501 Pencil Hardness Tester (supplier: Elcometer® Ltd.) consisted of pencils of differing hardness (6H – 6B) which were pushed across the surface of a film at a 45° angle. Pencils of increasing hardness were used until a visible line was seen (by eye) in the coating. The standard protocol followed was ASTM D3363.

Thermal Stability: Samples were heated at 300 °C for 5 h and the WCAs and CAH measurements were taken prior and post heating.

UV Stability: WCAs of samples were measured after 1, 2, 3, 4, 5, 6 and 7 days of exposure to UV in a sealed UV light box. The CAH was measured after 7 days of UV exposure. A UV irradiance of 260 mW/cm^2 and emission wavelength of 365 nm were used.

Tape peel test: Scotch Magic™ Tape was manually attached to and removed from the films up to 600 times. WCAs were initially recorded periodically, and the CAH was recorded at the end.

Changes in WCA over time: The films were left on the lab bench and WCAs were measured every 10 days for 30 days to determine the stability and potential changes in WCA over time.

5.4 Results and Discussion

To learn about the effect of CeO_2 on the overall properties of the **SH** film, various concentrations of the [$Ce(dbm)_4$] precursor were deposited on top of the **SH** film (**Study 1**). In addition, a multi-layered approach (**Study 2**) was pursued to compare to the films of **Study 1**. All **SH/CeO_2** films were compared to their counterparts, i.e. films without the superhydrophobic underlayer. All [$Ce(dbm)_4$] depositions took place via AACVD at 450 °C with details on the amounts used in **Tables 17** and **18**. The first part of this section will be on the films of **Study 1** and then followed by the results on the films of **Study 2** however, for some results, both studies will be discussed simultaneously. Performance testing and an evaluation and comparison between the films of **Study 1** and **2** will follow thereafter.

The superhydrophobic undercoat was based on the composition described previously in **Chapter 2**, comprised of SYLGARD 184, a 50:50 hybrid mixture of stearic acid and palmitic acid which are all low surface energy reagents. Silica NPs were needed to provide the roughness as roughness is a pre-requisite for superhydrophobic materials.

As mentioned previously, AACVD of the **SH** film occurred by thermophoretic effects leading to the physisorption of the gas phase polymer-fatty acid-coated SiO_2 NPs onto the glass substrate top plate (furthest away from the carbon block).[66] The glass substrate with the newly-deposited **SH** film was removed and placed onto the carbon block of the AACVD rig for the deposition of the CeO_2 over-layer.

The films were treated with a plasma cleaner prior to the [$Ce(dbm)_4$] deposition to improve the uniformity of the deposited CeO_2 film. On plasma treatment, the **SH** films became superhydrophilic (WCA <10°) due to the formation of hydroxyl groups acting as nucleation sites for [$Ce(dbm)_4$]. The **SH** films surface-tuned with CeO_2 were characterised by analytical, chemical and performance testing, namely, FTIR, PXRD, Raman, UV-vis, XPS, SEM/EDS, performance and functional (wettability and self-cleaning).

By depositing a limited range of concentrations of [$Ce(dbm)_4$], changes in the overall WCAs were observed both across the concentration range and across the film (from inlet to outlet of the AACVD rig). The reductions in WCA observed for

the CeO_2 films were much more significant relative to the **SH/TiO_2** films, where TiO_2 was deposited as a second layer, as described in **Chapter 3**. Hence, due to the significant changes in WCA observed, this demonstrated the presence of CeO_2; reductions in WCAs prior and post-$Ce(dbm)_4$ deposition were observed for all [$Ce(dbm)_4$] trialled. Interestingly, an increase in [$Ce(dbm)_4$] did not always lead to a linear decrease in WCA. Film **SH/CeO_2/0.2** (lowest [$Ce(dbm)_4$]) had a WCA of 94 ± 6°, for film **SH/CeO_2/0.3,** this reduced further to 77 ± 4° and for film **SH/CeO_2/0.4** the WCA increased to 130 ± 11°. For film **SH/CeO_2/0.5**, the WCA reduced to 112 ± 6°, for film **SH/CeO_2/0.6** it reduced even further to 93 ± 2° and then increased slightly for film **SH/CeO_2/0.7** to 110 ± 6°. Without quantitative measurements of the CeO_2 film thickness for all the **SH/CeO_2** films, increasing [$Ce(dbm)_4$] was not always assumed to increase the thickness of the CeO_2. It was difficult to determine the thickness of the **SH/CeO_2** films due to the complexity of the underlying superhydrophobic morphology. It was previously reported by Oh *et al.* that WCAs were proportional to the thickness of the rare earth oxide films.[76] Thinner films led to reductions in surface energy and hence increases in WCA.

Across the film, the highest WCA was observed at Area 1 (closest to outlet) to Area 6 (closest to inlet) however, for the areas in between, a linear trend was not observed, but this was sometimes accommodated for by the large standard deviation. This variation in WCA is observed in **Figure 5.02**. The WCAs showed deposition closer to the inlet (Area 6) and less so in Areas 1 and 2, displaying negligible changes in WCA in these areas. There was some deposition in Area 3 but significant deposition in Areas 4, 5 and 6 potentially due to the predisposition of [$Ce(dbm)_4$] to thermally degrade easily. The deposition of [$Ce(dbm)_4$] studied in **Study 1** was surface rate limited as the WCAs and thickness were similar on varying [$Ce(dbm)_4$]. Film **CeO_2/0.2** had an estimated thickness of *ca.* 4 ± 3 nm. This was also confirmed by the noisy Si peak in the Si 2p scan, indicative of the glass substrate, as XPS surface scans penetrate a depth of approximately 5 nm. On the other hand, film **CeO_2/0.7** had an estimated thickness of 7 ± 3 nm. For film **CeO_2/5L** there was an increase in WCA to 57° and an increase in film thickness to 54 ± 9 nm, indicative of a mass transport limited reaction where the amount of [$Ce(dbm)_4$] brought to the surface determines the thickness per unit time.

Interestingly, for the control films with the highest and lowest [Ce(dbm)$_4$] deposited on FTO glass, i.e. films **CeO$_2$/0.2** and **CeO$_2$/0.7**, the WCAs were similar of 50° and 51°, respectively. This indicated that increasing the concentration of [Ce(dbm)$_4$] did not have a significant influence on the thickness of the CeO$_2$ deposited. Any changes in the **SH/CeO$_2$** films were due to the rough morphology of the superhydrophobic underlayer.

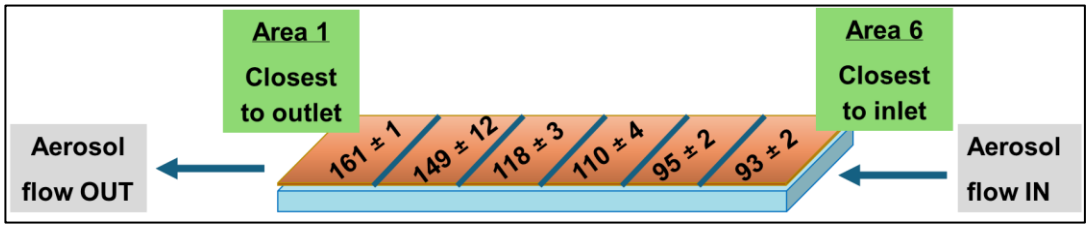

Figure 5.02. *Variations in WCA across film* ***SH/CeO$_2$/0.6****.*

The relative amounts of CeO$_2$ on the **SH** films for **Studies 1** and **2** were determined via XPS as a means of adding context to the measured WCAs, **Figure 5.02**. The results of this were compared to the films of **Study 2** where several layers of a set concentration of [Ce(dbm)$_4$] were deposited on top of the **SH** film. For this analysis, **Studies 1** and **2** were analysed together. The results of this were compared to the films of **Study 2** where several layers of a set concentration of [Ce(dbm)$_4$] were deposited on top of the **SH** film.

To determine the raw peak area ratio via XPS, four areas within each film were scanned and an average of the areas were calculated. For both **Studies 1** and **2**, the standard deviation errors increased with increasing peak area. Low peak areas (indicative of low Ce content) had small errors and *vice versa*, which arose due to the method of calculation. If the raw peak area of Si was small (indicating good coverage), it increased the overall raw peak area ratio and hence resulted in large error bars. These large error bars also indicated large variance in the Si peak areas. **Study 1** confirmed the lack uniformity of the CeO$_2$ film deposition by utilising this route. For instance, at [Ce(dbm)$_4$] of 0.0080 g mol^{-1} and 0.0086 g mol^{-1} (i.e. films **SH/CeO$_2$/0.4** and **SH/CeO$_2$/0.6**, respectively), the graph showed a low Ce/Si raw peak area ratio which was close to 0. However, if these depositions were to fit the observed graphical trend, these values should have been higher. In addition, the WCAs for film **SH/CeO$_2$/0.4** remained superhydrophobic and film **SH/CeO$_2$/0.6** was hydrophobic; based on the WCA and peak area ratios, these films were not consistent with our expectation.

Relative to film **SH**, even a small amount of CeO_2 reduced the WCA significantly but as more CeO_2 was deposited, the WCA recovered and became more hydrophobic. Ideally, higher concentrations of $[Ce(dbm)_4]$ should have been investigated but due to decomposition of the $[Ce(dbm)_4]$ precursor in the baffle, this was not possible as it could have led to complete blockage of the baffle.

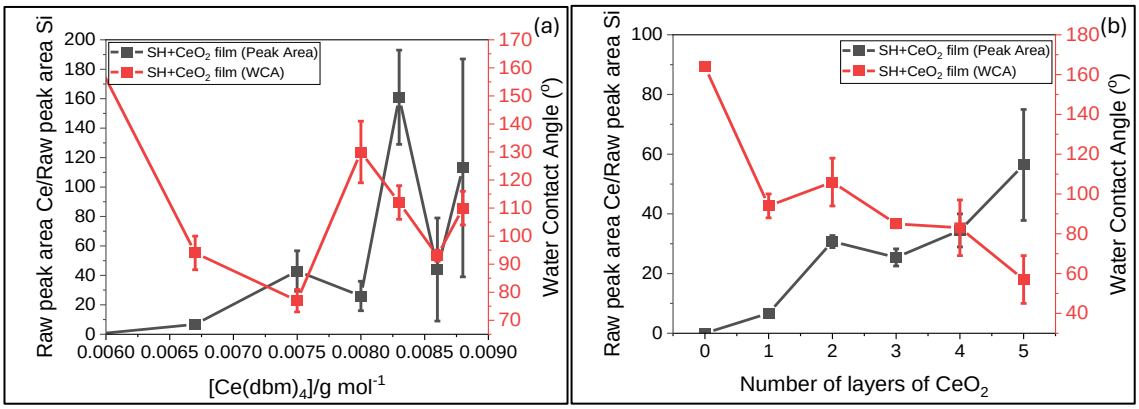

Figure 5.03. *Graphs showing the relationship between the water contact angle and the raw peak area of Ce and Si generated from XPS vs. (a) $[Ce(dbm)_4]$ (b) number of layers of CeO_2 deposited.*

Generally, for **Study 1**, there was a reduction in transmittance on increasing $[Ce(dbm)_4]$ however, this was not linear, with some increase in percentage transmittance with decreasing $[Ce(dbm)_4]$, **Table 17**. Reasons for this deviation could have been due to the fast deposition rate of the AACVD process and the rough morphology of the underlying **SH** film. Interestingly, the transmittance of films **CeO_2/0.2** and **CeO_2/0.7** only differed by 10%, potentially confirming the minimal changes in CeO_2 film thickness with the increased $[Ce(dbm)_4]$ precursor concentration.

As seen in **Figure 5.03(a)** there was not much variation in raw peak area values for the films of **Study 1** due to small differences in the raw peak areas between the starting (**SH/CeO_2/0.2**) and higher masses (**SH/CeO_2/0.7**). The intermediate concentrations had small Ce/Si raw peak area ratios which potentially indicated a thin continuous film therefore, **Study 2** was instead pursued where the number of layers of CeO_2 were varied (via repeated deposition of a set of concentrations of $[Ce(dbm)_4]$).

Interestingly, **Study 2**, a layer-by-layer deposition route led to a clear reduction in WCA as the number of layers of CeO_2 increased. The trend observed in this study contrasted slightly to the trend observed in **Study 1**. For **Study 1**, when the Ce/Si raw peak area ratio was around 120, the WCA was *ca.* 110° although for

Study 2 a WCA of *ca.* 100° had a Ce/Si raw peak area ratio of *ca.* 30. However, on depositing 3 layers/4 layers/5 layers, the Ce/Si raw peak area ratio remain low with low error bars and a return to low WCAs; this trend was not observed in **Study 1**, potentially indicating the patchiness of the overall CeO_2 deposition. For **Study 1**, films **CeO_2/0.2** and **CeO_2/0.7** had Ce/Si raw peak area ratios and WCAs of 154 and 51° and 828 and 50°, respectively. For **Study 2**, films **CeO_2/1L** and **CeO_2/5L** had Ce/Si raw peak area ratios and WCAs of 154 and 51° and 1414 and 53°, respectively. This showed that a multi-layered approach was a more reliable route to more uniform surface modification of a **SH** film relative to a single one-pot deposition of variable precursor concentrations, **Figure 5.04**. It is important to note that films **CeO_2/0.2** and **CeO_2/1L** are the same film. Reports by Khan *et al.* explain the impact of surface O/Ce ratios on the overall hydrophobicity of CeO_2 films.[158] A higher O/Ce ratio indicated greater surface oxygen sites with respect to the cerium sites leading to hydrophilicity as oxygen sites facilitated hydrogen bonding with water molecules. Potential anomalies and non-linear changes in WCA for **Study 2** may have been attributed to the O/Ce ratio imbalance or patchiness of the AACVD process.

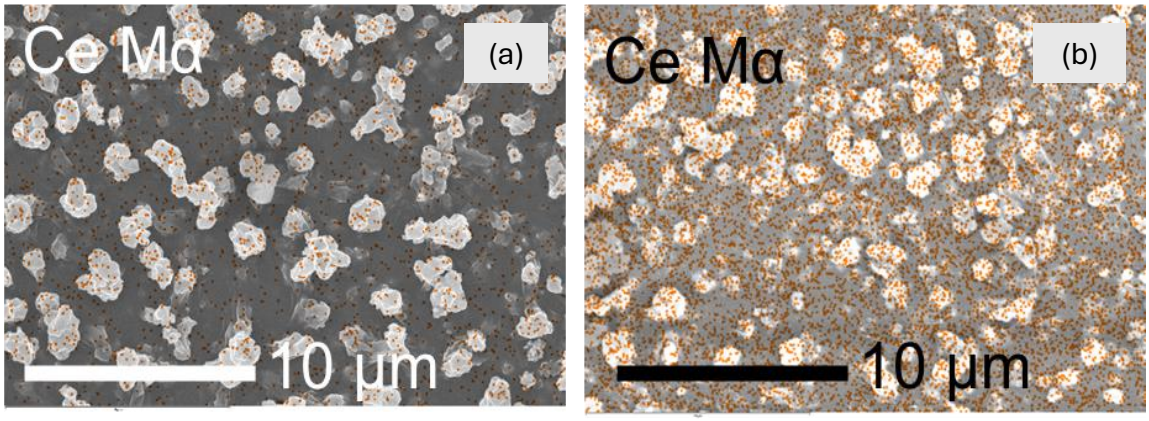

Figure 5.04. *EDS-generated images (Ce Mα) of films (a)* ***SH/CeO_2/0.7*** *and (b)* ***SH/CeO_2/5L***.

SEM images were taken of films **SH/CeO_2/0.2** and **SH/CeO_2/0.7**. The overall morphology of the superhydrophobic undercoating remained similar however, at high magnification (x50,000), the emergence of consistently sized spherical particles coating these networks were present as well as in the matrix of the film. This suggested island growth of the CeO_2 nanoparticles on the superhydrophobic structures. Relative to the **SH** film (**Chapter 2**), these globular CeO_2 nanoparticles were not present in the uncoated **SH** film; here, they were consistent in size and ranged from *ca.* 116 nm – 140 nm, with a greater presence in the **SH/CeO_2/0.7**

films. Interestingly, the SEM images of both films were similar, corroborated by the root-mean-square roughness, also confirming the similarity in concentration of [Ce(dbm)$_4$]. Overall, this led to a reduction in root-mean-square roughness from 0.28 μm for the **SH** film to 0.24 μm for film **SH/CeO$_2$/0.2** and finally to 0.23 μm for film **SH/CeO$_2$/0.7**.

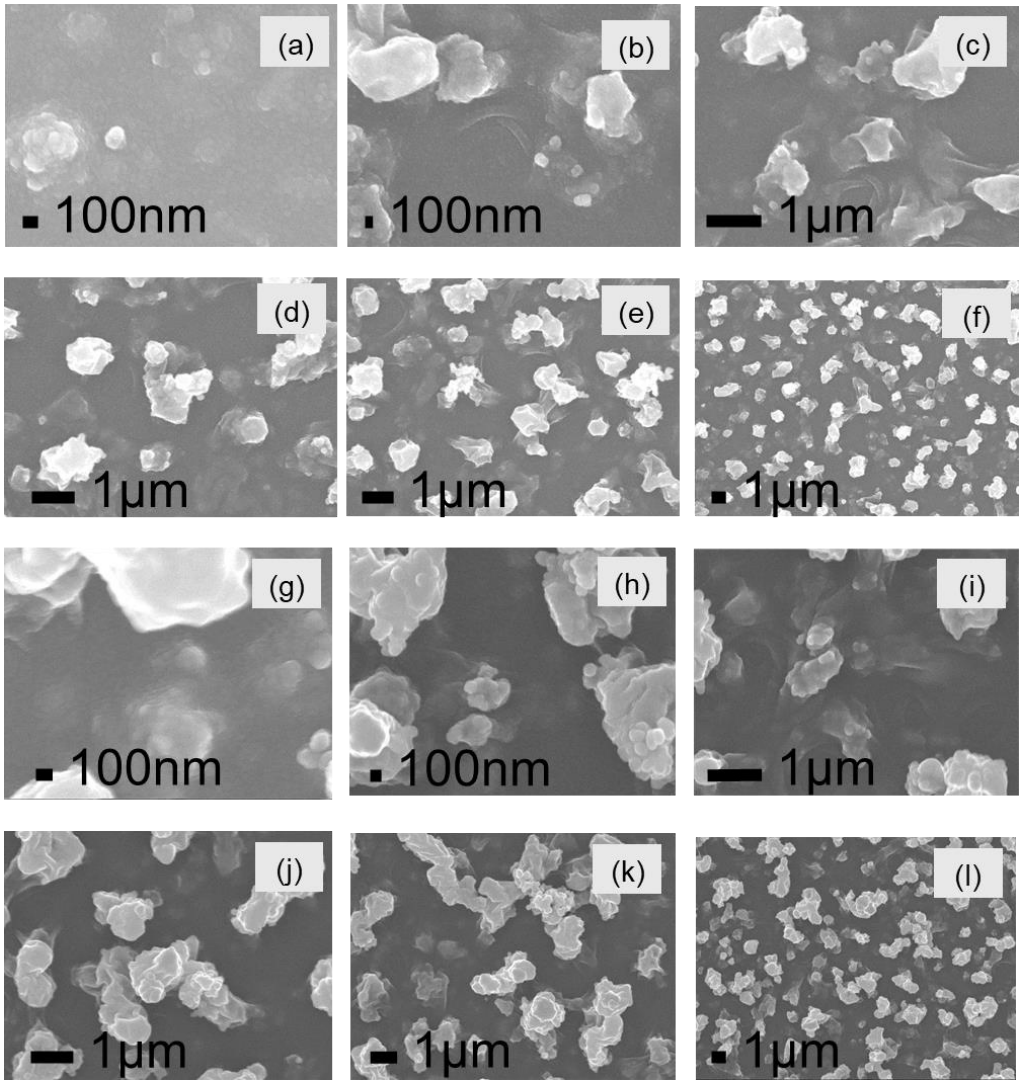

Figure 5.05. *SEM images of **SH/CeO$_2$** films; images (a) – (f) are of film **SH/CeO$_2$/0.2** and images (g) – (l) are of film **SH/CeO$_2$/0.7**.*

EDS scans of films **SH/CeO$_2$/0.2** and **SH/CeO$_2$/0.7** were also taken and compared, **Figures 5.06** and **5.07**. Scans were initially taken for 10 min but the duration of the scan was increased to 20 min to improve the reliability. In both cases, the C Kα scans confirmed successful carbon coating of the films, prior to the scan. Green and purple dots, representing O Kα and Si Kα appeared uniformly spread across the images, with a greater quantity of spots for film **SH/CeO$_2$/0.7**. Although the penetration depth of EDS is large, O and Si appeared to cover most of the surface and the wt% of Ce remained relatively different, of

ca. 0% and 23% for films **SH/CeO_2/0.2** and **SH/CeO_2/0.7**, respectively, potentially suggesting a thin coating of CeO_2. Nevertheless, the Ce Mα spots indicated that Ce was spread across the whole surface and was not concentrated on the interconnected clusters. In contrast to TiO_2 discussed in **Chapter 3,** the CeO_2 coating was quite thin, even with the highest concentration of $[Ce(dbm)_4]$.

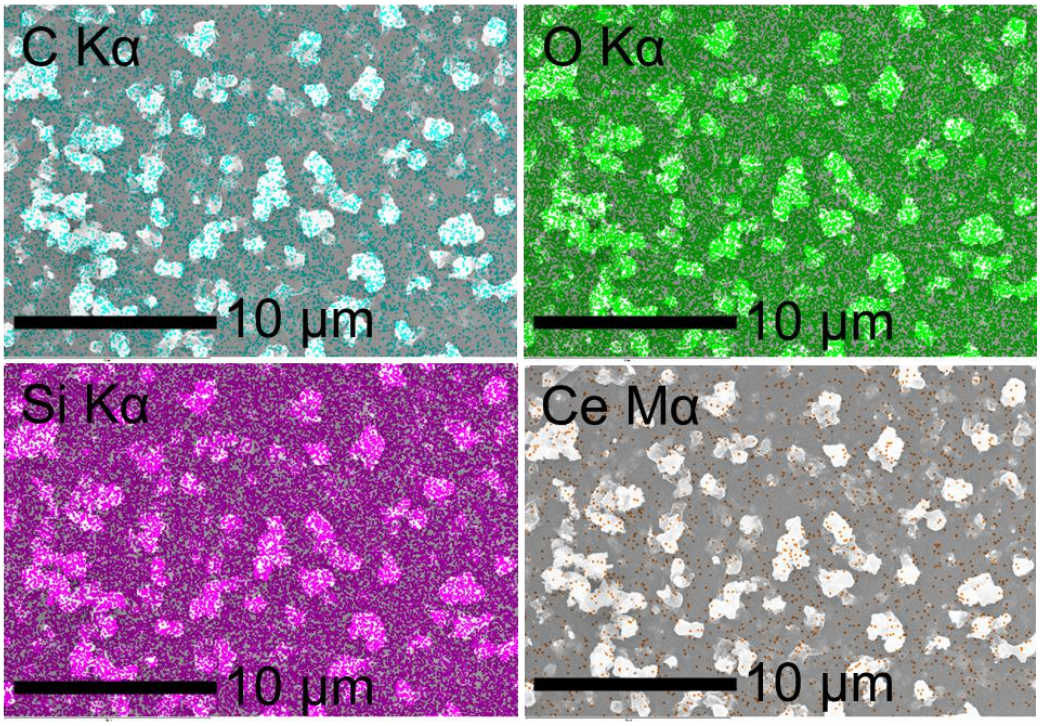

Figure 5.06. *EDS-generated images (C Kα O Kα, Si Kα and Ce Mα) of film* ***SH/CeO_2/0.2****.*

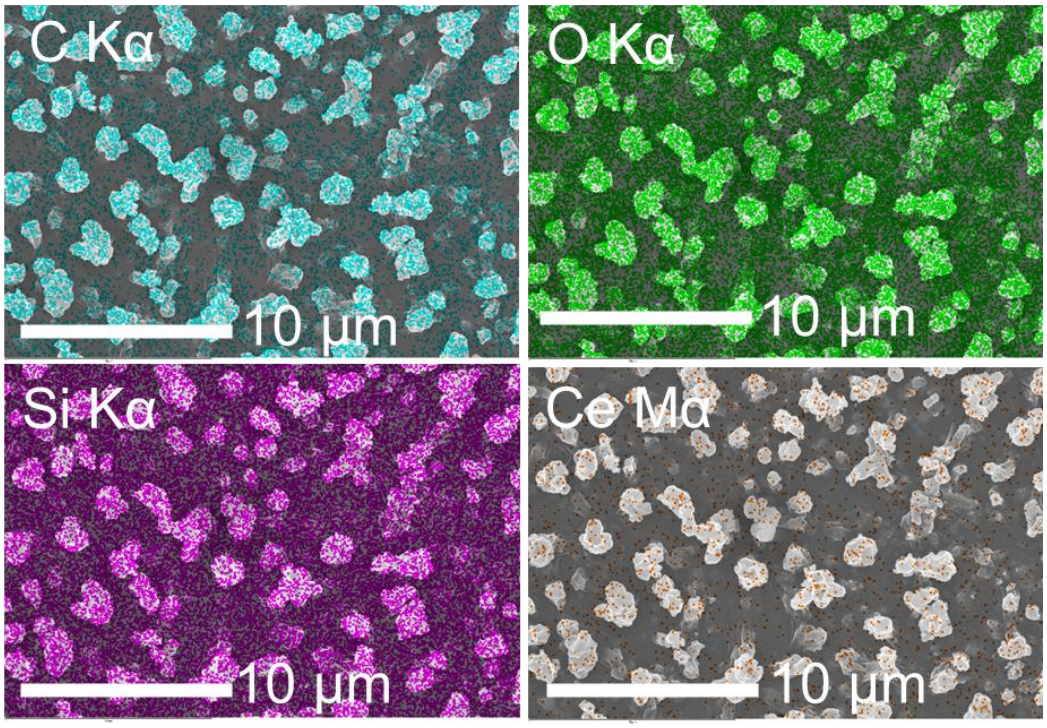

Figure 5.07. *EDS-generated images (C Kα O Kα, Si Kα and Ce Mα) of film* ***SH/CeO_2/0.7****.*

Thus far, the data outlined indicated the presence of CeO_2 due to the Ce detected in the EDS scans and the reductions in WCA suggested a thin coating of CeO_2. The absence of some of the reference peaks in the PXRD patterns were due to the non-crystallinity of the resulting films. Difficulties in depositing CeO_2 relative to TiO_2 via AACVD (**Chapter 3**) may have been because TTIP readily dissolves in toluene, hence transports readily to the heated AACVD rig, decomposing to form TiO_2. Relative to TTIP, $[Ce(dbm)_4]$ must be solubilised in a greater volume of solvent. In addition, $[Ce(dbm)_4]$ does not have a facile decomposition route such as TTIP. Another problem was the decomposition of the $[Ce(dbm)_4]$ precursor in the baffle prior to entering the AACVD rig for a heterogenous reaction to form CeO_2. This pre-decomposition of precursor has been reported previously when depositing other Ce precursors.[162]

As expected, the Raman spectrum of **CeO_2/x** had better-defined signals than the **SH/CeO_2** films. **SH/CeO_2/0.2** had less well-defined peaks potentially due to the thin CeO_2 coating, leading to penetration through to the **SH** film and amorphous glass substrate. Although faint, all peaks in **Figure 5.08**. displayed a small bulge at *ca.* 465 cm^{-1}.[168] In addition, the peaks pertaining to bulk CeO_2 were present at 550 cm^{-1} and 1100 cm^{-1}.[168] In addition, there was a small peak at 800 cm^{-1}, indicative of surface defects. The later signals at *ca.* 1360 cm^{-1} and 1605 cm^{-1} were more prominent in the scan of film **CeO_2/0.2**.[169]

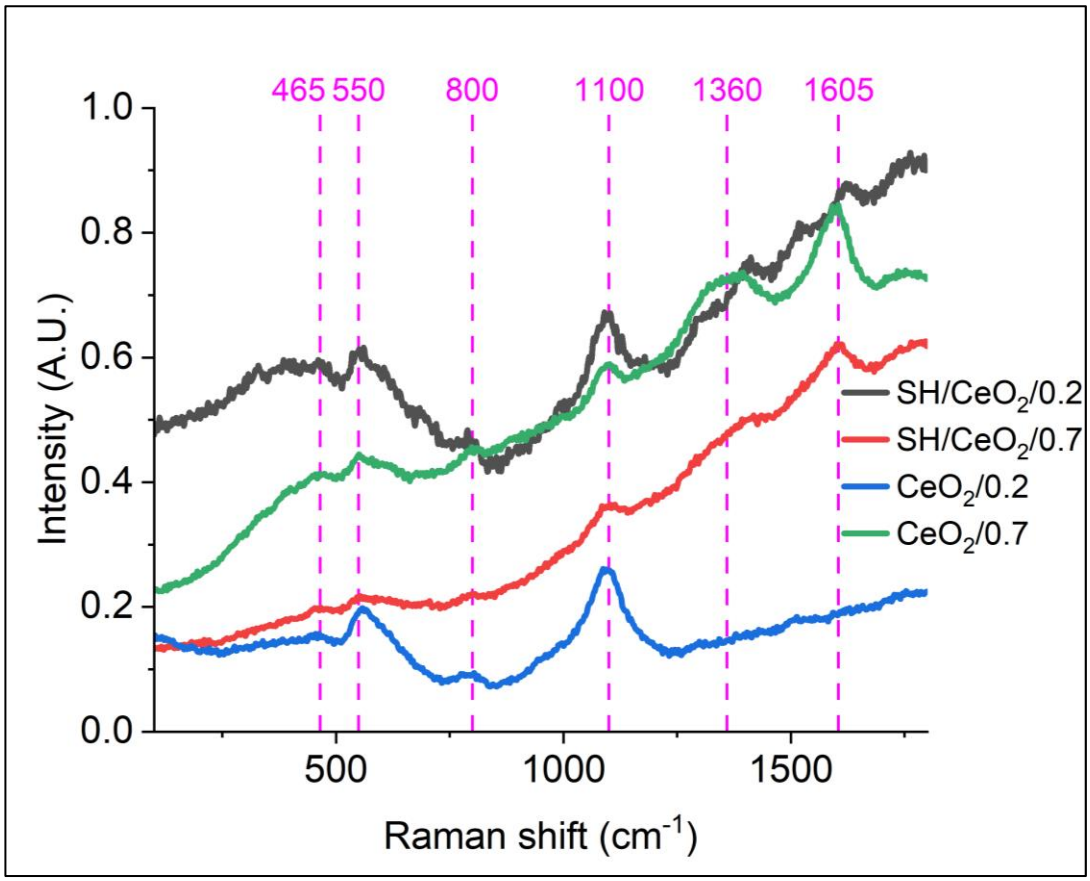

Figure 5.08. *Combined Raman spectrum for the films of* ***Study 1*** *(both* ***CeO₂/x*** *and* ***SH/CeO₂*** *films) with the highest and lowest [Ce(dbm)₄].*

PXRD was carried out to determine the presence of CeO_2 rather than the crystallinity of the film to later determine the effect of this additional coating on the **SH** film. Due to the poor resolution of the film and the inability to distinguish peaks when compared to the reference pattern, variable omega values were trialled. Omega = 2° was used as employing other omega values also resulted in similar PXRD patterns but weaker signals, especially for omega = 0.5°, **Figure 5.9(a)**. All patterns followed a similar trend. **Figure 5.09(b)** demonstrated the lack of crystallinity of the deposited CeO_2 films. Nevertheless, some peaks at *ca.* 28.6°, 33.1°, 47.5° and 56.4° particularly for film **CeO_2/0.7** can be deduced. However, due to the amorphous nature of the dual-layered films, the remaining 2θ values of *ca.* 59.2° and 69.5° (**COD: 9009008**) in film **SH/CeO_2/0.7** cannot be visualised.

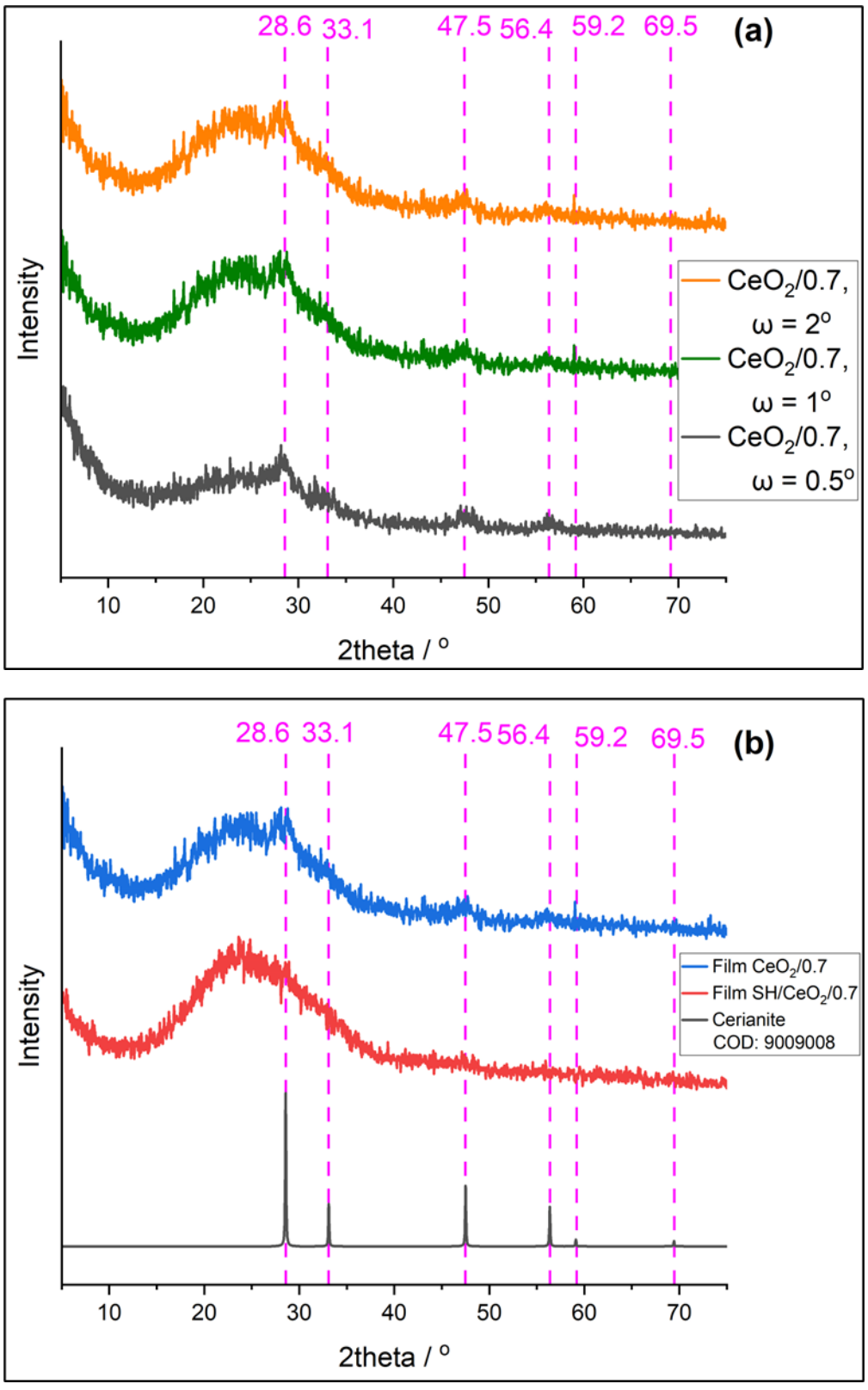

Figure 5.09. *PXRD patterns of (a) film* ***CeO_2/0.2*** *(lowest [Ce(dbm)$_4$]) ranging from Ω = 2° (yellow) to Ω = 0.5° (red). (b) films* ***CeO_2/0.7*** *(blue) and* ***CeO_2/0.7*** *(red) – highest mass of [Ce(dbm)$_4$]. Pattern (b) was compared to a cerianite reference pattern (****COD: 9009008****).*

Due to the difficulties with depositing variable concentrations of [Ce(dbm)$_4$], a separate study (**Study 2**) was conducted where the lowest concentration of [Ce(dbm)$_4$] was deposited up to five times, **Table 18**. XPS confirmed the presence of CeO_2 in all films, hence indicting that the **SH** films were modified after depositing [Ce(dbm)$_4$]. An example spectrum is **Figure 5.10**. In this case, little C was observed in the C 1s spectrum due to organic C, **Figure 5.10(a)**. Peaks in the O 1s spectrum, **Figure 5.10(b)**, confirmed the presence of adsorbed non-lattice oxygen containing species such as surface hydroxyls or carbonates at *ca.* 531.0 eV.[170] There were negligible amounts of Si, demonstrated by the noise in the Si 2p scan, **Figure 5.10(c)**. Interestingly, the Ce 3d spectrum contained many peaks primarily pertaining to the Ce(IV) state **Figure 5.10(d)**; the peaks categorised as "v" indicated the $3d_{5/2}$ states and "u" indicated $3d_{3/2}$ spin-orbit coupled states. The v''' and u''' peaks at *ca.* 899.0 eV and 916.5 eV, respectively, were due to $3d_{5/2}$ and $3d_{3/2}$, respectively. Each peak had satellites owing to the transfer of a maximum of electrons from the O 2p orbital to the Ce 4f orbital. The satellite peaks were evident at *ca.* 883.8 eV (v), 886.0 eV (v''), 900.7 eV (u) and 907.4eV (u''). All peaks align with previous literature reports.[167,170]

Comparing **Figure 5.10(c)** and **Figure 5.10(d)**, there was a lot of Ce and minimal Si suggesting that there were no pin holes in the film and that it was at least 5 nm thick (penetration depth of XPS) hence a potentially continuous CeO_2 film. Therefore, any variance in WCA measurements when comparing the plain **CeO_2/x** films to the **SH/CeO_2** films were due to the underlying microstructure.

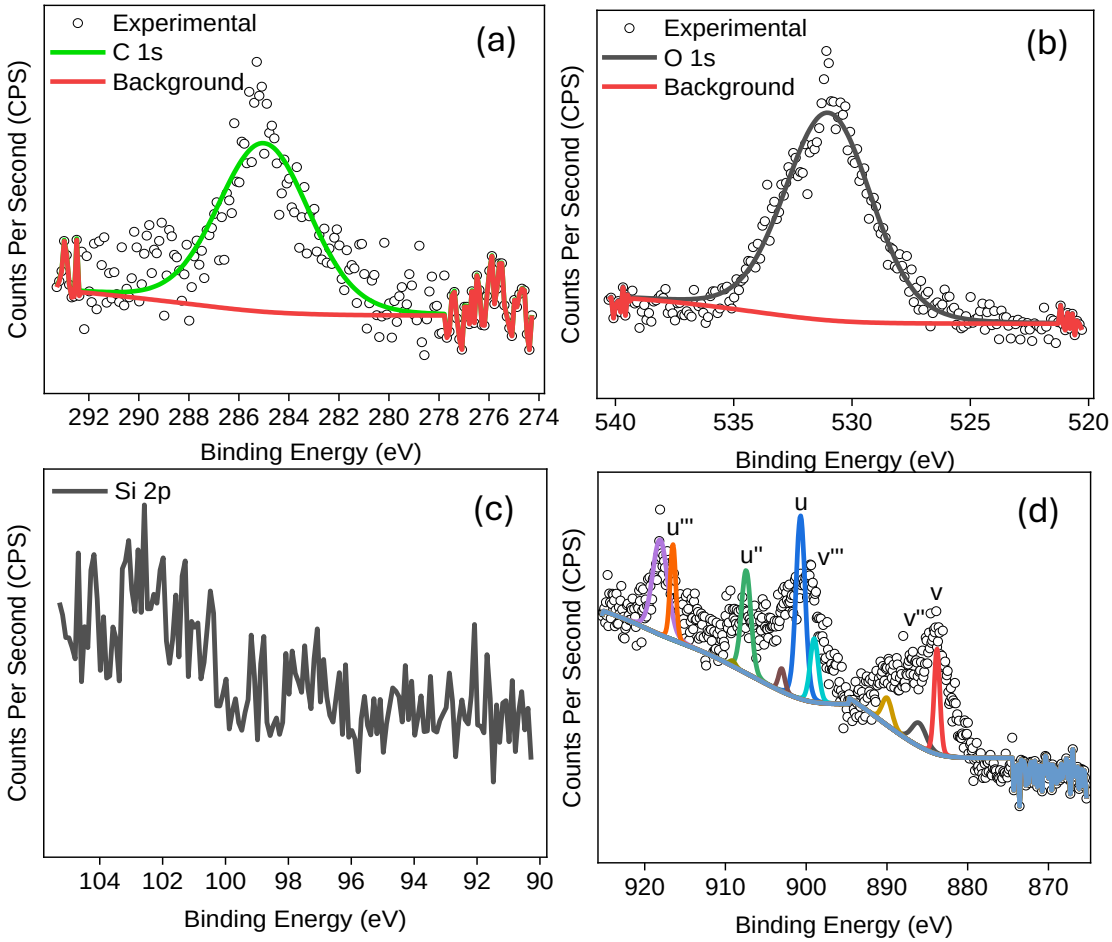

Figure 5.10. *XPS scans for the* ***SH/CeO₂/5L*** *film (a) C 1s (b) O 1s (c) Si 2p and (d) Ce 3d.*

In addition to XPS, FTIR spectroscopy was carried out to determine the bonds present in the CeO_2 surface modified **SH** film, **Figure 5.11**. The characteristic peaks of the **SH** film, described in **Chapter 2**, overlapped with the key Ce-O stretches, usually visualised at 855 cm^{-1} and 790cm^{-1}.[171] The peak at 1049 cm^{-1}, representing Si-O-Si asymmetric stretching vibrations of the **SH** film were still present yet the peak at 3000 cm^{-1} for the sp^3 C-H asymmetric stretch had been masked.

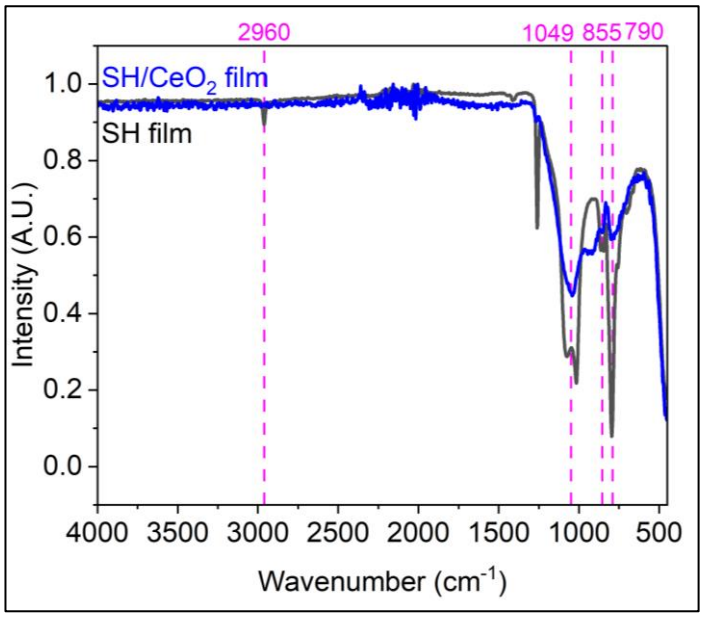

Figure 5.11. *Combined FTIR spectrum of films* ***SH*** *and* ***SH/CeO₂/5L*** *after surface modification with CeO_2.*

The **CeO_2/1L** film was scanned via SEM to compare its morphology to the films with the superhydrophobic undercoat and to visualise the subsequent morphology that arises through depositing [Ce(dbm)$_4$] via AACVD. The resulting morphology consisted of regularly shaped globular structures that were periodically and homogenously dispersed, **Figure 5.12**. The morphology of film **CeO_2/1L** was very similar to **CeO_2/5L**.

SEM revealed that as the number of layers of CeO_2 increased, the number of globular CeO_2 clusters also increased, primarily on the interconnected network of particles of the superhydrophobic underlayer. More detail on the morphology of the uncoated **SH** films can be found in **Chapter 2**. The morphologies of films **CeO_2/2L**, **CeO_2/3L** and **CeO_2/4L** remained similar which was also reflected in their similar WCAs of 106°, 85° and 83°, respectively. By film **CeO_2/5L**, these CeO_2 particles were coating the matrix and the greater quantity of CeO_2 agglomerates were reflected in the drop in WCA to 57°. A potential reason may not be due to changes in the morphology but also due to an increase in surface energy – PDMS and CeO_2 have surface energies of 0.019 – 0.021 J/m^2 and 1.2 J/m^2, respectively.[19,128,172] Interestingly, the root-mean-square roughness measurements remained consistent at 0.25 µm. This may have been due to the generation of CeO_2 nanoparticles which may have been below the detection limit of the optical microscope and hence not implemented in the Sq values.

Relative to the **SH/CeO_2/yL** films**,** these globular agglomerates were most prominent in film **SH/CeO_2/5L, Figure 5.13**. These globular aggregates were easily spotted at lower magnifications (*ca.* x5,000) for film **SH/CeO_2/5L** than for film **SH/CeO_2/0.7** (*ca.* x15,000). For film **SH/CeO_2/5L**, the individual particles ranged from *ca.* 150 nm to 250 nm with clusters of two or more nanoparticles starting at *ca.* 450 nm. In contrast, for film **SH/CeO_2/0.7**, only CeO_2 NPs were present as individual particles and were sized at *ca.* 115 nm – 140 nm. It could be that the multi-layered deposition process (**Study 2**) facilitated the formation of clusters as CeO_2 nanoparticles would add onto the CeO_2 nanoparticles from the previous layers as more CeO_2 films were deposited. Unlike for the **SH/TiO_2** films (**Chapter 3**), the CeO_2 particles did not evenly coat the superhydrophobic structures although the individual TiO_2 particles observed in films **SH/TiO_2** were 250 nm – 350 nm. This may have been due to the decomposition of the $[Ce(dbm)_4]$ precursor in the baffle leading to a reduced $[Ce(dbm)_4]$ for the heterogenous reaction in the heated chamber and/or a lower reactivity.

Similarly, the %T also remained relatively consistent for all presented films (*ca.* 26% – 22%) and relative to the **SH** film a <10% decrease was observed, demonstrating minimal changes to the matrix and the ability for visible light to penetrate through. Unlike the **SH/TiO_2** films described in **Chapter 3**, the morphology of the **SH/CeO_2** films did not become flat, confirmed by the root-mean-square height reducing to 0.25 µm rather than 0.18 µm as observed for the **SH/TiO_2** films. Relative to the films of **Study 1,** the superhydrophobic morphology appeared to be coated better in **Study 2.** However, relative to the **SH/TiO_2** films (**Chapter 3**), a greater number of CeO_2 layers must be deposited to achieve the range of thicknesses obtained for the **SH/TiO_2** films. Relative to film **SH/CeO_2/0.7** of **Study 1**, the wt% of film **SH/CeO_2/5L** reached 36% compared to 23%.

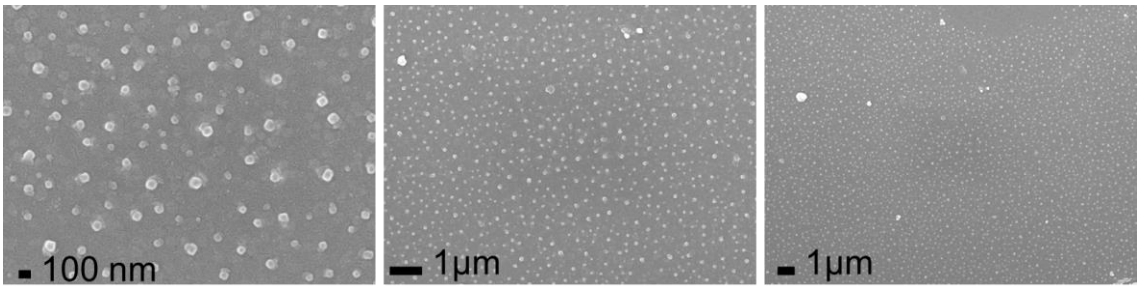

Figure 5.12. *SEM images of the morphology of film* ***CeO_2/1L****.*

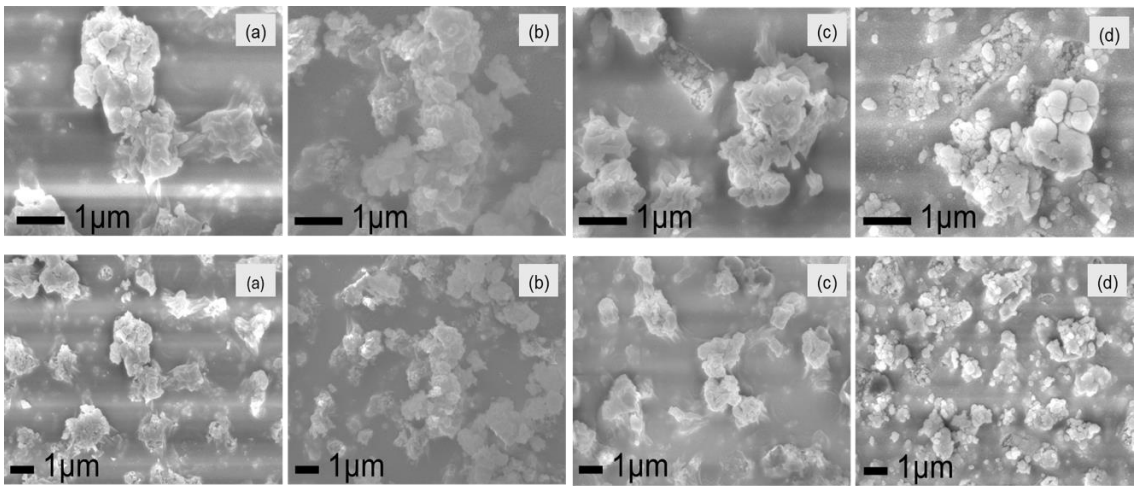

Figure 5.13. *SEM images of* ***SH/CeO₂/yL*** *films (****Study 2****) depicting changes in morphology as the number of layers increase. (a)* ***SH/CeO₂/2L*** *(b)* ***SH/CeO₂/3L*** *(c)* ***SH/CeO₂/4L*** *(d)* ***CeO₂/5L****.*

All major peaks relating to cerianite (CeO_2) were visualised in the tested sections of films **CeO_2/5L** and **SH/CeO_2/5L** (**Study 2**), **Figure 5.14,** confirming that CeO_2 was indeed deposited on the films. Unlike the films of **Study 1**, the superhydrophobic underlayer did not influence the resulting PXRD pattern for **Study 2**.

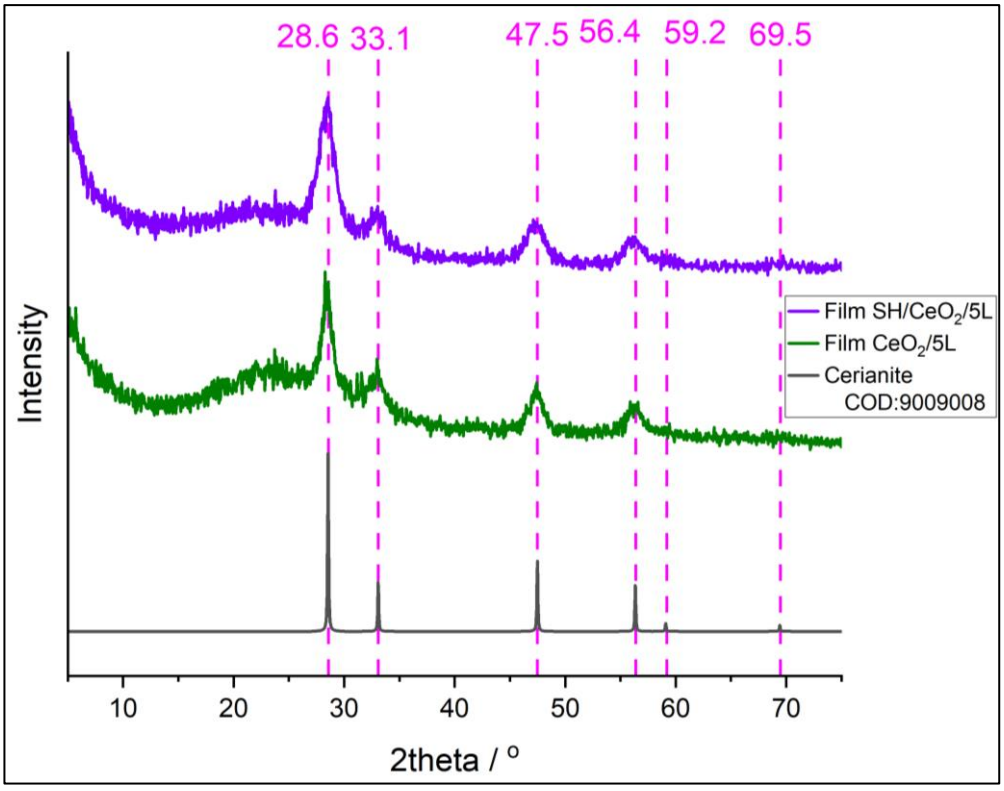

Figure 5.14. *PXRD patterns of film* ***SH/CeO₂/5L*** *(purple) and* ***SH/CeO₂/0.7*** *(green) – greatest number of CeO_2 layers. The pattern was compared to a cerianite reference pattern (****COD: 9009008****).*

5.5 Functional, Durability and Performance Testing

Table 19. *The WCA, CAH and sliding angles for films deposited with the highest and lowest [Ce(dbm)$_4$] (**Study 1**) and films with the least and greatest CeO_2 layers (**Study 2**).*

Film name	**WCA (º)**	**Sliding angle (º)**	**CAH (º)**
Barrier coated FTO glass substrate	61 ± 4	42 ± 2	20 ± 9
Superhydrophobic (SH)	165 ± 2	4 ± 1	20 ± 6
CeO_2/0.2	51 ± 6	29 ± 2	23 ± 17
CeO_2/0.7	50 ± 4	49 ± 1	25 ± 11
SH/CeO_2/0.2	94 ± 6	21 ± 1	9 ± 3
SH/CeO_2/0.7	110 ± 6	35 ± 5	22 ± 8
CeO_2/1L	51 ± 6	29 ± 2	23 ± 17
CeO_2/5L	53 ± 13	24 ± 1	21 ± 7
SH/CeO_2/1L	94 ± 6	21 ± 1	9 ± 3
SH/CeO_2/5L	57 ± 12	14 ± 4	14 ± 4

The WCAs of the films of **Study 1** and **Study 2** were discussed and compared to the raw peak area ratios derived from XPS earlier in the **Results & Discussion**Error! Reference source not found. section of this chapter. Further w ettability characterisation was carried out to further understand the functional properties of the films, **Table 19**. Interestingly, the CAH of the studies demonstrated similar trends where films without the superhydrophobic underlayer, namely the CeO_2 deposited on FTO glass substrates had high CAHs *ca.* 21° - 25° demonstrating inhomogeneity as a result of grain boundaries, resulting in pinning of the water droplets across the film's surface (Wenzel wetting behaviour). This was visualised by pipetting water-based methylene blue droplets onto the films at a tilted angle where water droplets appeared pinned to the surface forming an irregularly shaped sphere, **Figure 5.15**. In all cases, although the water droplet slid down the material's surface, subsequent methylene blue drops on the same area were completely immersed in the droplet's water residue and did not slide off in the form of an irregularly shaped droplet, as previously described. The methylene blue droplet only regained its pinned-spherical shape

on reaching a dry part of the film. Azimi *et al.* obtained CAHs of *ca.* 40° - 58° and Yasmeen *et al*. also obtained relatively high CAH values for CeO_2 films.[159,164] This was also confirmed by the high sliding angles (>24°), limiting the droplet's ability to slide across the surface. This pinning effect reduced as the CeO_2 coverage increased with increased CeO_2 layers. This also indicated that a rough superhydrophobic underlayer facilitated the movement of water droplets across the surface as the CAH and SA were lower in all cases, relative to their counterparts without the superhydrophobic underlayer.

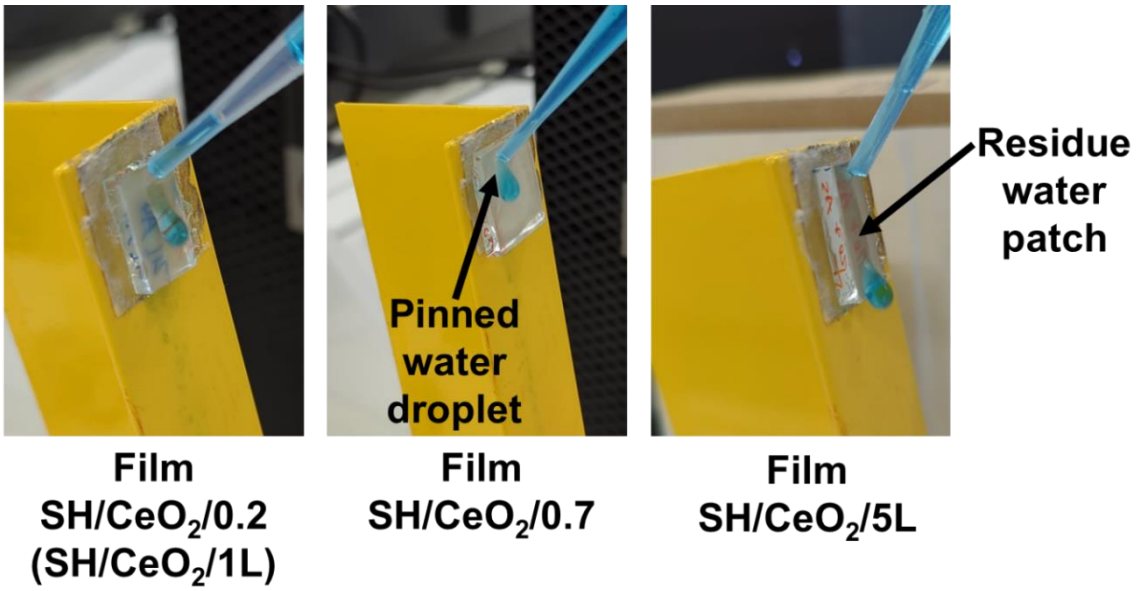

Figure 5.15. *The visual representation of the water repellence of films* ***SH/CeO₂/0.2****,* ***SH/CeO₂/0.7*** *and* ***SH/CeO₂/5L*** *using methylene blue.*

As a result of the WCA, SA and CAH measurements, films **SH/CeO₂/0.2** (also known as film **SH/CeO₂/1L**), **SH/CeO₂/0.7** and **SH/CeO₂/5L** were pursued for further testing to better understand their durability. Initially pencil hardness testing was carried out and films **SH/CeO₂/0.2, SH/CeO₂/0.7** and **SH/CeO₂/5L** could tolerate pencil hardness' of F, 3H and greater than 6H, respectively. This indicated that an increased concentration of deposited CeO_2 boosted the overall durability relative to the uncoated **SH** film with a hardness of F. Relative to the **SH/TiO₂** films deposited via AACVD (**Chapter 3**), these films displayed similar levels of tolerable hardness due to the strong MO bond which improved the durability of the film as the concentration of the MO precursor increased.

Within the Carmalt/Parkin research group and the literature, there have been reports on the increase in WCA of the CeO_2 films overtime.[173] Therefore, the films were left on a lab benchtop and the WCAs were measured *ca.* 10 days for 30

days. Interestingly, there was a reduction in WCA for all **SH/CeO_2** films in **Study 1** and **Study 2** and across all 30 days of the investigation, **Figure 5.16**. There was the occasional increase in WCA (film **SH/CeO_2/5L**) however in most cases, this reduced after a few days. In line with the literature, the **CeO_2/0.2**, **CeO_2/1L** and **CeO_2/5L** films had an increase in WCA as the days progressed.[173] Explanations for this included the absorption of hydrocarbons which lowered the overall surface energy and contribute to the rough microstructure.[110] In spite of this, there is no clear microscopic-level explanation for this observed attribute. However, film **SH/CeO_2/0.7** demonstrated a decrease in WCA of *ca.* 18°. This may have been due to a high O/Ce ratio. If this is high, it creates greater areas for hydrogen bonding with H_2O, potentially atmospheric moisture, reducing the WCA.[158] This is especially due to the superhydrophobic underlayer significantly comprising of C, O, Si and H. The potential patchiness of the deposition may have exposed more O sites whereas for film **SH/CeO_2/5L**, where its XPS spectrum (**Figure 5.10)** demonstrated a pin-hole free CeO_2 film of at least 5 nm.

Although there have been literature reports on the durability, particularly heat durability of CeO_2, after 5 h of heating films **SH/CeO_2/0.7** and **SH/CeO_2/5L** at 300 °C, they both became superhydrophilic. Therefore, it was impossible to measure the WCA and resulting CAH. However, film **SH/CeO_2/0.2** (also known as film **SH/CeO_2/1L**) became hydrophilic with a WCA of 29 ± 3°. Azimi *et al.* annealed a sintered ceria pellet at 1000 °C for 5 h.[159] The resulting film had a 3° increase in WCA, contrary to the results demonstrated in this Chapter, potentially due to heat-treating for 5 h rather than 2 h as reported in the literature. Similarly, Yasmeen *et al.* saw maintained hydrophobicity (maximum reduction in WCA of *ca.* 5°) on annealing CeO_2 films deposited on glass substrates for 2 h at various temperatures from 200 – 500 °C.[164] Similarly Oh *et al.* reported a 38% decrease in WCA for a CeO_2 on annealing the films in air at 500 °C for 2 h.[76] In fact, reductions in WCA were observed for all rare-earth oxides annealed at the same time and for the same duration. The reason for the reduction in hydrophobicity on annealing was due to a material's hygroscopy.[174] A highly hygroscopic material absorbs more moisture, leading to O-H bonds with the rare earth oxides' surface rendering it hydrophilic. High temperature annealing (and possibly durations) facilitated these interactions.[76] Nonetheless, hygroscopy depends on the electronegativity of the metal with highly electronegative elements displaying low

hygroscopy and hence high hydrophobicity.[175] Ce has a relatively low electronegativity of 1.12 relative to other rare earth oxides (e.g. Y: 1.22 and Er: 1.24), hence high hygroscopic nature, a rationale for the low WCA on annealing at 300 °C for 5 h.[76]

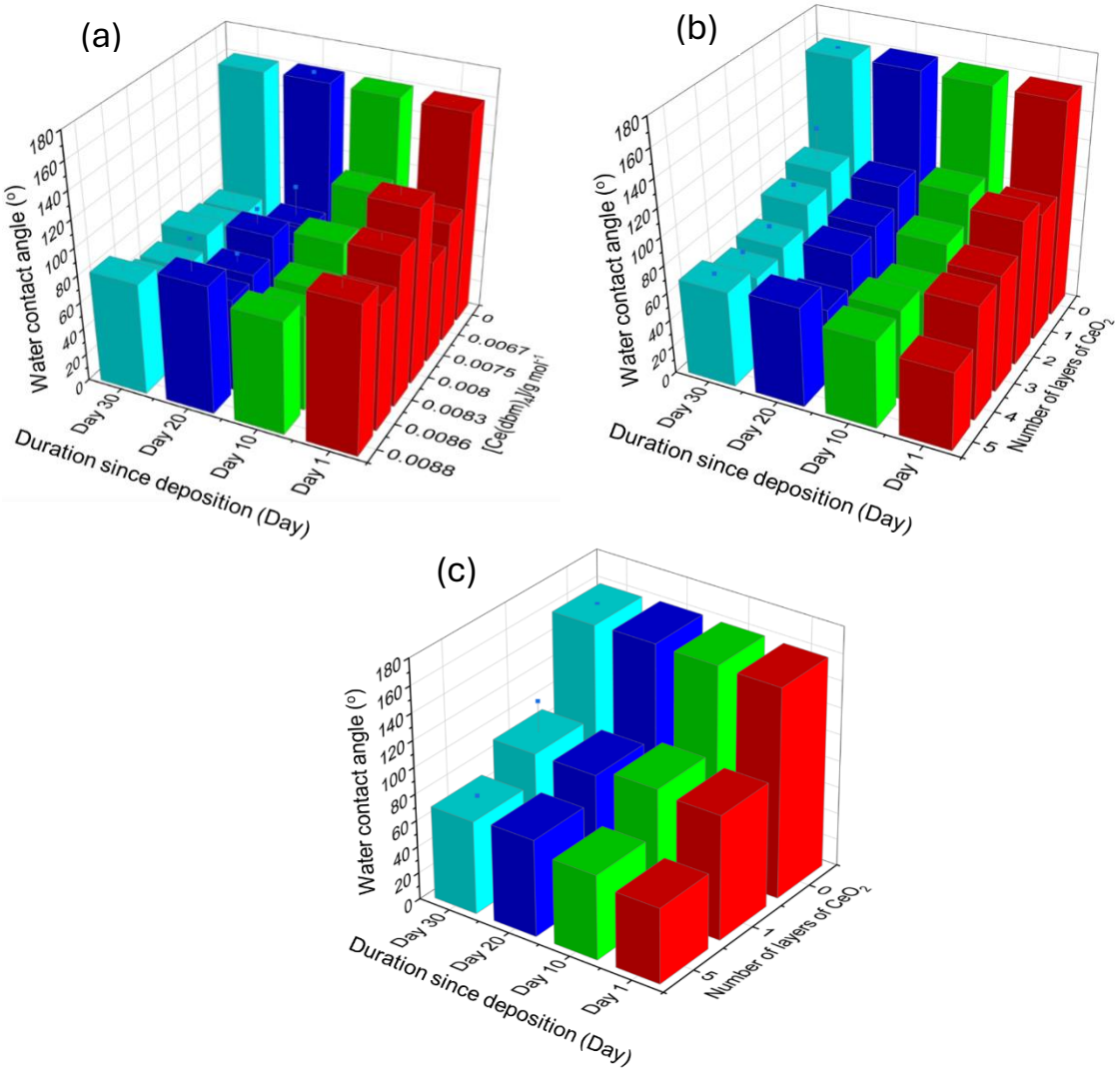

Figure 5.16. *A study of the changes in WCA across a 30-day period for (a)* ***Study 1****:* ***SH/CeO₂*** *films only (b)* ***Study 2****:* ***SH/CeO₂*** *films only and (c)* ***Study 2****:* ***CeO₂*** *films.*

Films **SH/CeO₂/0.2**, **SH/CeO₂/0.7** and **SH/CeO₂/5L** were irradiated with UV light for 7 days, **Figure 5.17**. Focusing on the first two days of exposure, the biggest reduction in WCA was for film **SH/CeO₂/0.7**, where the WCA of the film reduced from 91 ± 3° to 67 ± 15° (*ca.* 24°). There are reports for rare earth oxides more generally losing their hydrophobicity over time.[164] The UV light may have facilitated the absorption of atmospheric moisture due to the hygroscopy of CeO_2 and hence induced hydrophilicity in the film.[174] The second biggest reduction was

for film **SH/CeO$_2$/0.2** of *ca.* 8° indicating the formation of some hydrogen bonding to CeO$_2$ but less than for film **SH/CeO$_2$/0.7** due to a lower concentration of [Ce(dbm)$_4$] used. Finally, film **SH/CeO$_2$/5L** had minimal decrease in WCA potentially indicating that a multi-layered approach provided greater overall protection to the polymer-based superhydrophobic undercoat or that the hydrogen bonding of moisture to the Ce centre had occurred prior to UV irradiation. Interestingly, film **SH/CeO$_2$/5L** exhibited an increase in WCA of *ca.* 9° by the seventh day of UV exposure as reported by Li *et al* who regenerated the hydrophobicity of CeO$_2$ films deposited on glass substrates via UV.[176] Film **SH/CeO$_2$/0.2** demonstrated a minimal increase in WCA by the seventh day which could have been due to the movement of the hydrocarbons from the superhydrophobic underlayer on exposure to UV as demonstrated by work by Oh *et al*.[156] It is important to add that the **SH** film retained superhydrophobicity across all days of the study as per **Chapter 2**, **Section 2.5**. The large standard deviation measured for films **SH/CeO$_2$/0.2** and **SH/CeO$_2$/0.7** as the investigation progressed indicated the destruction of the film and potentially exposure of the underlying rough morphology in cases where the WCA was greater than the starting value. From these studies, it is clear that morphology and multi-layered approaches (a **SH** film or the film itself) greatly influence wettability. The CAH of films **SH/CeO$_2$/0.2** and **SH/CeO$_2$/5L** increased to 17 ± 7° and 16 ± 4°, respectively. The CAH of film **SH/CeO$_2$/0.7** decreased to 20 ± 7°.

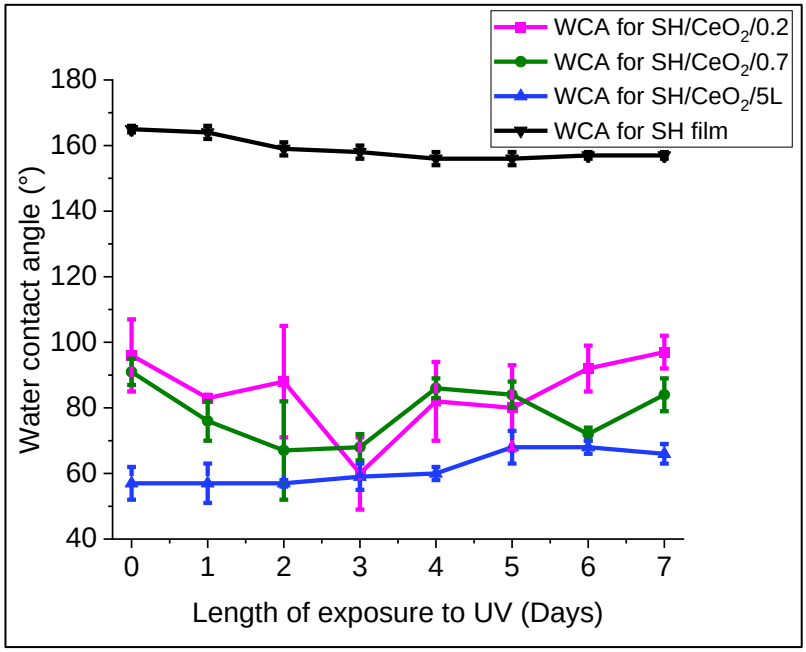

Figure 5.17. *Graph showing changes in WCA for films* ***SH/CeO$_2$/0.2****,* ***SH/CeO$_2$/0.7*** *and* ***SH/CeO$_2$/5L*** *over a 7-day UV irradiation study.*

Table 20. *Changes in WCA of films* ***SH/CeO₂/0.2*** *(****SH/CeO₂/1L****),* ***SH/CeO₂/0.7*** *and* ***SH/CeO₂/5L****.*

	Water contact angle (°)		
Cycle number	Film **SH/CeO₂/0.2** and **SH/CeO₂/1L**	Film **SH/CeO₂/0.7 (Study 1)**	Film **SH/CeO₂/5L (Study 2)**
Before test	82 ± 15	90 ± 13	62 ± 2
After 5 cycles	61 ± 4	79 ± 6	73 ± 1
After 10 cycles	68 ± 2	84 ± 7	59 ± 2
After 20 cycles	69 ± 7	74 ± 3	59 ± 2
After 30 cycles	74 ± 8	79 ± 8	58 ± 2
After 50 cycles	73 ± 7	79 ± 14	54 ± 1
After 75 cycles	66 ± 6	80 ± 3	48 ± 0
After 100 cycles	65 ± 4	72 ± 6	52 ± 2
After 125 cycles	71 ± 9	81 ± 4	53 ± 0
After 150 cycles	64 ± 11	75 ± 3	44 ± 0
After 175 cycles	71 ± 8	69 ± 1	51 ± 5
After 200 cycles	67 ± 6	79 ± 4	62 ± 8
After 250 cycles	68 ± 11	66 ± 2	43 ± 0
After 300 cycles	63 ± 8	68 ± 3	44 ± 3
After 350 cycles	67 ± 8	69 ± 3	50 ± 0
After 400 cycles	68 ± 9	72 ± 4	46 ± 2
After 500 cycles	64 ± 6	66 ± 5	50 ± 2
After 600 cycles	69 ± 11	66 ± 2	46 ± 2
CAH	21 ± 9	24 ± 6	15 ± 3

Film **SH/CeO₂/5L** had a lower reduction in WCA (16°) relative to film **SH/CeO₂/0.7** (24°), indicating greater durability through utilising a multi-layered approach. Interestingly, film **SH/CeO₂/1L** had the lowest reduction in WCA of only 12°. This unanticipated difference may have been due to the film thickness of the dual-layered films and hence the point in the thickness spectrum that the tape peel had taken taken place. The WCAs prior and post the tape peel test were subtracted from each other. The WCAs recorded prior and post-tape peeling of film **SH/CeO₂/0.7** were akin to the values reported in the literature although the deposition technique used was 50 spray coats of a CeO_2 NP solution rather than AACVD.[164] The actual WCAs (rather than the difference) obtained for film

SH/CeO_2/5L were significantly lower than the literature. Nevertheless, the standard deviation for film **SH/CeO_2/0.7** remained relatively high indicating an inhomogeneous deposition whereas on many occasions, the standard deviation for film **SH/CeO_2/5L** was zero. This is also corroborated by the high CAH of film **SH/CeO_2/0.7** relative to film **SH/CeO_2/5L, Table 19.** Interestingly, for all tested films, the CAH increased **(Tables 19** and **20).** For instance, film **SH/CeO_2/1L** initially started with a CAH of 9 ± 3° which rose to 21 ± 9°, film **SH/CeO_2/5L** started at 14 ± 4° which increased to 15 ± 3° and finally film **SH/CeO_2/0.7** originally had a CAH of 22 ± 8° which 24 ± 6° became after 600 tape peel cycles. In all cases, these increases confirmed the inhomogeneity of the film's surface (e.g. flat and rough patches, CeO_2-coated superhydrophobic NPs and no CeO_2-coated superhydrophobic NPs).

Generally, the WCA reduced as the number of tape peel cycles increased indicating the removal of the rough morphology. As demonstrated previously in the EDS scans, **Figure 5.04**, the Ce did not cover the whole surface for either **SH/CeO_2/0.7** or **SH/CeO_2/5L**. Therefore, any decrease followed by increase in WCA may have been due to exposure of some parts of the underlying rough morphology and potentially removal of CeO_2 as compared to its counterpart, CeO_2 deposited on plain FTO glass had WCAs of *ca.* 50°. Interestingly, the WCA did not become >150°, even for film **SH/CeO_2/1L** after 600 tape peel cycles either due not reaching the bulk **SH** film or due to chemical changes to the properties of the underlying superhydrophobic layer, no longer rendering it superhydrophobic.

In relation to titania deposited onto **SH** films via AACVD (**Chapter 3**), the calculated range for the changes in WCA remained similar to those quantified for the **SH/CeO_2** films confirming similar durability and changes to the morphology.

5.6 Summary

CeO_2 surface modified **SH** films were deposited by two routes. The first (**Study 1**) involved varying the concentration of the $[Ce(dbm)_4]$ precursor and the second (**Study 2**) involved depositing layers of a fixed concentration of the same precursor. The $[Ce(dbm)_4]$ precursor was deposited via AACVD at 450 °C. Study 2 confirmed enhanced uniformity by depositing the CeO_2 via a multi-layered approach.

Increased concentration of $[Ce(dbm)_4]$ showed a non-linear increase in WCA and transmittance confirming the non-uniformity of this deposition method as well as the limited range of trialled precursor concentrations. In fact, film thickness measurements indicated that their counterparts – films **CeO_2/0.2** and **CeO_2/0.7** had no increase in film thickness, confirming that the $[Ce(dbm)_4]$ used were minimal. The standard WCA for the CeO_2 films deposited by AACVD were 50°. The root-mean-square height measurements confirmed changes to the morphology in increased $[Ce(dbm)_4]$ and SEM exhibited the formation of spherical particles which were smaller than for the films of **Study 2**. EDS scans also confirmed the lack of uniformity of the CeO_2 film. Unfortunately, it was difficult to confirm the successful deposition of CeO_2 for the films fabricated by **Study 1** as the analytical methods displayed conflicting results, potentially due to the patchiness of the depositions.

XPS confirmed that **Study 2**, a multi-layered approach, produced uniform pin-hole free CeO_2 films in contrast to **Study 1**. The improved deposition process was visualised in the SEM images of the resulting films, containing spherical CeO_2 nanoparticles clustering on the superhydrophobic particles and also within the matrix. The PXRD patterns for the films of **Study 1** revealed that CeO_2 was deposited in an amorphous form with some key peaks obscured by the broadness of the peak. Alternatively, **Study 2** produced patterns of some crystallinity with all peaks matching the reference for cerianite.

In both studies, significant deposition challenges were encountered primarily as the $[Ce(dbm)_4]$ is a solid precursor with a limited decomposition window causing pre-decomposition. The pre-decomposition of the $[Ce(dbm)_4]$ precursor in the baffle and the heated AACVD rig was unavoidable causing some blockage and better film formation on parts of the substrate closest to the inlet of the rig. In both

cases, changes in WCA may have been due to the increased surface energy of CeO_2 relative to the components of the **SH** film.

Unfortunately, the films of either study did not display enhanced self-cleaning properties with comparatively similar contact angle hysteresis measurements relative to the uncoated **SH** film and **SH/TiO_2** films deposited via AACVD, >20°. As with the **SH/TiO_2** films deposited via AACVD, the additional MO layer(s) improved the overall durability, with the ability to tolerate “harder” pencils than the **SH** film alone. Unlike previous reports, most of the films did not show an improvement in hydrophobicity when left untouched for a 30-day study. Surprisingly, the **SH/CeO_2** as well as the **SH/TiO_2** films deposited by AACVD demonstrated poor thermal and some UV stability (namely film **SH/CeO_2/0.7**) relative to the uncoated **SH** films.

The work within this chapter demonstrates the possibility of depositing CeO_2 on top of a **SH** film via AACVD. It confirms that a multi-layered approach of depositing several layers of CeO_2 improves the film’s coverage rather than varying the concentration of the solid precursor in a one-pot procedure.

Conclusion & Future Work

Investigations for this PhD thesis have followed three main routes. The first was the fabrication of a fluorine-free superhydrophobic film followed by its surface modification by TiO_2 via AACVD and ALD and finally, surface modification of the same superhydrophobic film by CeO_2 via AACVD. The aim was to fabricate multi-functional coatings displaying water repellence, photocatalytic activity and enhanced robustness relative to non-surface modified superhydrophobic films.

Within **Chapter 2**, reproducible fluorine-free superhydrophobic films were fabricated from a 50:50 mixture of stearic acid and palmitic acid, SYLGARD 184, its respective curing agent and SiO_2 NPs. This simple mixture afforded films with WCAs exceeding 160°. Superhydrophobicity may have arisen from the rough topology of the interconnected network of particles, generated by the combination of all reagents and low surface energy of the fatty acids and SYLGARD 184. Investigations into tuning the AACVD parameters such as deposition temperature and duration as well as changes to deposition mixture were pursued to determine the best combination for maintained superhydrophobicity. The deposition temperature had a significant effect on the resulting water contact angles, with a deposition temperature of 400 °C leading to a hydrophobic water contact angle (129 ± 7°). A deposition temperature 40 °C led to a superhydrophobic water contact angle of 162 ± 2° due to changes in the morphology and roughness of the film.

Further studies into the concentration of the precursor mixture and deposition length concluded that more reliable repeats were obtained by altering the former rather than the latter. This is because it was harder to control the rate of aerosol formation which was dependent on the volume of precursor solution in the flask and temperature of the humidifier. The humidifier would switch off at elevated temperatures. Later work demonstrated that halving the concentration of the precursor mixture resulted in equally superhydrophobic films with higher water contact angles, improved transmittance values (*ca.* 34 %) and less wastage. Although the films exhibited poor transmittance (<20 %), they displayed retained superhydrophobicity after several mechanical durability tests such as UV exposure, tape peel testing and heat-treatment.

Subsequently, **Chapter 3** focused on the surface tuning of the fluorine-free superhydrophobic film fabricated in **Chapter 2** by TiO_2 (precursor: TTIP) via AACVD. By varying the concentration of the TTIP precursor, dual-layered **SH/TiO_2** films were produced. Although a reduction in water contact angle was seen with increasing TTIP concentration, the resulting films demonstrated variable wettability, even across the film, confirmed by the large WCA standard deviations. As expected, the standard deviations of the WCAs reduced with increasing TTIP concentration. Nevertheless, plasma treatment was required for all superhydrophobic films prior to TiO_2 deposition to improve coverage. A gradual increase in the density of the TiO_2 agglomerates coating the superhydrophobic film and its matrix was observed with increasing TTIP concentration, leading to a reduction in Sq roughness values from 0.28 μm for the uncoated superhydrophobic film to 0.18 μm for the film with the greatest TTIP concentration.

Although there was also a significant reduction in contact angle hysteresis with increasing TTIP concentration and hence physical self-cleaning properties, there was an improvement in chemical self-cleaning (photocatalytic) properties determined by stearic acid degradation testing. The **SH/TiO_2** films outcompeted the TiO_2 films without the superhydrophobic underlayer due to an increase in surface area, displaying a 50% reduction in stearic acid coverage. It was not possible to use the standard Resazurin dye due to poor coverage and adhesion of the dye to the superhydrophobic film. Unlike the uncoated **SH** film, the **SH/TiO_2** films displayed poorer robustness with loss of hydrophobicity on exposure to heat and UV light. Nevertheless, the TiO_2 provided significant protection against the hardest tested pencil (6H).

For comparison, the superhydrophobic films were also surface modified with TiO_2 deposited via ALD (precursor: TDMAT and ozone) to compare the deposition process and precursor. As TDMAT was more reactive than the TTIP precursor, ultrathin conformal layers of TiO_2 were deposited. Even at 4 nm, changes in WCA were observed with relatively lower standard deviations. Nevertheless, due to the increased surface area of the superhydrophobic film, it was more challenging to control the deposition conditions than for a plain FTO substrate or Si wafer. Hence, for **Study B** of this chapter, plasma treatment of the superhydrophobic films negatively influenced the subsequent TiO_2 deposition with the TDMAT

precursor. This contrasted with the films fabricated in **Chapter 3**, where plasma treatment was necessary for even a thin coating of TiO_2 on top of the superhydrophobic film.

In both **Studies A** and **B**, it was difficult to observe clear changes to the morphology by SEM on the addition of a TiO_2 film. Nevertheless, spectroscopic analysis such as XPS and Raman confirmed the successful deposition of TiO_2 for all films. Photocatalytic activity was also improved relative to the uncoated superhydrophobic films however, it was not as enhanced as the **SH/TiO_2** films of **Chapter 3**. As with the **SH/TiO_2** films of **Chapter 3**, there was a reduction in physical self-cleaning properties. There was a smaller reduction in water contact angle after 400 tape peel cycles relative to the **SH/TiO_2** films of **Chapter 3**. This suggested stronger adhesion between the TiO_2 film and superhydrophobic undercoat of the ALD-deposited films and the lack of exposure of the superhydrophobic undercoat with increased tape peel cycles.

Finally, the superhydrophobic films described in **Chapter 2** were surface tuned with CeO_2 via AACVD. Initially, the concentration of the $[Ce(dbm)_4]$ precursor solution was varied to deposit CeO_2 films of varying thickness (**Study 1**). However, the precursor used, $[Ce(dbm)_4]$, was a solid and posed several challenges from poor dissolution through to pre-decomposition in the baffle. As a result, a limited range of precursor solution concentrations could be deposited. To overcome these challenges, a multilayered deposition approach (**Study 2**) was pursued leading to a more uniform CeO_2 coating by the 5^{th} layer of CeO_2. SEM revealed the clustering of CeO_2 nanoparticles which primarily focused on the hierarchical roughness but with increased CeO_2, also coated the matrix. WCAs reduced from 94° for a single CeO_2 layer to 57° for five layers of CeO_2. Methylene blue water repellence testing showed that the droplet pinned to the surface leading to a reduction in physical self-cleaning. In addition, the **SH/CeO_2** films demonstrated poor mechanical durability, with significant reductions in water contact angle on exposure to UV-light, heat and on being left untouched on a lab benchtop for 30 days.

Despite the challenges described on surface modifying a superhydrophobic film with a metal oxide, this work demonstrated that it is possible to tune the surface of a superhydrophobic film and achieve observable changes in properties (morphology, wettability, photocatalytic activity and durability).

Future work could focus on the improvement of the properties of the superhydrophobic film and/or surface modified-dual layered films. A simple approach would be to incorporate a third fatty acid to the 50:50 stearic acid and palmitic acid precursor mixture to determine how the morphology and water contact angle changes. As previously described in **Chapter 2**, particles of 3 different size ranges led to enhanced water contact angles relative to the films with 2 size ranges. The third fatty acid could be longer or shorter than stearic acid.

In a separate study, it would be interesting to determine how using a completely different combination of fatty acids to stearic acid and palmitic acid could affect the properties of the resulting films from its morphology through to its water contact angle and durability. For example, one could employ fatty acids within the range of “very long-chain fatty acids” with carbon chain lengths of C22 to C28. Within this range of fatty acids, it would also be intriguing to utilise unsaturated fatty acids to establish whether the fatty acid would bind through its C=C to the reactants, determined by XPS and hence, what the effect, if any, would be on the film.

In addition to changes to the precursor mixtures, future work could involve depositing the above precursor mixtures by various bottom-up techniques such as dip-coating and spin-coating. These techniques are easier to implement and significantly “greener” therefore, achieving the same properties with a more sustainable technique would be promising. Similarly, various substrates could be utilised for deposition such as metal plates, woods and cotton for a greater range of applications including furniture and clothing.

With regards to the surface modification of the superhydrophobic films with metal oxides, rare earth oxides such as Er and Y which are more hydrophobic than Ce, should be deposited via ALD for greater deposition control and hence uniformity of the film. As mentioned in **Chapter 5**, there were significant challenges in the solvation and deposition of the [$Ce(dbm)_4$] precursor hence, a liquid precursor could be deposited instead such as [$Ce(mmp)_4$] where mmp is 1-(methoxy)-2-methyl-2-propanolato. Although it is known for having a lower thermal stability, it may be possible to deposit it at significantly lower deposition temperatures than previously used for the [$Ce(dbm)_4$] precursor.

Alternatively, more reactive titania precursors such as titanium diisopropoxide bis(acetylacetonate) should be deposited on the superhydrophobic films via AACVD. In addition, metal oxides, metal sulfides and metal nitrides could also be deposited on top of the superhydrophobic films via ALD or AACVD to investigate their resultant properties.

Additional investigations into the combination of two or more metal oxides deposited onto a single superhydrophobic film should be investigated to determine whether it is possible to fabricate multi-layered films (rather than dual-layered) multi-functional superhydrophobic coatings. Finally, to potentially improve the adhesion of the films and physical self-cleaning properties whilst attempting to maintain the chemical self-cleaning behaviour of the dual-layered films further, it would be interesting to deposit the metal oxide first and then the superhydrophobic material.

Publications

1. F. Chen, J. J. Kalmoni, S. Liu, C. J. Carmalt, Robust, Fluorine-Free Superhydrophobic Films on Glass via Epoxy silane Pretreatment (in review at ACS Langmuir)

2. J. J. Kalmoni, C. S. Blackman, C. J. Carmalt, Tuneable Wetting of Fluorine-Free Superhydrophobic Films via Titania Modification to Enhance Durability and Photocatalytic Activity, Adv. Mater. Interfaces, 2024, 2400519
   DOI: https://doi.org/10.1002/admi.202400519

3. J. Huo, C. D. L. Reyes, J. J. Kalmoni, S. Park, G. B. Hwang, S. Sathasivam, C. J. Carmalt, Superhydrophobic Hexadecyltrimethoxysilane-Modified Fumed Silica Nanostructure/Poly(butyl methacrylate) Composite Thin Films via Aerosol-Assisted Deposition: Implications for Self-Cleaning Surfaces, *ACS Appl. Nano Mater.*, 2023, **6**, 16383–16391.
   DOI: https://doi.org/10.1021/acsanm.3c02575

4. J. J. Kalmoni, F. L. Heale, C. S. Blackman, I. Parkin, C. J. Carmalt, A Single-Step Route to Robust and Fluorine-Free Superhydrophobic Coatings via Aerosol-Assisted Chemical Vapor Deposition, *Langmuir* 2023, **39**, 22, 7731-7740.
   DOI: https://doi.org/10.1021/acs.langmuir.3c00554

5. S. Park, J. Huo, J. Shin, K. J. Heo, J. J. Kalmoni, S. Sathasivam, G. B. Hwang, Production of an EP/PDMS/SA/AlZnO Coated Superhydrophobic Surface through an Aerosol-Assisted Chemical Vapor Deposition Process, *Langmuir* 2022, **38**, 25, 7825–7832.
   DOI: https://doi.org/10.1021/acs.langmuir.2c01060

Division of labour/Author contribution statement

Dr. Joanna Borowiec and Dr. Shuhui Liu carried out XPS scanning of all films.

Dr. Shuhui Liu carried out the SEM and EDS presented in **Figures 4.08, 4.09, 4.10** and **4.11.**

References

1 W. Barthlott and C. Neinhuis, Purity of the sacred lotus, or escape from contamination in biological surfaces, *Planta*, 1997, **202**, 1–8.

2 J. Jeevahan, M. Chandrasekaran, G. Britto Joseph, R. B. Durairaj and G. Mageshwaran, Superhydrophobic surfaces: a review on fundamentals, applications, and challenges, *J. Coatings Technol. Res.*, 2018, **15**, 231–250.

3 L. B. Boinovich, A. M. Emelyanenko, V. K. Ivanov and A. S. Pashinin, Durable icephobic coating for stainless steel, *ACS Appl. Mater. Interfaces*, 2013, **5**, 2549–2554.

4 G. Barati Darband, M. Aliofkhazraei, S. Khorsand, S. Sokhanvar and A. Kaboli, Science and Engineering of Superhydrophobic Surfaces: Review of Corrosion Resistance, Chemical and Mechanical Stability, *Arab. J. Chem.*, 2020, **13**, 1763–1802.

5 T. Wang, X. Hu and S. Dong, A general route to transform normal hydrophilic cloths into superhydrophobic surfaces, *Chem. Commun.*, 2007, 1849–1851.

6 S. P. Dalawai, M. A. Saad Aly, S. S. Latthe, R. Xing, R. S. Sutar, S. Nagappan, C. S. Ha, K. Kumar Sadasivuni and S. Liu, Recent Advances in durability of superhydrophobic self-cleaning technology: A critical review, *Prog. Org. Coatings*, 2020, **138**, 105381.

7 K. Manoharan and S. Bhattacharya, Superhydrophobic surfaces review: Functional application, fabrication techniques and limitations, *J. Micromanufacturing*, 2019, **2**, 59–78.

8 K. Koch and W. Barthlott, Superhydrophobic and superhydrophilic plant surfaces: An inspiration for biomimetic materials, *Philos. Trans. R. Soc. A Math. Phys. Eng. Sci.*, 2009, **367**, 1487–1509.

9 Y. Wang, X. Yao, S. Wu, Q. Li, J. Lv, J. Wang and L. Jiang, Bioinspired Solid Organogel Materials with a Regenerable Sacrificial Alkane Surface Layer, *Adv. Mater.*, 2017, **29**, 1–7.

10 P. Roach, N. J. Shirtcliffe and M. I. Newton, Progess in superhydrophobic

surface development, *Soft Matter*, 2008, **4**, 224.

11 L. Gao and T. J. McCarthy, Contact angle hysteresis explained, *Langmuir*, 2006, **22**, 6234–6237.

12 T. Huhtamäki, X. Tian, J. T. Korhonen and R. H. A. Ras, Surface-wetting characterization using contact-angle measurements, *Nat. Protoc.*, 2018, **13**, 1521–1538.

13 H. B. Eral, D. J. C. M. 'T Mannetje and J. M. Oh, Contact angle hysteresis: A review of fundamentals and applications, *Colloid Polym. Sci.*, 2013, **291**, 247–260.

14 X. J. Guo, C. H. Xue, S. Sathasivam, K. Page, G. He, J. Guo, P. Promdet, F. L. Heale, C. J. Carmalt and I. P. Parkin, Fabrication of robust superhydrophobic surfaces via aerosol-assisted CVD and thermo-triggered healing of superhydrophobicity by recovery of roughness structures, *J. Mater. Chem. A*, 2019, **7**, 17604–17612.

15 S. S. Chhatre, J. O. Guardado, B. M. Moore, T. S. Haddad, J. M. Mabry, G. H. McKinley and R. E. Cohen, Fluoroalkylated silicon-containing surfaces-estimation of solid-surface energy, *ACS Appl. Mater. Interfaces*, 2010, **2**, 3544–3554.

16 J. N. Israelachvili, in *Intermolecular and Surface Forces*, ed. J. N. Israelachvili, Elsevier, 3rd edn., 2011, pp. 341–380.

17 E. Poli, K. H. Jong and A. Hassanali, Charge transfer as a ubiquitous mechanism in determining the negative charge at hydrophobic interfaces, *Nat. Commun.*, 2020, **11**, 1–13.

18 I. Ahmad and C. W. Kan, A Review on Development and Applications of Bio-Inspired Superhydrophobic Textiles, *Materials (Basel).*,2016, **9**, 1-34.

19 S. Vudayagiri, M. D. Junker and A. L. Skov, Factors affecting the surface and release properties of thin polydimethylsiloxane films, *Polym. J.*, 2013, **45**, 871–878.

20 B. Shaoxian and W. Shizhu, in *Gas Thermohydrodynamic Lubrication and Seals*, Academic Press, Cambridge, 1st edn., 2019, pp. 143–165.

21 S. Parvate, P. Dixit and S. Chattopadhyay, Superhydrophobic Surfaces: Insights from Theory and Experiment, *J. Phys. Chem. B*, 2020, **124**,

1323–1360.

22 D. A. Onishchenko, Analytical approach to the calculation of the design values of the loads associated with discrete ice features, *Proc. Int. Conf. Port Ocean Eng. under Arct. Cond. POAC*, 2009, **2**, 1013–1023.

23 R. N. Wenzel, Resistance of solid surfaces to wetting by water, *Ind. Eng. Chem.*, 1936, **28**, 988–994.

24 A. B. D. Cassie and Baxter S., Wettability of porous surfaces, *Trans. Faraday Soc.*, 1944, **40**, 546–551.

25 Y. Deng, C. Peng, M. Dai, D. Lin, I. Ali, S. S. Alhewairini, X. Zheng, G. Chen, J. Li and I. Naz, Recent development of super-wettable materials and their applications in oil-water separation, *J. Clean. Prod.*, 2020, **266**, 1–26.

26 G. Smyth, in *Nanocoatings and Ultra-Thin Films*, eds. A. S. H. Makhlouf and I. Tiginyanu, Woodhead Publishing, Cambridge, 1st edn., 2018, pp. 3–23.

27 P. Kothary, X. Dou, Y. Fang, Z. Gu, S. Y. Leo and P. Jiang, Superhydrophobic hierarchical arrays fabricated by a scalable colloidal lithography approach, *J. Colloid Interface Sci.*, 2017, **487**, 484–492.

28 M. K. Meena, A. Sinhamahapatra and A. Kumar, Superhydrophobic polymer composite coating on glass via spin coating technique, *Colloid Polym. Sci.*, 2019, **297**, 1499–1505.

29 Q. F. Xu, B. Mondal and A. M. Lyons, Fabricating superhydrophobic polymer surfaces with excellent abrasion resistance by a simple lamination templating method, *ACS Appl. Mater. Interfaces*, 2011, **3**, 3508–3514.

30 S. Wang, C. Liu, G. Liu, M. Zhang, J. Li and C. Wang, Fabrication of superhydrophobic wood surface by a sol-gel process, *Appl. Surf. Sci.*, 2011, **258**, 806–810.

31 L. Xie, Z. Tang, L. Jiang, V. Breedveld and D. W. Hess, Creation of superhydrophobic wood surfaces by plasma etching and thin-film deposition, *Surf. Coatings Technol.*, 2015, **281**, 125–132.

32 P. Marchand, I. A. Hassan, I. P. Parkin and C. J. Carmalt, Aerosol-

assisted delivery of precursors for chemical vapour deposition: expanding the scope of CVD for materials fabrication, *Dalt. Trans.*, 2013, **42**, 9406–9422.

33 H. Lee, S. Hong, K. Yang and K. Choi, Fabrication of 100 nm metal lines on flexible plastic substrate using ultraviolet curing nanoimprint lithography, *Appl. Phys. Lett.*, 2006, **88**, 1–4.

34 H. Zhang, J. Gan, Y. Wu and Z. Wu, Biomimetic high water adhesion superhydrophobic surface via UV nanoimprint lithography, *Appl. Surf. Sci.*, 2023, **633**, 157610.

35 F. Liu, A. Liu, W. Tao and Y. Yang, Preparation of UV curable organic/inorganic hybrid coatings-a review, *Prog. Org. Coatings*, 2020, **145**, 105685.

36 K. Keerthi, S. D. George, R. Ongole and V. K. Unnikrishnan, Fabrication of a Low Cost Superhydrophobic Substrate for Surface Enhanced Laser-Induced Breakdown Spectroscopy and Its Utility through Identification of Electrolyte Variation for Oral Cancer Detection, *ACS Biomater. Sci. Eng.*, 2024, **10**, 1153–1161.

37 A. Y. Y. Ho, E. Luong Van, C. T. Lim, S. Natarajan, N. Elmouelhi, H. Y. Low, M. Vyakarnam, K. Cooper and I. Rodriguez, Lotus bioinspired superhydrophobic, self-cleaning surfaces from hierarchically assembled templates, *J. Polym. Sci. Part B Polym. Phys.*, 2014, **52**, 603–609.

38 L. Dong, Z. Zhang, R. Ding, L. Wang, M. Liu, Z. Weng, Z. Wang and D. Li, Controllable superhydrophobic surfaces with tunable adhesion fabricated by laser interference lithography, *Surf. Coatings Technol.*, 2019, **372**, 434–441.

39 Y. Si and Z. Guo, Superhydrophobic nanocoatings: from materials to fabrications and to applications, *Nanoscale*, 2015, **7**, 5922–5946.

40 J. Wang, X. Chen, Y. Kang, G. Yang, L. Yu and P. Zhang, Preparation of superhydrophobic poly(methyl methacrylate)-silicon dioxide nanocomposite films, *Appl. Surf. Sci.*, 2010, **257**, 1473–1477.

41 B. Nomeir, S. Lakhouil, S. Boukheir, M. A. Ali and S. Naamane, Recent progress on transparent and self-cleaning surfaces by superhydrophobic

coatings deposition to optimize the cleaning process of solar panels, *Sol. Energy Mater. Sol. Cells*, 2023, **257**, 112347.

42 V. Jokinen, E. Kankuri, S. Hoshian, S. Franssila and R. H. A. Ras, Superhydrophobic Blood-Repellent Surfaces, *Adv. Mater.*, 2018, **30**, 1705104–1705114.

43 T. Wang, Y. Si, S. Luo, Z. Dong and L. Jiang, Wettability manipulation of overflow behavior: Via vesicle surfactant for water-proof surface cleaning, *Mater. Horizons*, 2019, **6**, 294–301.

44 F. Xiao, S. Yuan, B. Liang, G. Li, S. O. Pehkonen and T. Zhang, Superhydrophobic CuO nanoneedle-covered copper surfaces for anticorrosion, *J. Mater. Chem. A*, 2015, **3**, 4374–4388.

45 I. S. Bayer, Superhydrophobic Coatings from Ecofriendly Materials and Processes: A Review, *Adv. Mater. Interfaces*, 2020, **7**, 1–25.

46 F. L. Heale, K. Page, J. S. Wixey, P. Taylor, I. P. Parkin and C. J. Carmalt, Inexpensive and non-toxic water repellent coatings comprising SiO_2 nanoparticles and long chain fatty acids, *RSC Adv.*, 2018, **8**, 27064–27072.

47 M. A. Osman and U. W. Suter, Surface treatment of calcite with fatty acids: Structure and properties of the organic monolayer, *Chem. Mater.*, 2002, **14**, 4408–4415.

48 J. Ju, X. Yao, X. Hou, Q. Liu, Y. S. Zhang and A. Khademhosseini, A highly stretchable and robust non-fluorinated superhydrophobic surface, *J. Mater. Chem. A*, 2017, **5**, 16273–16280.

49 Z. Habib, M. Song, S. Ikram and Z. Zahra, Overview of Per- and Polyfluoroalkyl Substances (PFAS), Their Applications, Sources, and Potential Impacts on Human Health, *Pollutants*, 2024, **4**, 136–152.

50 J. Y. Huang, S. H. Li, M. Z. Ge, L. N. Wang, T. L. Xing, G. Q. Chen, X. F. Liu, S. S. Al-Deyab, K. Q. Zhang, T. Chen and Y. K. Lai, Robust superhydrophobic TiO_2@fabrics for UV shielding, self-cleaning and oil-water separation, *J. Mater. Chem. A*, 2015, **3**, 2825–2832.

51 V. H. Dalvi and P. J. Rossky, Molecular origins of fluorocarbon hydrophobicity, *Proc. Natl. Acad. Sci. U. S. A.*, 2010, **107**, 13603–13607.

52 J. Zha, S. S. Ali, J. Peyroux, N. Batisse, D. Claves, M. Dubois, A. P. Kharitonov, G. Monier, T. Darmanin, F. Guittard and L. N. Alekseiko, Superhydrophobicity of polymer films via fluorine atoms covalent attachment and surface nano-texturing, *J. Fluor. Chem.*, 2017, **200**, 123–132.

53 A. Zhuang, R. Liao, S. C. Dixon, Y. Lu, S. Sathasivam, I. P. Parkin and C. J. Carmalt, Transparent superhydrophobic PTFE films via one-step aerosol assisted chemical vapor deposition, *RSC Adv.*, 2017, **7**, 29275–29283.

54 A. Tombesi, S. Li, S. Sathasivam, K. Page, F. L. Heale, C. Pettinari, C. J. Carmalt and I. P. Parkin, Aerosol-assisted chemical vapour deposition of transparent superhydrophobic film by using mixed functional alkoxysilanes, *Sci. Rep.*, 2019, **9**, 1–12.

55 S. Xiang and W. Liu, Self-Healing Superhydrophobic Surfaces: Healing Principles and Applications, *Adv. Mater. Interfaces*, 2021, **8**, 1-23.

56 Y. Wang, Y. Liu, J. Li, L. Chen, S. Huang and X. Tian, Fast self-healing superhydrophobic surfaces enabled by biomimetic wax regeneration, *Chem. Eng. J.*, 2020, **390**, 124311.

57 N. Bai, Q. Li, H. Dong, C. Tan, P. Cai and L. Xu, A versatile approach for preparing self-recovering superhydrophobic coatings, *Chem. Eng. J.*, 2016, **293**, 75–81.

58 S. S. Cassidy, K. Page, C. I. D. L. Reyes, E. Allan, I. P. Parkin and C. J. Carmalt, Modification of Commercial Polymer Coatings for Superhydrophobic Applications, *ACS Omega*, 2024, **9**, 7154–7162.

59 C. Wang and Z. Guo, A comparison between superhydrophobic surfaces (SHS) and slippery liquid-infused porous surfaces (SLIPS) in application, *Nanoscale*, 2020, **12**, 22398–22424.

60 D. Wang and Z. Guo, A bioinspired lubricant infused surface with transparency, hot liquid boiling resistance and long-term stability for food applications, *New J. Chem.*, 2020, **44**, 4259–4537.

61 G. Polizos, G. G. Jang, D. B. Smith, F. A. List, M. G. Lassiter, J. Park and P. G. Datskos, Transparent superhydrophobic surfaces using a spray

coating process, *Sol. Energy Mater. Sol. Cells*, 2018, **176**, 405–410.

62 S. A. Campbell and R. C. Smith, Chemical vapour deposition, *High-K Gate Dielectr.*, 2003, **1**, 65–88.

63 W. A. Bryant, The fundamentals of chemical vapour deposition, *J. Mater. Sci.*, 1977, **12**, 1285–1306.

64 C. E. Knapp and C. J. Carmalt, Solution based CVD of main group materials, *Chem. Soc. Rev.*, 2016, **45**, 1036–1064.

65 N. J. Janowicz, H. Li, F. L. Heale, I. P. Parkin, I. Papakonstantinou, M. K. Tiwari and C. J. Carmalt, Fluorine-Free Transparent Superhydrophobic Nanocomposite Coatings from Mesoporous Silica, *Langmuir*, 2020, **36**, 13426–13438.

66 S. Ashraf, C. S. Blackman, G. Hyett and I. P. Parkin, Aerosol assisted chemical vapour deposition of MoO_3 and MoO_2 thin films on glass from molybdenum polyoxometallate precursors; thermophoresis and gas phase nanoparticle formation, *J. Mater. Chem.*, 2006, **16**, 3575–3582.

67 S. Li, K. Page, S. Sathasivam, F. Heale, G. He, Y. Lu, Y. Lai, G. Chen, C. J. Carmalt and I. P. Parkin, Efficiently texturing hierarchical superhydrophobic fluoride-free translucent films by AACVD with excellent durability and self-cleaning ability, *J. Mater. Chem. A*, 2018, **6**, 17633–17641.

68 A. Zhuang, R. Liao, Y. Lu, S. C. Dixon, A. Jiamprasertboon, F. Chen, S. Sathasivam, I. P. Parkin and C. J. Carmalt, Transforming a Simple Commercial Glue into Highly Robust Superhydrophobic Surfaces via Aerosol-Assisted Chemical Vapor Deposition, *ACS Appl. Mater. Interfaces*, 2017, **9**, 42327–42335.

69 M. Leskelä and M. Ritala, Atomic layer deposition (ALD): From precursors to thin film structures, *Thin Solid Films*, 2002, **409**, 138–146.

70 G. N. Parsons, S. M. George and M. Knez, Progress and future directions for atomic layer deposition and ALD-based chemistry, *MRS Bull.*, 2011, **36**, 865–871.

71 R. W. Johnson, A. Hultqvist and S. F. Bent, A brief review of atomic layer deposition: From fundamentals to applications, *Mater. Today*, 2014, **17**,

236–246.

72 M. Ritala and J. Niinistö, Industrial Applications of Atomic Layer Deposition, *ECS Trans.*, 2019, **25**, 641–652.

73 S. M. George, Atomic layer deposition: An overview, *Chem. Rev.*, 2010, **110**, 111–131.

74 N. Chen, D. H. Kim, P. Kovacik, H. Sojoudi, M. Wang and K. K. Gleason, Polymer Thin Films and Surface Modification by Chemical Vapor Deposition: Recent Progress, *Annu. Rev. Chem. Biomol. Eng.*, 2016, **7**, 373–393.

75 J. Yarbrough, F. Pieck, A. B. Shearer, P. Maue, R. Tonner-Zech and S. F. Bent, Area-Selective Atomic Layer Deposition of $Al2O_3$ with a Methanesulfonic Acid Inhibitor, *Chem. Mater.*, 2023, **35**, 5963–5974.

76 I. K. Oh, K. Kim, Z. Lee, K. Y. Ko, C. W. Lee, S. J. Lee, J. M. Myung, C. Lansalot-Matras, W. Noh, C. Dussarrat, H. Kim and H. B. R. Lee, Hydrophobicity of rare earth oxides grown by atomic layer deposition, *Chem. Mater.*, 2015, **27**, 148–156.

77 K. Wang, S. Yu, W. Li, Y. Song, P. Gong, M. Zhang, H. Li, D. Sun, X. Yang and X. Wang, Superhydrophobic and photocatalytic synergistic Self-Cleaning ZnS coating, *Appl. Surf. Sci.*, 2022, **595**, 153565.

78 P. N. Wani, S. K. Kale, S. S. Dahiwale, U. T. Nakate, S. U. Ekar, Y. T. Nakate, P. S. More, M. T. Sarode and Y. B. Khollam, Ion beam irradiation: Novel approach for preparation of Ag coated N doped nanocrystalline anatase TiO_2 films, *Mater. Sci. Eng. B*, 2023, **288**, 116212.

79 Y. Cao, A. Salvini and M. Camaiti, Multi-functional TiO_2-based nanocomposite coating with durable superhydrophobicity and enhanced photocatalytic and antimicrobial properties for the sustainable maintenance of building stones, *Constr. Build. Mater.*, 2023, **404**, 133139–133152.

80 H. N. C. Dharma, J. Jaafar, N. Widiastuti, H. Matsuyama, S. Rajabsadeh, M. H. D. Othman, M. A. Rahman, N. N. M. Jafri, N. S. Suhaimin, A. M. Nasir and N. H. Alias, A Review of Titanium Dioxide (TiO_2)-Based Photocatalyst for Oilfield-Produced Water Treatment, *Membranes*

(Basel)., 2022, **12**, 1-22.

81 Y. Nosaka and A. Y. Nosaka, Reconsideration of Intrinsic Band Alignments within Anatase and Rutile TiO_2, *J. Phys. Chem. Lett.*, 2016, **7**, 431–434.

82 Q. Wang, Z. Liu, D. Liu, G. Liu, M. Yang, F. Cui and W. Wang, Ultrathin two-dimensional $BiOBr_xI_{1-x}$ solid solution with rich oxygen vacancies for enhanced visible-light-driven photoactivity in environmental remediation, *Appl. Catal. B Environ.*, 2018, **236**, 222–232.

83 P. Varshney and S. S. Mohapatra, Durable and regenerable superhydrophobic coatings for brass surfaces with excellent self-cleaning and anti-fogging properties prepared by immersion technique, *Tribol. Int.*, 2018, **123**, 17–25.

84 R. Xing, S. S. Latthe, A. K. Bhosale, R. Li, A. Madhan Kumar and S. Liu, A novel and facile approach to prepare self-cleaning yellow superhydrophobic polycarbonates, *J. Mol. Liq.*, 2017, **247**, 366–373.

85 F. I. Il'darkhanova, G. A. Mironova, K. G. Bogoslovsky, V. V. Men'Shikov and E. D. Bykov, Development of paint coatings with superhydrophobic properties, *Prot. Met. Phys. Chem. Surfaces*, 2012, **48**, 796–802.

86 R. Guo, Y. Bao, X. Zheng, J. Chen, H. Yang, W. Zhang, C. Liu and J. Xu, Superhydrophobic and Photocatalytic Synergistic Self-Cleaning Coating Constructed by Hierarchically Structured Flower-like Hollow SiO 2 @ TiO 2 Spheres with Oxygen Vacancies, *ACS Appl. Mater. Interfaces*, 2023, **15**, 47447–47462.

87 J. H. Lee, E. J. Park, D. H. Kim, M. Jeong and Y. D. Kim, Superhydrophobic surfaces with photocatalytic activity under UV and visible light irradiation, *Catal. Today*, 2016, **260**, 32–38.

88 A. Ansari and N. M. Nouri, A one step self-cleaning surface with robust superhydrophobic and photocatalytic properties: Electrostatic sprayed fluorinated ethylene propylene mixed with nano TiO_2–SiO_2 particles, *Ceram. Int.*, 2023, **49**, 57–66.

89 F. L. Heale, M. Einhorn, K. Page, I. P. Parkin and C. J. Carmalt, Dual-scale TiO_2 and SiO_2 particles in combination with a fluoroalkylsilane and

polydimethylsiloxane superhydrophobic/superoleophilic coating for efficient solvent-water separation, *RSC Adv.*, 2019, **9**, 20332–20340.

90 C. Agustín-Sáenz, M. Machado and A. Tercjak, Polyfluoroalkyl-silica porous coatings with high antireflection properties and low surface free energy for glass in solar energy application, *Appl. Surf. Sci.*, 2020, **509**, 144864.

91 T. Nishino, M. Meguro, K. Nakamae, M. Matsushita and Y. Ueda, The lowest surface free energy based on -CF3 alignment, *Langmuir*, 1999, **15**, 4321–4323.

92 C. R. Crick, J. C. Bear, P. Southern and I. P. Parkin, A general method for the incorporation of nanoparticles into superhydrophobic films by aerosol assisted chemical vapour deposition, *J. Mater. Chem. A*, 2013, **1**, 4336–4344.

93 S. Park, J. Huo, J. Shin, K. J. Heo, J. J. Kalmoni, S. Sathasivam, G. B. Hwang and C. J. Carmalt, Production of an EP/PDMS/SA/AlZnO Coated Superhydrophobic Surface through an Aerosol-Assisted Chemical Vapor Deposition Process, *Langmuir*, 2022, **38**, 7825–7832.

94 F. L. Heale, PhD Thesis, University College London, 2020.

95 J. J. Kalmoni, F. L. Heale, C. S. Blackman, I. P. Parkin and C. J. Carmalt, A Single-Step Route to Robust and Fluorine-Free Superhydrophobic Coatings via Aerosol-Assisted Chemical Vapor Deposition, *Langmuir*, 2023, **39**, 7731–7740.

96 C. Kapridaki and P. Maravelaki-Kalaitzaki, TiO_2-SiO_2-PDMS nano-composite hydrophobic coating with self-cleaning properties for marble protection, *Prog. Org. Coatings*, 2013, **76**, 400–410.

97 Y. Li, B. P. Zhang, C. H. Zhao and J. X. Zhao, Structure transition, formation, and optical absorption property study of Ag/SiO_2 nanofilm by sol-gel method, *J. Mater. Res.*, 2012, **27**, 3141–3146.

98 S. S. Latthe, H. Imai, V. Ganesan and A. V. Rao, Superhydrophobic silica films by sol-gel co-precursor method, *Appl. Surf. Sci.*, 2009, **256**, 217–222.

99 C. R. Crick and I. P. Parkin, A single step route to superhydrophobic

surfaces through aerosol assisted deposition of rough polymer surfaces: Duplicating the lotus effect, *J. Mater. Chem.*, 2009, **19**, 1074–1076.

100 S. Yu, Z. Guo and W. Liu, Biomimetic transparent and superhydrophobic coatings: From nature and beyond nature, *Chem. Commun.*, 2015, **51**, 1775–1794.

101 S. C. Dixon, W. J. Peveler, N. Noor, J. C. Bear and I. P. Parkin, Superhydrophobic Au/polymer nanocomposite films via AACVD/swell encapsulation tandem synthesis procedure, *RSC Adv.*, 2016, **6**, 31146–31152.

102 M. Liu, J. Sun and Q. Chen, Influences of heating temperature on mechanical properties of polydimethylsiloxane, *Sensors Actuators, A Phys.*, 2009, **151**, 42–45.

103 K. S. Jaw, C. K. Hsu and J. S. Lee, The thermal decomposition behaviors of stearic acid, paraffin wax and polyvinyl butyral, *Thermochim. Acta*, 2001, **367**–**368**, 165–168.

104 G. McHale, N. J. Shirtcliffe and M. I. Newton, Contact-angle hysteresis on super-hydrophobic surfaces, *Langmuir*, 2004, **20**, 10146–10149.

105 G. Caminoa, S. M. Lomakin and M. Lazzari, Polydimethylsiloxane thermal degradation. Part 1. Kinetic aspects., *Polymer (Guildf).*, 2001, **42**, 2395–2402.

106 X. Zhu, Z. Zhang, X. Men, J. Yang, X. Xu and X. Zhou, Plasma/thermal-driven the rapid wettability transition on a copper surface, *Appl. Surf. Sci.*, 2011, **257**, 3753–3757.

107 C. G. Jothi Prakash and R. Prasanth, Approaches to design a surface with tunable wettability: a review on surface properties, *J. Mater. Sci.*, 2021, **56**, 108–135.

108 F. Chen, Y. Wang, Y. Tian, D. Zhang, J. Song, C. R. Crick, C. J. Carmalt, I. P. Parkin and Y. Lu, Robust and durable liquid-repellent surfaces, *Chem. Soc. Rev.*, 2022, **51**, 8476–8583.

109 V. Diesen, M. Jonsson and I. P. Parkin, Improved texturing and photocatalytic efficiency in TiO_2 films grown using aerosol-assisted CVD and atmospheric pressure CVD, *Chem. Vap. Depos.*, 2013, **19**, 355–362.

110 G. Shukla, C. Kumar and S. Angappane, Structural Properties and Wettability of TiO_2 Nanorods, *Phys. Status Solidi Basic Res.*, 2019, **256**, 1–7.

111 M. Yu, L. Yang, L. Yan, T. Wang, Y. Wang, Y. Qin, L. Xiong, R. Shi and Q. Sun, ZnO nanoparticles coated and stearic acid modified superhydrophobic chitosan film for self-cleaning and oil–water separation, *Int. J. Biol. Macromol.*, 2023, **231**, 123293.

112 Y. Wang, Z. Huang, R. S. Gurney and D. Liu, Superhydrophobic and photocatalytic PDMS / TiO 2 coatings with environmental stability and multifunctionality, *Colloids Surfaces A*, 2019, **561**, 101–108.

113 S. Wahyuningsih, R. E. Cahyono, F. N. Aini and A. H. Ramelan, Preparation Titanium Dioxide Combined Hydrophobic Polymer with Photocatalytic Self-Cleaning Properties, *Bull. Chem. React. Eng. Catal.*, 2020, **15**, 874–884.

114 L. Miao, L. F. Su, S. Tanemura, C. A. J. Fisher, L. L. Zhao, Q. Liang and G. Xu, Cost-effective nanoporous SiO_2-TiO_2 coatings on glass substrates with antireflective and self-cleaning properties, *Appl. Energy*, 2013, **112**, 1198–1205.

115 D. Lee, M. F. Rubner and R. E. Cohen, All-Nanoparticle Thin-Film Coatings, *Nano Lett.*, 2006, **6**, 2305–2312.

116 K. J. Heo, J. H. Yoo, J. Shin, W. Huang, M. K. Tiwari, J. H. Jung, I. P. Parkin, C. J. Carmalt and G. B. Hwang, Transition from the Wenzel to Cassie-Baxter state by PFOTES/TiO_2 nanoparticles leading to a mechanically robust and damage/contamination-recoverable surface, *J. Mater. Chem. A*, 2024, **12**, 3886–3895.

117 C. Garlisi, E. Trepci, X. Li, R. Al Sakkaf, K. Al-Ali, R. P. Nogueira, L. Zheng, E. Azar and G. Palmisano, Multilayer thin film structures for multifunctional glass: Self-cleaning, antireflective and energy-saving properties, *Appl. Energy*.

118 J. Liu, L. Ye, S. Wooh, M. Kappl, W. Steffen and H. J. Butt, Optimizing Hydrophobicity and Photocatalytic Activity of PDMS-Coated Titanium Dioxide, *ACS Appl. Mater. Interfaces*, 2019, **11**, 27422–27425.

119 M. J. Powell, R. Quesada-Cabrera, A. Taylor, D. Teixeira, I. Papakonstantinou, R. G. Palgrave, G. Sankar and I. P. Parkin, Intelligent Multifunctional $VO_2/SiO_2/TiO_2$ Coatings for Self-Cleaning, Energy-Saving Window Panels, *Chem. Mater.*, 2016, **28**, 1369–1376.

120 J. J. Kalmoni, C. S. Blackman and C. J. Carmalt, Tuneable Wetting of Fluorine-Free Superhydrophobic Films via Titania Modification to Enhance Durability and Photocatalytic Activity.

121 A. Mills, N. Wells and C. O'Rourke, Correlation between Δabs, ΔrGB (red) and stearic acid destruction rates using commercial self-cleaning glass as the photocatalyst, *Catal. Today*, 2014, **230**, 245–249.

122 P. Vitanov, P. Stefanov, A. Harizanova and T. Ivanova, XPS characterization of thin $(Al_2O_3)_x(TiO_2)_{1-x}$ films deposited on silicon, *J. Phys. Conf. Ser.*, 2008, **113**, 2–6.

123 S. Praserthdam, M. Rittiruam, K. Maungthong, T. Saelee, S. Somdee and P. Praserthdam, Performance controlled via surface oxygen-vacancy in Ti-based oxide catalyst during methyl oleate epoxidation, *Sci. Rep.*, 2020, **10**, 1–10.

124 W. E. Slink and P. B. DeGroot, Vanadium-titanium oxide catalysts for oxidation of butene to acetic acid, *J. Catal.*, 1981, **68**, 423–432.

125 L. L. Larina, O. Omelianovych, V. D. Dao, K. Pyo, D. Lee and H. S. Choi, Energy band alignment at the heterointerface between a nanostructured TiO_2 layer and Au22(SG)18clusters: Relevance to metal-cluster-sensitized solar cells, *Nanoscale*, 2021, **13**, 175–184.

126 P. Praveen, G. Viruthagiri, S. Mugundan and N. Shanmugam, Structural, optical and morphological analyses of pristine titanium di-oxide nanoparticles - Synthesized via sol-gel route, *Spectrochim. Acta - Part A Mol. Biomol. Spectrosc.*, 2014, **117**, 622–629.

127 A. Chae, S. Doo, D. Kim, T. Y. Ko, T. Oh, S. J. Kim, D. Y. Koh and C. M. Koo, Tunable $Ti_3C_2T_x$MXene-Derived TiO_2 Nanocrystals at Controlled pH and Temperature, *Langmuir*, 2022, **38**, 12657–12665.

128 O. V. Almjasheva, Formation and structural transformations of nanoparticles in the TiO_2–H_2O system, *Nanosyst. Physics, Chem. Math.*,

2016, **7**, 1031–1049.

129 Q. Liu, J. Yu and H. Wang, The role of the substrate roughness in contact angle hysteresis and dynamic deviation, *Int. J. Heat Mass Transf.*, 2020, **148**, 118985.

130 R. Quesada-Cabrera, A. Mills and C. O'Rourke, Action spectra of P25 TiO_2 and a visible light absorbing, carbon-modified titania in the photocatalytic degradation of stearic acid, *Appl. Catal. B Environ.*, 2014, **150**–**151**, 338–344.

131 W. Lin, J. Zheng, L. Yan and X. Zhang, Sol-gel preparation of self-cleaning SiO_2-TiO_2/SiO_2-TiO_2 double-layer antireflective coating for solar glass, *Results Phys.*, 2018, **8**, 532–536.

132 C. Tao, X. Zou, K. Du, G. Zhou, H. Yan, X. Yuan and L. Zhang, Fabrication of robust, self-cleaning, broadband TiO_2–SiO_2 double-layer antireflective coatings with closed-pore structure through a surface sol-gel process, *J. Alloys Compd.*, 2018, **747**, 43–49.

133 I. Dundar, A. Mere, V. Mikli, M. Krunks and I. O. Acik, Thickness effect on photocatalytic activity of TiO_2 thin films fabricated by ultrasonic spray pyrolysis, *Catalysts*, 2020, **10**, 1–13.

134 A. Vahl, S. Veziroglu, B. Henkel, T. Strunskus, O. Polonskyi, O. C. Aktas and F. Faupel, Pathways to tailor photocatalytic performance of TiO_2 thin films deposited by reactive magnetron sputtering, *Materials (Basel).*, 2019, **12**, 2840–2858.

135 R. Gorthy, A. Wasa, J. G. Land, Z. Yang, J. A. Heinemann, C. M. Bishop and S. P. Krumdieck, Effects of post-deposition heat treatment on nanostructured TiO_2-C composite structure and antimicrobial properties, *Surf. Coatings Technol.*, 2021, **409**, 126857.

136 X. Wang, S. M. Tabakman and H. Dai, Atomic layer deposition of metal oxides on pristine and functionalized graphene, *J. Am. Chem. Soc.*, 2008, **130**, 8152–8153.

137 N. P. Dasgupta, X. Meng, J. W. Elam and A. B. F. Martinson, Atomic layer deposition of metal sulfide materials, *Acc. Chem. Res.*, 2015, **48**, 341–348.

138 H. Tiznado, M. Bouman, B. C. Kang, I. Lee and F. Zaera, Mechanistic details of atomic layer deposition (ALD) processes for metal nitride film growth, *J. Mol. Catal. A Chem.*, 2008, **281**, 35–43.

139 T. O. Kääriäinen, S. Lehti, M. L. Kääriäinen and D. C. Cameron, Surface modification of polymers by plasma-assisted atomic layer deposition, *Surf. Coatings Technol.*, 2011, **205**, S475–S479.

140 L. Zhang, Y. Feng, Y. Li, Y. Jiang, S. Wang, J. Xiang, J. Zhang, P. Cheng and N. Tang, Stable construction of superhydrophobic surface on polypropylene membrane via atomic layer deposition for high salt solution desalination, *J. Memb. Sci.*, 2022, **647**, 120289.

141 L. C. Wang, Y. Y. Han, K. C. Yang, M. J. Chen, H. C. Lin, C. K. Lin and Y. T. Hsu, Hydrophilic/hydrophobic surface of $Al2O_3$ thin films grown by thermal and plasma-enhanced atomic layer deposition on plasticized polyvinyl chloride (PVC), *Surf. Coatings Technol.*, 2016, **305**, 158–164.

142 S. V. Zhukovsky, A. Andryieuski, O. Takayama, E. Shkondin, R. Malureanu, F. Jensen and A. V. Lavrinenko, Experimental Demonstration of Effective Medium Approximation Breakdown in Deeply Subwavelength All-Dielectric Multilayers, *Phys. Rev. Lett.*, 2015, **115**, 1–5.

143 J. Nikkola, J. Sievänen, M. Raulio, J. Wei, J. Vuorinen and C. Y. Tang, Surface modification of thin film composite polyamide membrane using atomic layer deposition method, *J. Memb. Sci.*, 2014, **450**, 174–180.

144 S. Lee, H. Yoon, S. Lee, S. min Chung and H. Kim, Investigation of the hydrophilic nature and surface energy changes of HfO_2 thin films prepared by atomic layer deposition, *Vacuum*, 2024, **219**, 112756.

145 C. Hirschberg, N. S. Jensen, J. Boetker, A. Ø. Madsen, T. O. Kaäriaïnen, M. L. Kaäriaïnen, P. Hoppu, S. M. George, M. Murtomaa, C. C. Sun, J. Risbo and J. Rantanen, Improving Powder Characteristics by Surface Modification Using Atomic Layer Deposition, *Org. Process Res. Dev.*, 2019, **23**, 2362–2368.

146 M. Szindler, M. M. Szindler, P. Boryło and T. Jung, Structure and optical properties of TiO_2 thin films deposited by ALD method, *Open Phys.*, 2017, **15**, 1067–1071.

147 L. Aarik, T. Arroval, R. Rammula, H. Mändar, V. Sammelselg and J. Aarik, Atomic layer deposition of TiO_2 from $TiCl_4$ and O_3, *Thin Solid Films*, 2013, **542**, 100–107.

148 C. Jin, B. Liu, Z. Lei and J. Sun, Structure and photoluminescence of the TiO_2 films grown by atomic layer deposition using tetrakis-dimethylamino titanium and ozone, *Nanoscale Res. Lett.*, 2015, **10**, 1-9.

149 Y. Jang, B. Yang, J. Shin and J. An, Ultraviolet light-induced wettability control of ultrathin atomic layer deposited TiO_2 film surface, *Thin Solid Films*, 2017, **642**, 151–156.

150 B. Abendroth, T. Moebus, S. Rentrop, R. Strohmeyer, M. Vinnichenko, T. Weling, H. Stöcker and D. C. Meyer, Atomic layer deposition of TiO_2 from tetrakis(dimethylamino) titanium and H2O, *Thin Solid Films*, 2013, **545**, 176–182.

151 R. L. Wilson, C. E. Simion, C. S. Blackman, C. J. Carmalt, A. Stanoiu, F. Di Maggio and J. A. Covington, The effect of film thickness on the gas sensing properties of ultra-thin TiO_2 films deposited by atomic layer deposition, *Sensors (Switzerland)*, 2018, **18**, 1-13.

152 R. K. Sahoo, A. Das, S. K. Singh and B. K. Mishra, Synthesis of surface modified SiC superhydrophobic coating on stainless steel surface by thermal plasma evaporation method, *Surf. Coatings Technol.*, 2016, **307**, 476–483.

153 E. J. Ekoi, A. Gowen, R. Dorrepaal and D. P. Dowling, Characterisation of titanium oxide layers using Raman spectroscopy and optical profilometry: Influence of oxide properties, *Results Phys.*, 2019, **12**, 1574–1585.

154 S. Alofi, C. O'Rourke and A. Mills, Photocatalytic destruction of stearic acid by TiO_2 films: Evidence of highly efficient transport of photogenerated electrons and holes, *J. Photochem. Photobiol. A Chem.*, 2023, **435**, 114273.

155 J. B. Han, X. Wang, N. Wang, Z. H. Wei, G. P. Yu, Z. G. Zhou and Q. Q. Wang, Effect of plasma treatment on hydrophilic properties of TiO_2 thin films, *Surf. Coatings Technol.*, 2006, **200**, 4876–4878.

156 S. Oh, J. Shim, D. Seo, M. J. Shim, S. C. Han, C. Lee and Y. Nam,

Organic/inorganic hybrid cerium oxide-based superhydrophobic surface with enhanced weather resistance and self-recovery, *Prog. Org. Coatings*, 2022, **170**, 106998.

157 K. An, C. Long, Y. Sui, Y. Qing, G. Zhao, Z. An, L. Wang and C. Liu, Large-scale preparation of superhydrophobic cerium dioxide nanocomposite coating with UV resistance, mechanical robustness, and anti-corrosion properties, *Surf. Coatings Technol.*, 2020, **384**, 125312.

158 S. Khan, G. Azimi, B. Yildiz and K. K. Varanasi, Role of surface oxygen-to-metal ratio on the wettability of rare-earth oxides, *Appl. Phys. Lett.*, 2015, **106**, 1-5.

159 G. Azimi, R. Dhiman, H. M. Kwon, A. T. Paxson and K. K. Varanasi, Hydrophobicity of rare-earth oxide ceramics, *Nat. Mater.*, 2013, **12**, 315–320.

160 G. Carchini, M. García-Melchor, Z. Łodziana and N. López, Understanding and Tuning the Intrinsic Hydrophobicity of Rare-Earth Oxides: A DFT+U Study, *ACS Appl. Mater. Interfaces*, 2016, **8**, 152–160.

161 G. Malandrino, R. Lo Nigro, C. Benelli, F. Castelli and I. L. Fragalà, Volatile CeIII hexafluoroacetylacetonate glyme adducts as promising precursors for the MOCVD of CeO_2 thin films, *Chem. Vap. Depos.*, 2000, **6**, 233–238.

162 J. McAleese, J. C. Plakatouras and B. C. H. Steele, The use of Ce(fod)4 as a precursor for the growth of ceria films by metal-organic chemical vapour deposition, *Thin Solid Films*, 1996, **280**, 152–159.

163 S. Liang, C. S. Chern, Z. Q. Shi, P. Lu, Y. Lu and B. H. Kear, Control of CeO_2 growth by metalorganic chemical vapor deposition with a special source evaporator, *J. Cryst. Growth*, 1995, **151**, 359–364.

164 S. Yasmeen, M. R. Khan, K. Park, Y. Cho, J. W. Choi, H. S. Moon and H. B. R. Lee, Preparation of a hydrophobic cerium oxide nanoparticle coating with polymer binder via a facile solution route, *Ceram. Int.*, 2020, **46**, 12209–12215.

165 V. Kumar, W. F. Chen, X. Zhang, Y. Jiang, P. Koshy and C. C. Sorrell, Properties and performance of photocatalytic CeO_2, TiO_2, and CeO_2–TiO_2

layered thin films, *Ceram. Int.*, 2019, **45**, 22085–22094.

166 M. A. Ehsan, R. Naeem, A. Rehman, A. S. Hakeem and M. Mazhar, Facile fabrication of CeO_2–TiO_2 thin films via solution based CVD and their photoelectrochemical studies, *J. Mater. Sci. Mater. Electron.*, 2018, **29**, 13209–13219.

167 M. Evans, F. Di Maggio, C. Blackman and G. Sankar, AACVD synthesis of catalytic gold nanoparticle-modified cerium(IV) oxide thin films, *Phys. Status Solidi Curr. Top. Solid State Phys.*, 2015, **12**, 996–1000.

168 A. Filtschew, K. Hofmann and C. Hess, Ceria and Its Defect Structure: New Insights from a Combined Spectroscopic Approach, *J. Phys. Chem. C*, 2016, **120**, 6694–6703.

169 A. S. Dezfuli, M. R. Ganjali, H. R. Naderi and P. Norouzi, A high performance supercapacitor based on a ceria/graphene nanocomposite synthesized by a facile sonochemical method, *RSC Adv.*, 2015, **5**, 46050–46058.

170 K. Kuntaiah, P. Sudarsanam, B. M. Reddy and A. Vinu, Nanocrystalline $Ce_{1-x}Sm_xO_{2-\delta}$ (x = 0.4) solid solutions: Structural characterization versus CO oxidation, *RSC Adv.*, 2013, **3**, 7953–7962.

171 N.Ramjeyanthi, M. Alagar and D. Muthuraman, Synthesis, Structural and Optical Behavior of Cerium Oxide Nanoparticles by Co-Precipitation Method, *Int. J. Sci. Res. Sci. Technol.*, 2018, **4**, 1009–1013.

172 S. Hayun, S. V. Ushakov and A. Navrotsky, Direct measurement of surface energy of CeO_2 by differential scanning calorimetry, *J. Am. Ceram. Soc.*, 2011, **94**, 3679–3682.

173 L. Agosta, D. Arismendi-Arrieta, M. Dzugutov and K. Hermansson, Origin of the Hydrophobic Behaviour of Hydrophilic CeO_2, *Angew. Chemie - Int. Ed.*, 2023, **62**, 1–6.

174 A. S. Wexler and Z. Ge, Hydrophobic particles can activate at lower relative humidity than slightly hygroscopic ones: A Köhler theory incorporating surface fixed charge, *J. Geophys. Res.*, 1998, **103**, 6083–6088.

175 S. Jeon and H. Hwang, Effect of hygroscopic nature on the electrical

characteristics of lanthanide oxides (Pr_2O_3, Sm_2O_3, Gd_2O_3, and Dy_2O_3), *J. Appl. Phys.*, 2003, **93**, 6393–6395.

176 X. P. Li, Y. L. Sun, C. W. Luo and Z. S. Chao, UV-resistant hydrophobic CeO_2 nanomaterial with photocatalytic depollution performance, *Ceram. Int.*, 2018, **44**, 13439–13443.